Development of a boosted decision tree antineutrino photon near detector sample for T2K, and design of the Hyper-Kamiokande outer detector and DAQ

Menai Ruby Lamers James, MPhys (Hons)

Department of Physics

Lancaster University

A thesis submitted for the degree of

Doctor of Philosophy

July, 2024

Abstract

The Tokai-to-Kamioka (T2K) experiment makes world-leading measurements of the neutrino oscillation parameters using a high-purity beam of $\overset{(-)}{\nu}_\mu$, which are produced at the Japan Proton Accelerator Research Complex (J-PARC). They are detected at a near detector site, and at the far detector, Super-Kamiokande, 295 km away. The future Hyper-Kamiokande (Hyper-K) experiment, will make precision neutrino oscillation measurements, alongside a broad physics programme.

Due to its proximity to the beam source, the T2K near detector, ND280, can constrain systematic uncertainties on the flux and cross section parameters relevant to oscillation analyses. The events are split into sub samples, and the work in this thesis describes the addition of a new $\bar{\nu}$ charged current sample, CC-Photon. A new boosted decision tree particle identification tool was developed to improve the purity of the sample. The CC-Photon sample selection has an efficiency of $\sim$40% and purity of $\sim$42%, making it useful for the near detector, ND, fit. Detector systematics related to the new sample were evaluated. The fractional uncertainty on the predicted event rate of the CC-Photon sample was reduced from $\sim$ 14% to $\sim$2% after adding the sample to the ND fit. Improved parameter constraints will be propagated to the far detector.

Hyper-K will begin operation in 2027. It is expected to have better sensitivity to the oscillation parameters than any accelerator neutrino experiment currently in operation therefore its design must be robust. To ensure that the data acquisition system will be sufficient at handling the large quantity of data, a calculation of the detector data rate is made in this thesis. The Hyper-K outer detector is designed such that it will be efficient at detecting cosmic muon backgrounds, accounting for electronic failures which will emerge as the detector ages. Mitigation strategies are optimised in this thesis.

Declaration

The work presented in this thesis is a result of the author's individual work or in collaboration with members of the T2K and Hyper-Kamiokande collaborations. All work which was not performed by the author is appropriately referenced. The material has not been submitted, either in whole or in part, for a degree at this, or any other university. The author undertook this work as a student at Lancaster University and the Rutherford Appleton Laboratory

The primary contribution of the work presented in this thesis to the T2K experiment involved the development of the new antineutrino CC-Photon sample, and accompanying particle identification tool. The author was responsible for this sample development work with input from T2K collaborators in the selection development group. New detector systematic uncertainties were evaluated by the author with assistance from the selection, systematics and validation working group and conveners. Additional work was conducted for this group to validate the latest set of input files, known as 'production 7'. The new photon sample was implemented into the near detector fitting framework with assistance from collaborators in the near detector fitting, oscillation analysis, and MaCh3 working groups.

For the T2K experiment, work was also conducted as an on-call data acquisition expert, aiding in maintenance of the power supplies, electronic systems and general operation. Additional online shifts were performed during the COVID-19 pandemic in ensuring the INGRID detector was correctly operational.

The work conducted for the Hyper-Kamiokande collaboration involved performing a calculation of the data rate expected with aid from the data acquisition group. In turn some of the inputs used in event simulation were provided from the Kamioka cluster,

with external assistance from other members of the Hyper-Kamiokande collaboration. In addition to this work, evaluations of the failure scenarios that the outer detector of Hyper-Kamiokande may experience were undertaken. The work was possible with input from collaborators in the Hyper-Kamiokande outer detector working group. Alongside other factors, this work helped other more senior collaborators in making decisions regarding the electronic module configuration of the detector.

This thesis does not exceed the maximum permitted word length of 80,000 words including appendices and footnotes, but excluding the bibliography. A rough estimate of the word count is: 49215

Acknowledgements

Without the support and encouragement from lots of wonderful people with varying knowledge of particle physics, it would not have been possible for me to complete this work.

I want to start by thanking my supervisors: Helen O'Keeffe, Federico Nova, and Anna Holin, who have guided me throughout the last three and a half years and provided such valuable suggestions at every turn. I am very grateful to be one of few PhD students to have had three supervisors! Your combined knowledge in our supervision meetings was fundamental to my success in completing this PhD. I would also like to thank Alfons Weber who assisted in my supervision for the first few months of my PhD and shared lots of wisdom during that short period.

Alongside the support from my supervisors, I would also like to express my appreciation to members of the T2K and Hyper-K physics groups at Lancaster University; and the T2K/SK/HK group at the Rutherford Appleton Laboratory. In particular, I would like to thank Tristan Doyle for his help with the photon analysis as the expert on the neutrino version of this work. I would also like to thank Matt Lawe and Tom Dealtry for their assistance in helping me get to grips with all the T2K and Hyper-K software at the start of my PhD.

Thank you to the STFC for funding this work via my STFC RAL studentship, which was undertaken at Lancaster University and the Rutherford Appleton Laboratory.

I am very grateful for all the support which the memebers of the T2K and Hyper-Kamiokande collaborations provided in the various working groups I have had the privilege of working in with you. Special thanks to the T2K collaborators: Alexander Izmaylov, Sophie King, Kamil Skwarczynski, and Ewan Miller for their support during

the various phases of my T2K analysis, and to anyone else who has at any point provided feedback on my work. Members of the DAQ and OD group were instrumental in their help tackling all things software and spreadsheets. The data rate work was regarded as a rare instance where pie charts were encouraged. I look forward to continuing my work on Hyper-K after this PhD is finished!

During my six months living in Japan, I learnt a lot, and made many new friends along the way. Firstly, I would like to thank the ND280 DAQ group: Helen, Alfons, Giles, Clarence, Tomislav, Lukas, Weijun and Dan, for teaching me about the various misbehaviours of the ND280, and the many trips to Joyful Honda for tasty lunches. I also went on many adventures around Japan, including my first (and likely last) skiing trip! I would not have had anywhere near as much fun had it not been for Henry Wallace, Nick Latham, Katharina Lachner, Paul Morrison, Adam Speers, Ewan Miller, and everyone else local to Tokai at some point during my stay.

I must also thank my friends: Alice, Chrissie, the music gals, everyone from my undergrad days, and all of my friends from home, for their love and support throughout my thesis, especially during the tiresome lockdown days. I don't think many of you have a clue what my thesis is about, but I appreciate you being by my side before I started, and hopefully long after this work is finished.

Hopefully James, you realise just how much I appreciate everything you do for me, and all the support you provide. Finally, I want to thank my family: my parents, Carolien and Wyn, my brother, Ruben, Anti Eleri and Uncle Stephen. You have always been there for me, and I will be forever grateful for everything you have done for me. Anti Cerys, Mamgu and Dadcu, and Opa and Oma have each been a great inspiration to me and I know how very proud they would all have been to see me finish this PhD.

Contents

List of Figures

List of Tables

Chapter 1

Introduction

This thesis will be split into two parts. The first sections will detail the work undertaken for the Tokai-to-Kamioka (T2K) experiment, a current long baseline neutrino experiment which aims to better constrain the neutrino oscillation parameters using an accelerator neutrino beam.

The second part of the thesis will detail work carried out for the Hyper-Kamiokande (Hyper-K) experiment, a next generation water Cherenkov detector, currently under construction. The physics programme at Hyper-K is rich and includes precise measurements of the neutrino oscillation parameters, searches for nucleon (proton) decay, and observations of neutrinos from astronomical sources such as supernove.

The second chapter of this thesis will detail the theory behind neutrino physics. It will delve into the history of neutrinos, including its discovery, and give a detailed description of the theory of neutrino oscillations alongside an overview of the current understanding of the various oscillation parameters. This chapter will also describe some of the most important neutrino experiment facilities, and detail the various neutrino sources used in these experiments.

The next chapter will present an overview of the T2K experiment, including a description of the various detectors at the near and far detector facilities. Chapters 4 and 5 introduce the T2K analysis of this thesis - the development of a new near detector (ND) sample, with details on the various software tools and cuts implemented. The relevant detector systematic uncertainties associated with the new ND sample will be discussed.

Chapter 6 will describe the ND oscillation analysis, and include results of the ND fit using the new ND sample. This new ND sample will be officially included in new T2K oscillation analyses in 2025, which will use more data and an upgraded ND.

The second half of the thesis detailing the Hyper-K analyses, begins from chapter 8. An overview of the Hyper-K experiment is given, with details of the detector design, with special attention given to the outer detector (OD) (which serves as a cosmic ray muon veto) and data acquisition system design: the two areas of analysis relevant to this thesis. A description of the physics programme of Hyper-K, and its expected sensitivities is also given in chapter 8. The calculation of the far detector data rate, which is key to ensuring a data acquisition system that is robust to all event sources, is described in the following chapter. Chapter 10 investigates cases where failures may occur in the OD. This work describes two failure scenarios and considers ways in which the detector design may mitigate losses when failures occur. The final chapter presents conclusions and discusses future work.

Chapter 2

Theory of Neutrino Physics

2.1 Discovery of the Neutrino

The neutrino was first hypothesised in 1931 to explain the observed electron energy spectrum of nuclear beta decay [1]. Beta decay was thought to transform a nucleus into a lighter nucleus alongside the emission of an electron. In this two body decay, due to conservation of energy, the outgoing electron energy would be:

$$E_e = \left(\frac{m_A^2 - m_B^2 + m_e^2}{2m_A} \right) \tag{2.1}$$

where E_e is the energy of the outgoing electron, and $m_{A,B,e}$ are the masses of particles A, B and the outgoing electron. This two body decay involves the transformation of particle A to B, with the emission of the electron. In such a case, the electron energy would be fixed. However in 1914, when James Chadwick measured the energy of outgoing electrons from the beta decay of radium, it was discovered that the electron's energy varied, producing a continuous energy spectrum [2]. This discovery appeared

to violate energy conservation. In Wolfgang Pauli's letter beginning "Dear Radioactive Ladies and Gentlemen" [3] the neutrino was first postulated in an attempt to fix this supposed breaking of energy conservation. At the time, Pauli's neutrino was referred to as the "neutron" and was hypothesised to be electrically neutral, with spin 1/2 and its mass to be of the order of the electron mass or less [4]. Enrico Fermi later established a theoretical description of the three-body beta decay including the newly hypothesised particle, renaming it "neutrino" in the process [5]. It was not until 1956 that the neutrino was detected by Clyde Cowan and Frederick Reines [6] by searching for the inverse beta decay process:

$$\bar{\nu}_e + p \rightarrow e^+ + n \tag{2.2}$$

The large flux of electron antineutrinos needed to produce a detectable signal was attained using a nuclear reactor at the Savannah River Plant. A multi-layered detector made out of water tanks loaded with cadmium provided a proton target for the neutrinos. The water tanks were sandwiched between plastic scintillator detectors, and were used to observe inverse beta decay. In the experiment, an initial pair of 511 keV photons from positron annihilation provided a prompt signal. The resulting neutron was then captured through its interaction with the cadmium, which produced an excited state. When the excited state decayed, a single gamma was emitted and then detected. This second gamma signal was delayed with regard to the prompt photon signal by several micro seconds. Inverse beta decay events were tagged by observing both signals in coincidence. As the observed rate of coincidence was 20 times greater than the expected background, the discovery of the electron neutrino was confirmed.

In 1962, Leon Lederman, Melvin Schwartx and Jack Steinberger discovered the muon

neutrino [7]. The Brookhaven National Laboratory produced a muon neutrino beam for the experiment: the first accelerator neutrinos. The neutrino beam was formed by producing pions which then decayed into muons and muon neutrinos:

$$\pi^+ \rightarrow \mu^+ + \nu_\mu \tag{2.3}$$

An iron shield was used to absorb all non-neutrino particles, leaving only a muon neutrino beam. Behind the shield, a spark chamber recorded the tracks from particles produced in neutrino interactions with a neon target. A total of 29 events containing a single muon were observed. If a muon neutrino were identical to an electron neutrino, the number of electron events observed would be approximately equal to the number of muon events detected. However, only six electron-like events were observed. The results proved that the muon neutrinos were distinct from the electron neutrinos observed by Reines and Cowan. These newly discovered neutrinos were named muon neutrinos.

After the discovery of the tau lepton in 1975, it was assumed based on the weak interaction modelling, that an equivalent tau neutrino must exist. It was not until 2000 that the third neutrino type, the tau neutrino, and the final known neutrino flavour, was discovered by the DONUT experiment at Fermilab [8]. The observation was characterised by a kink in the particle track, an indication of tau decay into a charged particle with large transverse momentum. A total of four tau neutrino interactions were observed.

2.2 The Standard Model

The Standard Model is a robust theoretical model which describes the fundamental particles and their interactions. Neglecting gravity, these particles interact via one or more of three fundamental forces, which are mediated via gauge bosons. The forces are the strong force, mediated via gluons; electromagnetic force, via photons; and weak force, via the $W^{\pm}$ and Z^0 bosons. The fundamental particles which interact with these forces are divided into several groups. The first group, bosons, have integer spin. There are four spin-1 bosons which behave as the force carriers. There is also one further spin-0 boson: the Higgs boson. The Higgs boson is responsible for the non-zero mass of other Standard Model particles. The second group, fermions, have half-integer spin, and constitute all currently known matter. These fermions can be further divided into quarks and leptons.

In the Standard Model neutrinos are leptons. This means they lack colour and thus cannot participate in strong interactions. As the neutrino is electrically neutral, they cannot interact electromagnetically either. This leaves the weak interaction as the only viable interaction type for neutrinos to use. The weak force is also known to only interact with particles with left-handed chirality, and antiparticles with right-handed chirality. The chirality of a particle and antiparticle are defined as:

$$u_L = \frac{(1-\gamma^5)}{2}u \qquad \text{for particles} \tag{2.4}$$

$$\nu_L = \frac{(1+\gamma^5)}{2}\nu \qquad \text{for antiparticles} \tag{2.5}$$

where u and ν represent the particle spinor, and the gamma matrix γ^5 is:

$$\gamma^5 = \begin{pmatrix} 0 & 0 & 1 & 0 \\ 0 & 0 & 0 & 1 \\ 1 & 0 & 0 & 0 \\ 0 & 1 & 0 & 0 \end{pmatrix} \tag{2.6}$$

The helicity is the product of the spinor and momentum, which determines if the particle spin is pointing in the direction of motion.

The helicity and chirality of neutrinos was verified in 1958 by Goldhaber [9]. The chirality of neutrinos was confirmed to be left-handed and the helicity as -1, whereas antineutrinos were right-handed and their helicity equal to +1. This is only true assuming neutrinos are massless, which has since been disproved. When considering neutrinos with mass, helicity is no longer equal to chirality, and may flip.

According to the Standard Model, the neutrino is massless. However results from recent experiments indicate they have a small but finite mass. This is in contradiction to the Standard Model and points to new physics. Experiments such as KATRIN attempt to determine the neutrino mass by measuring the end-point of the tritium β-decay spectrum [10]. The global best limit on the neutrino mass, and current upper-limit set by KATRIN is $m_\nu < 0.45$ eV (90% confidence limit (CL)).

To date, only three light active neutrino flavours have been observed: the electron, muon and tau. The width of the Z^0 resonance is used to determine the total number of light active neutrino flavours experimentally. The total width of the Z^0 resonance,

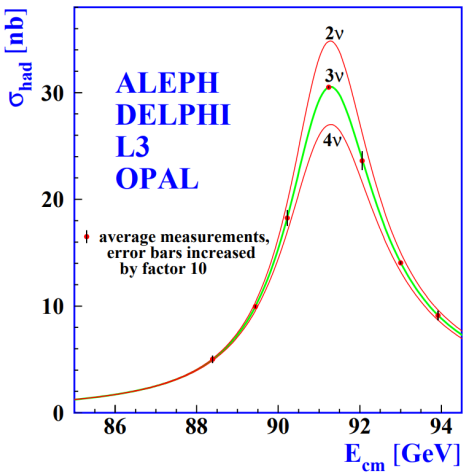

Figure 2.1: Hadron production cross-section around the Z^0 resonance. Two, three and four neutrino flavour cross-section predictions are indicated on the plot, assuming negligible neutrino mass [11].

can also be evaluated as the sum of its partial widths:

$$\Gamma_Z = 3\Gamma_{l^+l^-} + \Gamma_{hadrons} + N_\nu \Gamma_{\nu\bar{\nu}} \tag{2.7}$$

where $\Gamma_{l^+l^-}$, $\Gamma_{hadrons}$ and $\Gamma_{\nu\bar{\nu}}$ are the partial widths of the Z^0 decay to charged lepton pairs, hadrons and neutrino/antineutrino pairs respectively. The lepton pairs, l^+l^-, are e^+e^-, $\mu^+\mu^-$ and $\tau^+\tau^-$. Using experimental measurements of Γ_Z, $\Gamma_{e^+e^-}$, $\Gamma_{\mu^+\mu^-}$, $\Gamma_{\tau^+\tau^-}$ and $\Gamma_{hadrons}$, and the Standard Model predictions for $\Gamma_{\nu\bar{\nu}}$, the number of neutrino flavours, N_ν could be determined. The ALEPH, DELPHI, L3 and OPAL experiments all made measurements of the number of neutrino flavours which can couple to the weak interaction, and determined, in a combined result, to be 3.00 ± 0.08, which is in agreement with the three known light neutrino flavours [11]. It is possible that other neutrino flavours exist, however they must be heavier than the known neutrino flavours and have right-handed chirality. Such neutrinos are known as 'sterile' neutrinos [12]

and due to their chirality they do not participate in weak interactions.

2.3 Charged Current Neutrino Interactions

Neutrino interactions can be mediated via Charged Current (CC) or Neutral Current (NC) processes. For the purpose of standard neutrino oscillation analysis, such as the one described in this thesis, only the CC channels are considered as they result in the emission of a charged lepton of the same flavour as the neutrino, meaning the flavour of the interacting neutrino is known: allowing a better understanding of the oscillated neutrinos and thus the oscillation parameters. The NC interactions instead create a background to neutrino oscillation results as they do not produce a charged lepton in the final state. The alternative final states of NC interactions such as the production of a neutral pion which then decays into photons, may be incorrectly reconstructed as an electron - thus appearing as a CC signal event.

As the neutrino energy increases, different interaction modes dominate as seen in figure 2.2.

At lower neutrino energies, less than 1 GeV, interactions known as quasi-elastic (QE) are dominant. The neutrino CCQE interaction is:

$$\nu_l + n \rightarrow l^- + p$$

At comparable, and slightly higher energies than CCQE interactions occur, are meson charge exchange interactions, also referred to as 2-particle 2-hole (2p2h) neutrino interactions. The interaction involves the exchange of current with two nucleons, and also results in the emission of two nucleons from the nucleus [14].

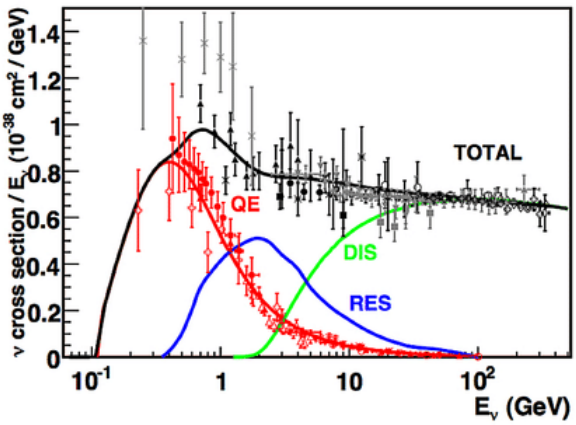

Figure 2.2: Neutrino CC cross section as a function of energy. Different dominating processes, quasi-elastic (QE), resonant (RES) and deep inelastic scattering (DIS) are indicated [13].

At slightly higher energies, 1-5 GeV, resonant (RES) interactions contribute the most to the neutrino interaction cross section. In these interactions, the nucleon enters an excited state, Δ-resonance, and upon decay back to a nucleon emits a pion. The most common neutrino interactions are:

$$\nu_\mu + p \rightarrow \mu^- + p + \pi^+$$

$$\nu_\mu + n \rightarrow \mu^- + p + \pi^0$$

$$\nu_\mu + n \rightarrow \mu^- + n + \pi^+$$

At energies above 5 GeV, deep inelastic scattering (DIS) interactions becomes dominant in the neutrino cross section. In DIS interactions, the nucleus is fragmented due to the neutrino interacting with the constituent quark. A high multiplicity of hadrons are produced in such an interaction. Feynman diagrams of the three processes, CCQE, RES and DIS, are found in figure 2.3.

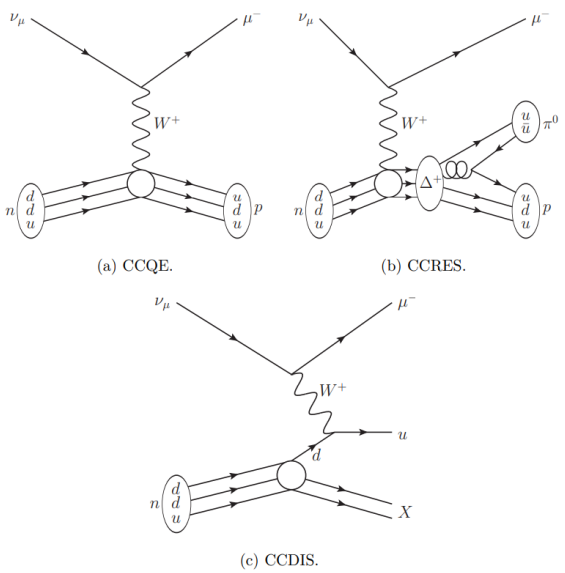

(a) CCQE. (b) CCRES.

(c) CCDIS.

Figure 2.3: Feynman diagrams of the CC quasi-elastic (CCQE), resonant (CCRES) and deep inelastic scattering (CCDIS) neutrino interactions for an incoming ν_μ [15].

2.4 The Solar Neutrino Problem

Stars such as the Sun produce an abundance of neutrinos from nuclear fusion reactions. For example, the proton-proton chain, which fuses protons to create heavier particles. The chain eventually results in ^{8}B decay, which produces a measurable flux of neutrinos.

$$^8_5\mathrm{B} \rightarrow \ ^8_4\mathrm{Be} + e^- + \nu_e \tag{2.8}$$

Along the proton-proton chain, neutrinos are emitted following various reactions, with different fluxes, and originate from different layers of the Sun's core, as shown in figure 2.4. These nuclear reactions are of interest to astrophysicists as a probe of the inner working of stars.

The flux of the neutrinos emitted by the Sun was predicted using the Standard Solar Model, developed by John Bahcall [17]. In 1968, Raymond Davis Jr. decided to test the

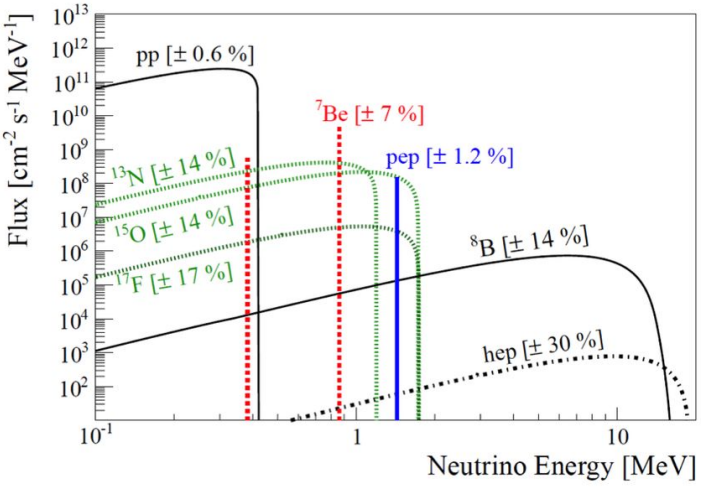

Figure 2.4: The solar neutrino flux, with relative contribution to the flux from the proton-proton chain shown in red [16].

solar model by measuring the flux of the neutrinos produced during the proton-proton chain [18]. The neutrinos were detected through inverse beta decay interactions:

$$\nu_e + {}^{37}\mathrm{Cl} \rightarrow {}^{37}\mathrm{Ar} + e^- \tag{2.9}$$

The detector tank contained 520 tons of chlorine and was located in the Homestake gold mine, South Dakota. Over a period of 25 years, 2200 ^{37}Ar atoms were detected, corresponding to a solar neutrino flux of 2.46 ± 0.16 (stat.)± 0.16 (syst.) Solar Neutrino Unit (SNU), defined as 10^{-36} captures per target atom per second. This flux was about a factor 3 lower than the $7.6^{+1.3}_{-1.1}$ SNU expected by Bahcall's solar model. This discrepancy between the theoretical prediction and experimental result became known as the solar neutrino problem. The apparent discrepancy led to extensive scrutiny of both the Solar Standard Model and of the experimental results presented by Davis. However no issues were found in either case. Three other experiments confirmed the

discrepancy. Kamiokande, in 1989 [19], a water Cherenkov detector, GALLEX in 1992 [20] and SAGE [21] in 1991, which both used a gallium target. Kamiokande observed interactions via Elastic Scattering (ES), and GALLEX and SAGE searched for inverse beta decay. GALLEX and SAGE were both sensitive to low energy neutrinos produced from the initial proton-proton reaction, due to switching from the use of chlorine to gallium as a target, lowering the energy threshold to 423 keV. As this is the dominant production process of the Sun, this added sensitivity allowed a direct probe of solar luminosity. Kamiokande, SAGE and GALLEX, each observed approximately half of the expected neutrino flux as predicted by the Solar Standard Model.

It was not until 2002 when the Sudbury Neutrino Observatory (SNO) made measurements of ^{8}B solar neutrinos, that the discrepancy was resolved. The SNO heavy water detector was sensitive to solar neutrino interactions mediated by both the CC and NC interactions, alongside ES [22]. CC interactions are sensitive to electron neutrinos only, meaning Davis and the other experiments were sensitive to electron neutrinos only. Elastic scattering and NC interactions however are sensitive to all neutrino flavours. Although ν_μ and ν_τ elastic scattering, which are mediated via only the Z boson, are suppressed, as ν_e elastic scattering can proceed via both W or Z exchange.

$$\nu_e + d \rightarrow p + p + e^- \text{ (CC)}$$
$$\nu_x + d \rightarrow p + n + \nu_x \text{ (NC)}$$
$$\nu_x + e^- \rightarrow \nu_x + e^- \text{ (ES)}$$

where ν_x refers to any of the three known neutrino flavours, ν_e, ν_μ, ν_τ. The results from the SNO CC process agreed with the measured value from Davis, (and the other experiments), and was around a third of the value predicted by the Solar Standard

Model. The NC process was equally sensitive to all flavours of neutrino. Thus, it could be used to measure the total flux of solar neutrinos irrespective of any flavour change that had occurred. The measured flux from NC interactions was in agreement with the flux predicted by the Standard Solar Model. The ratio of flux measured by the CC process to that measured by the NC process was not equal to one, which indicated that neutrino oscillations were occurring. The solution to the solar neutrino problem was that neutrinos change flavour as they propagate through the Sun. At around the same time, further evidence of neutrino oscillation was discovered in the atmospheric neutrino sector, which is described in the next section.

2.5 Atmospheric Neutrinos

When high energy cosmic rays interact with the nuclei of the upper layers of the Earth's atmosphere, showers of hadrons are produced. These hadrons, such as pions, decay into muons and muon neutrinos, which in turn decay into positrons and neutrinos.

$$\begin{aligned} \pi^+ \rightarrow & \mu^+ + \nu_\mu \\ & \hookrightarrow e^+ + \bar{\nu}_e + \nu_\mu \end{aligned} \tag{2.10}$$

The charge conjugated equivalent of equations 2.10 also occur. Assuming no oscillations, the ratio of the neutrino fluxes would naively be assumed to be:

$$R = \frac{\nu_\mu(\bar{\nu}_\mu)}{\nu_e(\bar{\nu}_e)} = 2 \tag{2.11}$$

A deviation from this theoretical prediction of no oscillation was observed by IMB [23], Kamiokande [24], and Super-Kamiokande (Super-K) [25]. By dividing atmospheric neutrino samples into upward and downward going categories, it is possible to establish two neutrino samples with different baselines, the distances between where they were produced and where they were detected. There is an approximately 13,000 km (diameter of Earth) difference between the two samples. The ratio of the neutrino flavours was found to be significantly smaller than the no-oscillation expectation, with a deficit of muon neutrinos present: $R = 0.65 \pm 0.05(\text{stat.}) \pm 0.08(\text{syst.})$ [25]. A zenith angle dependence in the muon neutrino deficit, and no up-down asymmetry in the electron neutrino samples was observed in the data. The deficit of muon neutrinos was due to $\nu_\mu \rightarrow \nu_\tau$ oscillation, which in turn has a dependence on the energy and distance travelled by the neutrino. This result was the first significant indication of neutrino oscillations, even before the SNO results.

2.6 Neutrino Oscillations

Currently neutrinos have only been described according to the flavour of the lepton which is produced in a neutrino interaction, e.g. an electron neutrino is the only neutrino type which interacts weakly to produce an electron. To preserve universality in the weak sector, Nicola Cabibbo introduced the Cabibbo angle in the quark sector [26]. This later evolved into the Cabibbo–Kobayashi–Maskawa (CKM) matrix which determines the mixing of the mass quark eigenstates involved in a weak interaction [27]. An equivalent format can be applied to the neutrino sector, where the neutrino flavours, ν_e, ν_μ, ν_τ correspond to weak eigenstates. A combination of mass eigenstates produces a weak eigenstate. These mass eigenstates exist as free massive particles,

unlike the weak eigenstates which only exist when participating in a weak interaction. The neutrino sectors equivalent of the CKM matrix which describes the mixing of the weak eigenstates is the Pontecorvo–Maki–Nakagawa–Sakata (PMNS) matrix, U_{PMNS}. It can be parametrised by three mixing angles, θ_{12}, θ_{13}, and θ_{23} and one complex phase, δ_{CP}:

$$U_{\mathrm{PMNS}} = \begin{pmatrix} 1 & 0 & 0 \\ 0 & c_{23} & s_{23} \\ 0 & -s_{23} & c_{23} \end{pmatrix} \begin{pmatrix} c_{13} & 0 & s_{13}e^{-i\delta_{\mathrm{CP}}} \\ 0 & 1 & 0 \\ -s_{13}e^{i\delta_{\mathrm{CP}}} & -0 & c_{13} \end{pmatrix} \begin{pmatrix} c_{12} & s_{12} & 0 \\ -s_{12} & c_{12} & 0 \\ 0 & -0 & 1 \end{pmatrix} \tag{2.12}$$

where $c_{jk} = \cos(\theta_{jk})$, $s_{jk} = \sin(\theta_{jk})$, where i and j = 1,2,3 and i$\neq$j, and δ_{CP} is the Charge Parity (CP) violating phase. The parameters which describe the PMNS matrix can be grouped to describe the neutrino sector most sensitive to that parameter: atmospheric (θ_{23}), solar (θ_{12}), and reactor/accelerator ($\theta_{13}, \delta_{\mathrm{CP}}$). An additional matrix, incorporating the Majorana phases, may also be added to the PMNS matrix as an additional multiplicative term. If neutrinos are Dirac particles, this additional Majorana component of the PMNS matrix is not required:

$$\begin{pmatrix} e^{i\alpha} & 0 & 0 \\ 0 & e^{i\beta} & 0 \\ 0 & 0 & 1 \end{pmatrix}$$

where the Majorana phases $\alpha = \beta = 0$ if neutrinos are Dirac particles. They are however required if neutrinos are Majorana particles, meaning a particle is its own antiparticle. Thus far there is no evidence to suggest neutrinos are Majorana particles, although experiments such as GERDA [28], CUORE [29], KamLAND-Zen [30], LEGEND [31],

SNO+ [32], and SuperNEMO [33] continue to explore this possibility by searching for a process called neutrinoless double beta decay.

2.7 Two Flavour Neutrino Oscillation

Neutrino oscillations are a quantum mechanical effect. To understand the quantum mechanical properties of neutrinos, a simpler two flavour case can be considered, using a 2 x 2 mixing matrix involving two neutrino flavours α and β undergoing rotation by angle θ:

$$\begin{pmatrix} \nu_\alpha \\ \nu_\beta \end{pmatrix} = \begin{pmatrix} U_{\alpha 1} & U_{\alpha 2} \\ U_{\beta 1} & U_{\beta 2} \end{pmatrix} \begin{pmatrix} \nu_2 \\ \nu_3 \end{pmatrix} = \begin{pmatrix} \cos\theta & \sin\theta \\ -\sin\theta & \cos\theta \end{pmatrix} \begin{pmatrix} \nu_1 \\ \nu_2 \end{pmatrix} \tag{2.13}$$

where $\nu_{\alpha,\beta}$ represent the weak states, and $\nu_{1,2}$ represent the mass states. The time evolution of a free particle can then be described as:

$$|\nu_{1,2}(t,L)\rangle = |\nu_{1,2}(0)\rangle\, e^{-i(E_{1,2}t - p_{1,2}L)} = |\nu_{1,2}(0)\rangle\, e^{-i\phi_{1,2}} \tag{2.14}$$

where t is the time after the creation of the neutrino, L is the distance travelled between creation and time t, E is the energy of the neutrino, p is the three momentum of the neutrino, and the angle $\phi = Et - pL$ is Lorentz invariant. The value of $\hbar$ is assumed to be 1 for these calculations. From the mixing matrix, in equation 2.13, the weak eigenstates can be written as:

$$|\nu_\alpha(t)\rangle = \cos\theta\,|\nu_1(t)\rangle + \sin\theta\,|\nu_2(t)\rangle = \cos\theta\,|\nu_1(0)\rangle\, e^{-i\phi_1} + \sin\theta\,|\nu_2(0)\rangle\, e^{-i\phi_2} \tag{2.15}$$

The weak eigenstates may then be expressed in terms of the mass eigenstates at t=0:

$$\begin{aligned}|\nu_\alpha(t=0)\rangle =& \cos\theta\,|\nu_1(0)\rangle\, e^{-i\phi_1} + \sin\theta\,|\nu_2(0)\rangle\, e^{-i\phi_2} \\ =&(\cos^2\theta e^{-i\phi_1} + \sin^2\theta e^{-i\phi_2})\,|\nu_\alpha(0)\rangle + \sin\theta\cos\theta(e^{-i\phi_1} - e^{-i\phi_2})\,|\nu_\beta(0)\rangle\,.\end{aligned} \tag{2.16}$$

The probability of observing state β at time t, from its initial state α is:

$$P(\nu_\alpha \to \nu_\beta) = |\,\langle\nu_\beta|\nu_\alpha(t)\rangle\,|^2 \tag{2.17}$$

The probability of observing $\nu_\mu \to \nu_\tau$ oscillations, one of the oscillation channels of interest to atmospheric and accelerator experiments, is:

$$P(\nu_\mu \to \nu_\tau(t)) = \sin^2(2\theta_{23})\sin^2\left(\frac{\phi_3 - \phi_2}{2}\right) \tag{2.18}$$

Due to the relativistic nature of neutrinos and the Lorentz invariant properties of ϕ, further approximations can be made. As the neutrino is relativistic, $E \simeq p$:

$$\phi_3 - \phi_2 = (E_3 - E_2)t - (p_3 - p_2)L \simeq \left(\frac{m_3^2 - m_2^2}{2E}\right)L = \frac{\Delta m_{32}^2 L}{2E} \tag{2.19}$$

where $E_k = \sqrt{p_k^2 + m_k^2} \simeq E_k + \frac{m_k^2}{2E_k}$, making approximations using the Taylor expansion. Finally, the two flavour oscillation probability is reached:

$$P(\nu_\mu \to \nu_\tau) = \sin^2(2\theta_{23})\sin^2\left(\frac{\Delta m_{32}^2 L}{4E}\right) \tag{2.20}$$

It is possible to convert this equation into a probability using more intuitive units:

$$P(\nu_\mu \to \nu_\tau) = \sin^2(2\theta_{23}) \sin^2\left(\frac{1.27\Delta m^2_{32} L}{E}\right) \tag{2.21}$$

where L is given in meters and E is in MeV. The survival probability, of an initial flavour state remaining constant at some later time t, can then be defined as:

$$\begin{aligned} P(\nu_\mu \to \nu_\mu) =& 1 - P(\nu_\mu \to \nu_\tau) & (2.22)\\ =& 1 - \sin^2(2\theta_{23}) \sin^2\left(\frac{1.27\Delta m^2_{32} L}{E}\right) & (2.23) \end{aligned}$$

2.8 Three Flavour Neutrino Oscillation

Equation 2.21 may be rewritten for three flavour oscillation as:

$$\begin{aligned} P\left(\overset{(-)}{\nu}_\alpha \to \overset{(-)}{\nu}_\beta\right) = \delta_{\alpha\beta} &- 4 \sum_{k>l=1}^{3} \Re\left(U_{\alpha k} U^*_{\beta k} U^*_{\alpha l} U_{\beta l}\right) \sin^2\left(\frac{\Delta m^2_{kl}}{4E}\right) \\ &\pm 4 \sum_{k>l=1}^{3} \Im\left(U_{\alpha k} U^*_{\beta k} U^*_{\alpha l} U_{\beta l}\right) \sin^2\left(\frac{\Delta m^2_{kl}}{4E}\right) \cos\left(\frac{\Delta m^2_{kl} L}{4E}\right) \end{aligned} \tag{2.24}$$

The three flavour oscillation probability introduces the CP-violating phase, δ_{CP}, and two mass-squared difference terms, Δm^2_{kl}. These differences are Δm^2_{21}, and Δm^2_{31}. As the sum of the three mass squared differences is zero, the third mass squared difference, Δm^2_{32}, is defined as $\Delta m^2_{32} = \Delta m^2_{31} - \Delta m^2_{21}$. One unknown of these mass squared differences is the mass ordering. Solar neutrino and reactor experiments have confirmed that the sign of Δm^2_{21} is positive. As the sign of Δm^2_{32} is yet to be determined, two mass orderings are possible: normal mass ordering, $m_3 > m_2 > m_1$ or inverted mass ordering,

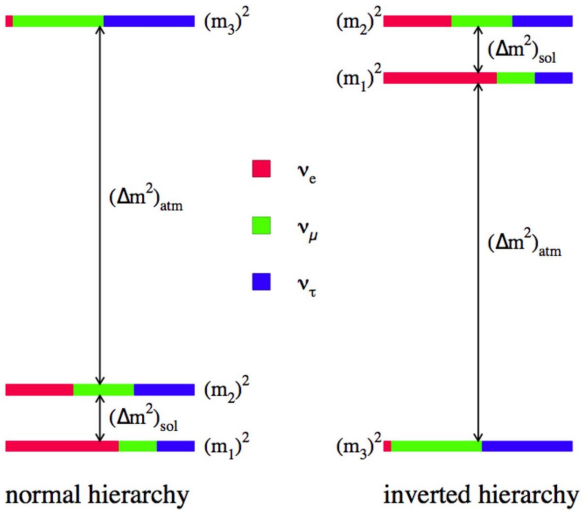

Figure 2.5: The two mass ordering schemes for neutrinos [34]. The mass ordering is also referred to as the mass hierarchy, as is shown in the figure.

$m_3 < m_1 < m_2$, as shown in figure 2.5. Determining the mass ordering of neutrinos remains an open question, key to understanding the neutrino mass mechanism. The CP phase, δ_{CP}, can also be determined via oscillation experiments. CP violation would result in differing oscillation probabilities for neutrinos and antineutrinos. Thus to determine the magnitude of the CP phase in the PMNS matrix, the quantity $\Delta P_{\alpha\beta} = P(\nu_\alpha - \nu_\beta) - P(\bar{\nu}_\alpha - \bar{\nu}_\beta)$ can be measured [35]. From equation 2.24 this quantity can be defined as:

$$\Delta P_{\alpha\beta} = \pm 16 J \sin\left(\frac{\Delta m^2_{21} L}{4E}\right) \sin\left(\frac{\Delta m^2_{31}}{4E}\right) \sin\left(\frac{\Delta m^2_{32}}{4E}\right) \tag{2.25}$$

where J is the Jarlskog invariant parameter:

$$J = \frac{1}{8} \cos\theta_{13} \sin 2\theta_{12} \sin 2\theta_{13} \sin 2\theta_{23} \sin\delta_{\text{CP}} \tag{2.26}$$

This implies that the three mixing angles must all be non-zero so that the CP violating phase, δ_{CP}, is measurable. It is only possible to measure δ_{CP} as the value of θ_{13} is relatively large, i.e. not close to 0. CP violation has already been observed in the quark sector [36], however it is not significant enough to explain the matter dominance of the Universe. The discovery of CP violation in the neutrino sector could help to explain the matter-antimatter imbalance, furthering physicists understanding of the formation of the early Universe.

2.9 Matter Effects

The oscillation probabilities considered so far assume neutrinos propagate through a vacuum. In reality, neutrinos also propagate through matter, such as the Earth, introducing additional changes to the oscillation probabilities. In matter, all neutrino flavours can interact via NC interactions and ν_e can also interact via CC interactions. This is because matter contains electrons but no muons or taus. An additional potential is included to the interaction Hamiltonian of ν_e to account for the additional CC interactions in matter. This correction to the behaviour of ν_e in matter is known as the Mikheyev-Smirnov-Wolfenstein (MSW) effect [37][38]. Matter effects introduce an additional term to oscillation calculations:

$$\begin{aligned} &\mp 8\frac{aL}{4E}c_{13}^2 s_{13}^2 s_{23}^2(1-2s_{13}^2)\cos\left(\frac{\Delta m_{32}^2}{4E}\right)\sin\left(\frac{\Delta m_{31}^2}{4E}\right) \\ &\pm 8\frac{a}{\Delta m_{31}^2}c_{13}^2 s_{13}^2 s_{23}^2(1-2s_{13}^2)\sin\left(\frac{\Delta m_{31}^2}{4E}\right) \end{aligned} \tag{2.27}$$

where c_{ij} and s_{ij} refer to $\cos\theta$ and $\sin\theta$, a $= 7.56 \times 10^{-5} \times \rho \times E_\nu$ [eV^2], ρ is the matter density [g cm^{-3}] and E_ν is the neutrino energy [GeV]. The sign of these additional

terms are reversed when considering antineutrinos. This can mimic a CP-violating signal. Therefore, accounting for matter effects in the neutrino sector is very important when seeking to determine whether CP-violation occurs.

2.10 Reactor Neutrino Experiments

Reactor experiments such as KamLAND [39], RENO [40], Daya Bay [41] and Double CHOOZ [42], use nuclear power plants as their source of antineutrinos. The detectors are situated within either a short distance of the reactors, less than 2 km, or involve a longer baseline such as KamLAND with a mean distance of 180 km. The large electron antineutrino flux produced by the reactors is measured using the inverse beta decay process to determine the disappearance probability at a variety of baselines. KamLAND was the first of the reactor experiments to confirm electron antineutrino disappearance from a reactor source to 99.95% CL. [43]. Using 53 Japanese reactors as neutrino sources of varying distances and energies, the experiment had sensitivity to the oscillation probability as a function of the neutrino energy and baseline, as shown in figure 2.6.

2.11 Accelerator Neutrino Experiments

Building on the principles developed by Lederman, Schwartz, and Steinberger, many modern neutrino experiments use an accelerator as a neutrino source. A detailed example of how a neutrino beam is produced, is given in section 3. The neutrino beam is usually characterised before oscillation at a ND, less than $\sim$1 km from the neutrino source. The neutrino beam is then aimed towards a detector a long distance

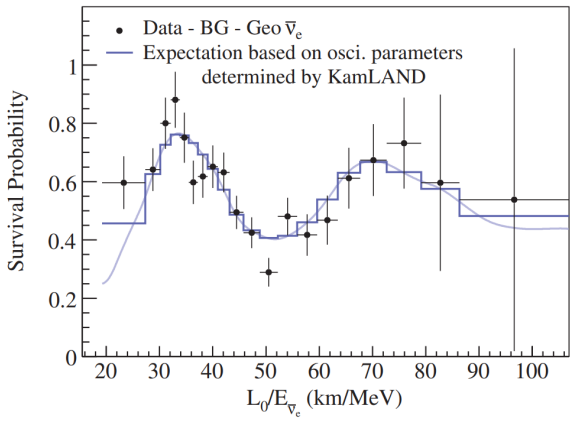

Figure 2.6: The ratio of $\bar{\nu}_e$ events (with backgrounds subtracted) to no oscillation expected spectrum as a function of L_0/E. The best fit line for oscillation is shown. The data points are for L_0=180 km assuming all antineutrinos were produced from the same reactor [44].

from the production point, of the order of hundreds of kilometers. The first long baseline neutrino experiment was K2K [45], in Japan. The experiment used a 98% pure ν_μ beam with mean energy of 1.3 GeV. Its ND complex included a series of fine grained detectors and a one kton water Cherenkov detector. The far detector (FD) was also a water Cherenkov detector, known as Super-K located 250 km from the neutrino source. Super-K continues to be used by T2K as its FD, and is detailed in section 3. Though the experiment did not find evidence of ν_e appearance, it was able to set limits on neutrino oscillation parameters via analysis of ν_μ disappearance [46]. Other long baseline experiments which are no longer active include MINOS [47] and OPERA [48]. MINOS was located in the USA, and was designed to search for ν_μ disappearance [49]. The MINOS experiment made use of both a near and far detectors in their analysis. The ND was located 1 km from the NuMI beam source, and the FD was located 735 km from the source. Both detectors were functionally identical, steel-scintillator sampling calorimeters [50]. By having similar detectors, many of the detector systematic

uncertainties cancelled leading to greater confidence in any oscillation results presented. MINOS completed a diverse physics measurement programme, and performed a joint ν_μ disappearance and ν_e appearance analysis, using both accelerator and atmospheric data [51]. OPERA is the final major inactive long baseline experiment which provided significant results in the neutrino oscillation sector [52]. The CNGS ν_μ beam at CERN was used and the experiment designed with the intention of measuring $\nu_\mu \rightarrow \nu_\tau$. This meant searching for tau signal events, differing from other experiments which only searched for muons and electrons. A finely segmented detector using 150,000 emulsion cloud chamber detectors was used to identify the tau signature kink topology, due to its decay into a muon. Although the sample size of signal events was statistically limited, a 5σ discovery of $\nu_\mu \rightarrow \nu_\tau$ oscillation was made. The next generation of long baseline neutrino experiments, which are currently in operation, T2K and NOνA, utilise the same facilities as was used by K2K and MINOS respectively.

Some experiments, including T2K [53] and NOνA [54], utilise the off-axis technique. This technique means the detectors are not placed directly in the beamline, but instead are located a small distance away to the side of the beam axis. This allows the detector to sample a smaller range of the beam energy distribution, specifically a lower energy region. This dependence is related to the meson kinematics as they decay in the beampipe, and result in an angular dependence on the neutrino energy:

$$E_\nu(\theta_\nu) = \frac{0.43 E_\pi}{1 + \gamma^2 \theta_\nu^2} \tag{2.28}$$

where $\gamma = \frac{E_\pi}{m_\pi}$, E_π is the energy of the decaying meson, and θ_ν is the angle of the emitted neutrinos relative to the beam axis. This results in a reduction in the neutrino flux as a result of shifting away from the centre of the beam. This method is utilised to target

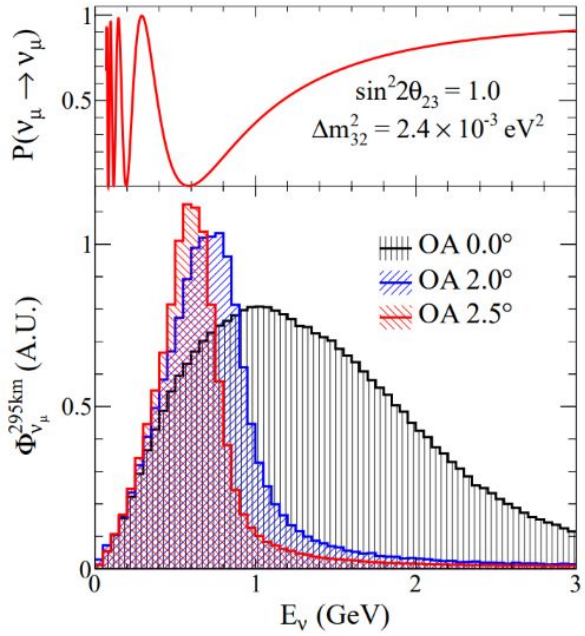

Figure 2.7: The T2K muon survival probability and flux at different off-axis angles [55].

neutrinos of a specific energy, dependent on the neutrino baseline, so that the neutrino oscillation probability can be maximised, as is shown in figure 2.7. The resulting beam is referred to as a narrow-band beam. Other experiments instead choose to use a wide beam for various reasons such as increasing the flux, and probing a broader neutrino energy spectrum.

The T2K experiment will be described in detail in section 3. The NOνA experiment utilises off-axis 2 GeV neutrinos produced by the NuMI beamline at Fermilab [54]. Unlike most experiments, the detectors are located at the surface. To handle the large flux of cosmic muons which would provide a significant background at the surface, the detectors must have excellent tracking capabilities. The detector target is liquid scintillator. The ND is 300 tons, and the FD is 14 ktons. NOνA provide key measurements of neutrino oscillation parameters as is described in section 2.13. A joint

T2K-NOνA analysis is in progress, which will be of interest due to the combination of both experiments' statistics, and due to the different technologies, neutrino energies and analysis techniques of the two collaborations.

Future long baseline experiments such as Hyper-K [56], which will be discussed in detail in section 7, and DUNE [57] are also planned to begin operation in the next ten years. DUNE will be built in the USA as part of the Fermilab neutrino physics programme [57]. The experiment consists of a series of liquid Argon TPC (LArTPC) NDs and a large LArTPC FD situated 1300 km from the source. The relatively new LArTPC technology will advance tracking capabilities allowing precision measurements. It is hoped that with newer technologies, increased neutrino beam power, and larger detectors, that these new experiments will be able to better determine the oscillation parameters as described in section 2.13.

2.12 Astrophysical Neutrino Observatories

A source of neutrinos with energies far higher, TeV-PeV scale, than the sources detailed in previous experiments is found from astrophysical sources such as supernova remnants, active galactic nuclei and gamma ray bursts. Experiments such as IceCube [58], ORCA/KM3NeT [59] and their predecessors, all use large natural water targets such as the Antarctic ice and Mediterranean sea, respectively, as a target. By instrumenting a large region it is possible to make interesting discoveries both astronomically and with regard to neutrino oscillations. IceCube have reported signal events originating from the Galactic plane with confidence up to 4.5σ [60].

Parameter	Global Fit Measurement	Leading Experiment(s)
$\sin^2(\theta_{12})$	$0.307^{+0.013}_{-0.012}$	KamLAND [62]
$\sin^2(\theta_{23})$ (Inv M.O.) $\sin^2(\theta_{23})$ (Norm M.O.)	0.539 ± 0.022 0.546 ± 0.021	T2K [63], NOνA [64]
$\sin^2(\theta_{13})$	0.0220 ± 0.0007	Double Chooz [41], RENO [65], Daya Bay [66]
Δm^2_{32} (Inv. M.O.) Δm^2_{32} (Norm. M.O.)	$-2.51 \pm 0.07 \times 10^{-3}\text{eV}^2$ $2.45 \pm 0.07 \times 10^{-3}\text{eV}^2$	T2K [63], NOνA [64]
Δm^2_{21}	$7.53 \pm 0.18 \times 10^{-5}\text{eV}^2$	KamLAND [67] [68]
δ_{CP}	$1.36^{+0.20}_{-0.16}$	T2K [63], NOνA [64]

Table 2.1: The global best fit results for each of the neutrino oscillation parameters [61]. Inv. M.O. refers to the inverted mass ordering, and Norm. M.O. to the normal mass ordering. The leading experiment(s) for each result is shown, however, the results are a global fit combining results from many experiments.

2.13 Current Neutrino Oscillation Knowledge

The neutrino sector makes use of measurements made from a range of experiments, such as solar, atmospheric, reactor, and accelerator neutrino experiments. These different experiments are sensitive to different oscillation parameters, and when combined, degeneracies found in one experiment alone can be mitigated. Table 2.1 shows the best measurements of the oscillation parameters, using the Particle Data Group (PDG) summary [61].

The δ_{CP} parameter is the least well known of the oscillation parameters, and tension between the measurements of different experiments are prevalent. A value of $\delta_{\text{CP}} = 0$ or π would indicate that CP is conserved in neutrino oscillations, whereas any other value would be evidence of CP violation, where $\delta_{\text{CP}} = \frac{\pi}{2}$ indicates maximal CP violation in the neutrino sector. The T2K one-dimensional contour for the measurement of δ_{CP} is shown in figure 2.8. To conclusively demonstrate that CP violation is present in neutrino oscillations, the CP conserving values must be excluded to 5σ.

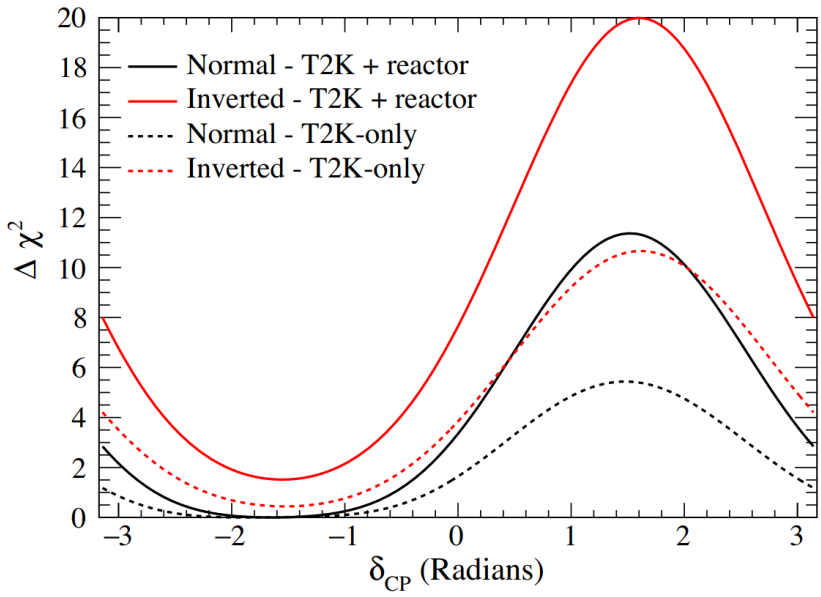

Figure 2.8: The T2K measurement of δ_{CP} showing $\Delta\chi^2 = -2\ln(L/L_{max})$ both with and without the reactor constraint on θ_{13} and for both normal and inverted mass ordering [69].

Chapter 3

The T2K Experiment

The T2K experiment is a long baseline neutrino oscillation experiment situated in Japan. The experiment uses a neutrino beam produced in Tokai by the Japan Proton Accelerator Research Complex (J-PARC). This neutrino beam passes through a suite of detectors, situated 280 m downstream of the source, that are designed to characterise the unoscillated beam. The neutrino beam travels 295 km through Japan to reach the FD, Super-K, located in Kamioka. A diagram of the T2K experiment is shown in figure 3.1. The aim of the experiment is to use a muon neutrino beam to study

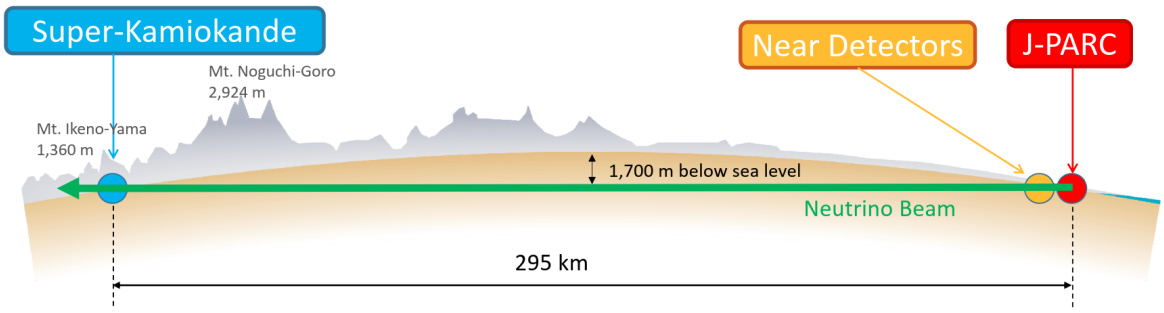

Figure 3.1: Schematic diagram of the T2K experiment [53].

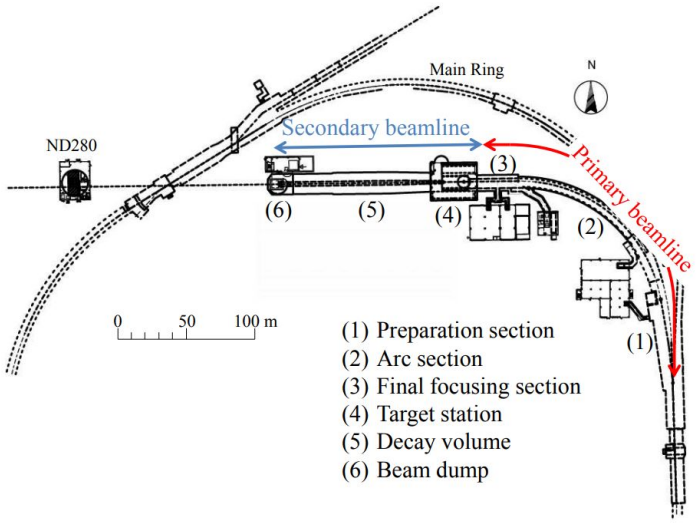

Figure 3.2: The T2K neutrino baseline with relevant components labelled [53].

muon neutrino disappearance and electron neutrino appearance channels. From these processes, the PMNS mixing parameters θ_{23}, θ_{13} and Δm^2_{23} can be measured, and δ_{CP} constrained.

3.1 The T2K Neutrino Beam

To produce a neutrino beam, the J-PARC accelerator complex collides a 30 GeV proton beam, consisting of eight bunches per spill, which is directed towards a graphite target. The primary beamline first focuses the protons at an angle of 2.5° away from the FD in Kamioka in order to produce a narrow-band beam as described in section 2.11. This means that the FD is 'off-axis' This is accomplished in two steps: first the preparation section, followed by the focusing section, as shown in figure 3.2.

During the preparation stage the beam is bent by 80.7° using 11 conducting and 14 doublet superconducting magnets [70]. In the focusing region, ten conducting magnets

direct the beam towards the target while ensuring the beam is directed downwards by 3.637° to send the neutrinos through the Earth towards the FD.

The stability, intensity, position, profile and loss-rate of the neutrino beam are measured using a series of monitors. The proton beam profile is monitored by the Optical Transition Radiation (OTR) monitor [71]. The OTR monitor contains a thin aluminium-alloy foil situated at an angle 45° with respect to the beam direction. The visible light produced when the beam enters the foil, from transition radiation, is detected by a charge injection device camera to produce an image of the beam profile. Once the beam has been oriented correctly so that it is aimed at the neutrino beam target, the products of the interaction with the target enter the secondary beamline.

The target is a graphite rod, which is 91.4 cm long and 2.6 cm in diameter. The graphite core is surrounded by a 2 mm thick graphite tube, which in turn is surrounded by a 0.3 mm titanium case [70]. When the protons interact with the carbon target, secondary hadrons, primarily pions and kaons, are produced.

To ensure that these mesons are all directed towards the neutrino detectors, three magnetic horns are used to focus the pions and kaons. The horns operate at 320 kA, and produce a maximal magnetic field of 2.1 T. The first horn, which is positioned around the target, collects the mesons. The second and third horns then focus these mesons to produce a beam. By tuning the beam with these horns, the neutrino flux at the FD increases by a factor of ~ 16 (relative to the flux when the horns have no current) at the peak energy. It is possible to invert the polarity of the horns so as to select either positively or negatively charged mesons. By selecting positively charged mesons the resulting decay will produce a neutrino beam, this is called Forward Horn Current (FHC) mode. Alternatively, selecting negatively charged mesons will produce

an antineutrino beam, Reverse Horn Current (RHC) mode. Once these mesons have been collected, they enter the decay volume. This volume is 96 m long, allowing the mesons to decay in flight. To produce a (anti)neutrino beam, the mesons decay as follows:

$$\begin{aligned} \pi^+ &\to \mu^+ + \nu_\mu, \qquad K^+ \to \mu^+ + \nu_\mu \\ \pi^- &\to \mu^- + \bar{\nu}_\mu, \qquad K^- \to \mu^- + \bar{\nu}_\mu \end{aligned} \tag{3.1}$$

The resulting beam is dominated by muon (anti)neutrinos, however there is a non-negligible electron (anti)neutrino contribution from processes such as:

$$\begin{aligned} K^+ &\to \pi^0 + e^+ + \nu_e, \qquad \mu^+ \to e^+ + \nu_e + \bar{\nu}_\mu \\ K^- &\to \pi^0 + e^- + \bar{\nu}_e, \qquad \mu^- \to e^- + \bar{\nu}_e + \nu_\mu \end{aligned} \tag{3.2}$$

As the T2K experiment is interested in ν_e appearance channels resulting from neutrino oscillations, understanding this intrinsic background is vital to distinguishing between signal and background for this analysis.

In RHC-mode, there is also a not insignificant contribution of wrong-sign neutrino contamination as seen in figure 3.3. This is due to the fact that a proton beam impacting a target produces $\sim$3 times more π^+ than π^-. It is also present in FHC-mode, but its effects are smaller than in RHC-mode. This background is produced when mesons pass through the centre of the horn and are unaffected by the magnetic field, and therefore are not rejected. The event rate is also enhanced in wrong sign RHC-mode due to the larger neutrino interaction cross section [72].

Downstream of the decay volume region is a beam dump. This contains a 75 ton graphite block, surrounded by 17 iron plates. Neutrinos will pass through this region,

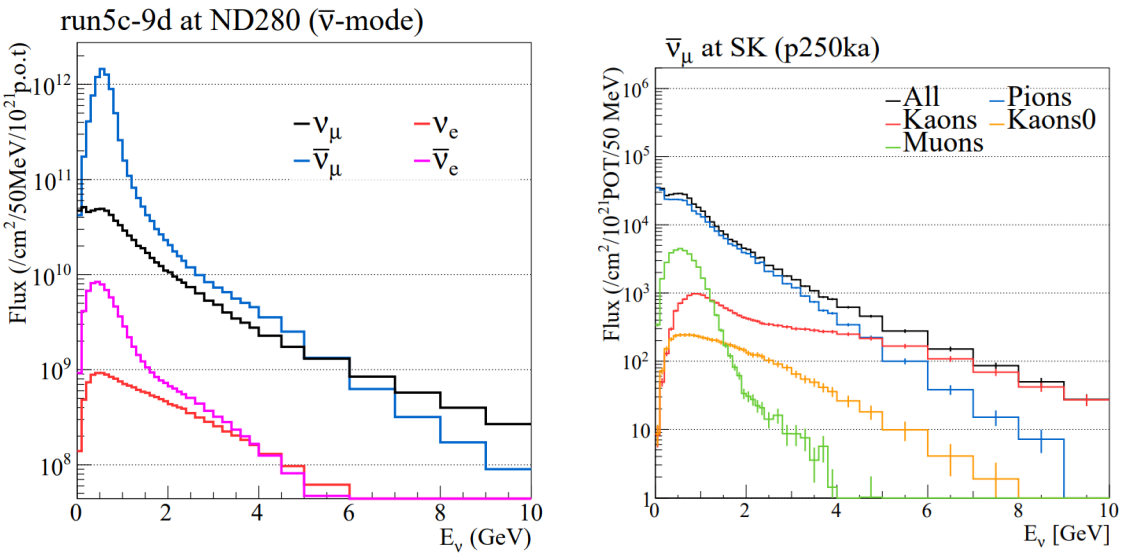

Figure 3.3: Unoscillated neutrino flux expected at the ND for antineutrino-mode (left) and the flux at the FD in antineutrino-mode (right) [72].

but most other particles such as hadrons and muons under ∼5 GeV/c, will stop in the volume. Muons above ∼5 GeV/c will pass through the beam dump, and are used as a sample to monitor the neutrino beam [73].

The muon monitor is used to define characteristics of the neutrino beam on a bunch-by-bunch basis. The muon profile is determined assuming a two-body pion decay, which is responsible for producing most of the neutrinos forming the beam. Using the direction of the centre of the muon profile to the centre of the target, the direction of the neutrino beam can be determined and monitored.

3.2 The Near Detector Complex

A series of specialised detectors are located 280 m downstream from the neutrino production target. These detectors are used to monitor the beam, make cross section

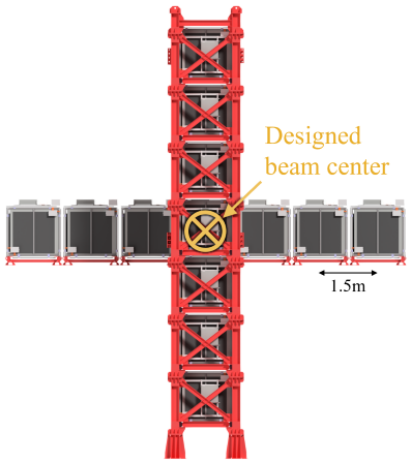

Figure 3.4: The INGRID on-axis detector. The 14 identical modules are arranged as a cross to monitor the neutrino beam properties.

measurements and characterise the unoscillated neutrino beam.

3.2.1 Interactive Neutrino GRID

The Interactive Neutrino GRID (INGRID) detector is positioned at the centre of the beam axis, referred to as on-axis, where the width of the neutrino beam is 5 m. The purpose of the detector is to monitor the neutrino beam direction and intensity. The detector is composed of 14 identical iron and scintillator modules. These modules are oriented to create a cross pattern along the vertical and horizontal axes relative to the beam direction, as seen in figure 3.4.

Each module consists of a sandwich of nine iron plates and 11 tracking scintillators. These are then surrounded by veto scintillator planes, to exclude events which occur outside of the module. The scintillator planes contain a hole down its central axis, with a wavelength shifting (WLS) fibre threaded through the hole, to collect the scintillation light. Each WLS fibre is connected to a Multi Pixel Photon Counter

(MPPC), which converts the light into an electrical signal and this is read out by the front-end electronics. Each module provides a 7.1 ton iron mass as a neutrino target. This large target mass ensures enough interactions occur to allow monitoring of the beam [53].

By measuring the neutrino interactions on iron, it is possible to determine the centre of the neutrino beam to better than 0.4 mrad. The beam direction must be within 1 mrad of the expected beam center. The stability of the beam is measured on a monthly basis [74]. The neutrino event rate is measured on a daily basis to ensure the stability of the neutrino beam intensity. The beam is considered to be stable if the rate is constant within a statistical uncertainty of $\sim$1.7 %.

3.2.2 The off-axis near detector (ND280)

The off-axis ND, ND280, is also located 280 m downstream of the target. However, in contrast to INGRID which is located on the beam's axis, ND280 is positioned at 2.5° off-axis of the beam centre similarly to the FD. The detector's purpose is to determine the flux, energy spectrum, electron neutrino contribution of the unoscillated beam and the wrong-sign content of the beam. It is important these properties are understood such that systematic uncertainties at the FD are minimised. Due to the large flux of neutrinos, as the detector is in close proximity to the beam source, the detector is also successful in providing a diverse neutrino interaction cross section programme. A series of magnetised subdetectors are combined to provide a full event reconstruction and identification of the neutrino interactions. A diagram of the detector is shown in figure 3.5. The subdetectors will be detailed in this section.

Two Fine Grained Detectors (FGDs) form part of the ND280, and these are

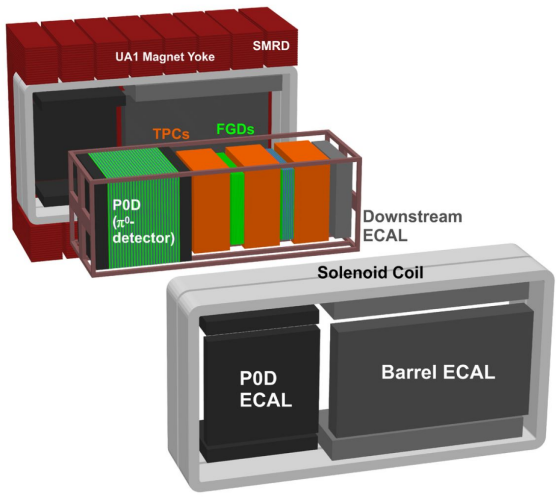

Figure 3.5: Exploded view of the ND280 detector. The PØD ECal, and barrel ECal is fixed to the magnet yoke. The neutrino beam enters the detector from the left of the diagram [53].

sandwiched between the three Time Projection Chambers (TPCs). These subdetectors form the tracker region of the ND280. Upstream of the tracker is the π^0 detector, PØD. Surrounding the tracker detectors and the PØD is the electromagnetic calorimeter (ECal). Enveloping all of these detector is the magnet, with side ranged muon detectors sandwiched in-between gaps of the magnet.

Since 2022, a major upgrade of the ND280 is in progress. The PØD [75] was removed and is being replaced with a series of new detectors: a Super-FGD, Time of Flight, and several High Angle TPCs. These new detectors are detailed in section 3.2.3.

3.2.2.1 The Fine-Grained Detectors

The FGDs provide a target mass for neutrino interactions in the ND280 [76]. A series of 9.61 mm × 9.61 mm × 1864.3 mm scintillator bars are oriented perpendicular to the beam to achieve the granularity required for the detector to reconstruct single tracks,

and to accurately determine the vertex position. A total of 192 scintillator bars are oriented in the horizontal direction, with a further 192 bars in the vertical direction. One 'XY module' consists of 384 scintillating bars: 192 bars oriented horizontally, which are attached to a further 192 vertically oriented bars. The first FGD, most upstream, known as FGD1, contains fifteen XY modules. The second FGD, FGD2, is composed of seven XY modules. The bars are coated with a reflective layer of TiO_2. A WLS fibre is placed through the axial hole, which is connected to a MPPC to digitise the light signal.

In FGD2, there are an additional six water target modules, alongside the seven XY plastic scintillating modules. The modules of the detector alternate from plastic scintillator to water. By having two different target materials, it is possible to make cross section measurements on both carbon and water. The water target is especially useful when making comparisons to the FD, which also uses water as a target. Each of the FGDs provides a $\sim$1 ton neutrino target. The FGDs tracking capabilities are also essential in identifying particle types and tracking of stopping particles (particles which do not exit the FGD volume). The FGD is able to identify particles by calculating the energy loss per unit length, dE/dX. To identify a particle, the total energy loss in the FGD is computed and compared with theoretical predictions as shown in figure 3.6.

3.2.2.2 Time Projection Chambers

The TPCs provide excellent tracking and particle identification (PID) capabilities [77]. Using the 0.2 T magnetic field, which operates around the tracker, it is possible to make a series of measurements related to any passing charged particles. A TPC is composed of two boxes one inside the other, and each TPC is 2.3 m $\times$ 2.4 m $\times$ 1.0

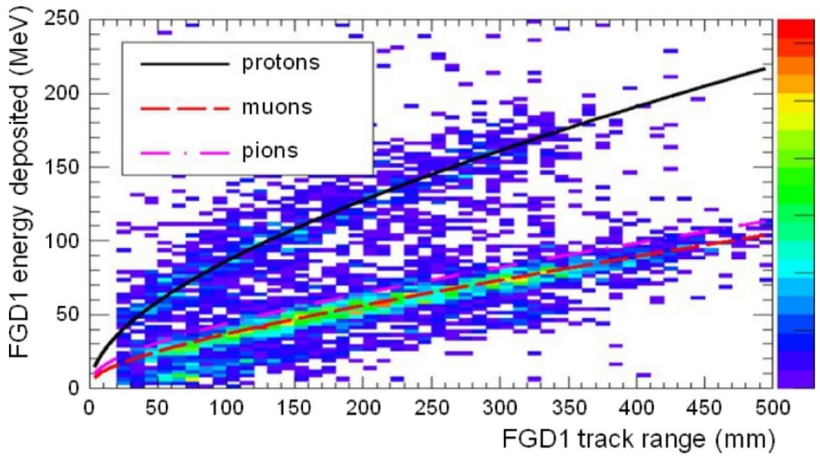

Figure 3.6: Energy deposited vs track range for particles stopping in FGD1. Scatter plot shows neutrino beam data stopping particles, and curves indicate MC predictions for protons, muons and pions [76].

m. The inner box is filled with an argon gas mixture, Ar:CF_4:iC_4C_{10}, and behaves as a field cage, and contains a cathode in its centre. The second box is filled with CO_2 and behaves as an insulator, as it is at ground potential. As charged particles pass through the TPCs, ionisation in the gas occurs. The resulting electrons drift from the central cathode to the readout planes. The electron signal is multiplied and sampled using a bulk micromegas detector. The micromegas have a high gain, and detect the electron signal before converting into an electrical signal. Twelve micromegas modules comprise two columns, with one on the top and one on the bottom of the inner box. The walls between the cathode and micromegas are covered in conducting strips, forming a voltage divider which provides an electric field along the drift direction of the magnetic field. Fine segmentation, 1728 pads per micromegas module, of these detectors provides a full 3D reconstruction of the traversing charged particles.

The most upstream TPC is TPC1, with TPC2 located in the centre of the ND280, and TPC3 the most downstream of the three. As was shown in figure 3.5, they are

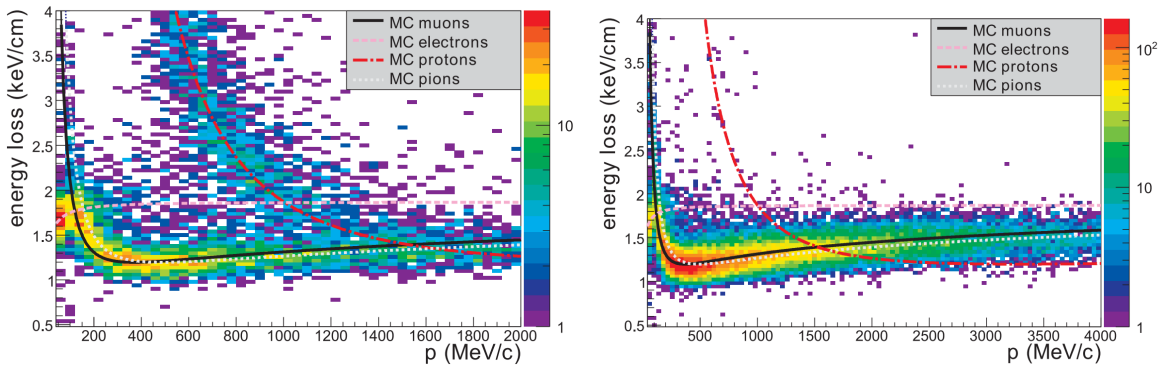

Figure 3.7: Energy loss of particles traversing the TPCs as a function of momentum for negatively and positively charged particles from neutrino interactions. Shown are expected curves for muon, electron, protons and pions [77].

sandwiched between the FGDs to reconstruct any particles in-going or outgoing of the TPCs. Due to the magnetic field, the curvature of charged particles in the TPCs permit measurements of momentum and charge. The PID measurements, involving the particle energy loss, such as those performed by the FGDs are also possible in the TPCs as shown in figure 3.7 [77]. However PID is better in the TPCs compared to the FGDs. The resolution of ionisation energy loss measurements in the TPCs for minimum ionising particles is $7.8 \pm 0.2\%$. A minimum ionising particle is a particle which loses near minimal energy as it propagates through matter, such as a muon. Different particles lose different amounts of energy allowing a PID to be made. It is therefore possible for the TPCs to distinguish between electrons, and muons. The probability of incorrectly identifying a muon as an electron is 0.2% for tracks below 1 GeV/c.

3.2.2.3 Electromagnetic Calorimeter

The ECal surrounds the FGDs and TPCs. It is a lead-scintillator sampling calorimeter which is split into three regions: the PØD ECal which will surround the upgrade

subdetectors, and used to surround the PØD at the most upstream part of the detector; the Barrel-ECal (Br-ECal), which surrounds the tracker; and the downstream ECal (Ds-ECal), which is in the most downstream region of the detector. The PØD-ECal and Br-ECal both consist of six modules, two at the top, two at the bottom, and two at the side. The Ds-ECal is a single module.

An ECal module comprises of layers of scintillating polystyrene and lead sheets. The lead sheets act as a radiator to produce electromagnetic showers and to also provide a neutrino interaction target. A module is thick enough such that at least 10 electron radiation lengths, X_0, should contain more than 50% of the emitted energy from photon showers produced by a π^0 decay [78]. The Br-ECal contains 31 layers, 10 X_0, and the Ds-ECal contains 34 layers, 11 X_0. The PØD-ECal contains six scintillating layers, and has thicker lead, 4 mm rather than 1.75 mm, than the other ECal modules. The layers are thicker to aid in π^0 reconstruction which were made in the PØD module. These layers alternate their orientation by 90° to provide a full reconstruction of the electromagnetic showers. A scintillating layer contains a WLS fibre which runs down the centre of each bar. Any light which is produced by charged particles passing through the 2.04 - 2.34 m long bars will be detected by the WLS fibre and transferred to the MPPCs to be counted. The Ds-ECal WLS fibres are double-ended, meaning they are read out at both ends; whereas the Br-ECal alternates between double and single-readout. In the case of the single-readout bars, one end is mirrored with aluminium and the other is connected to an MPPC.

The ECal surrounds the FGDs and TPCs to provide full 3D reconstruction, including neutral particles that the inner trackers may miss. By providing detailed reconstruction of electromagnetic showers, additional PID measurements may be made

using different methods than are used by the FGDs and TPCs [78].

3.2.2.4 Magnet

The FGDs, TPCs, and ECal, are surrounded by a 0.2 T magnet. The magnetic field allows for measurements of particle momenta and charge in the inner detectors by bending charged particle tracks. The magnet is composed of aluminium coils to form the horizontal dipole field, and the flux return yoke. The magnet is split into two C-shaped segments which can be moved on rails such that the magnet may be opened to access the inner components of the ND280 detector.

3.2.2.5 Side Muon Range Detector

The side muon range detector (SMRD) is located in the air gaps of the magnet yoke. It consists of plastic scintillating layers which aim to detect any escaping muons from neutrino interactions, and to measure the momenta of these particles. It also detects background events from neutrino interactions in the SMRD, and provides a cosmic muon trigger for the global ND280 system. The SMRD system consists of 192 horizontally oriented and 248 vertically oriented modules. These modules are made from polystyrene-based scintillator with a WLS fibre inserted into the centre of the panel, with readout on both ends. The WLS fibre is arranged in a serpentine shape such that even coverage of the module is achieved and the use of photosensors is minimised.

3.2.3 ND280 Upgrade Detectors

In recent years upgrades have been made to the ND280 detector to reduce the systematic uncertainties on flux and cross section parameters, currently at $\sim$6%, down to $\sim$4% for

T2K operation, and ∼3% for Hyper-K operation [79]. Three new subdetectors: the Super-FGD, High Angle TPC and Time of Flight (TOF) detector will all be located in the empty cavern where the PØD used to reside - upstream of the current ND280 tracker. Upstream of the upgraded detectors, the calorimeter upstream of the PØD remains, and is used as a veto, and to track neutral particles.

The Super-FGD is composed of two million 1 cm^3 scintillator cubes, with each side read out by a WLS fibre, providing 3D reconstruction [80]. The detector will be sandwiched between two High-Angle TPCs which are readout by resistive micromegas modules - providing high resolution tracking and PID. Surrounding these detectors will be six TOF planes, which will provide an excellent timing resolution of ∼130 ps [81]. The TOF may also inform in PID measurements and provide cosmic triggers to the other upgraded detectors. With updated technologies, such as the use of machine learning, and a higher granularity in the Super-FGD, it will be possible to achieve a 4π solid angle coverage of charged particles, providing a better comparison to the FD, which selects events without angular constraints. There are also additional improvements in reconstruction: a lower proton momentum threshold of 300 MeV/c, ability to measure neutron kinematics, and increased statistics from doubling the target mass. The improved reconstruction capabilities of the upgraded detectors will be important in reducing the cross section and flux uncertainties relevant to neutrino oscillation analyses. It is hoped that the post-fit uncertainties will be reduced by 30% with the addition of the upgraded detector data [79].

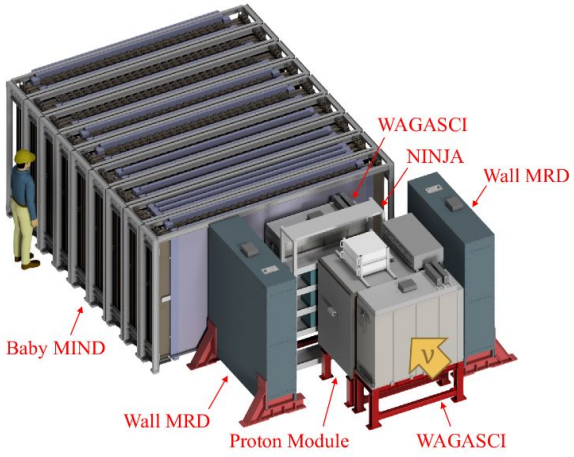

Figure 3.8: Schematic diagram of the WAGASCI and BabyMIND detectors [82] [83].

3.2.4 WAGASCI and BabyMIND

The ND280 complex includes an additional two subdetectors: WAter-Grid-And-SCIntillator (WAGASCI) and Magnetised Iron Neutrino Detector (BabyMIND). They are located at an off-axis angle of 1.5° to the beam, providing a beam spectrum with mean energy of 0.86 GeV. A diagram showing the WAGASCI and BabyMIND detectors is shown in figure 3.8.

The WAGASCI detector contains 0.6 tons of water and 1280 plastic scintillating bars. The water target provides 80% of the fiducial volume region and is greater in mass when compared with the FGD2 water target. It is useful to have another ND with a water interaction target, to better understand the neutrino cross section on water. Its large angular acceptance also matches that of the FD.

Surrounding the WAGASCI detector are the proton modules. These are tracking detectors composed of two types of scintillator bars. The scintillator bars also act as a secondary neutrino target [82]. Either side of the WAGASCI detector are two muon range detectors (MRDs) which aim to detect escaping particles.

The BabyMIND lies downstream of the WAGASCI detector, within a uniform magnetic field of 1.5 T. The purpose of this detector is to track and measure the momenta of muons with a high efficiency. The BabyMIND is a combination of 33 magnetised iron plates and 18 scintillator planes [84].

The two detectors are capable of providing cross section measurements, and work is in progress to add the data of these detectors to the T2K oscillation analyses in the future.

3.3 Super-Kamiokande

The FD of the T2K experiment where the oscillated neutrinos are detected is Super-Kamiokande (Super-K) [85]. It is located 295 km from the neutrino beam source and also sits at a 2.5° off-axis angle, the same angle as the ND280 off-axis detector. Super-K is a 50 kton ultra pure water Cherenkov detector with a diameter of 39 m and height of 42 m. The detector is located under a 1 km rock overburden to reduce cosmic muon background. A diagram of the detector is shown in figure 3.9.

The detector is split into two regions, an inner detector (ID) and an outer detector (OD). The physics interactions of interest to long baseline neutrino oscillation measurements are made in the ID, which is instrumented with 11,129 photomultiplier tubes (PMTs), each 50 cm in diameter. The OD surrounds the ID and is tasked with detecting cosmic muons which are a background to neutrino interactions. The OD accomplishes this task with a rejection efficiency of nearly 100% through the use of 1,885 PMTs which are 20 cm in diameter and point outwards, away from the main tank. The ID is optically separated from the OD by a 50 cm wide stainless steel scaffold structure. This structure is also wrapped in highly reflective Tyvek to aid the optical

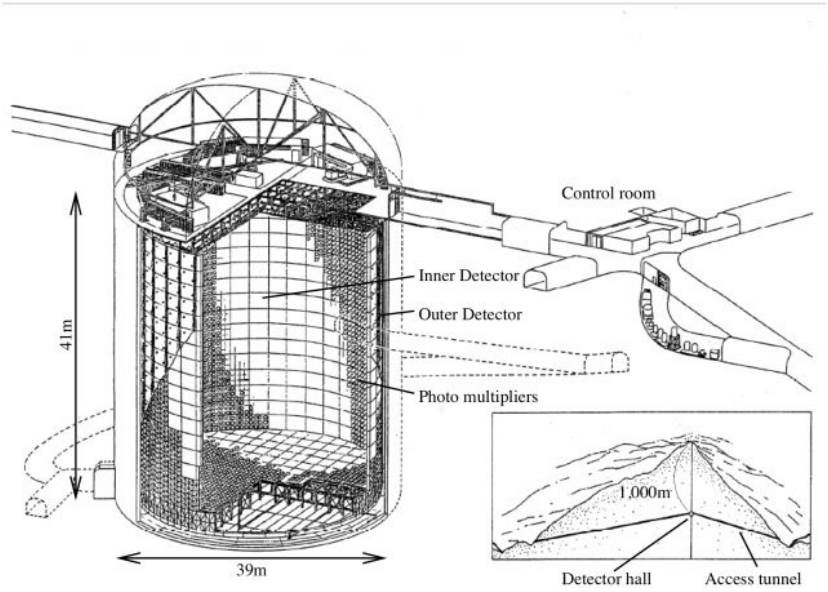

Figure 3.9: Sketch of the Super-K detector site [86].

separation and reflect light into the OD PMTs.

These PMTs detect charged particles via the Cherenkov light emitted as they travel through the water. Following a neutrino interaction in the water, a charged lepton, potentially alongside other particles dependening on the interaction type, is emitted. To produce Cherenkov radiation, the charged particle must be travelling faster than the speed of light in the medium such that the emitted photons produce a coherent wavefront emitted outwards with a fixed angle. It is also possible for the charged lepton to scatter as it travels through space causing it to lose momentum during these processes. The two primary charged leptons that Super-K searches for are muons and electrons, from the ν_μ beam and from ν_e appearance. As the mass of a muon is around 200 times greater than that of an electron, the momentum loss from the scattering of an electron leads to more electromagnetic showers than for muons. This leads to a difference in the Cherenkov rings which are observed by the detector. Muons tend

to have sharp well-defined rings, whereas electrons produce a 'fuzzy' ring due to the overlapping of multiple Cherenkov rings.

In theory $\nu_\mu \rightarrow \nu_\tau$ oscillations could also be measured, however a neutrino energy of above 3.5 GeV is required to produce a τ lepton. Given the neutrino flux has been tuned to peak at a neutrino energy of 0.6 GeV, the probability of observing a neutrino with energy high enough to exceed the threshold of detection for a ν_τ is low. Also, the τ leptons immediately decay to the other lepton flavours, making direct detection of a τ very challenging as it would be purely based on event kinematics [87].

The FD observes a variety of neutrino interaction types. The majority are CCQE interactions as the neutrino beam peaks at 0.6 GeV. In data it is not possible to be certain of the interaction type that occurred, therefore they are instead categorised by the number of each ring type observed. The single muon-like ring (1Rμ) and one electron-like ring (1Re) have been described. It is also possible to detect a delayed electron-like ring, which is initiated by a delayed Michel electron (referred to as 'd.e.'). A Michel electron is produced as a result of a muon decaying into an electron. A CC single pion-like interaction can be inferred by the presence of 1Re and 1 d.e.. A ν_μ interaction may also observe a d.e. as well. Recently a new sample was introduced to observe a CC single-pion from a muon ring, requiring 1Rμ, and 2 d.e.. These additional CC pion enhancing samples are currently only implemented in neutrino-mode. For antineutrino-mode it is only the 1Re and 1Rμ samples which are included in the oscillation analysis. This is because despite the detector receiving similar levels of Protons On Target (POT), the neutrino flux is suppressed for antineutrino mode, as shown earlier in figure 3.3 meaning these additional samples do not contain enough statistics in RHC mode.

In a tracking detector, a magnetic field is required to separate neutrino and antineutrino events by measuring the charge of the outgoing lepton. However, Super-K does not use a magnetic field, and it can make this differentiation by tagging the outgoing neutrons produced in antineutrino interactions. As neutrons are neutral particles they cannot be detected using Cherenkov light. Instead neutron capture is used to produce photons. Neutron capture can occur on the hydrogen nuclei of the water, with the emission of a single 2.2 MeV photon. They can also be captured on gadolinium (Gd), where a cascade of photons totalling 8 MeV, is emitted after a 180 μs delay from the prompt signal [88]. The Super-K detector was recently updated to add Gd to the water. Introducing Gd doping increases the cross section of neutron capture. This increases the detector's capabilities in separating antineutrino interactions from backgrounds through the inverse beta decay process. The goal is that 0.1% of the water mass will be gadolinium sulphate once doping is complete [89]. With the addition of Gd, the neutron capture efficiency is expected to increase from <20% to ∼90% due to the increased energy of the emitted photons and time delay allowing better separation from photons produced by other particles.

Chapter 4

Antineutrino Charged Current Photon Sample Selection

The ND280 is used in oscillation analyses to constrain flux and cross section parameters and determine the wrong-sign background and electron (anti)neutrino contamination in the beam[53]. To better define these parameters, ND events are split into topological categories based on the reconstructed final state particles. The Monte Carlo (MC) is then fitted to data for each sample, in terms of the lepton kinematics, as described in section 6. The topological categorisation of previous antineutrino samples related to the pion multiplicity of the final state [90], referred to as the multipi selection. It split events into three categories: a sample with no pions, CC0π; with only one negatively charged pion, CC1π^-; and events with more than one pion, CC-Other. These topologies typically tagged CCQE, CCRES and DIS interactions respectively.

The neutrino-mode equivalent of this selection also includes photon and proton multiplicity topologies [91]. The photon topology searches for at least one photon in the event; and the proton multiplicity samples split the CC0π sample into two dependent

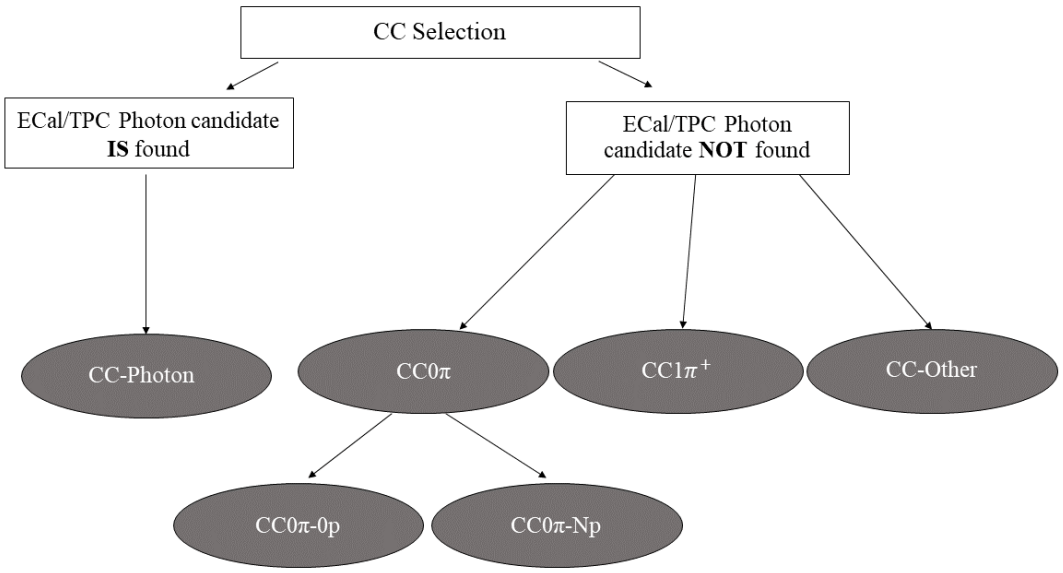

Figure 4.1: The selection logic of the neutrino-mode pion, photon and proton topology selection.

on whether or not a proton is present in the final state. A diagram of the neutrino-mode selection logic is shown in figure 4.1.

The antineutrino sample has been updated to include a fourth category 'CC-Photon' which requires at least one photon in the final state. Due to the selection logic, which will be outlined in section 4.3, improvements in the purity of the CC0π and CC1π^- samples are also achieved due to the addition of a photon sample. This section details the selection method for the photon sample.

4.1 Data and MC Samples

When developing the photon tagged sample for antineutrino-mode, a switch to a new production of files was implemented [92]. The new production contains major updates

to the neutrino interaction model implemented, improvements to reconstruction algorithms, updated detector geometry and a full reprocessing of the physics analyses. The validation of these files was completed using a subset of MC and data files, and once it was determined that validation was complete, the remaining files were processed. When the work in this thesis was completed, only two of the four antineutrino runs, referring to data-taking periods, were available for processing correctly with regard to optimising cuts. The reason the other two runs were not available was due to a change in the re-weighting scheme which had not been fully migrated to the analysis software tools, HIGH Level Analysis2 at the ND (HighLAND2), used for this work. However, for the work completed in section 6 all runs were included: runs 2 to 9. This is because a different software framework was used in this case, where re-weighting could be implemented correctly.

The runs used for the development of the selection and optimisation of photon tagging, as well as detector systematic uncertainty calculations were runs 6 and 7, referring to data accumulated between 2014 and 2016. The runs are also tagged according to the presence or absence of water in the PØD modules - run 6 involved an air target, and run 7 involved a water target. In addition to MC describing neutrino interactions which occur within the ND280 detector volume, referred to as 'magnet' MC, an additional simulation of interactions with the cavern rock and magnet of the ND280 is added. This MC simulation is referred to as 'sand'. These interactions have a small contribution to the rate of events selected in this analysis, but are included for completeness. Details on the number of POT obtained for each of these runs can be found in table 4.1.

The magnet and sand MC files used for this analysis, were produced using NEUT

T2K Run	Data POT ($\times 10^{20}$)	MC POT ($\times 10^{20}$)	Sand MC POT ($\times 10^{20}$)
6	3.41	33.03	22.89
7	2.44	33.30	22.89

Table 4.1: T2K data-taking antineutrino-mode runs used for this analysis for data and MC.

MC generator version 5.4.0 [93]. Sand neutrino interactions are simulated to originate outside of the magnet, in the surrounding rock or other material. They occur within the same time window as a Fiducial Volume (FV) event, and cause backgrounds to physics events. The generator simulates CCQE neutrino-nucleon interactions according to the Benhar Spectral Function (SF) [94]. The nuclear model assumes an axial mass of M_A^{QE} = 1.21 GeV/c^2. For non-QE interactions, the relativistic Fermi gas model [95] is used to simulate the initial momentum distribution of the nucleon. The 2p2h interaction model is described in Nieves et al. [96]. The model simulates RES pion production using the Rein-Sehgal model [97] where the invariant hadronic mass is $W \leq$2 GeV. The DIS cross section for $W >$1.3 GeV is simulated using GRV98 parton distribution functions with Bodek-Yang corrections [98]. To ensure no double counting with RES interactions, DIS interactions where a single pion is produced are suppressed when $W \leq$2 GeV. In cases where $W >$2 GeV, the PYTHIA/JETSET tools [99] are used for hadronisation. Final state interactions, where a hadron from a neutrino interaction goes on to interact with another nucleon before exiting the nuclear environment, are simulated with an intranuclear cascade [100].

After the particles have been simulated using NEUT, they are passed to Geant4 [101] to determine what the expected ND280 response would be for each MC event. To undertake physics analyses on the data and simulated MC at ND280, the software framework HighLAND2 is used. This software allows users to easily use and develop

new event selections, by applying a series of cuts to select events of interest to the analyser. Once a selection has matured and no further development on the selection and detector systematics uncertainties are anticipated, the new selection may be migrated to Propagation of SYstematics and CHaracterisation of Events (PSYCHE). Here the cuts cannot be modified and the variables which may be plotted are reduced to only the essential list relevant to the final selections and detector systematic uncertainties. This succinct propagation method allows for a more time-efficient processing of smaller files, and reduces room for error.

4.2 Charged Current Selection

Only Charged Current (CC) neutrino interaction samples are included in the oscillation analysis. Any Neutral Current (NC) events are omitted due to low purity, and samples are parameterised using the outgoing charged lepton kinematics, of which there are none in NC interactions. To select CC interactions, a series of cuts are applied to the MC and data events. The cuts are as follows:

Event Quality

An antineutrino beam is generated by striking protons, at a rate of 0.3 Hz, into a graphite target. These protons are grouped into bunches, with eight protons per bunch extracted in a time window of 15 ns. The bunches are then further categorised into a spill, containing eight bunches each in ~ 5 μs. It is only the protons contained in a spill that are associated with the beam trigger, which are selected. The mean and width of each bunch is measured, and tracks are selected only if they are within 4σ from the centre of a bunch.

Event Multiplicity

At least one reconstructed track crossing TPC2 or TPC3, referring to the second and third TPCs where TPC1 is the most upstream, must be found in the event. This is necessary as a TPC is used to measure the momentum and determine the PID of charged particles.

Quality and Fiducial

The reconstructed vertex must lie inside the FGD1 or FGD2 Fiducial Volume, FV. The most upstream FGD is known as FGD1, and the most downstream as FGD2. The FV is defined as: $|x| < 874.51$ mm, $-819.51 < y < 929.51$ mm, $136.875 < z < 447.375$ mm for FGD1, and $|x| < 860.00$ mm, $-805.00 < y < 915.00$ mm, $1483.75 < z < 1807.38$ mm for FGD2. The reconstructed interaction vertex is defined by the start position of the reconstructed charged lepton track. If the track has a low angle, relative to the beam direction, the vertex is instead defined by the intersection of the reconstructed antimuon track with the XY plane of the z position of the most upstream FGD hit of the track. The FGD FV is defined such that the interaction vertex occurs within the FGD target material. Therefore in the x and y direction it is only tracks which reconstruct the vertex at least 5 scintillator bars from the edge of the XY module that are accepted. A cut in the z position of the FV definition excludes the most upstream XY module of FGD1, and for FGD2, only the first scintillator bar is removed. To improve the quality of the selected tracks, shorter tracks with fewer than 19 TPC clusters are not selected. A cluster is defined as a set of neighbouring pads in a row or column.

Leading Track

To identify the antimuon candidate in an antineutrino CC interaction, the highest momentum positively charged track is identified. The track must originate from the FGD FV.

Upstream Background Veto

Sometimes reconstruction failures occur where the antimuon vertex is reconstructed as originating in the FGD FV, but in reality it occurs further upstream of the FGD. To reject these events, a veto is placed on any event where the second highest momentum track's start position occurs 150 mm upstream of the antimuon candidate. For the FGD2 selection, an additional cut is placed on any event where the second highest momentum track starts in the FGD1 FV.

Broken Track

Another instance of track reconstruction failure may occur where the track originating in the FGD FV is split into two. The first being fully contained in the FGD, and the second beginning in the last layers of the FGD and then passing into the TPC. The reconstruction will tag the second track as being the antimuon candidate in this case. If the antimuon candidate begins in the final two layers of the FGD, and an isolated FGD track is also present, the event is rejected.

Muon PID

The TPC PID tools are used to determine if the antimuon candidate is indeed muon-like. The TPC determines the PID by measuring the energy deposited in the TPC and compares it to the expected energy deposit under different particle hypotheses: muon, electron, pion and proton. The 'pull' value, δ_i, is defined by comparing the expected energy deposit under a given particle hypothesis to the measured energy loss in the TPC gas. The value is normalised by the deposited energy resolution. The pull value is calculated for each TPC segment separately. A likelihood under each particle hypothesis, $\mathscr{L}_i$, is then constructed using these pull values:

$$\mathscr{L}_i = \frac{P_i}{P_\mu + P_e + P_\pi + P_p} (\text{where } i = \mu, e, \pi, p) \tag{4.1}$$

where the probability density functions, P_i, are:

$$P_i = \frac{1}{\sigma_i} \exp\left(- \sum_j^{TPC} \frac{\delta_j^2(i)}{2} \right) (\text{where } i = \mu, e, \pi, p) \tag{4.2}$$

where σ is the energy deposit resolution and the sum is performed on each j-th TPC segment of the track, where j varies depending on how many TPC segments the track contains and is 1, 2 or 3. Muons and pions are generally difficult to distinguish between using this method as the Bethe-Bloch energy loss curves are similar across the entire momentum spectrum as seen in figure 3.7. The Bethe-Bloch formula can be used to determine the energy loss of charged particles due to ionisation in a material. Equally above ∼800 MeV/c muons and protons become hard to distinguish due to the overlapping energy loss Bethe-Bloch distributions. To select antimuons for the CC selection, two likelihood cuts, one for a muon hypothesis and the other for a minimally ionising particle (MIP) -like object hypothesis, are applied:

$$\mathscr{L}_\mu > 0.1 \tag{4.3}$$

$$\mathscr{L}_{MIP} = \frac{\mathscr{L}_\mu + \mathscr{L}_\pi}{1 - \mathscr{L}_\mu} > 0.9 \text{ if } p < 500 \text{ MeV/c} \tag{4.4}$$

p refers to the momentum of the antimuon candidate.

4.2.1 Pion Selection

The CC events selected can be split further according to the pion content of the event. A PID check, using the TPC or FGD, is made on all tracks other than the antimuon candidate to determine whether they are likely to be a pion [102]. A pion-like track must be in the same time bunch as the antimuon candidate and originate in the same FGD FV as the antimuon candidate. If the track crosses a TPC it must pass the TPC quality cut before moving onto the TPC PID cut. The PID cut on positive tracks considers three particle hypotheses: pions, positrons, protons, and for negative tracks, two particle hypotheses: pions and electrons. The likelihood is calculated using the pulls from the particle hypotheses:

$$\mathscr{L}_{MIP} = \frac{\mathscr{L}_{\mu} + \mathscr{L}_{\pi}}{1 - \mathscr{L}_{\mu}} > 0.8 \text{ if } p < 500 \text{ MeV/c} \tag{4.5}$$

$$\mathscr{L}_{\pi} > 0.3 \tag{4.6}$$

The track must pass both particle likelihood checks to be classified as a pion [90]. It is also possible to identify charged pions which do not enter the TPC, but do leave a track in the FGD. For higher momentum pions, a PID using energy deposited in the FGD is used. A pion pull is calculated for the track and it is tagged as a pion if the FGD pull is $-2 < \delta_{\pi} < 2.5$. If the track does not have sufficient hits to provide a reliable FGD PID calculation, it is possible to infer the presence of a pion from a Michel electron. The pion decays to a muon (and muon antineutrino), which in turn decays to an electron (also a muon neutrino and an electron neutrino), known as a Michel electron. If a track is identified in the FGD outside of the beam time window, and contains at least 7 hits for FGD1, or 6 for FGD2, it is tagged as a Michel electron.

4.3 Photon Selection

It is also possible to identify photons using the TPCs. This is possible when photons, typically from π^0 decay, pair-produce to create an electron, positron pair. If either the electron or positron is identified in the TPC, and its likelihood matches that of an electron, it can be used to infer the presence of a photon. These photons were used in the selection of CC events with a photon.

In addition to the photons tagged using the TPC, photons detected in the ECal were included in the CC-Photon sample. The majority of photons originate from decaying π^0s, however other decay processes were also included in the signal definition. Five different photon sources were included in the true CC-Photon signal definition. Table 4.2 shows the photon sources and their fractional contribution to antineutrino CC events which produce signal in the ECal which were CC-Photon in truth, as generated by the MC.

Signal Channel	Fraction
$\pi^o \rightarrow \gamma + \gamma$	86.49%
$\eta \rightarrow \gamma + \gamma$	6.11%
$\eta \rightarrow \pi^0 + X \rightarrow \gamma + \gamma + X$	5.25%
$K \rightarrow \pi^0 + X \rightarrow \gamma + \gamma + X$	1.73%
$\Lambda \rightarrow \pi^0 + X \rightarrow \gamma + \gamma + X$	0.42%

Table 4.2: The fraction of photons detected in the ECal in antineutrino CC-Photon events that were produced by each signal channel in MC.

The underlying interaction modes of the true CC-Photon signal events correspond primarily to neutral pion production, multipion production and DIS, corresponding to 38.1%, 30.6% and 12.3% respectively.

A photon is detected in the ECal by searching for an isolated object. An isolated

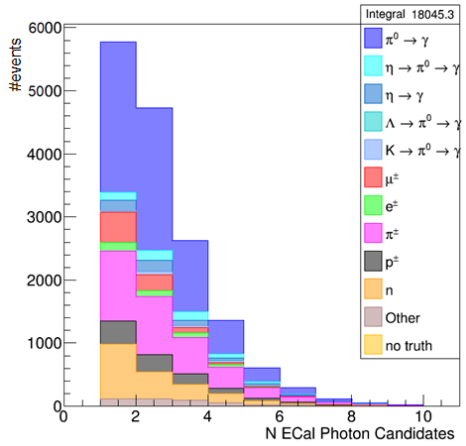

Figure 4.2: Number of isolated ECal objects in an event, labelled according to the true particle type of the shower. Events with no isolated ECal object were not shown in this plot. In the event the object was a photon in truth, the decay chain resulting in the photon is shown. For events where there was more than one ECal object, the categorisation of the object with the most electromagnetic PID is shown.

object is defined such that the track has no component from any other subdetector. The track should be contained entirely in the ECal.

An event may contain multiple isolated ECal objects, although only one must be tagged as photon-like for the event to be categorised into the CC-Photon sample. The number of isolated ECal objects for all CC events is shown in figure 4.2.

Once a sample of isolated ECal objects has been collected, a series of cuts were applied to select photons. These cuts were on the number of hits present in the ECal object; PIDMipEm, which ensures the ECal object was electromagnetic-like; and innermost ECal layer hit, which ensures the ECal shower begins in the first layers of the ECal. These cuts are detailed in the next section.

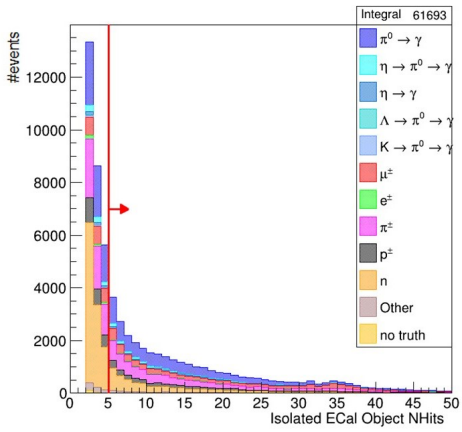

Figure 4.3: The number of hits for each isolated ECal object in CC events. For events where there was more than one ECal object, the object with the most electromagnetic PID is shown.

4.3.1 Number of ECal Hits

A new, improved ECal reconstruction algorithm was introduced in the latest MC production. In previous analyses, the ECal object was required to contain at least five hits for the reconstruction to succeed. For the latest production, the hit threshold has been reduced to require only two hits. This was possible due to a new low energy clustering algorithm [92]. The newly introduced low hit ECal objects primarily reconstruct neutrons. The PID tools and variables used to select photons (see section 4.3.2), were not intended for use with objects with less than 5 hits. Therefore to avoid tagging these low energy neutrons and ensure reconstruction tools were reliable it was required that the isolated ECal object had at least five hits. The hit distribution is shown in figure 4.3.

4.3.2 PIDMipEm

The variable PIDMipEm is an abbreviation of particle identification, minimally ionising particle, electromagnetic. It determines whether or not the ECal object is more $\gamma/e^{\pm}$-like, or minimally ionising. The variable is constructed using a series of low-level ECal variables. These variables are:

- Circularity, a measure of the width of the ECal object relative to its length.
- QRMS, the variance of the hit charge distribution.
- Truncated max ratio, the ratio of the charge found in the highest charge layer against the lowest charge layer, where the highest and lowest 20% of charged hits are removed to reduce noise.
- Front back ratio, the ratio of the total charge in the region furthest from the tracker to the total charge in the region nearest to the tracker.

A distribution of the PIDMipEm for the isolated ECal objects is shown in figure 4.4. A cut on this variable requires PIDMipEm $<$ -7 for the ECal object to be tagged as photon-like.

4.3.3 Innermost ECal Layer Hit

The innermost ECal layer hit determines in which layer of the ECal the nearest hit to the centre of the tracker was reconstructed. As the ECal is made of alternating lead and plastic scintillator, a photon originating from the FGD, in the center of the detector, is likely to shower in the first few layers. If the particle was instead detected in the outer layers of the ECal, i.e. nearer the SMRD, it is more likely to have been due to a pile-up

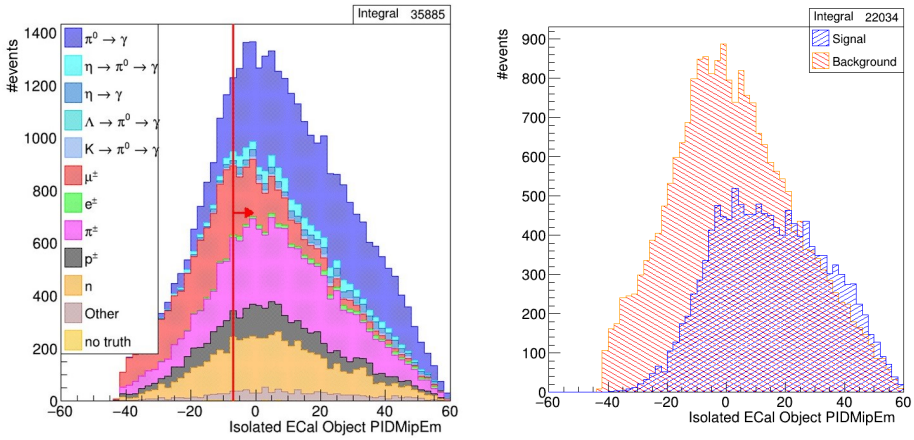

Figure 4.4: The PIDMipEm of each object in the event. The isolated ECal objects were required to contain at least five hits to ensure reliable reconstruction. The left figure demonstrates the true particle type of the ECal object and is a stacked histogram, with the right figure showing the signal and background separation and is an overlay of histograms. The red line indicates the cut applied to select photons.

interaction. A pile-up event is where a second neutrino interaction occurs outside of the FV, but its emitted particles leave hits in the ECal in the same time window as a FV interaction. The distribution for the innermost ECal layer hit is found in figure 4.5.

A cut on this variable was developed for the neutrino-mode equivalent of this analysis to reduce the number of CC0π events being reconstructed as a CC-Photon event. These background events occur due to pile-up, which becomes more probable with higher beam power. It was required that the ECal object has an innermost ECal layer hit < 7 to be photon-like.

4.3.4 Photon Selection Summary

An ECal photon sample was collected having searched for isolated ECal objects and applied the three cuts: number of hits, PIDMipEm and innermost ECal layer hit.

The TPC tagged photon sample was then combined with the ECal photons to form

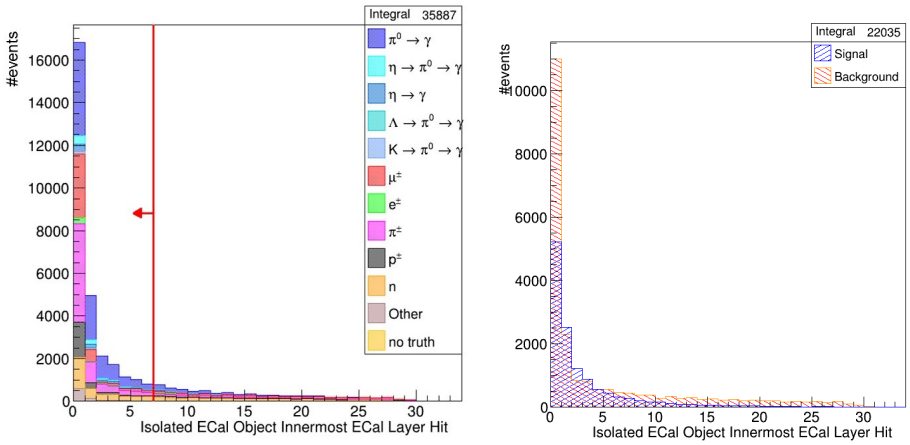

Figure 4.5: The innermost ECal layer hit for every isolated ECal object in an event. The object was required to contain at least five hits to ensure accurate reconstruction. The left figure demonstrates the true particle type of the ECal object, with the right figure showing the signal and background separation. The red line indicates the cut applied to select photons.

the CC-Photon sample. The topology and true antimuon candidate particle type of the CC-Photon sample is shown in figure 4.6.

The purity of the sample at this point was 29% and the efficiency was 53%. Purity and efficiency are defined as:

$$\text{Purity} = \frac{(\#\text{selected events which are correctly identified}}{\#\text{selected events})} \tag{4.7}$$

$$\text{Efficiency} = \frac{(\#\text{selected events})}{(\#\text{events generated by the MC})} \tag{4.8}$$

The purity of the CC-Photon sample was low, and would not be useful in constraining flux and cross section parameters. It can be seen in the true particle distribution that significant background arose from the antimuon candidate being incorrectly identified. There was a low momentum pion background peak and a higher

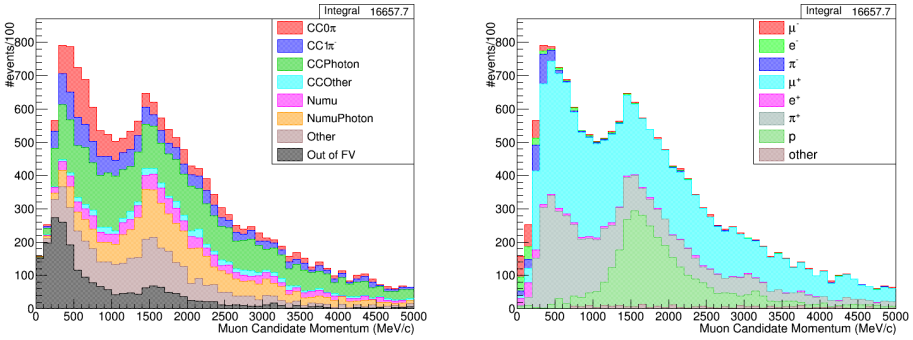

Figure 4.6: The CC-Photon sample as selected by the TPC π^0s and ECal photons, as a function of antimuon candidate momentum. The left plot shows the true topology of the sample and the right shows the true particle type of the antimuon candidate. The histograms shown are stacked.

momentum proton peak between 1.25 and 2.5 GeV/c. It can be seen in figure 4.7 that the background originated from wrong-sign backgrounds (neutrino interactions rather than antineutrino), out of FV, and 'other', primarily NC interactions.

The backgrounds from these protons and pions should therefore be rejected from all CC events, rather than reassigned to a different signal sample. As described in section 4.2 the antimuon candidate PID is determined using the energy deposited in the TPCs. At the momentum regions where the two background peaks emerge, the energy loss curves of the muon and proton or pion overlap, which cause issues with assigning the antimuon candidate correctly. To reduce such background events, a Boosted Decision Tree (BDT) method was developed.

4.4 Boosted Decision Trees

A decision tree consists of a series of binary cuts aimed at separating signal from background as seen in figure 4.8. A decision tree would likely be used when simple one-dimensional cuts are not sufficient, but in conjunction with other variables some

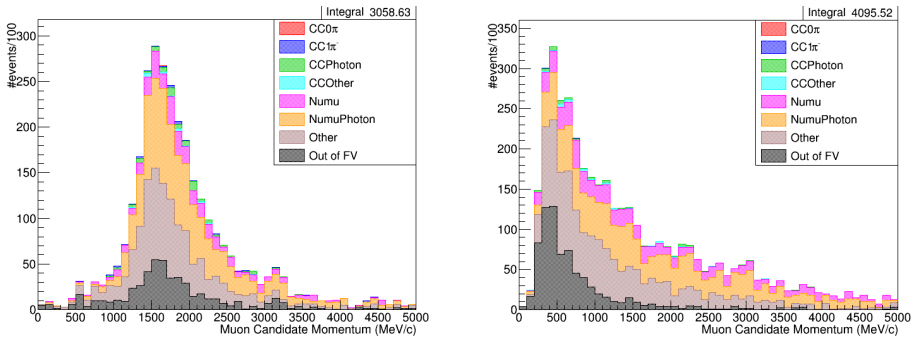

Figure 4.7: The left plot shows the true topology of the pion background in selected CC-Photon events, and the right plot shows the proton background in selected CC-Photon events, as a function of antimuon candidate momentum. The histograms shown are stacked.

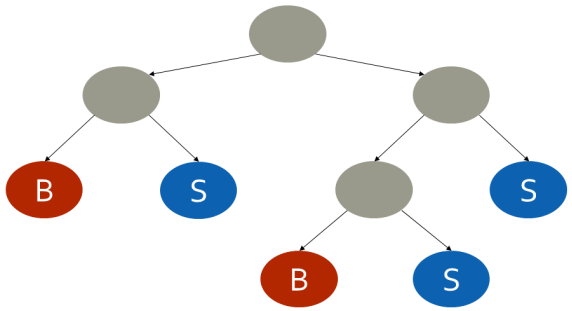

Figure 4.8: Structure of a decision tree branching between signal and background.

separation of signal and background becomes possible. A BDT is an adaptation of a decision tree aimed at improving its separation capabilities by introducing machine learning methods.

Variables with some degree of separation between signal and background are identified. A best cut point is found for each variable distribution by iterating over a number of equally spaced points in the distribution. The number of points considered is typically set to 20. From these possible cut points, the cut value with the greatest discrimination between signal and background is identified. This is repeated for each

input variable. The best cut point is defined using the Gini Index, G:

$$G = p(1-p) \tag{4.9}$$

where p is the purity $= \frac{S}{S+B}$, S is the number of signal events, and B is the number of background events. The input variables are ranked based on the Gini index value. The highest ranked variable is used as the first branch of the decision tree before iterating down, creating more branches, based on the input variable ranking. It is possible to construct a complicated decision tree with many branches, however this may lead to overtraining and poor performance when the decision tree is tested on an independent sample. A branch ends at its final node, known as a leaf, where final categorisation of signal and background is made. The branch becomes a leaf if only signal or background events remain; if the leaf contains fewer than some threshold of events; or if the number of branches exceeds its threshold.

A decision tree as described will likely provide an improved performance than simple rectangular cuts, however it will likely be overtrained and its performance will still be sub-optimal. Therefore a more effective decision method is introduced known as 'boosting'.

Development of a BDT begins by establishing a decision tree in the same manner as described previously. However from this initial calculation a new re-weighted tree can be created. The re-weighting of training events used in the second tree iteration is made to focus this time on the events the first tree failed to categorise correctly. For this analysis, the boosting method used was Adaptive Boosting (AdaBoost). The boost weighting is defined as:

$$\alpha_t = \frac{1}{2} \ln \left(\frac{1 - E_t}{E_t} \right) \tag{4.10}$$

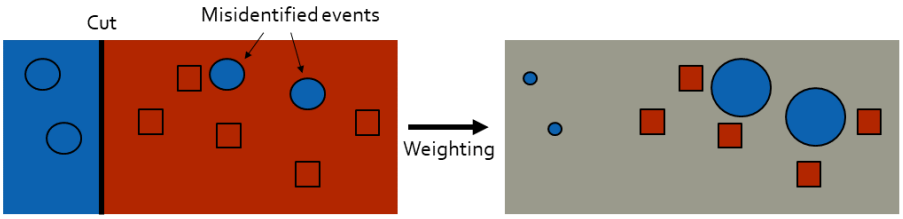

Figure 4.9: Diagram showing the re-weighting process. The cut is applied selecting events on the left side. After re-weighting, the events which were missed in the first iteration are given a larger weight to encourage a correct identification on the second iteration.

where E_t is the error rate:

$$E_t = \frac{\sum \text{Mis-classified event weights}}{\sum \text{All event weights}}. \tag{4.11}$$

The weight of the events are then altered using the boost:

$$w_i^{t+1} = w_i^t \alpha_t^\beta \tag{4.12}$$

where β is a user defined learning rate factor. This learning factor determines how high the priority is that the misclassified events are correctly identified by the next tree.

The same events are used for each tree, but the weight of each event will vary between trees. Once the re-weighted tree has been created, the ranking of variable discrimination is repeated, after the sample purity is updated. A schematic diagram of the re-weighting procedure is shown in figure 4.9.

This process of creating new trees with re-weighted events is repeated, targeting events which were mis-classified by the previous tree, until a forest of trees is created. A forest typically contains hundreds or thousands of trees. Once all trees in the forest

have been trained, a final BDT response, $R(x)$, is calculated for an event:

$$R(x) = \frac{\ln(\alpha_t)}{N_{tree}} \sum_{t=1}^{N_{tree}} R_t(x) \tag{4.13}$$

where N_{tree} is the number of trees in the forest, and $R_t, (x)$ the individual tree response, is set to either +1 or -1, depending on whether that tree would assign the event as signal or background respectively.

It is important with any machine learning technique that overtraining is avoided: where an algorithm has trained on the fine details of a specific sample which is not present in a new sample with a different seed, resulting in poor performance when applied to any sample other than that used for training. Too many trees in a forest, the AdaBoost factor set too high, or limited statistics in the training samples are all factors which contribute to over-training.

4.4.1 BDTs for Muon Candidate Identification

As shown in figure 4.6, two sources of background were present in the CC-Photon sample, with each source occurring in different momenta regions: pions up to 1.25 GeV/c, and protons between 1.25 and 2.5 GeV/c. Therefore to exploit differences between these individual backgrounds and the antimuon signal, two separate BDT types were trained for separating pions and antimuons, and protons and antimuons. Due to limitations in available MC statistics and to reduce modelling dependencies, 'particle gun' training samples were used. In a particle gun sample, single tracks of either antimuons, protons or positive pions were generated with the track vertex occurring in either FGD1 or FGD2. The tracks had a fixed angular distribution between 0 - 60°

Particle Type	FGD	Number of Events Generated
Muon High Momentum	FGD1	1 million
	FGD2	1 million
Proton	FGD1	1 million
	FGD2	1 million
Muon Low Momentum	FGD1	1 million
	FGD2	1 million
Pion	FGD1	1.5 million
	FGD2	1.5 million

Table 4.3: The total number of events generated for each BDT training sample. Events were generated for different particle types, momenta region and FGD FV.

relative to the beam direction. The momentum of the proton and antimuon samples were generated between 1.25 and 2.5 GeV/c. The pion and second antimuon samples were generated with momentum < 1.25 GeV/c. These momentum regions reflect the backgrounds seen in the CC-Photon MC sample. A summary of the number of particle gun events generated for each sample is shown in table 4.3. Additional pions were required to ensure similar statistics were available for both positive pion and antimuon samples after a set of pre-training cuts were applied. These pre-training cuts consisted of passing the standard CC selection, as described in section 4.2, without the muon PID cut applied. A check of the main track PDG particle code was made to ensure the sample was 100% pure, and during reconstruction no secondary particles were incorrectly identified as the main track. A final check was made to ensure the samples were approximately flat in momentum to ensure no biasing of the BDT training was made as shown in figures 4.10.

As both the MC and particle gun training samples were required to have passed the CC selection (although the particle gun samples omit the muon PID cut), all tracks contained a TPC and FGD segment. However, the TPC and FGD have limited variables

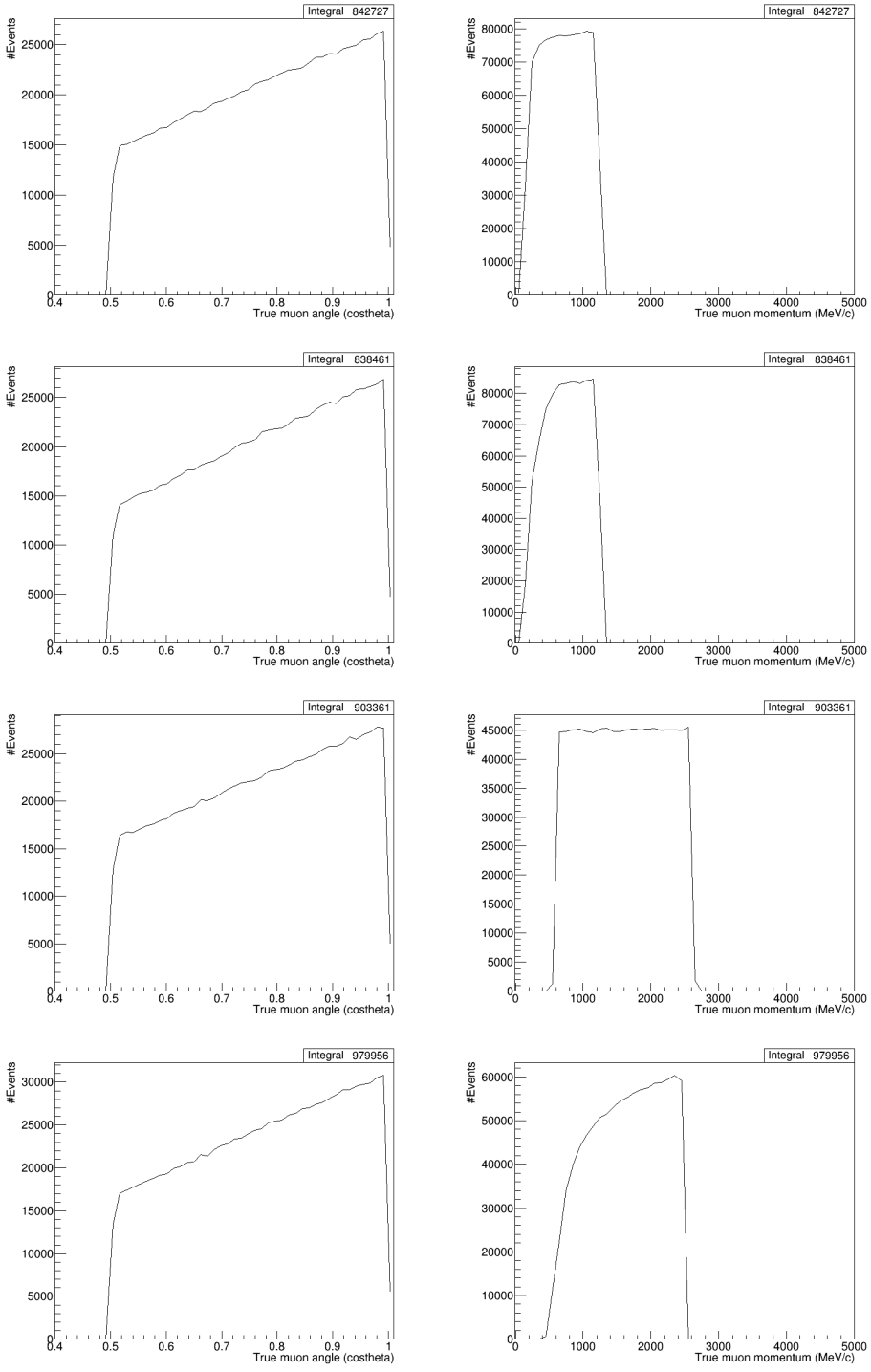

Figure 4.10: Reconstructed angle and momentum distributions of particle gun samples used for low momentum antimuon, positive pion, high momentum antimuon, proton (top to bottom) training samples.

that can be used as input to the BDT. Also given the TPC was used to determine the PID of particles in the CC selection, and the backgrounds arose due to the limitations of those techniques, the TPC variables were expected to assign a similar PID to the TPC energy loss method. Therefore ECal variables were also used in conjunction with the TPC and FGD variables. If the track did not enter the ECal, a default value was set for each variable such that the default lied adjacent to the variable distribution. The default was set near to the primary distribution so that the features of the variable were not lost in a coarsely binned distribution.

The full list of input variables was:

- **Global Track Length**: The track length as determined by the distance - $((x_i - x_f)^2 + (y_i - y_f)^2 + (z_i - z_f)^2)$.
- **Number of TPC Hits**: The total number of hits found in the first TPC entered by the track.
- **TPC Muon Pull**: The TPC pull value for the first TPC to detect the track, as defined in section 4.2, comparing the dE/dX of the particle under a muon hypothesis.
- **TPC Proton Pull (only used in antimuon - proton BDT)**: The TPC pull value for the first TPC to detect the track, as defined in section 4.2, comparing the dE/dX of the particle under a proton hypothesis.
- **Number of FGD Hits**: The total number of hits found in the FGD in which the track originated.
- **FGD Object Length**: The length of the track when only considering the distance travelled through the FGD in which the track originated.

- **ECal Object Energy**: The total energy deposited in the ECal.
- **ECal Object Difference in Start and End Position X**: $X_{\text{ECal end position}} - X_{\text{ECal start position}}$.
- **ECal Object Difference in Start and End Position Y**: $Y_{\text{ECal end position}} - Y_{\text{ECal start position}}$.
- **ECal Object PIDMipEm**: A PID variable describing how electromagnetic-like the ECal segment of the track is, as described in section 4.3.2.
- **Number of Hits in ECal Object**: The total number of hits found in the ECal.
- **ECal Object Length**: The length of the track's ECal segment.
- **ECal Object Energy/Length**: Energy deposited in the ECal divided by the length of the track's ECal segment.
- **ECal Object Shower Angle**: The opening angle of the ECal object, as calculated using Principal Component Analysis (PCA) on the 3D cluster hits [103].
- **ECal Object Circularity**: A measure of the width of the ECal object, as calculated using PCA on the 3D cluster hits.
- **ECal Object Transverse Charge Ratio**: A measure of the direction of the ECal object, by taking the ratio of the outer 50% of hits, to inner 50% of hits, relative to the center of the cluster.

- **ECal Object Truncated Max Ratio**: The ratio of the ECal object charge in the highest and lowest charge layers, where the highest and lowest 20% of charged hits are removed.
- **ECal Object Front Back Ratio**: The ratio of the total charge of the ECal object in the nearest and furthest regions from the tracker.
- **ECal Object Module Entered**: A variable defining which ECal module the ECal object was found.

The signal and background separation for these input variables for the particle gun samples can be found in appendix A.

When deciding which variables should be used as input to the BDT, two criteria were set to exclude certain variables:

- Signal and background distributions of the variable should have similar shapes in both particle gun and CC-Photon MC samples.
- When testing the variable over a control sample, the data and MC distributions should be similar with any differences understood.

The second criteria was established to ensure the systematic uncertainty was not inflated by any one variable. The control sample used for this verification was on CC events originating in the PØD. This sample is not included in any oscillation analysis meaning checks between MC and data can be made. The sample should also be a reasonable approximation of the physics samples, as the PØD is upstream of the tracker, meaning neutrino events from the PØD will likely contain a TPC, FGD and ECal segment. The data-MC distributions for the variables used in the BDT can be seen in appendix A.1.

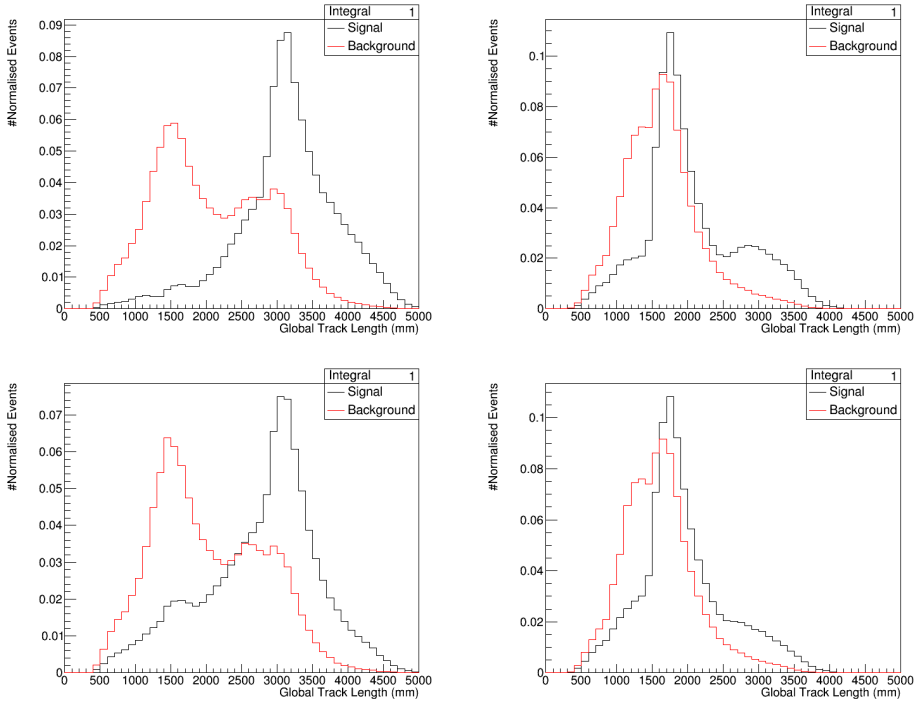

Figure 4.11: Distributions of track length for the particle gun training samples. The top plots show the proton-muon samples, and the bottom plots show the pion-muon samples. The left shows the FGD1 distribution, and the right is the FGD2 distributions.

Special considerations were made when adding the global track length variable to the BDT. The variable had good separation and was especially important to good BDT performance when the track did not contain an ECal segment. It was noted that a shape difference was present between the FGD1 and FGD2 events. This was expected as FGD2 is further downstream than FGD1, meaning there is less detector for the track to pass through to observe the differences in signal and background. The distributions can be seen in figure 4.11. To exploit this difference in shape between the FGD1 and FGD2 samples, the BDT's were further split based on the FGD topology.

The BDTs structures consist of 1200 trees, an AdaBoost value of 0.5, and the maximum number of branches was set to 3. These were optimised using a subset of the

	Percentage of Particle Type Removed by BDT (%)		
	Proton	Pion	Other Backgrounds
FGD1	82	74	74
FGD2	74	68	64

Table 4.4: The percentage of each background particle type removed from the CC-Photon sample by the BDT cut.

CCPhoton MC sample as a test sample to ensure no over-training was present.

After the BDTs were trained on the particle gun samples, the BDT response was applied to the CC-Photon MC. The distributions of the BDT response are shown in figure 4.12. Based on these distributions it was possible to apply a cut rejecting the protons and pions. In theory, the cuts should only be applied to the regions of phase space where the background was an issue, as this was the phase space the BDT had been designed to perform effectively in. However, model dependence would be introduced if momentum were used when deciding whether or not the cut should be applied. To avoid this model dependence, the BDT responses of both the proton-muon and pion-muon instances were plotted in two-dimensions as is shown in figure 4.13. The cut lines shown were optimised to ensure the CC-Photon sample purity was $\sim 40\%$ which is sufficiently high for a sample to be used in a ND fit.

After applying the cuts related to the PID BDTs, the purity of the CC-Photon sample increased from 29% (29%) to 41% (39%), with an efficiency of 40% (42%) for the FGD1 (FGD2) selection. The antimuon candidate was correctly identified in 80% (76%) of cases with the BDT added, relative to 56% (54%) of cases without the BDT. Table 4.4 summarises the percentage of each background particle type removed from the CC-Photon sample as a result of applying the BDT cut.

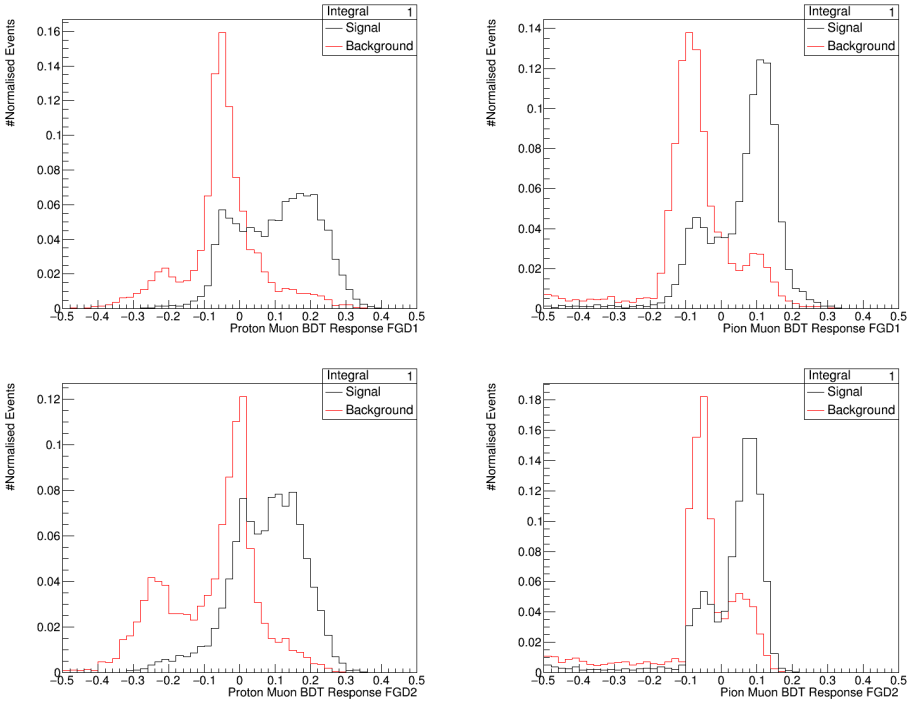

Figure 4.12: BDT response distributions on the CC-Photon MC. Left shows proton-muon BDT response and right is pion-muon BDT response. Top shows FGD1 BDTs and bottom shows FGD2 BDTs.

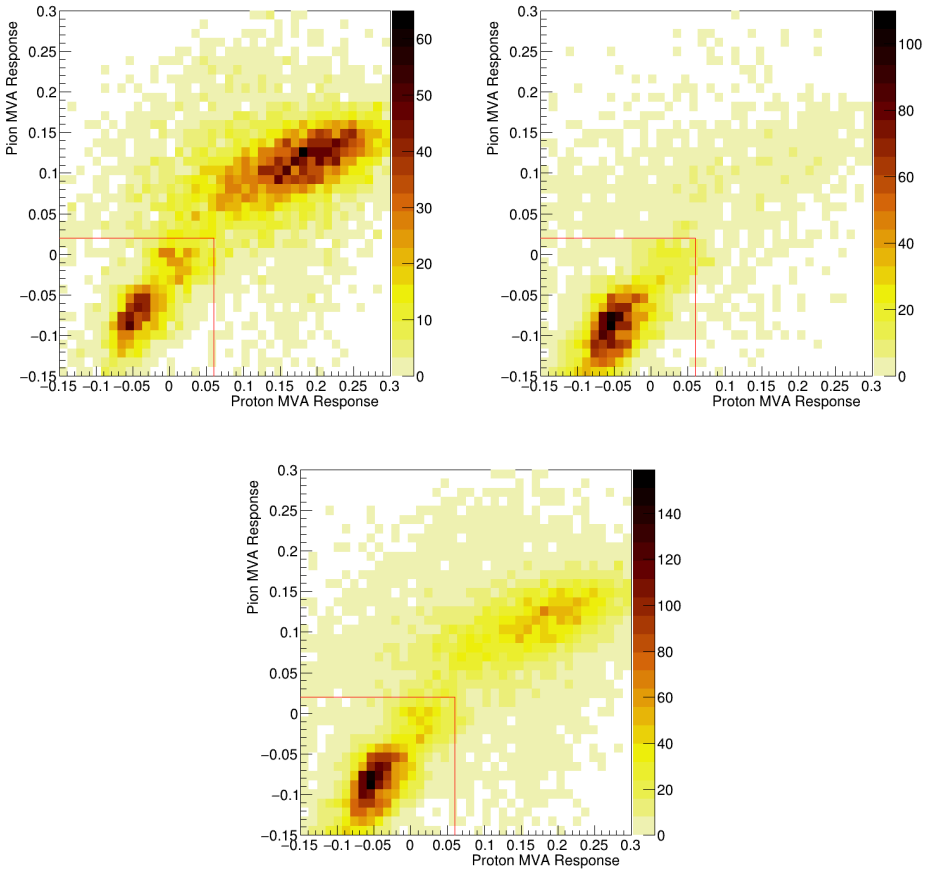

Figure 4.13: The 2D BDT response of the pion-muon and proton-muon BDT. The top shows the signal (left) and background (right) split, and the bottom shows the combined signal and background 2D response. The FGD1 response is shown. Note the z-axis scale varies between plots.

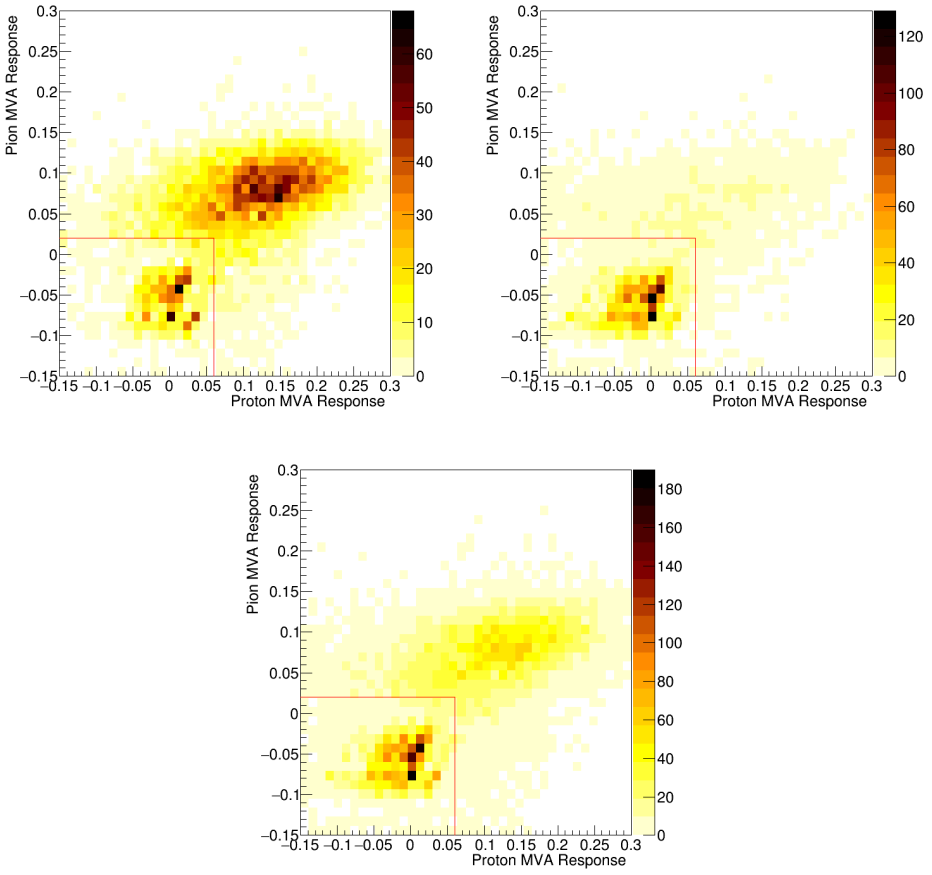

Figure 4.14: The 2D BDT response of the pion-muon and proton-muon BDT. The top shows the signal (left) and background (right) split, and the bottom shows the combined signal and background 2D response. The FGD2 response is shown. Note the z-axis scale varies between plots.

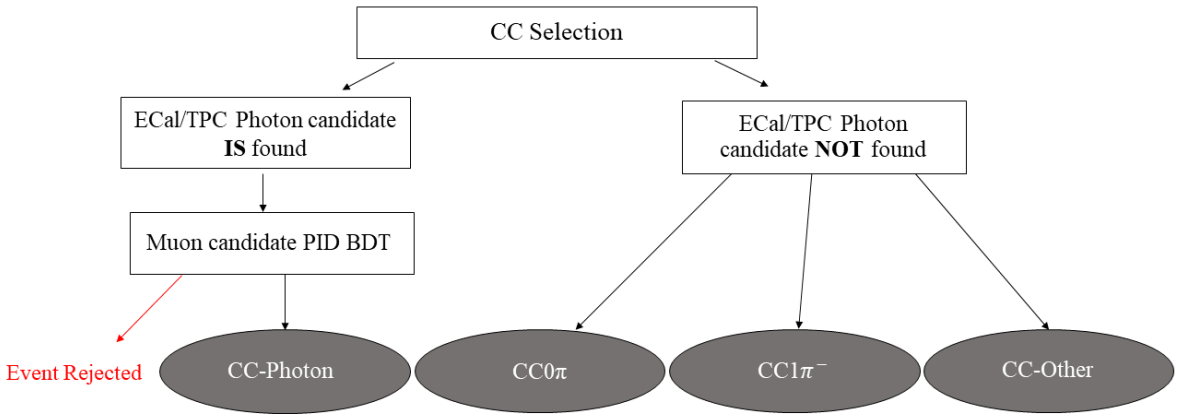

Figure 4.15: Flow diagram of the antineutrino CC multipi photon selection. The selection results in the selection of the CC0π, CC1π^-, CC-Other and CC-Photon samples. The selection method is common between the FGD1 and FGD2 selections.

4.5 Sample Summary

Following the selection of photons and pions in an event, it was possible to define the new antineutrino CC multipi photon selection, as is shown in the flow diagram in figure 4.15.

The final selected samples were characterised by the reconstructed particles in their final state:

CC0π: CC interaction with no pions or photons in the final state.

CC1π^-: CC interaction with exactly one reconstructed negatively charged pion and no photons in the final state.

CC-Other: CC interaction with one or more reconstructed positively charged pions, or more than one negatively charged pion, and no photons in the final state.

CC-Photon: CC interaction with at least one reconstructed photon in the final state.

This section describes the final samples, and quantifies the precision of the selection in extracting the desired event topologies for each of the four antineutrino ND samples.

Comparisons between data and MC were made while looking at the underlying MC true simulated information. Figures 4.16 and 4.17 describe the true particle type of the reconstructed antimuon candidate for the FGD1 and FGD2 samples, respectively. Table 4.5 summarises the relative contribution of each particle type to each of the four samples for both FGD1 and FGD2. As expected, the primary particle selected as the antimuon candidate for most samples was the positive muon. The background from cases where the positive pion from a wrong-sign neutrino interaction mimics that of an antimuon is introduced when it is incorrectly reconstructed as the highest momentum track in the event. There was also additional background from protons in the momentum region where the TPC energy loss curves of the proton and antimuon overlap causing issues in identification.

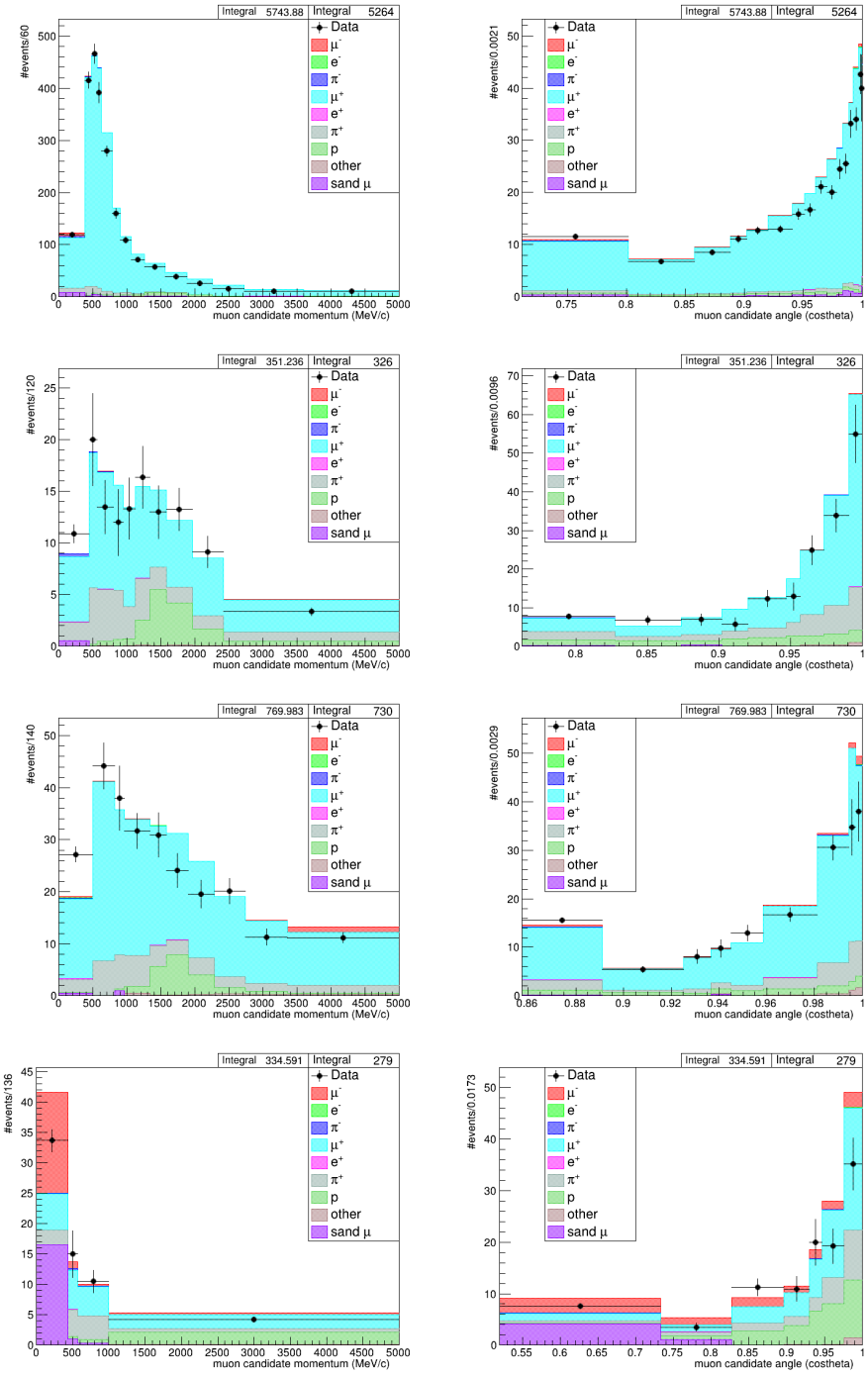

Figure 4.16: True composition of each antineutrino ND sample, CC0π, CC1π^-, CC-Photon and CC-Other, from top to bottom, for FGD1 in terms of the true particle type of the antimuon candidate. The histograms include under and over flow bins. The error bars indicate the statistical uncertainty.

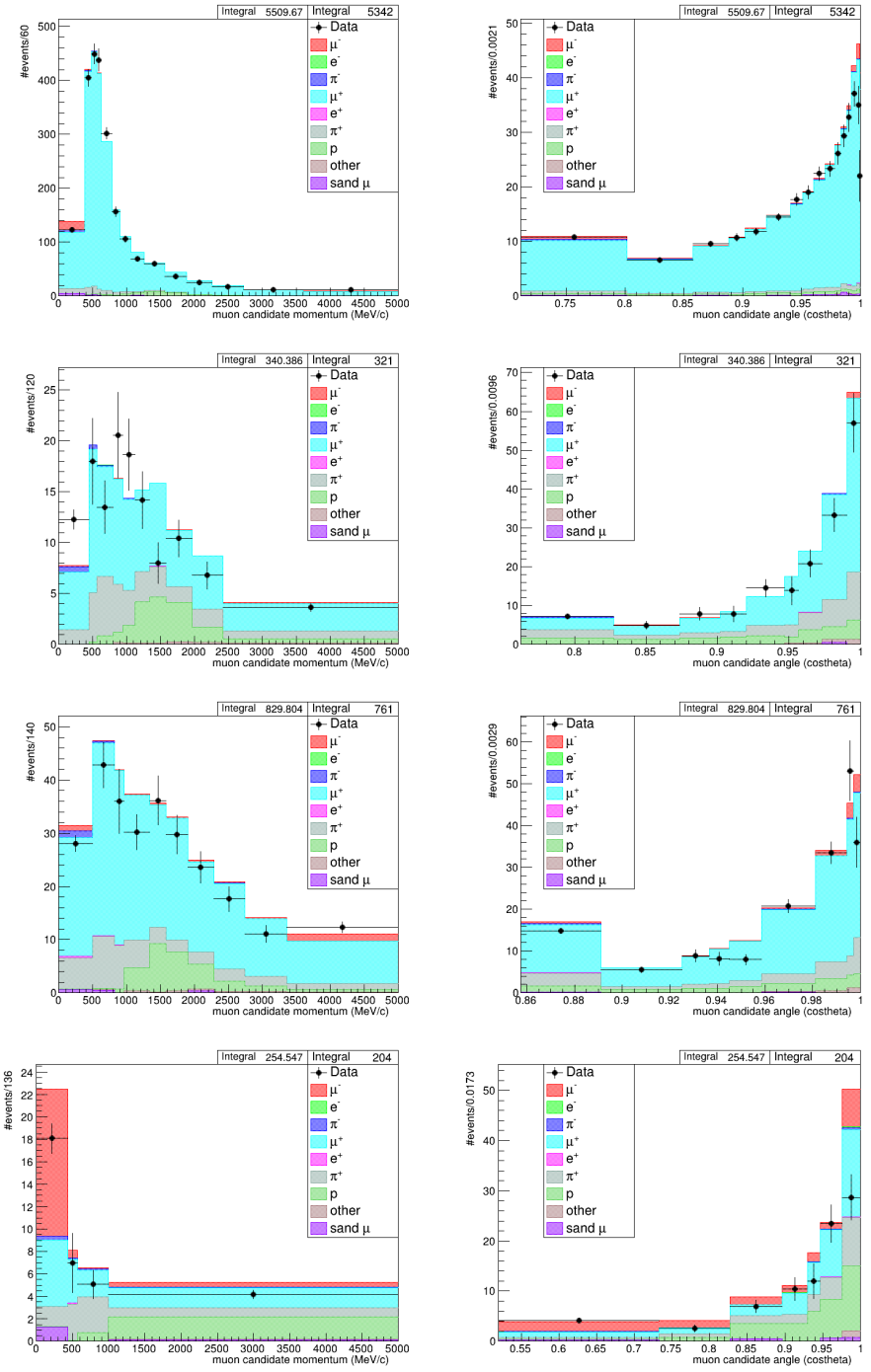

Figure 4.17: True composition of each antineutrino ND sample, CC0π, CC1π^-, CC-Photon and CC-Other, from top to bottom, for FGD2 in terms of the true particle type of the antimuon candidate. The histograms include under and over flow bins. The error bars indicate the statistical uncertainty.

The true topological content of each of the four samples is shown in figures 4.18 and 4.19, for the FGD1 and FGD2 samples respectively. Table 4.6 summarises the purity of each sample at selecting the topology it is targeting. The true topological definition of the CC0π sample is that the event must contain no mesons; CC1π^- must contain exactly one negatively charged pion and no other mesons; CC-Photon describes all of the decay channels as shown in table 4.2; CC-Other contains all other CC interactions which do not fit into any of the previous three categories. BKG refers to any event originating in the FGD FV which is not an antineutrino CC event. They are primarily neutrino events, or NC interactions. 'Out FV' refers to out of FV events, where the vertex does not originate in either FGD1 or FGD2, dependent on the selection of interest, but it does originate in the ND280 detector or magnet volume. Sand μ refers to any interaction generated by the sand MC, corresponding to a neutrino interaction with the cavern.

Figures 4.20 and 4.21 show the true contribution of each $\bar{\nu}$ interaction type simulated, for the FGD1 and FGD2 samples, respectively. Table 4.7 summarises the relative contribution of each interaction type to each sample. As expected the CC0π sample was predominantly composed of CCQE interactions, with a small contribution from 2p2h interactions. The CC1π^- sample was dominated by RES interactions with some contribution from background neutrino interactions where the particle type of the negative pion and antimuon had been reconstructed incorrectly, flipping the particle type reconstructed. The CC-Photon sample was made of a combination of RES interactions at lower energies, and DIS at higher energies. Finally the CC-Other sample was a combination of many different sources of background and some higher energy signal interaction types such as DIS. The low purity of the CC-Other sample

Sample	True Particle	True Composition (%)	
		FGD1	FGD2
CC0π	μ^-	0.9	2.2
	e^-	0.0	0.0
	π^-	0.4	0.6
	μ^+	93.4	91.8
	e^+	0.1	0.0
	π^+	2.9	2.3
	p	2.0	2.2
	other	0.1	0.1
	Sand muon	0.2	0.1
CC1π^-	μ^-	0.1	0.6
	e^-	0.0	0.0
	π^-	0.4	0.8
	μ^+	68.4	65.2
	e^+	0.1	0.1
	π^+	18.5	18.9
	p	11.7	13.3
	other	0.8	1.1
	Sand muon	0.1	0.0
CC-Photon	μ^-	1.5	2.6
	e^-	0.1	0.0
	π^-	0.2	0.6
	μ^+	80.3	76.2
	e^+	0.1	0.2
	π^+	11.2	11.6
	p	5.7	7.9
	other	0.9	0.8
	Sand muon	0.0	0.0
CC-Other	μ^-	21.6	22.0
	e^-	0.1	0.3
	π^-	0.5	0.9
	μ^+	41.6	37.1
	e^+	0.1	0.1
	π^+	14.3	15.6
	p	19.2	22.9
	other	0.8	0.8
	Sand muon	1.9	0.3

Table 4.5: True composition of each antineutrino ND sample, CC0π, CC1π^-, CC-Photon and CC-Other, from top to bottom, for FGD1 (left) and FGD2 (right) in terms of the true particle type of the antimuon candidate.

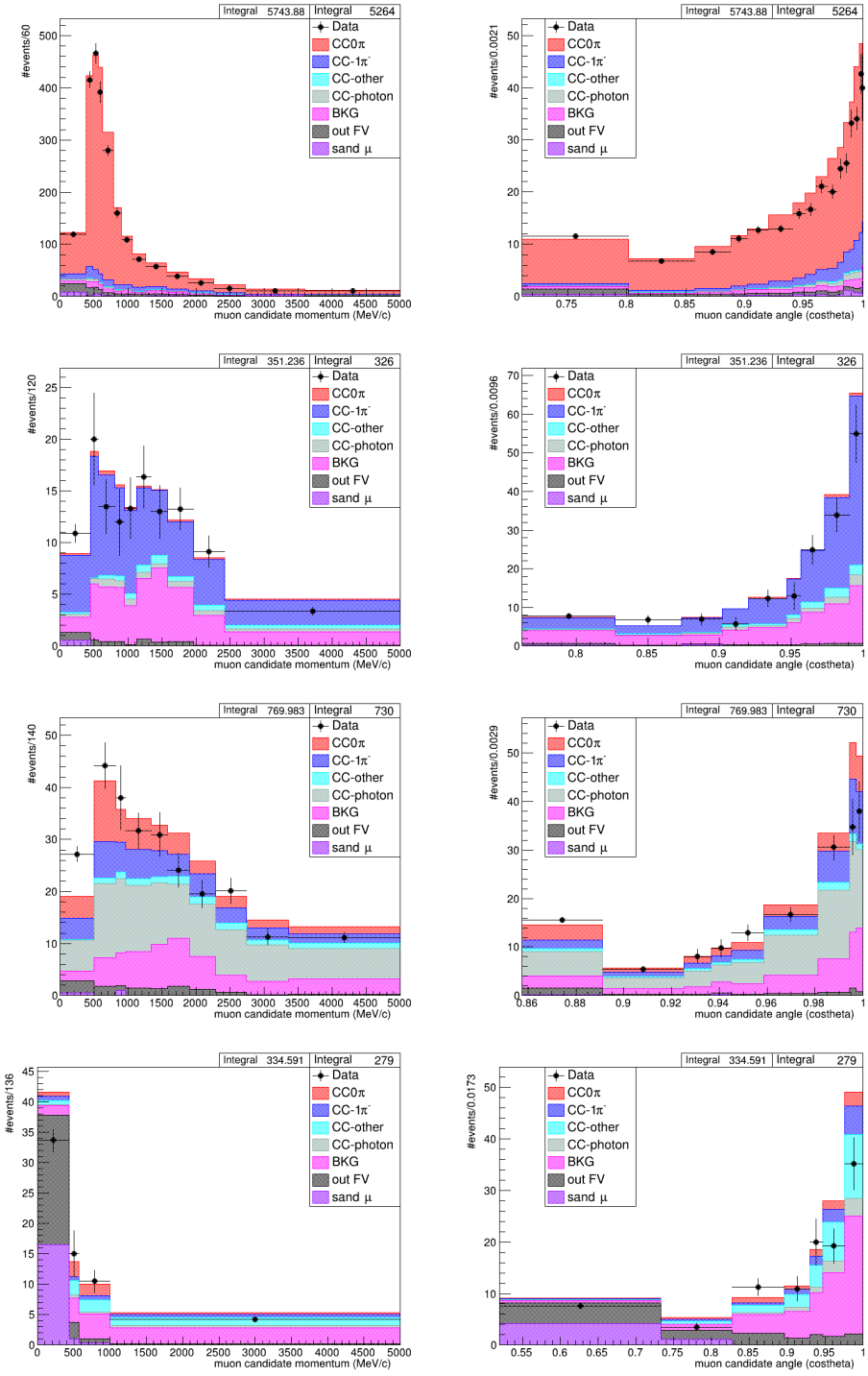

Figure 4.18: True composition of each antineutrino ND sample, CC0π, CC1π^-, CC-Photon and CC-Other, from top to bottom, for FGD1 in terms of topology. The histograms include under and over flow bins. The error bars indicate the statistical uncertainty.

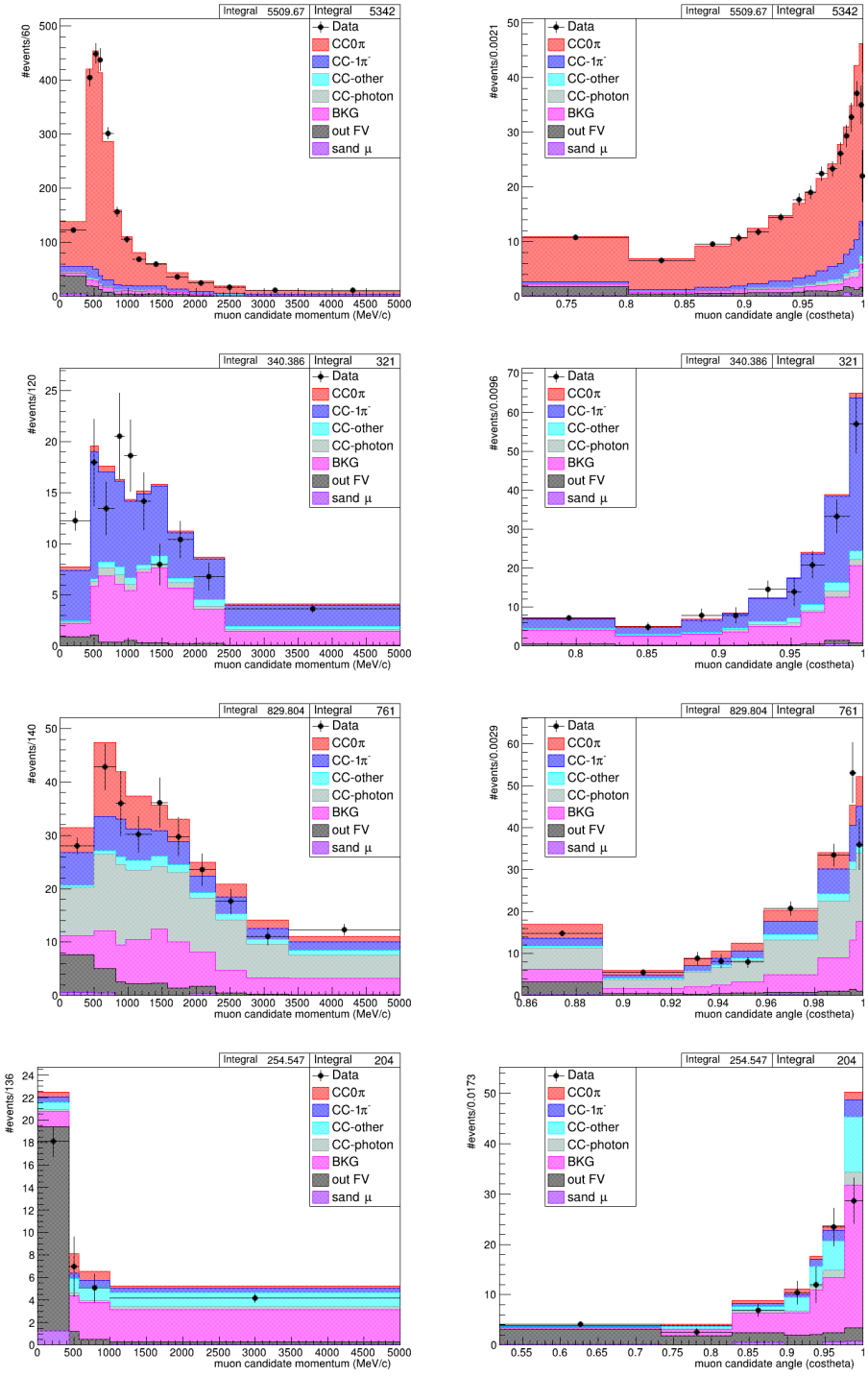

Figure 4.19: True composition of each antineutrino ND sample, CC0π, CC1π^-, CC-Photon and CC-Other, from top to bottom, for FGD2 in terms of topology. The histograms include under and over flow bins. The error bars indicate the statistical uncertainty.

Sample	Topology	True Composition (%)	
		FGD1	FGD2
CC0π	CC0π	81.5	79.8
	CC1π^-	7.7	7.2
	CC-Other	0.5	0.6
	CC-Photon	2.1	1.6
	BKG	3.7	4.1
	Out FV	4.2	6.5
	Sand muon	0.2	0.1
CC1π^-	CC0π	1.8	2.2
	CC1π^-	56.1	53.4
	CC-Other	5.0	5.1
	CC-Photon	5.1	3.8
	BKG	29.3	32.5
	Out FV	2.6	2.9
	Sand muon	0.1	0.0
CC-Photon	CC0π	16.1	16.0
	CC1π^-	16.5	15.6
	CC-Other	5.2	4.8
	CC-Photon	41.3	38.5
	BKG	17.1	18.4
	Out FV	3.4	6.6
	Sand muon	0.0	0.0
CC-Other	CC0π	6.8	5.1
	CC1π^-	7.7	6.8
	CC-Other	19.3	19.1
	CC-Photon	5.2	4.2
	BKG	30.8	37.2
	Out FV	28.3	27.2
	Sand muon	1.9	0.3

Table 4.6: True composition of each antineutrino ND sample, CC0π, CC1π^-, CC-Photon and CC-Other, from top to bottom, for FGD1 (left) and FGD2 (right) in terms of topology. The histograms include under and over flow bins. The error bars indicate the statistical uncertainty.

was expected as it is not a well-defined sample and simply covers all other categories which do not fall into either the CC0π, CC1π^- or CC-Photon categories.

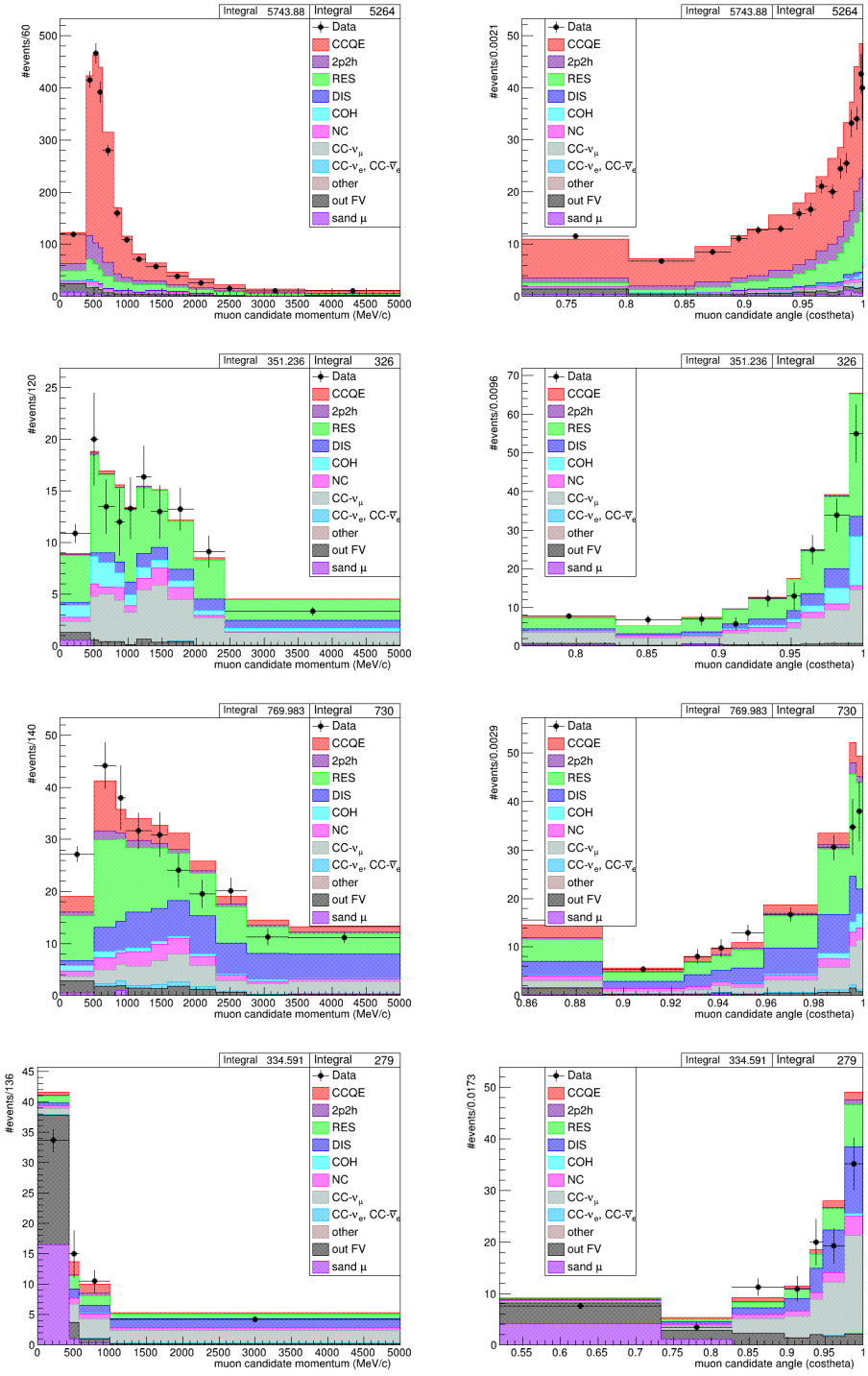

Figure 4.20: The true neutrino interaction type generated by the MC for each of the four samples, CC0π, CC1π^-, CC-Photon and CC-Other, from top to bottom, in FGD1. The histograms include under and over flow bins. The error bars indicate the statistical uncertainty.

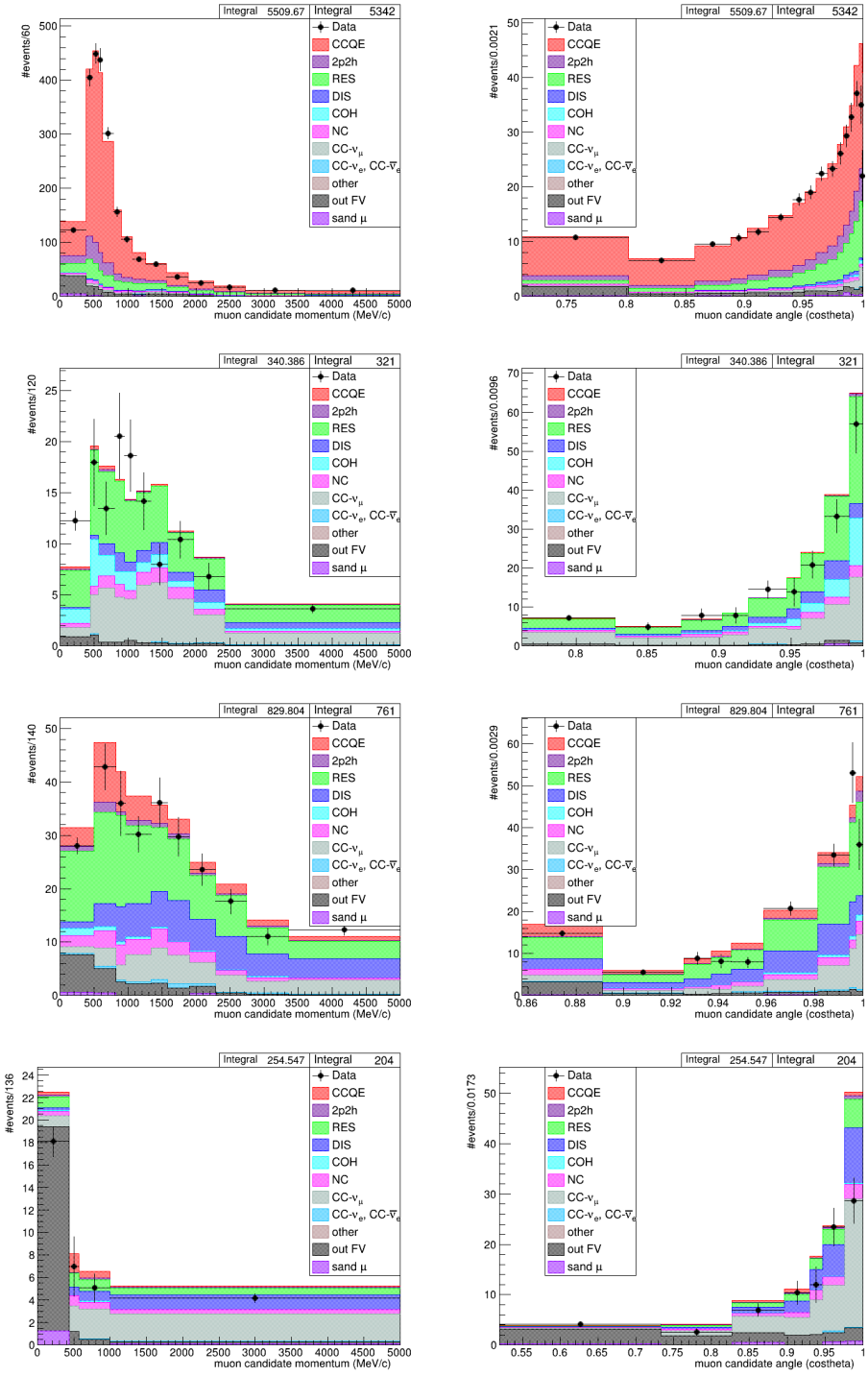

Figure 4.21: The true neutrino interaction type generated by the MC for each of the four samples, CC0π, CC1π^-, CC-Photon and CC-Other, from top to bottom, for FGD2. The histograms include under and over flow bins. The error bars indicate the statistical uncertainty.

Sample	Interaction Type	True Composition (%)	
		FGD1	FGD2
CC0π	CCQE	67.1	66.0
	2p2h	10.3	9.5
	RES	12.9	12.3
	DIS	1.2	1.2
	COH	0.4	0.3
	NC	2.1	2.1
	ν	1.5	1.9
	$\nu_e/\bar{\nu}_e$	0.1	0.1
	Out FV	4.2	6.5
	Sand muon	0.2	0.1
CC1π^-	CCQE	1.2	1.3
	2p2h	0.4	0.7
	RES	46.7	42.3
	DIS	11.0	10.4
	COH	8.8	9.8
	NC	5.0	6.1
	ν	24.3	26.1
	$\nu_e/\bar{\nu}_e$	0.1	0.3
	Out FV	2.6	2.9
	Sand muon	0.1	0.0
CC-Photon	CCQE	11.9	12.2
	2p2h	2.8	2.6
	RES	37.1	37.4
	DIS	25.1	21.4
	COH	2.1	1.4
	NC	5.4	5.8
	ν	10.4	11.5
	$\nu_e/\bar{\nu}_e$	1.2	1.1
	Out FV	3.8	6.6
	Sand muon	0.0	0.4
CC-Other	CCQE	5.2	3.3
	2p2h	1.1	1.3
	RES	12.6	11.1
	DIS	19.7	19.0
	COH	0.3	0.4
	NC	5.8	6.2
	ν	24.8	30.7
	$\nu_e/\bar{\nu}_e$	0.3	0.3
	Out FV	28.3	27.2
	Sand muon	1.9	0.3

Table 4.7: True composition of each antineutrino ND sample, CC0π, CC1π^-, CC-Photon and CC-Other, from top to bottom, for FGD1 (left) and FGD2 (right) in terms of interaction type.

Sample	χ^2/dof	
	FGD1	FGD2
CC0π	1.96	1.38
CC1π^-	1.26	1.44
CC-Photon	1.60	0.75
CC-Other	1.34	1.31

Table 4.8: The agreement between data and MC for the ND samples shown for the momentum distributions, such as those shown in figures 4.20 and 4.21.

Sample	χ^2/dof	
	FGD1	FGD2
CC0π	3.03	0.96
CC1π^-	1.29	0.77
CC-Photon	1.15	0.73
CC-Other	2.00	1.23

Table 4.9: The agreement between data and MC for the ND samples shown for the angular distributions, such as those shown in figures 4.20 and 4.21.

The level of agreement between data and MC is shown in tables 4.8 and 4.9 by considering the χ^2/dof for each sample, for both kinematic distributions. It was expected at this stage of the analysis that some disagreement be present as only statistical uncertainty was considered. In the next section, a description of the ND280 detector systematic uncertainties relevant to the ND samples will be discussed. There are also cross section and flux errors which were not considered at this stage, and the ND fit, as described in section 6, is used to better understand and constrain these parameters.

The ratio of data to MC events for each of the four antineutrino samples is shown as a function of the lepton kinematics in figures 4.22 and 4.23. There was relative agreement between all samples, and the statistics were too limited to draw many conclusions on the agreement of the MC simulation to data.

It is important that the samples selected represent a broad phase space, and that the

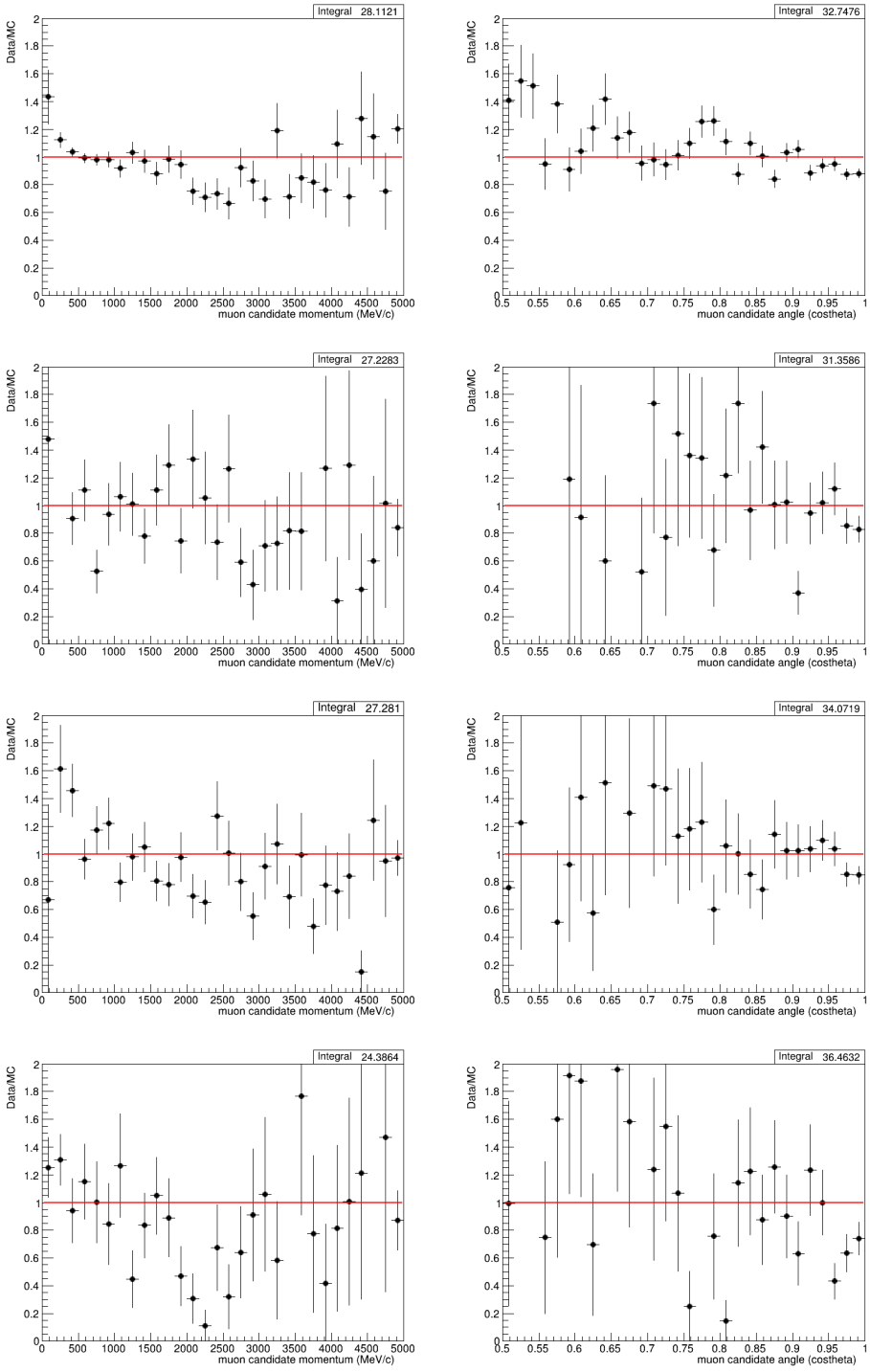

Figure 4.22: The ratio of data to MC for each of the four FGD1 samples, CC0π, CC1π^-, CC-Photon and CC-Other, from top to bottom, as a function of the antimuon kinematics. The error bars indicate the statistical uncertainty.

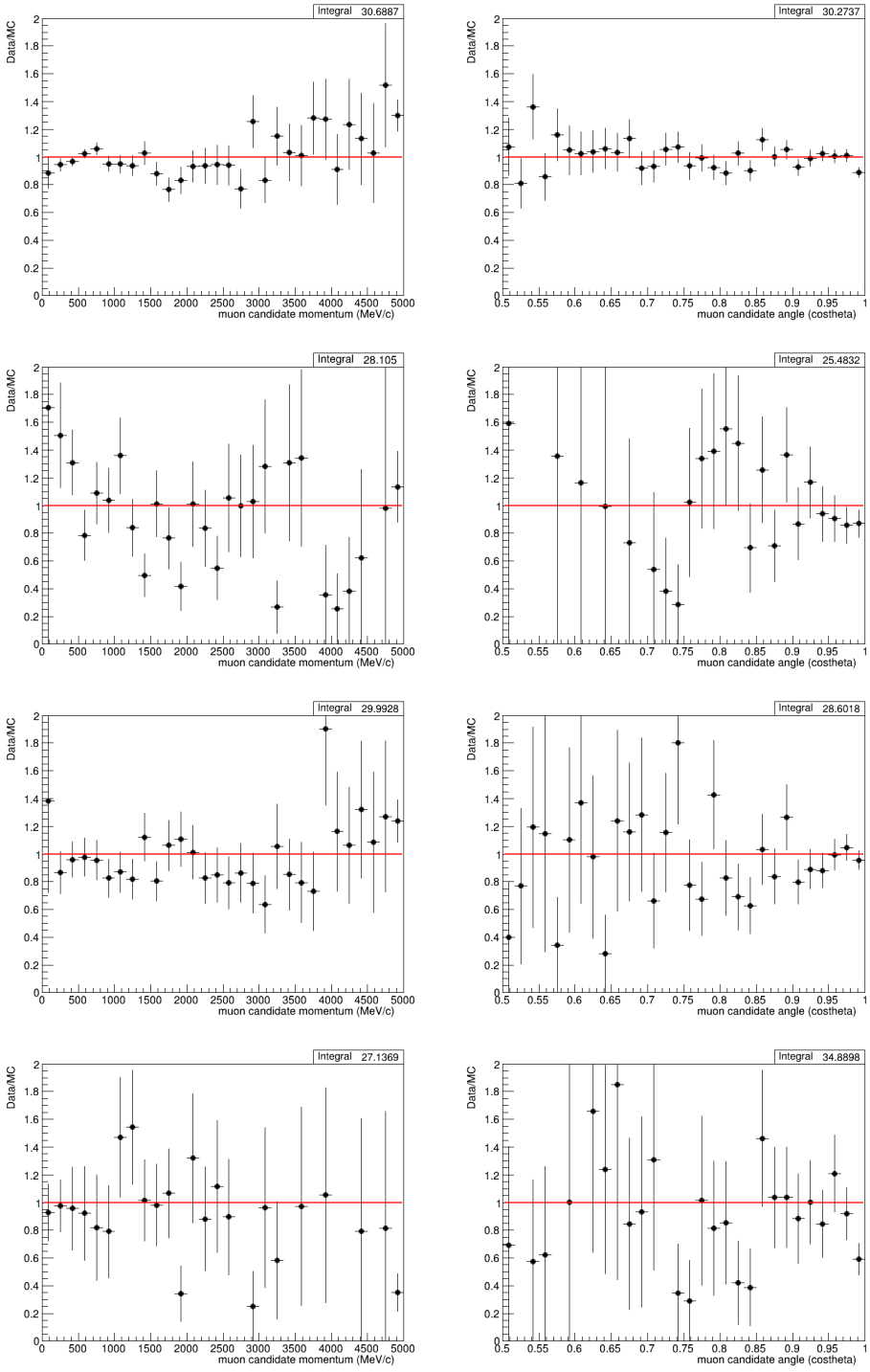

Figure 4.23: The ratio of data to MC for each of the four FGD2 samples, CC0π, CC1π^-, CC-Photon and CC-Other, from top to bottom, as a function of the antimuon kinematics. The error bars indicate the statistical uncertainty.

Sample	Efficiency (%)		Purity (%)	
	FGD1	FGD2	FGD1	FGD2
CC0π	69.4 ± 0.2	68.6 ± 0.2	81.7 ± 0.2	79.9 ± 0.2
CC1π^-	15.4 ± 0.3	15.5 ± 0.3	56.1 ± 0.8	53.4 ± 0.8
CC-Other	24.1 ± 0.9	21.6 ± 0.9	19.7 ± 0.7	19.2 ± 0.8
CC-Photon	39.6 ± 0.5	42.4 ± 0.5	41.3 ± 0.5	38.5 ± 0.5

Table 4.10: The selection efficiency and purity of each of the four samples following the antineutrino CC multipi photon selection for both FGD1 and FGD2. The statistical uncertainties on these values are indicated.

Sample	δEfficiency (%)		δPurity (%)	
	FGD1	FGD2	FGD1	FGD2
CC0π	-0.6	-0.4	+7.2	+7.2
CC1π^-	-3.9	-1.7	+10.7	+12.4
CC-Other	-2.4	-3.6	-6.6	-6.8

Table 4.11: The change to the selection efficiency and purity of each of the three multipi samples after adding photon tagging for both FGD1 and FGD2 [90].

efficiency in selecting events and the purity of the resulting events are consistent across the phase space. The distributions in figures 4.24 - 4.26 show the selection efficiency and purity as a function of the momentum kinematics. A summary of the total efficiency and purity of the selected samples is shown in table 4.10. The efficiency and purity of each sample as a function of the true antimuon kinematics, is shown in figures 4.24 to 4.27.

As the selection of photons occurred before splitting according to the pion topology, all of the other multipi samples: CC0π, CC1π^- and CC-Other, observed changes to their selection efficiency and purity relative to the selection without the photon sample. The changes to the samples are shown in table 4.11.

By introducing photon tagging, not only was a new ND sample created, but the purity of both the CC0π and CC1π^- increased from $\sim$75% to $\sim$82% and from $\sim$45% to $\sim$56% respectively. The CC-Other signal definition changed between the multipi and

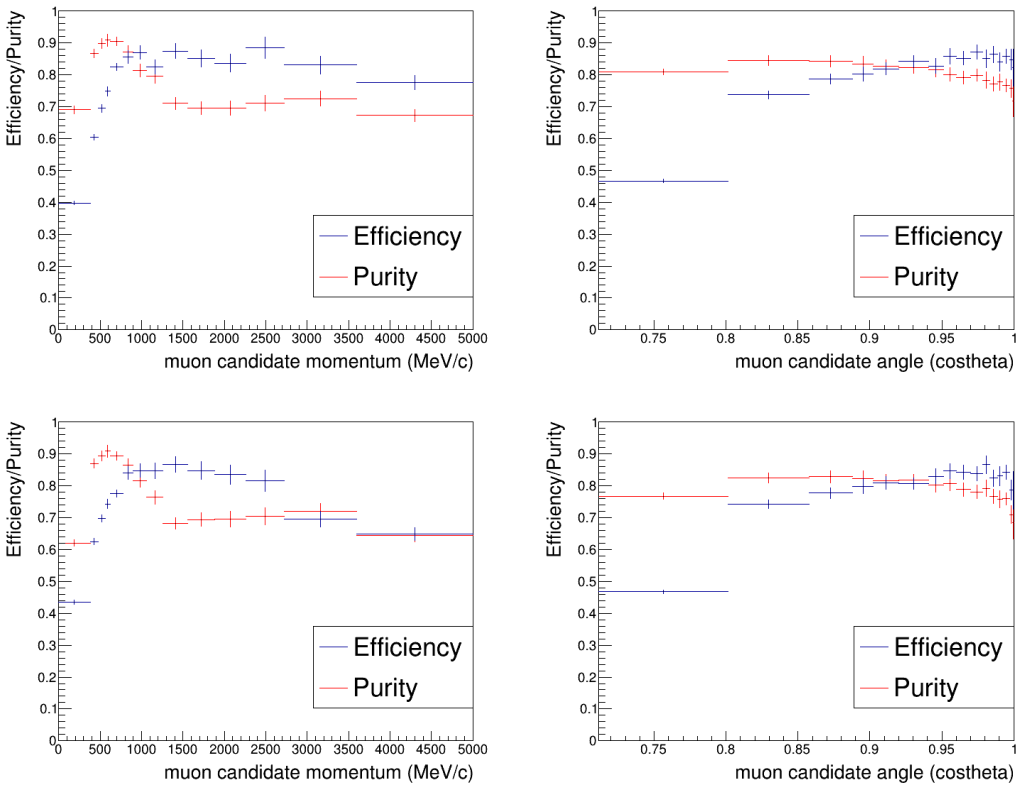

Figure 4.24: The efficiency (blue) and purity (red) of the CC0π sample for FGD1 (above) and FGD2 (below) in terms of the antimuon candidate momentum and angle.

multipi with photon selections and therefore the worsening performance of the sample is not of concern, as it is not a well defined sample, simply covering all other CC event types.

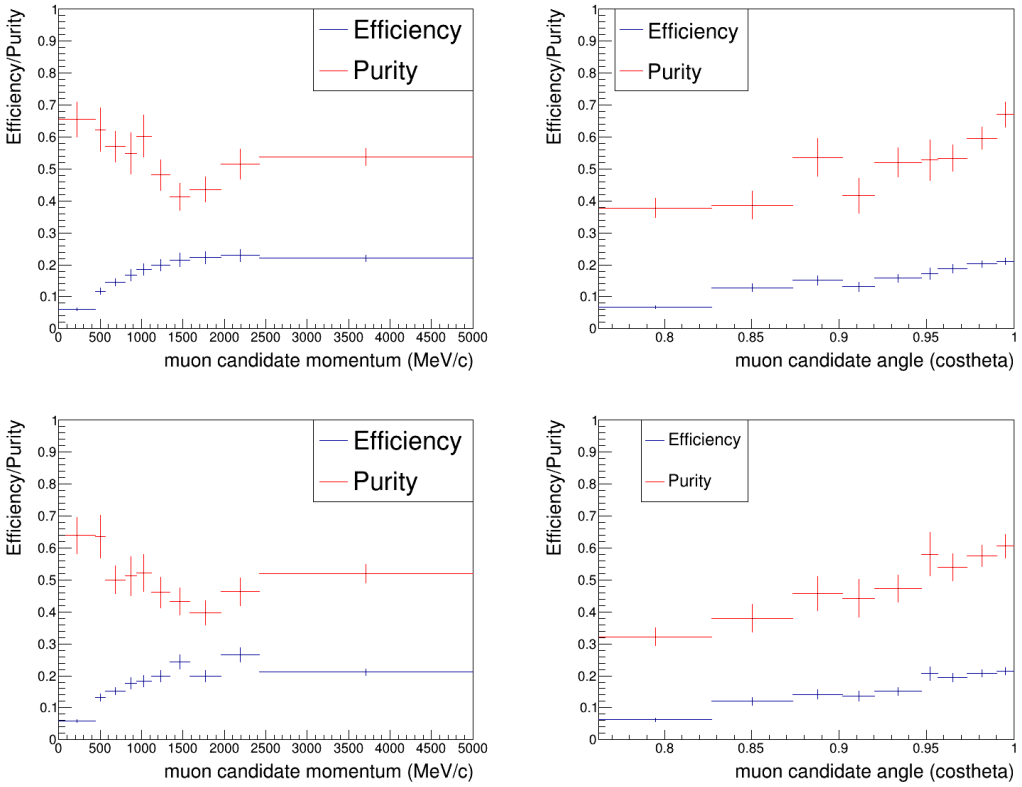

Figure 4.25: The efficiency (blue) and purity (red) of the CC1π^- sample for FGD1 (above) and FGD2 (below) in terms of the antimuon candidate momentum and angle.

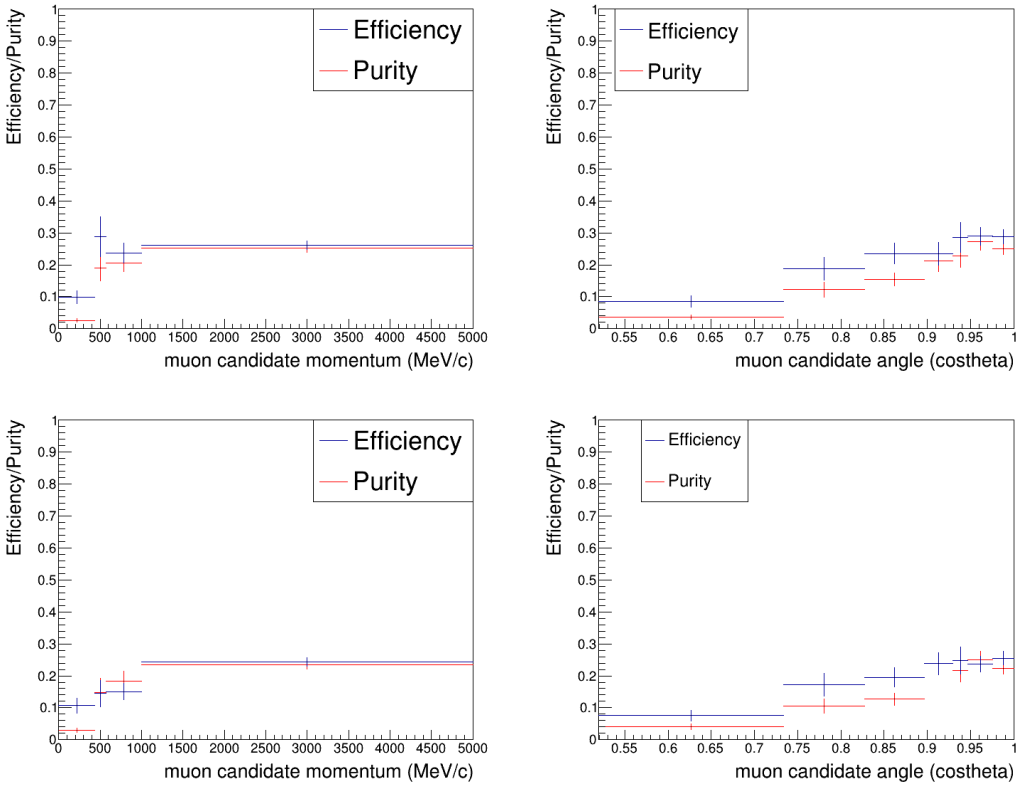

Figure 4.26: The efficiency (blue) and purity (red) of the CC-Other sample for FGD1 (above) and FGD2 (below) in terms of the antimuon candidate momentum and angle.

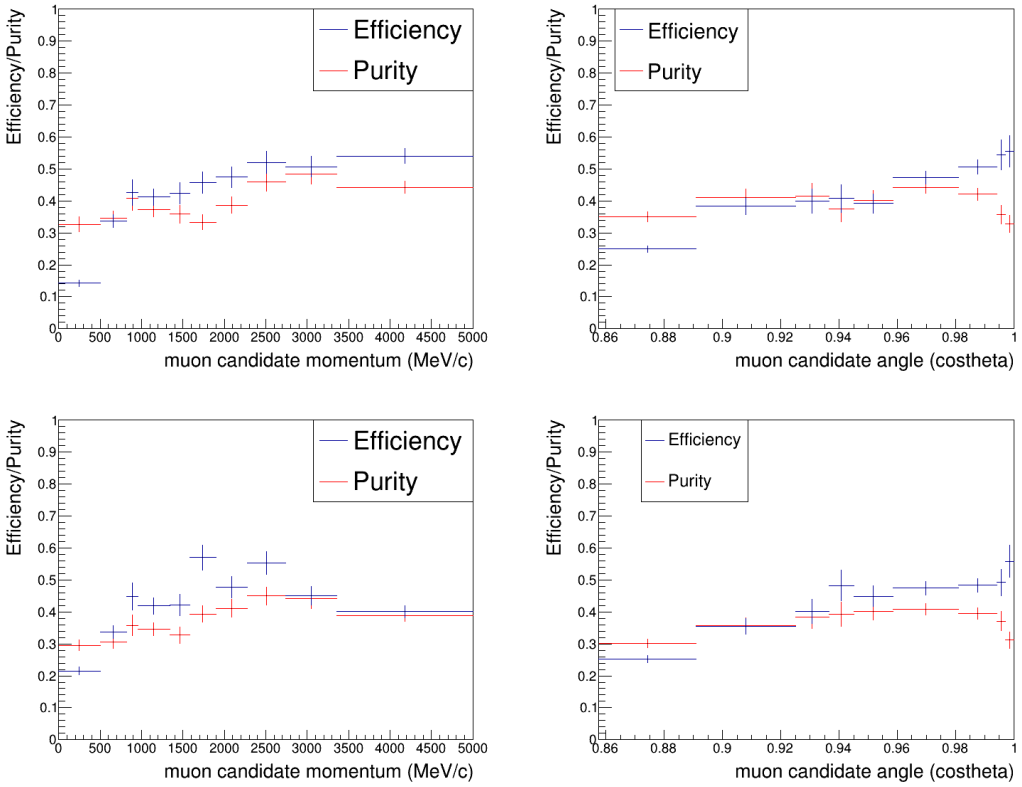

Figure 4.27: The efficiency (blue) and purity (red) of the CC-Photon sample for FGD1 (above) and FGD2 (below) in terms of the antimuon candidate momentum and angle.

Chapter 5

ND280 Detector Systematics

There are differences between the simulation of the ND and the real detector. These inconsistencies will in turn effect which events are selected for various samples, and the reconstructed kinematic properties of the tracks. To determine the magnitude of the systematic uncertainty for various responses, control samples are used. The events in these control samples are not used in any physics analysis, so it is possible to make comparisons of the data and MC to characterise the various systematic uncertainties. The magnitude of the uncertainty is calculated and propagated as the detector response uncertainty accordingly. The results are presented in terms of the relative error which is calculated by running 'toy experiments' and varying one source of systematic uncertainty at a time. A Gaussian is used where the systematic uncertainty mean is the central value of the distribution, and the width is the error of the systematic uncertainty. The toy experiment samples from this distribution and may result in events migrating in and out of samples, or between kinematic bins. The relative error is then defined as the Root Mean Squared (RMS) divided by the mean of the toy distribution of the number of events selected. This result is either shown in a distribution in terms of the

lepton kinematic bins, or as a relative integrated error for the whole sample. Some detector systematic uncertainties are common to all ND oscillation samples, and some are only relevant to certain topological samples. For example, as the muon PID BDT is only applied to the CC-Photon sample, it is only necessary to apply its corresponding uncertainty to this sample. Whereas the uncertainty on the fiduical mass of the FGD is relevant to all analyses as the oscillation analysis will always use the FGD as its target mass. This section will describe sources of detector systematic uncertainty relevant to all ND oscillation samples, with their full distributions, when applied to the CC-Photon sample, shown in appendix B. Detailed considerations for new sources of systematic uncertainty related to the new sample are explained. A description of the method in which the control sample discrepancy is propagated to a final systematic uncertainty value is also described.

5.1 Systematic Uncertainties for all $\bar{\nu}_\mu$ Interactions

A series of established systematic uncertainties are common between the previous iteration of the analysis, the $\bar{\nu}_\mu$ pion topology selection, and the CC-Photon selection. Each systematic uncertainty is described and analysed in detail in [104]. In appendix B, the systematic uncertainty distributions applied to the CC-Photon sample are shown as a function of the antimuon kinematics.

- **TPC cluster efficiency**

  This source of systematic uncertainty determines the probability of reconstructing a group of adjacent TPC pad hits, or clusters, where the cluster corresponds to a single point in the trace of ionised gas from a charged particle passing through

the TPC gas. This systematic uncertainty effects the TPC track quality cut used in CC selections, where at least 18 clusters must be present. The hits are clustered in the y direction (horizontal) if the angle of the track relative to the beam direction is less than 55°, otherwise the z direction (vertical) clusters are used. The difference between the MC and data is evaluated and propagated as a systematic uncertainty, allowing tracks to lose clusters due to the inefficiency between data and MC.

- **TPC track reconstruction efficiency**

  The efficiency of the TPC in reconstructing tracks from particles which pass through them is evaluated with this systematic uncertainty. A through-going beam and cosmic muon control sample is developed to evaluate the TPC track reconstruction algorithm. If the reconstruction algorithm fails to identify tracks correctly it could result in a miscounting of the total number of events in the CC sample, and introduce migration of events between sub-samples. A very high reconstruction efficiency, above 99% for each TPC, is found in both data and MC. The difference between the data and MC efficiency is the systematic uncertainty.

- **Charge sign identification**

  Two uncertainties are propagated when considering this systematic uncertainty. The probability that the local TPC charge identification is swapped; and the probability that the global tracking swaps the sign of the charge based on the local information. The charge of a track is determined based on its curvature in the TPC, assigning it either a positive or negative charge. If a track passes through multiple TPCs, the charge identification is determined by weighting the response of each individual TPC as a function of the number of hits deposited in

the TPC. Differences between the data and MC are propagated as the systematic uncertainty.

- **TPC PID**

  The TPC PID is determined by measuring the energy deposited in the TPC gas from a passing charged particle. The charge collected from this ionisation loss is calculated and compared with various particle hypotheses. The TPC PID is responsible for ensuring the muon and pion candidates are correctly identified. Control samples from beam events are used to determine the systematic uncertainty for selecting muons, protons, pions and electrons. Differences between data and MC in the pull distributions for each particle type are used as the systematic uncertainty.

- **TPC momentum resolution**

  In this systematic uncertainty a comparison between the TPC and global momentum resolution between data and MC is made. Based on the differences found, a smearing factor is applied and propagated as the systematic uncertainty. The smearing factor is determined by using the distribution of the inverse of the transverse momentum to the magnetic field, $1/p_T$, which is Gaussian in shape. The standard deviation of the fitted Gaussian is used as the smearing factor.

- **TPC momentum scale**

  This systematic uncertainty is obtained by using measurements of the magnetic field. Using a sample of cosmic muons passing through the FGD the momentum scale of the TPC measurement is compared to that of the momentum-by-range calculated in the FGD, dependent on the distance travelled by the track.

- **Magnetic field (B-field) distortions**

  Inaccuracies in the modelling of the magnetic field lead to bias in the calculation of the momentum of a track. A correction is applied to the MC to account for distortions in the B-field map, where each cluster is moved back to its ionisation point. It is also understood that electric field distortions are present, which affect the TPC momentum resolution. However no separate systematic uncertainty is calculated for this case, as it is already accounted for in the systematic uncertainty for the TPC momentum resolution.

- **FGD hybrid tracking efficiency**

  This systematic uncertainty aims to characterise the efficiency of the FGD in reconstructing contained tracks. This is important for FGD PID calculations which only use FGD contained tracks. Tracks which have both a TPC and FGD segment are selected and the ratio of the number of events with at least one isolated FGD object to the total number of events, is determined for data and MC. The process of hybridisation used in this systematic uncertainty evaluation is complex as detailed in [102].

- **Michel electron**

  This systematic uncertainty determines the detection efficiency and purity of Michel electrons, as were described in section 3.3. A sample of cosmic muons is used to determine the difference between the data and MC detection efficiency.

- **FGD PID**

  In the case where a particle stops in the FGD without interacting with the target mass, all of its kinetic energy is lost through ionisation. An estimate of the

particle mass can be determined by considering the energy deposited along the FGD segment and the distance travelled. The FGD can then determine the PID of the particle by constructing pulls in a similar way to the TPC PID methodology. Using tracks which stop in a FGD but also contain a TPC segment as a control sample, it is possible to compare the pull distribution for data and MC, for use as the systematic uncertainty.

- **FGD mass**

  There is an uncertainty on the mass of the FGD modules. The MC overestimates the density of the modules by 0.41%. There is also an additional uncertainty on the direct measurement of the spread of mass by 0.38%. For FGD2, which contains water layers, there is an additional uncertainty on the water mass and therefore the FV of FGD2.

- **Pion secondary interactions**

  This systematic uncertainty refers to cases where the pion interacts outside of the nucleus it was produced in. There is a significant difference between the behaviour simulated by Geant4 and results from external data. Therefore a weight is applied to account for these differences and is applied as a correction. The uncertainties of external data on pion interactions are then propagated as the systematic uncertainty.

- **Proton secondary interactions**

  This systematic uncertainty is an equivalent of the above mentioned pion secondary interaction systematic uncertainty but for protons leaving the nucleus instead. A similar procedure is applied for protons.

- **FGD-TPC matching efficiency**

  This efficiency estimates the ability of the reconstruction algorithm to match FGD tracks to TPC tracks. If the matching is not performed correctly, the interaction vertex may be mis-reconstructed, or the number of FGD FV events which pass the CC cuts may be miscounted. Through-going muons with two consecutive TPC segments are used as a control sample. The rate of tracks which also contain a FGD segment in-between the two TPC segments is used to estimate the systematic uncertainty.

- **Out Of Fiducial Volume (OOFV) background**

  These interactions types occur when the true vertex originates outside of the FGD FV but within the ND280 detector volume, while the reconstructed vertex is within the FGD FV. Many types of OOFV background interactions may occur, and the rate of each background type is considered. The events are split into nine different categories, corresponding to the reason why they are still selected in the analysis. These categories include backward events, OOFV inside the FGD, and cases where the parent of the track is neutral. The rate of OOFV events occurring in a CC-inclusive selection, is estimated to determine the systematic uncertainty. Using the difference in the OOFV rate for data and MC, for events occurring in the PØD, ECal and SMRD, a 20% rate uncertainty is applied. An additional uncertainty on the reconstruction is also applied to some of the OOFV categories such as backward events.

- **Sand event background**

  Alongside the magnet MC simulations, there are sand muon simulations. The systematic uncertainty estimates the difference in rates of tracks entering through

the upstream region of the PØD, and compares the data rate to the sand MC rate.

- **Pile-up**

  Pile-up refers to instances where more than one neutrino interaction occurs in the same time window, meaning tracks from one interaction may be attributed to a separate event causing issues in the categorisation of the sub-sample of the event. The primary cause of pile-up is from sand events occurring in the same time window as a beam magnet event. Studying the events which are rejected by the TPC1 veto it can be seen that most events are not true CC interactions. As the nominal beam neutrino MC does not account for sand muon coincidences, a correction is made to the MC. A comparison of the number of events failing the TPC veto in data and MC is used for this systematic uncertainty.

5.2 ECal Systematic Uncertainties used in Photon Selection

With the introduction of the new CC-Photon sample involving photon tagging from the ECal, the detector systematic uncertainties related to the ECal were introduced. These ECal systematic uncertainties related to:

- Track and shower reconstruction
- Matching objects to tracks from the tracker
- PIDMipEm
- Innermost ECal Layer Hit.

The first two sources of systematic uncertainty: ECal tracking efficiency and TPC-ECal matching were evaluated for the FHC photon tagging, and remain unchanged for the RHC case [105]. They are described in sections 5.2.1 and 5.2.2. However modifications were required for the ECal PIDMipEm and ECal photon pile-up systematic uncertainty evaluation, as described in sections 5.2.3 and 5.2.4.

5.2.1 ECal Tracking Efficiency

This systematic uncertainty aims to characterise the object reconstruction efficiency of the ECal. A sample of tracks exiting the TPC where the final layers of the TPC track are near the ECal, and the track direction points towards the ECal, are selected. It is assumed that these tracks enter the ECal, allowing the evaluation of the reconstruction capabilities of the ECal. The samples are further split to determine the reconstruction efficiency of the Br and Ds ECal separately. The efficiency is also determined separately for track-like particles such as muons, and shower-like particles like electrons. The reconstruction efficiency, $\text{Eff}_{\text{shower}}$, for showers is then determined to be:

$$\text{Eff}_{\text{shower}} = \frac{(\#\text{shower-like TPC candidate} \cap \text{ECal shower found})}{(\#\text{shower-like TPC candidate})}. \tag{5.1}$$

A similar equation is determined for tracks. The detector systematic uncertainty is determined by comparing the reconstruction efficiency for tracks and showers in both the Br- and Ds-ECal between data and MC. The reconstruction efficiency for all four samples is shown in figure 5.1.

The agreement is found to be good, within $\sim$5% for all four samples. This systematic uncertainty was only applied if the effect of the failed reconstruction would move the sample from or into the CC-Photon sample. If there was only one ECal photon identified

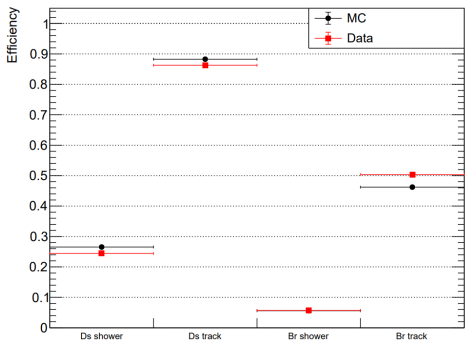

Figure 5.1: Reconstruction efficiency for showers and tracks in the Ds- and Br-ECals [105]. The red points represent the data efficiency, and the black points show the MC efficiency. The points for data and MC efficiency for showers in the Br-ECal overlap. The error bars represent the statistical uncertainty on these efficiencies, which are too small to be seen on this scale.

and no TPC tagged π^0; or there was neither an ECal photon or TPC tagged π^0 but there was a true unreconstructed photon-like particle in the ECal, then the systematic uncertainty was also applied.

5.2.2 TPC-ECal Matching Efficiency

The same control sample of tracks entering the ECal from the TPC is used to evaluate this systematic uncertainty. The control sample is further split according to particle type: muon-like, electron-like and proton-like. The particle type is determined using variables from the TPC. These tracks should all have entered the ECal and therefore the reconstruction algorithm should be able to match a segment from the TPC to a segment in the ECal. This matching efficiency, $\text{Eff}_{\text{match}}$, is determined to be:

$$\text{Eff}_{\text{match}} = \frac{(\#\text{tracks passing selection with an ECal segment})}{(\#\text{tracks passing selection})} \tag{5.2}$$

The same procedure of comparing the selection efficiency for data and MC for each sub-sample of particle-type and ECal sub-detector is made. It is found that the systematic uncertainty is <3% for each sample, and consistent with zero at the 2σ level. This systematic uncertainty was applied to any event which did not contain a reconstructed ECal photon but there was one in truth; or the CC-Photon event contained a single reconstructed ECal photon and no TPC photons.

5.2.3 PIDMipEm

The systematic uncertainty evaluation for PIDMipEm followed a similar procedure to that used to calculated the systematic uncertainty for PIDEmHip [105], however the variable has changed, as has the cut value, and required a more detailed analysis, as is described.

In this case, the accuracy of the variable in separating particle types was considered. Three particle control samples were determined: muons, electrons and protons. The selection procedures for each particle was detailed.

Muons

Through-going muon tracks, where the muon enters and exits the detector, which contain components from all three TPCs, and the ECal. Each TPC component must have a muon pull value: -2 $<\delta_\mu <$2. In previous iterations of this work a cosmic muon sample was also included, however at the time of this work, no cosmic muon files had been produced for production 7. The through-going muon sample statistics into both the Br- and Ds-ECal were sufficiently large for this work.

Electrons

A pair of tracks were selected: they were oppositely charged, originating within 10 cm

from one another, and both tracks began in the same FGD volume. Both tracks had at least one TPC component that passed the TPC energy loss measurements consistent with that of an electron: -2 < δ_e < 2. The invariant mass of the pair was less than 50 MeV/c^2, calculated using:

$$M^2_{\text{invariant}} = 2m^2_{\text{electron}} + 2(E_{\text{electron}} \times E_{\text{positron}} - \mathbf{p}_{\text{electron}} \cdot \mathbf{p}_{\text{positron}}) \tag{5.3}$$

A track was included in the control sample if either track entered the ECal.

Protons

Using neutrino-mode interactions, a proton sample was collected by searching for positive tracks with a proton TPC PID, with pull 0 <δ_p <2, and $|\delta_\mu|$ >10.

For each sample a cut of PIDMipEm > -7 was placed, the same cut value as was used to select photons for this analysis. The selection efficiency, Eff$_{PIDMipEm} > -7$ at this cut value, for each particle control sample was determined using:

$$\text{Eff}_{\text{PIDMipEm >-7}} = \frac{(\#\text{events with ECal object} \cap \text{PIDMipEm >-7})}{(\#\text{events with ECal object})}. \tag{5.4}$$

This efficiency was calculated for data and MC for each of the three particle control samples. It was then further split based on whether the ECal object was found in the Br- or Ds-ECal. A table showing the data and MC efficiencies for all samples is shown in table 5.1.

This variable has the ability to migrate events in and out of the photon sample, therefore any uncertainty should be applied in cases where the uncertainty would mean that the reconstructed object is rejected/selected when it previously was not. Therefore objects with a PIDMipEm value near to the cut line had the uncertainty applied, as

Sample	ECal Module	Data Efficiency (%)	MC Efficiency (%)	Data - MC Efficiency (%)
Muon	DS	4.88 ± 0.03	3.83 ± 0.02	0.98 ± 0.04
	Barrel	6.42 ± 0.07	4.55 ± 0.03	1.9 ± 0.1
Electron/Positron	DS	91.6 ± 0.6	91.5 ± 0.01	0.1 ± 0.5
	Barrel	78.8 ± 0.8	77.9 ± 0.2	0.8 ± 0.9
Proton	DS	43.1 ± 0.4	40.6 ± 0.1	2.5 ± 0.4
	Barrel	54.9 ± 0.5	53.2 ± 0.1	1.7 ± 0.6

Table 5.1: ECal PIDMipEm >-7 detector systematic uncertainty for all control samples.

events with very positive or negative PIDMipEm would not migrate over the cut line when the uncertainty is included. To determine which objects were 'near the cut line' the largest data-MC disagreement was selected: 2.5%. A region either side of the cut line was defined using this percentage, such that the region contained 2.5% of all ECal objects in the photon sample.

The total relative error of ECal PIDMipEm on all four ND samples is shown in figure 5.2 as a function of the antimuon kinematics. The integrated relative error of the CC-Photon sample was 0.1% (0.06%) for FGD1 (FGD2).

5.2.4 ECal Photon Pile-up

This systematic uncertainty aimed to account for cases where a true CC physics event originating in the fiducial volume had occurred, but another particle not related to the FGD interaction had produced hits in the ECal. If the hits formed an object which passed the subsequent photon-like cuts, and the hits occurred in the same time window as a beam event, a mis-reconstruction of the event topology would occur. Any event which passed the event quality cut as described in section 4.2 and also had no activity in the FGD fiducial volume was defined as a pile-up event. The difference in probability of

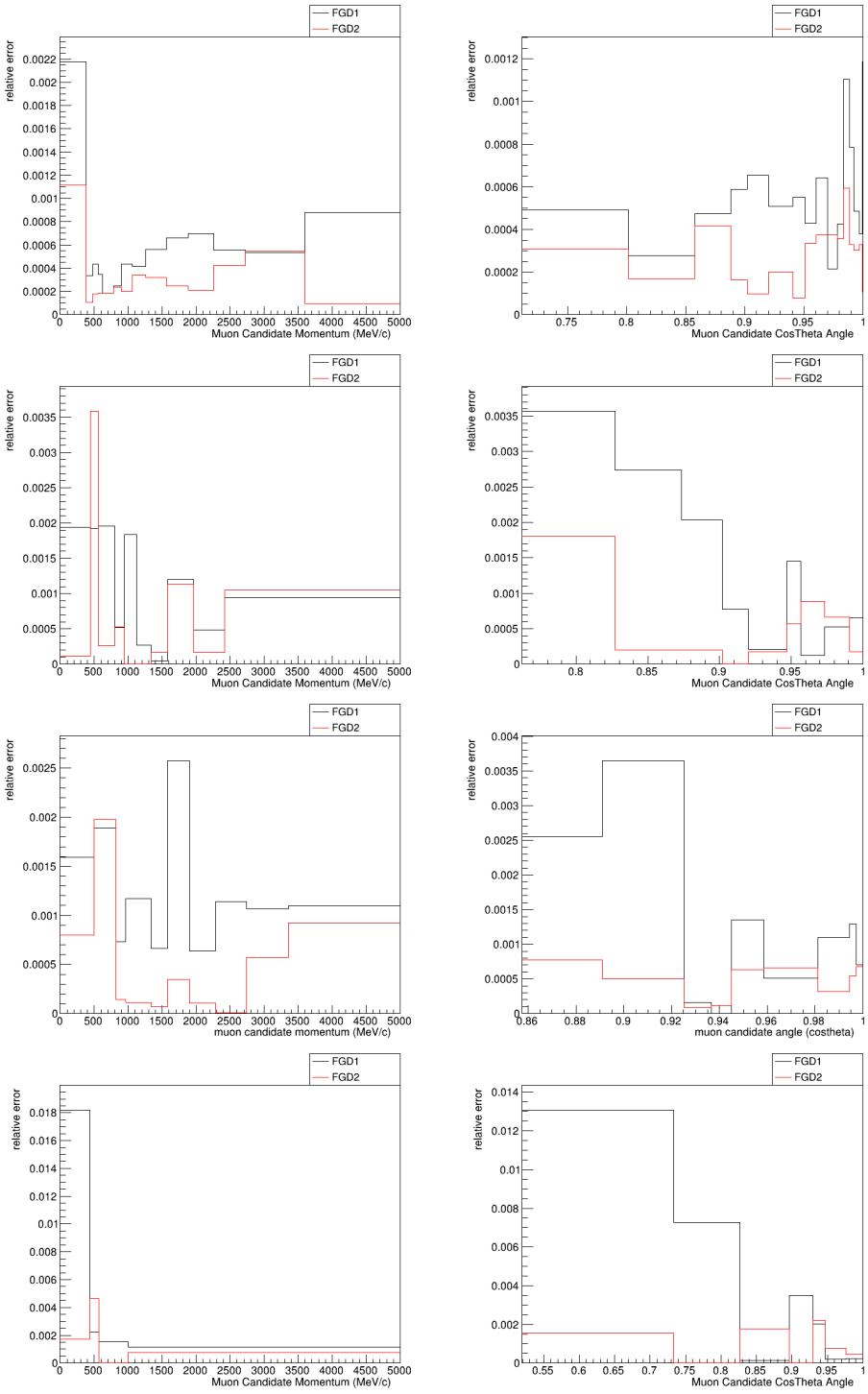

Figure 5.2: Average differential detector uncertainty for the ECal PIDMipEm systematic uncertainty for all four samples in terms of the reconstructed antimuon momentum and angle. The samples are CC0π, CC1π^-, CC-Photon and CC-Other from top to bottom.

Run Number	POT per spill / $\times 10^{13}$	MC Probability (%)	Data Probability (%)	Data - MC Probability (%)
5	0.99	0.883 ± 0.001	1.10 ± 0.01	0.22 ± 0.01
6	1.48	0.962 ± 0.001	1.523 ± 0.003	0.561 ± 0.003
7	1.96	1.540 ± 0.001	2.53 ± 0.01	0.99 ± 0.01
9	2.43	1.878 ± 0.002	2.39 ± 0.01	0.512 ± 0.01

Table 5.2: The probability of ECal pile-up occurring for each of the four RHC runs, with the POT per spill shown. The statistical uncertainity on the probability is shown.

ECal pile-up in data and MC is accounted for in the systematic uncertainty calculation. The ECal pile-up probability, $\text{Prob}_{\text{pile-up}}$ was defined as:

$$\text{Prob}_{\text{pile-up}} = \frac{(\#\text{events with an ECal photon} \cap \text{no FGD activity})}{(\#\text{events with no FGD activity})} \tag{5.5}$$

where an ECal photon was defined according to the photon selection: >4 ECal hits, PIDMipEm >-7, innermost ECal layer hit >7. The probability was determined for data and MC, and was further split by run number. For this work, as the run number increased the beam power also increased, leading to additional pile-up from consecutive neutrinos interacting in the same time window. The increasing beam power is better represented by the POT per spill. No significant difference was found between the pile-up probability of FGD1 and FGD2, therefore only the systematic uncertainty uncertainty for FGD1 was calculated and propagated to both cases. Table 5.2 and figure 5.3 show the probability of ECal photon pile-up occurring as a function of increasing POT per spill. The figure also includes data for the FHC runs as calculated in [105].

Some large disagreement was observed between the data and MC probability. This is because a large contributor to ECal pile-up had not been included in MC: sand interactions. If a sand interaction occurred in the same time window as a physics event

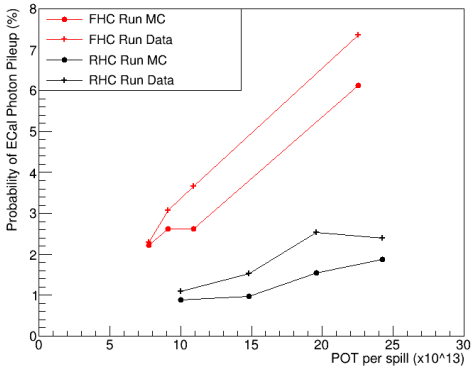

Figure 5.3: The probability (%) of an ECal photon pile-up event occurring as a function of the POT per spill, with neutrino-mode (FHC) and antineutrino-mode (RHC) runs indicated by red and black respectively. Circular points indicate MC and crosses show data.

from the FGD, it would pass into this analysis.

Although sand interaction files exist, there is no way to straightforwardly add these files to this work as the timing information is crucial when replicating the data. If the sand MC files were added, they would often over compensate the data probability, due to the inclusion of additional events not in coincidence with a beam trigger, leading to a similar disagreement as currently observed. As this source of disagreement between data and MC is large, it was possible to instead apply a data-driven re-weighting to the MC events to account for this known discrepancy, rather than apply a systematic uncertainty.

The total relative error of the ECal photon pile-up systematic uncertainty on all four ND samples is shown in figure 5.4 as a function of the antimuon kinematics. The integrated relative error of the CC-Photon sample was 0.9% (0.8%) for FGD1 (FGD2).

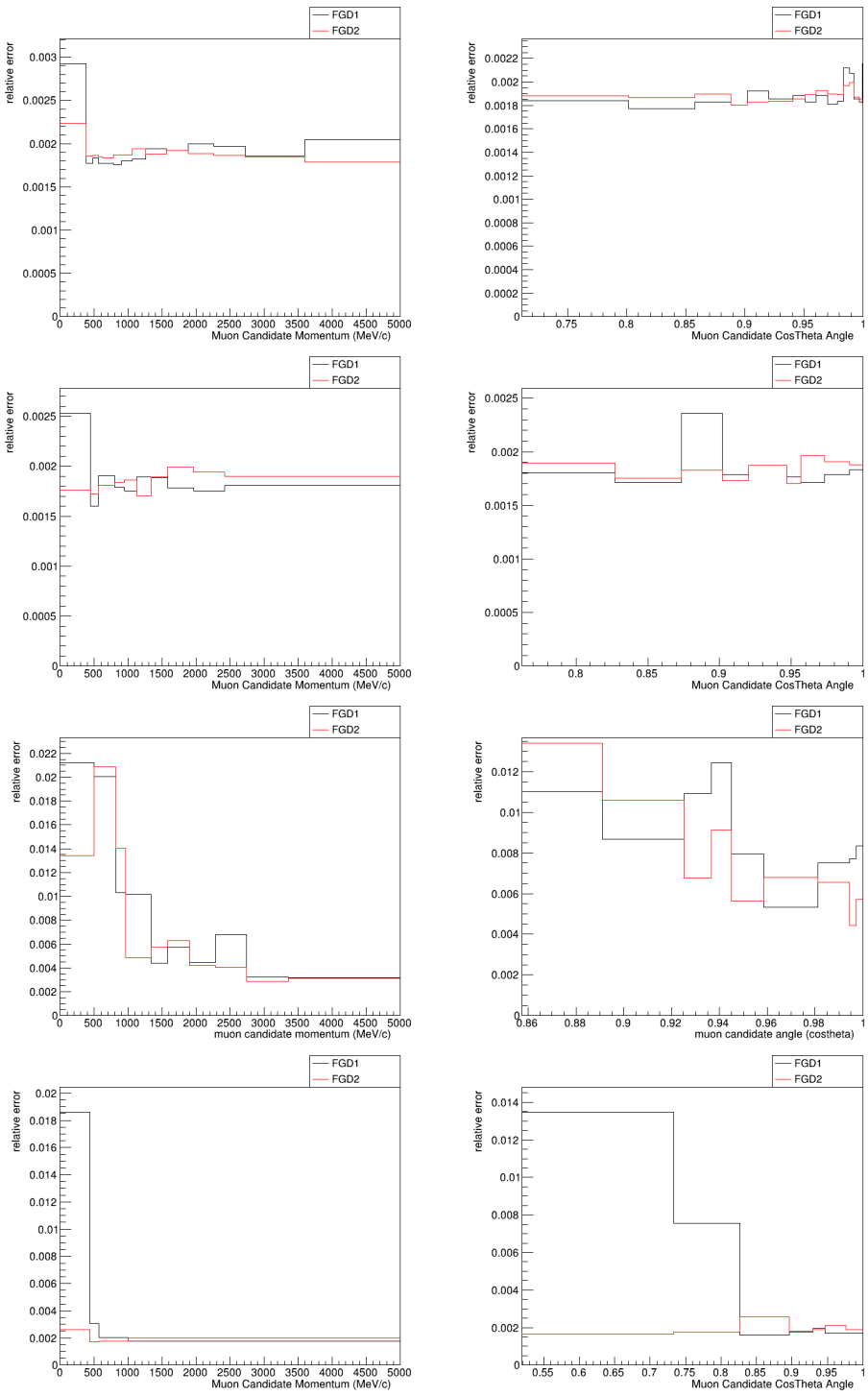

Figure 5.4: Average differential detector uncertainty for the ECal photon pile-up systematic uncertainty for all four samples in terms of the reconstructed antimuon momentum and angle. The samples are CC0π, CC1π^-, CC-Photon and CC-Other from top to bottom.

5.3 Muon PID BDT Systematic Uncertainty

The muon candidate PID BDT used a variety of subdetector variables. As multiple subdetectors were used, their corresponding uncertainties are also propagated through to the BDT response. If a track were mismodelled it could migrate above or below the cut line, thus changing the BDT response distribution and the number of events selected into the CC-Photon sample by the BDT. The systematic uncertainty associated with the BDT was determined based on the selection efficiency of the BDT when tested on control samples of one pure particle type. Due to differences in the response distributions, BDT uncertainties were calculated separately for FGD1 and FGD2. The control samples were selected to ensure a sample of well reconstructed events, none of which were selected for an oscillation analysis sample. Therefore the FV used was the PØD. For the events originating in the PØD, four cuts were applied:

- Event quality
- Total multiplicity
- Quality and fiducial
- Veto track

These cuts were based on the CC selection as discussed in section 4.2, although in this instance the fiducial volume was that of the PØD not the FGDs. Of these events, four particle samples were selected: muons, protons, pions and electrons. The selection procedure for the particle type is described below, and used both FHC and RHC data, from runs 4, 6, 7 and 8.

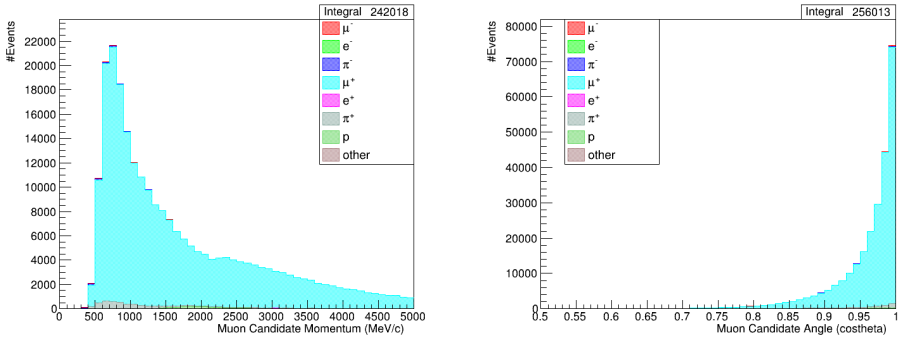

Figure 5.5: The PØD antimuon control sample used for evaluating the antimuon PID BDT as a function of the track momentum and angle.

5.3.1 Anti Muon Sample

The highest momentum track in the event was selected, and passed the following cuts:

- Positive charge
- Momentum >300 MeV/c in each TPC segment
- -2< δ_μ <2 in each TPC
- TPC $\mathscr{L}_\mu > 0.3$
- At least one FGD segment
- Track multiplicity < 7

This selection resulted in a antimuon sample purity of 96.9 $\pm$ 0.2%. The sample kinematics are shown in figure 5.5.

5.3.2 Proton Sample

The highest momentum track was also found for this sample but instead selected protons with the following cuts:

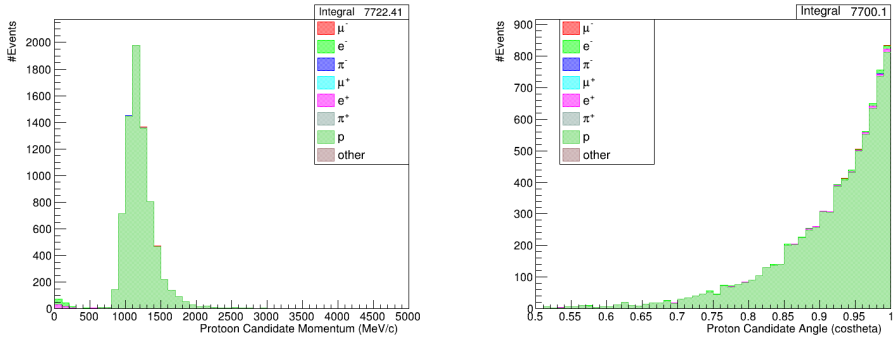

Figure 5.6: The PØD proton control sample used for evaluating the muon PID BDT as a function of the track momentum and angle.

- Positive charge
- $0 < \delta_p < 2$ for all TPC segments
- $\delta_\mu > 10$ or $\delta_\mu <$ -10, for all TPC segments

This selection provided a proton sample which was 99.6 $\pm$ 0.2% pure. The sample kinematics are shown in figure 5.6.

5.3.3 Pion Sample

Two separate selections were made to create a pure pion sample: one targeting positive pions and the other negative pions. The first case searched for the highest momentum positive track in the event and applied the following cuts to the track:

- TPC $\mathscr{L}_\pi > 0.3$
- TPC $\mathscr{L}_e < 0.05$
- Momentum < 1750 MeV/c

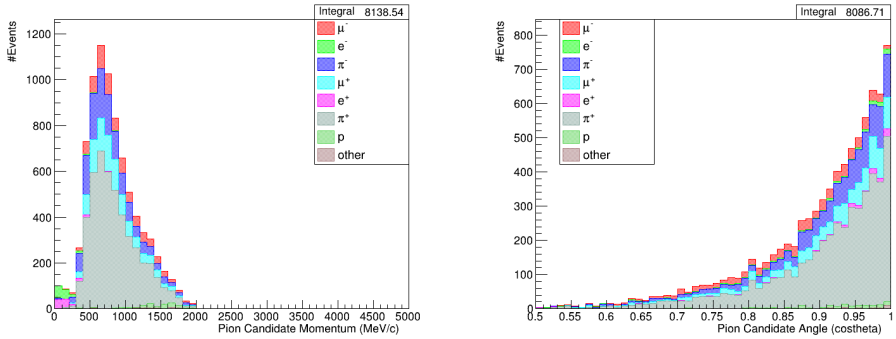

Figure 5.7: The PØD pion control sample used for evaluating the muon PID BDT as a function of the track momentum and angle.

For this pion sample the purity was 68%. The second pion sample searched for the second highest momentum track and the following cuts were applied:

- TPC $\mathscr{L}_{\pi} > 0.4$
- TPC $\mathscr{L}_{\mu} < 0.55$
- TPC $\mathscr{L}_{e} < 0.05$
- Momentum < 2000 MeV/c

A check was also made on the highest momentum track to ensure it was muon-like, by ensuring the TPC $\mathscr{L}_{\mu}$ of the track was greater than 0.3. This sample had a purity of $75.0 \pm 0.1\%$. Once both pion control samples were combined, accounting for overlaps in which events were selected between both methods, a purity of $73.6 \pm 0.1\%$ was achieved. The pion samples kinematics are shown in figure 5.7.

5.3.4 Electron Sample

A pair of tracks were required in this sample to choose an electron and positron pair with the following cuts applied:

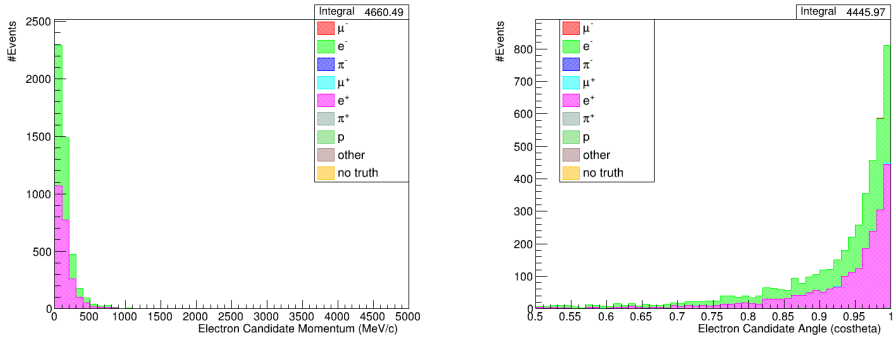

Figure 5.8: The PØD electron control sample used for evaluating the muon PID BDT as a function of the track momentum and angle.

- Tracks have opposite charge
- Tracks originate within 10 cm of one another
- -2 $< \delta_e <$ 2
- Invariant mass of pair $<$ 50 MeV/c^2

The pair of tracks did not need to originate from the PØD in this sample, but the vertex of the highest momentum track in the event was located in the PØD. Both tracks in the selection were included to create a combined selection of electrons and positrons. The sample had a purity of 99.8 $\pm$ 0.2%. The sample kinematics are shown in figure 5.8.

5.3.5 Evaluation Strategy

Once control samples were established, the BDT response for each sample was calculated. The 2D BDT response cut used to select the CC-Photon sample was applied to each control sample. The selection efficiency of the cut at tagging the particle type

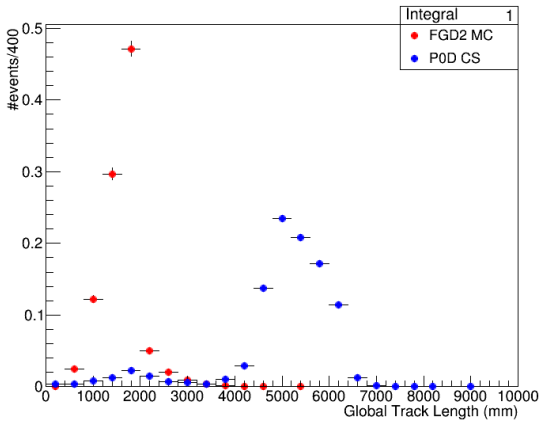

Figure 5.9: Normalised distribution of track length (mm) for the antimuon PØD control sample and the FGD2 CC-Photon signal events.

included in the sample was determined using the following definition:

$$\text{Selection Efficiency} = \frac{\#\text{events selected by BDT}}{\#\text{total events in control sample}} \tag{5.6}$$

This selection efficiency was calculated for both MC and data. This process was repeated for the second FGD BDT, so that the selection efficiency was determined for the FGD1 BDT and FGD2 BDT separately.

For FGD2 a biasing factor was noted in the method described. This bias affected the antimuon sample due to differences in the track length distribution of the control sample relative to the physics analysis sample. An antimuon track in the PØD sample is longer than the antimuons in the CC-Photon FGD2 sample, as shown in figure 5.9. Muon tracks tend to be through-going, meaning their track length is often the distance between the interaction vertex and the end of the ND280 tracker. Therefore the track length distribution shifted to larger values for the PØD originating sample, relative to the FGD2 sample. The track length variable was important in the structure of

Sample	Efficiency MC	Efficiency Data	Data - MC
Muon	90.8 ± 0.3%	90.4 ± 1.3%	-0.4 ± 1.4%
Proton	3.0 ± 0.1%	2.2 ± 0.5%	-0.9 ± 0.6%
Pion	48.4 ± 0.8%	51 ± 3%	2 ± 3%
Electron/Positron	3.3 ± 0.2%	4.4 ± 1.1%	1.1 ± 1.1%

Table 5.3: Muon PID BDT systematic uncertainties for FGD1.

Sample	Efficiency MC	Efficiency Data	Data - MC
Muon	52.5 ± 0.2%	47.9 ± 0.8%	-4.6 ± 0.9%
Proton	14.0 ± 0.3%	13.2 ± 1.4%	-0.8 ± 1.5%
Pion	50.0 ± 0.8%	49.8 ± 3%	-0.1 ± 3%
Electron/Positron	3.3 ± 0.2%	3.8 ± 1.0%	0.6 ± 1.0%

Table 5.4: Muon PID BDT systematic uncertainties for FGD2.

the BDT, due to its excellent signal and background discrimination. The change in the distribution in the PØD sample resulted in better performance in separating muons from other particle types, thus increasing the selection efficiency. To mitigate this issue, it would be preferable to adapt the control samples to better match the CC-Photon FGD2 samples. No viable alternative samples were found. Instead, the track length distribution of the PØD sample was scaled to better match the CC-Photon FGD2 distribution. A Gaussian distribution was fitted to the peak of the track length distribution of the CC-Photon FGD2 sample, and the PØD sample track length distribution was scaled such that its peak was located at the same position as the CC-Photon FGD2 sample. The scaling factor applied was 0.327. These changes were only applied to the antimuon FGD2 sample, as the track length distributions of other samples were decided to approximately match that of the PØD samples. The calculated efficiencies for all control samples are summarised in tables 5.3 and 5.4.

The systematic uncertainty calculated from the control samples were only applied to

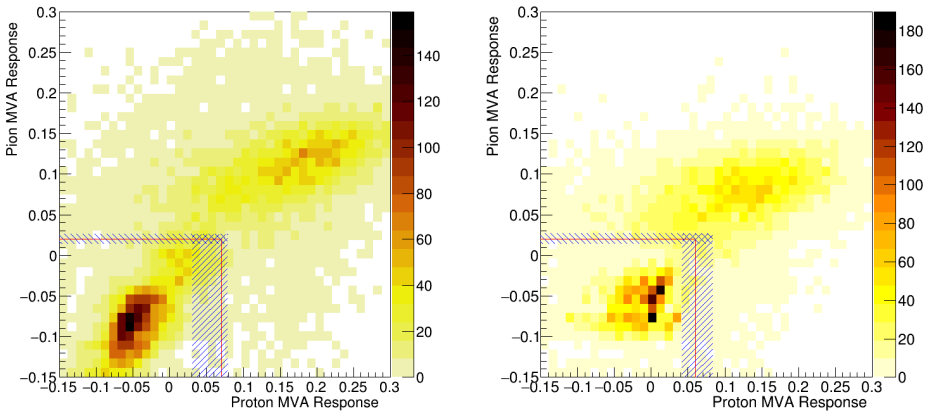

Figure 5.10: Region where PID BDT systematic uncertainty is applied for FGD1 and FGD2 samples (top and bottom). The red line shows the cut positions, hashed regions indicate events where systematic uncertainty is applied.

events which were likely to migrate over or below the BDT cut lines which would cause a change in the number of events selected or rejected by the BDTs. The region of events where the systematic uncertainty was applied was determined according to the largest disagreement between data and MC. The region was defined separately for the FGD1 and FGD2 BDTs, reflecting the different data and MC agreements. For the FGD1 BDT case the largest systematic uncertainty was ∼2% and for FGD2 it was ∼4.6%. Two boundaries were defined based on the two separate 1D cuts on the proton-muon and pion-muon BDT responses. In each of the one-dimensional planes, 2% or 4.6% of the total FGD1 and FGD2 events, respectively, surrounding the cut line were determined. The regions are shown in figure 5.10.

The total relative error of the antimuon candidate PID BDT systematic uncertainty for the CC-Photon sample is shown in figure 5.11 as a function of the lepton kinematics. The integrated relative error of the sample was 0.2% (0.4%) for FGD1 (FGD2).

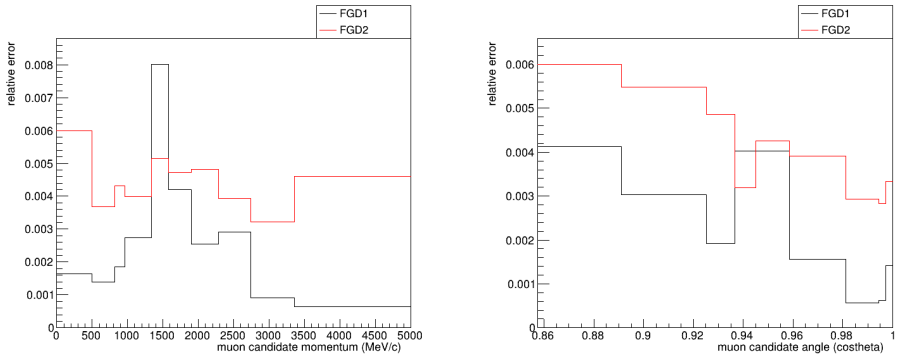

Figure 5.11: Average differential detector uncertainty for the muon PID BDT systematic uncertainty for the CC-Photon sample in terms of the reconstructed antimuon momentum and angle.

5.4 Detector Systematic Uncertainty Propagation

A broad set of detector systematic uncertainties have been determined to represent the sources of error in measurements which affect physics results. The effect of introducing the detector systematic uncertainties on physics analyses is determined by observing the shift in events selected by each sample when the detector parameter is varied by the systematic uncertainty. Two methods are used to estimate the detector systematics uncertainties: variation-like systematics uncertainties and weight-like systematics uncertainties [104].

The first type: variation-like systematic uncertainties involve fluctuating the central value of a given parameter according to it systematic uncertainty, to introduce a bias on that parameter, and observe the shift in the number of events selected with this new parameter value. The simulation is repeated many times, in what is described as a toy experiment. In total, 500 toy experiments are generated to reduce statistical fluctuations and sample from the full Gaussian distribution of the parameter with a new smeared parameter for each toy experiment. This type of detector systematic

uncertainty method is usually used for parameters related to reconstruction such as the scale and resolution of measurable values.

The second implementation method: weight-like systematic uncertainties, is less computationally intensive. They can be categorised in two ways, as either efficiency-like systematic uncertainties, which are used on variables related to detector reconstruction probability, and normalisation-like systematic uncertainties, which are used to broadly scale up or down sub-samples of events such as background rates.

5.4.1 Efficiency Systematic Uncertainties

The accuracy of reconstruction methods, such as the new PID BDT, is evaluated using an efficiency-like systematic uncertainty propagation. It is hoped that the control samples used to estimate the discrepancies between data and MC are representative samples of the phase space of the various physics samples which use the reconstruction tool. However, in reality this is not always accurate, therefore extrapolations are made between the control sample data and MC agreement and the physics samples data and MC agreement. It is assumed that the ratio between the efficiency calculated for data and MC in the control samples is equal to that of the physics samples:

$$\epsilon_{data} = \frac{\epsilon^{CS}_{data}}{\epsilon^{CS}_{MC}} \epsilon_{MC} \tag{5.7}$$

where $\epsilon_{data,MC}$ is the data, MC efficiency, and $\epsilon^{CS}_{data,MC}$ is the data and MC control sample efficiency. The MC efficiency can be accurately estimated as it is possible to consult the truth information of the event. However this is not possible with data, and extrapolations must be made using the control sample efficiencies, while also accounting

for statistical fluctuations:

$$\epsilon'_{data} = (r^{CS} + \alpha\delta r^{CS})\epsilon_{MC} \tag{5.8}$$

where $r^{CS} = \frac{\epsilon^{CS}_{data}}{\epsilon^{CS}_{MC}}$, and $\delta r^{CS} = \sqrt{(1 - r^{CS})^2 + (\delta r^{CS}_{stat})^2}$, where δr^{CS}_{stat} is the statistical error on the efficiency ratio, and α is a random variable following a normal distribution between 0 and 1. The value of ϵ_{MC} was set to 1 in the case of the PID BDT, but in some cases it is set to some other value to account for known discrepancies in the physics samples. To propagate this difference to the physics samples an efficiency weight, w_{eff}, is constructed and is defined as:

$$w_{eff} = \frac{\epsilon'_{data}}{\epsilon_{MC}}. \tag{5.9}$$

The inefficiency weight, w_{ineff}, is defined as:

$$w_{ineff} = \frac{1 - \epsilon'_{data}}{1 - \epsilon_{MC}}. \tag{5.10}$$

The efficiency weight is applied to MC tracks/events where a track/event is correctly reconstructed, and the inefficiency is invoked in the case a track/event is not correctly reconstructed. The event weight is then taken to be:

$$w_e = \prod_{j}^{N_{tracks}} (\delta_{jrec} w_{eff} + (1 - \delta_{jrec}) w_{ineff}), \tag{5.11}$$

where $\delta_{jrec} = 1$, if there is an association, and $\delta_{jrec} = 0$ if there is none. Using this weight, the detector systematic uncertainty for the event is calculated, using the covariance of the number of events calculated nominally by the MC to the number of

expected data events after extrapolation from the control sample efficiencies:

$$cov_{ij} = \frac{1}{N_{throws}} \sum_{s=1}^{Nthrows} (N_i^s - N_i^{MC})(N_j^s - N_j^{MC}) \tag{5.12}$$

where the number of predicted data events is,

$$N_i^s = \sum_{e=1}^{Nevents} w_{e,i}^s \tag{5.13}$$

where $w_{e,i}^s$ is the event weight for a given throw, s, of the value α for a given bin i.

5.4.2 Normalisation Systematic Uncertainties

This type of systematic uncertainty is used for sources such as pile-up and the FGD mass. It refers to a general scaling which effects the total number of expected events. In this case the event re-weighting of the category of systematic uncertainty, w_e, is:

$$w_e = 1 + \alpha.\delta_{e,cat} \tag{5.14}$$

where $\delta_{e,cat}$ is the associated systematic uncertainty of a category of events, such as pile-up, and α is a random variable, to propagate the variation of the systematic uncertainty. The variation in the number of selected events is determined using:

$$N_i^s = \sum_{e=1}^{Nevents} (\delta_{e,cat,i} w_e^s + (1 - \delta_{e,cat,i})) \tag{5.15}$$

where $\delta_{e,cat,i}$ is equal to 1 if the event is correctly categorised, and 0 if it is not.

5.5 Summary of ND280 Detector Systematic Uncertainties

The relative error of the four ND samples when all sources of detector systematic uncertainty were considered simultaneously, are shown in figure 5.12. The total average differential systematic uncertainty for FGD1 (FGD2) samples was 3.4% (3.6%) for the CC0π sample, 5.2% (7.2%) for the CC1π^- sample, 4.2 (5.7%) for the CC-Photon sample, and 6.8% (8.2%) for the CC-Other sample. Distributions of individual contributions of each detector systematic uncertainty to the CC-Photon sample are shown in appendix B.

A summary of the average differential error for all samples with each detector systematic uncertainty considered separately is shown in table 5.5. The primary contributions to the detector systematic uncertainties were: pion secondary interaction, TPC-ECal matching efficiency, ECal tracking efficiency, TPC track reconstruction efficiency and the TPC PID.

Figures 5.13 and 5.14 show the contribution of statistical and detector systematic uncertainty to the number of events selected for each sample as a function of the lepton kinematics. Some discrepancy between data and MC was still present but this was anticipated as the cross section and flux parameters had not been considered yet. The samples are used in a fit, as will be discussed in more detail in section 6, to better understand these parameters.

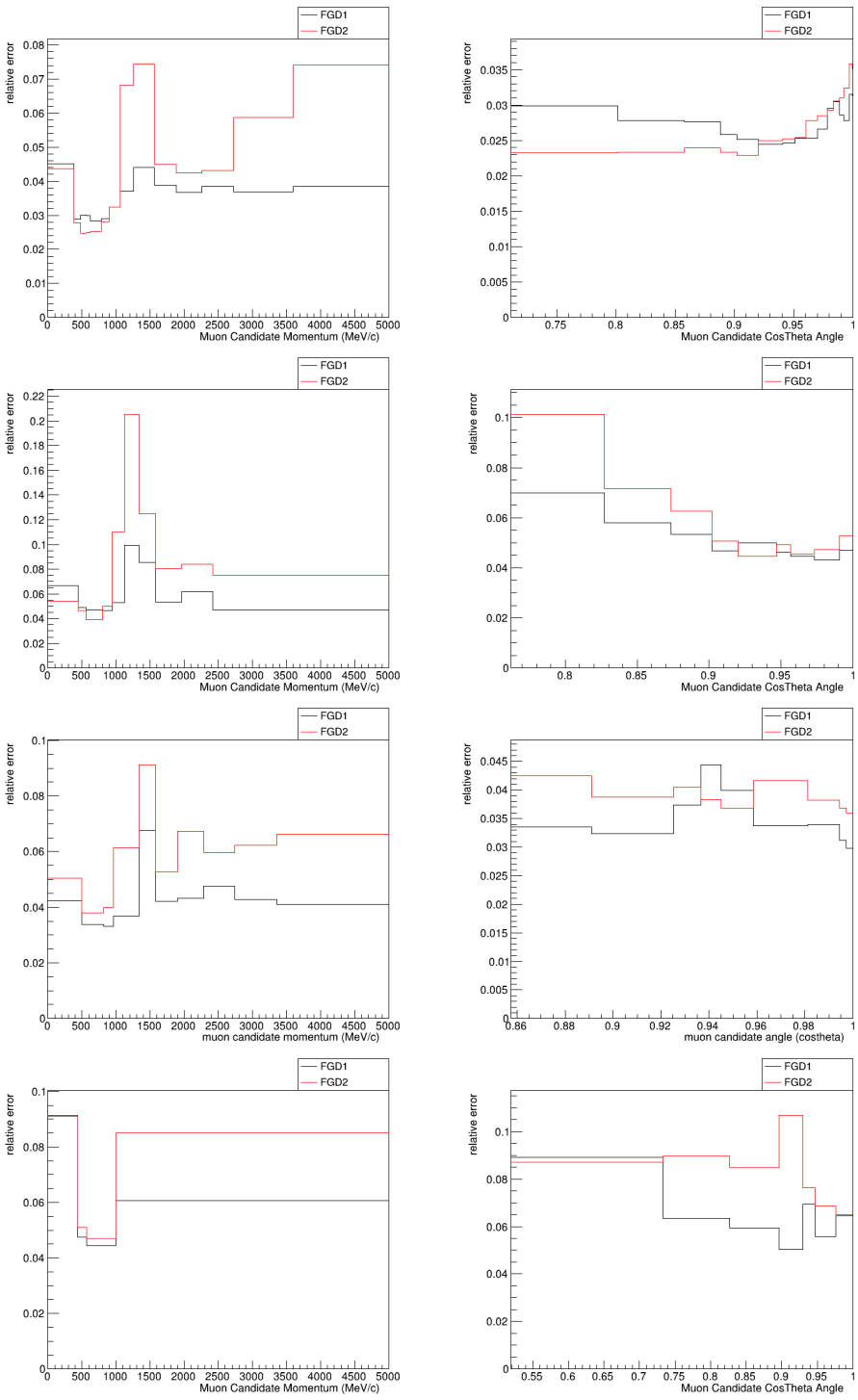

Figure 5.12: Average differential detector uncertainty for all sources of systematic uncertainty for all four samples, CC0π, CC1π^-, CC-Photon and CC-Other, from top to bottom, in terms of the reconstructed lepton momentum and angle.

Source of Error	Integrated total relative error (%)							
	CC0π		CC1π^-		CC-Photon		CC-Other	
	FGD1	FGD2	FGD1	FGD2	FGD1	FGD2	FGD1	FGD2
Variation Systematic Uncertainties								
B-field distortions	0.2	0.6	0.2	1.0	0.3	2.0	0.2	0.4
TPC momentum resolution	0.5	0.8	0.8	1.0	0.7	1.0	0.6	0.7
TPC momentum scale	0.8	0.9	0.8	0.7	0.7	0.7	0.3	0.3
TPC PID	0.7	1.0	2.0	5.0	2.0	3.0	2.0	5.0
FGD PID	0.07	0.04	1.0	0.6	-	-	0.2	0.1
Weight-like Systematic Uncertainties								
TPC cluster efficiency	0.008	0.008	0.02	0.02	0.02	0.02	0.03	0.02
TPC track reconstruction efficiency	1.0	1.0	2.0	2.0	0.5	1.0	0.7	2.0
Charge sign identification identification	0.007	0.004	0.01	0.008	0.02	0.004	0.02	0.005
FGD hybrid tracking efficiency	0.2	0.05	1.0	0.4	0.2	0.09	0.3	0.1
Michel electron	0.06	0.04	0.5	0.3	0.3	0.2	0.2	0.2
FGD mass	0.6	0.4	0.6	0.4	0.6	0.4	0.4	0.3
Pion secondary interactions	2.0	2.0	4.0	2.0	3.0	3.0	4.0	3.0
Proton secondary interactions	0.2	0.2	0.5	0.8	0.4	0.5	0.6	0.9
FGD-TPC matching efficiency	0.2	0.1	0.2	0.3	0.1	0.2	0.1	0.2
OOFV background	0.4	0.6	0.2	0.3	0.3	0.9	3.0	3.0
Pile-up	0.2	0.2	0.2	0.2	0.2	0.2	0.2	0.2
ECal tracking efficiency	0.3	0.3	1.0	1.0	1.0	1.0	1.0	2.0
TPC-ECal matching efficiency	2.0	1.0	1.0	1.0	0.2	0.2	0.8	0.4
ECal PIDMipEm	0.2	0.2	0.2	0.2	0.1	0.06	0.08	0.04
ECal Photon Pile-up	0.2	0.2	0.2	0.2	0.9	0.8	0.2	0.2
Muon PID BDT	-	-	-	-	0.2	0.4	-	-
Total	3.4	3.6	5.2	7.2	4.2	5.7	6.8	8.2

Table 5.5: The integrated total relative error for each of the sources of detector systematic uncertainty considered for each of the ND samples.

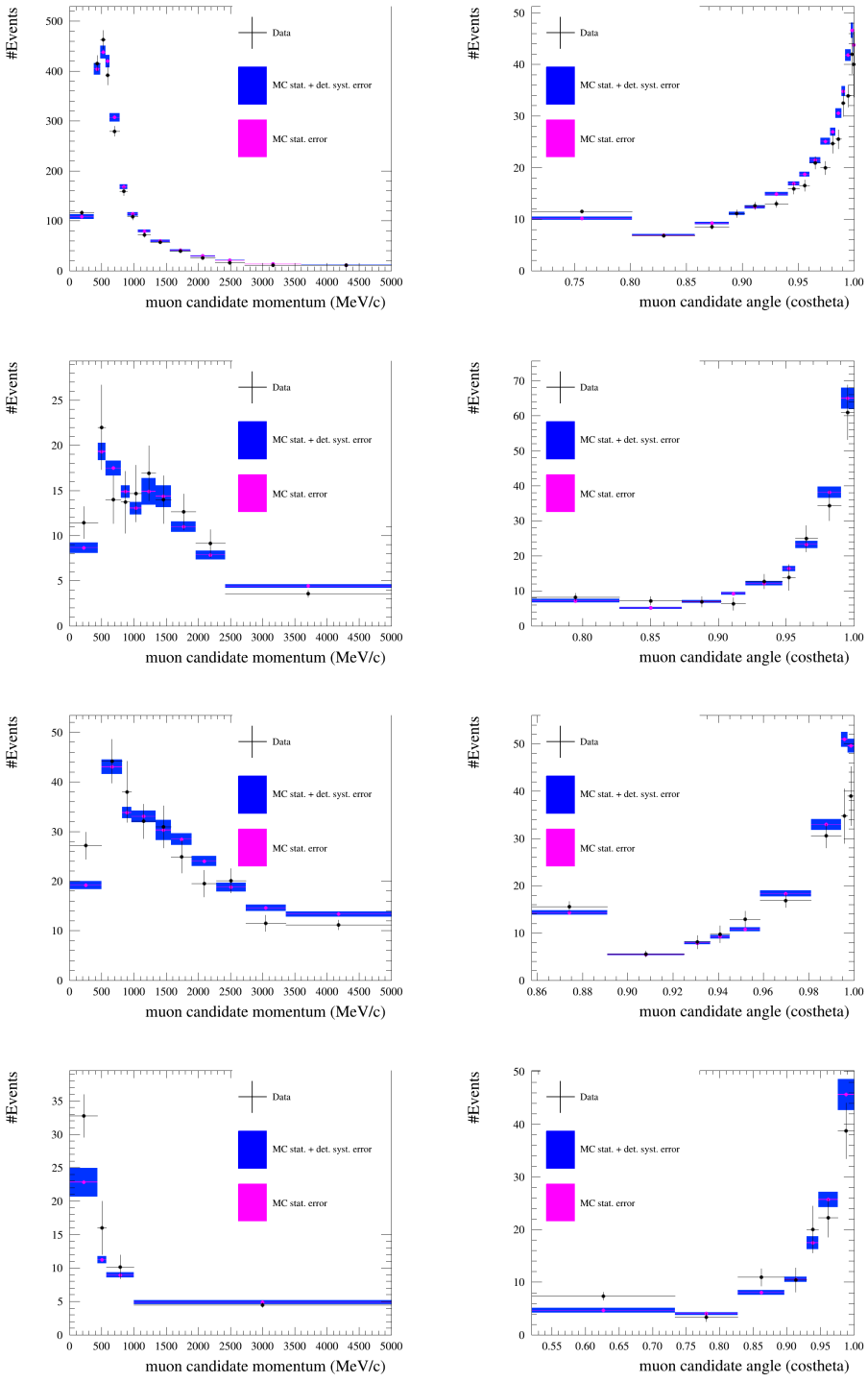

Figure 5.13: The statistical and detector systematic uncertainties on the number of events selected for each FGD1 sample, CC0π, CC1π^-, CC-Photon and CC-Other, from top to bottom, as a function of the lepton momentum and angle.

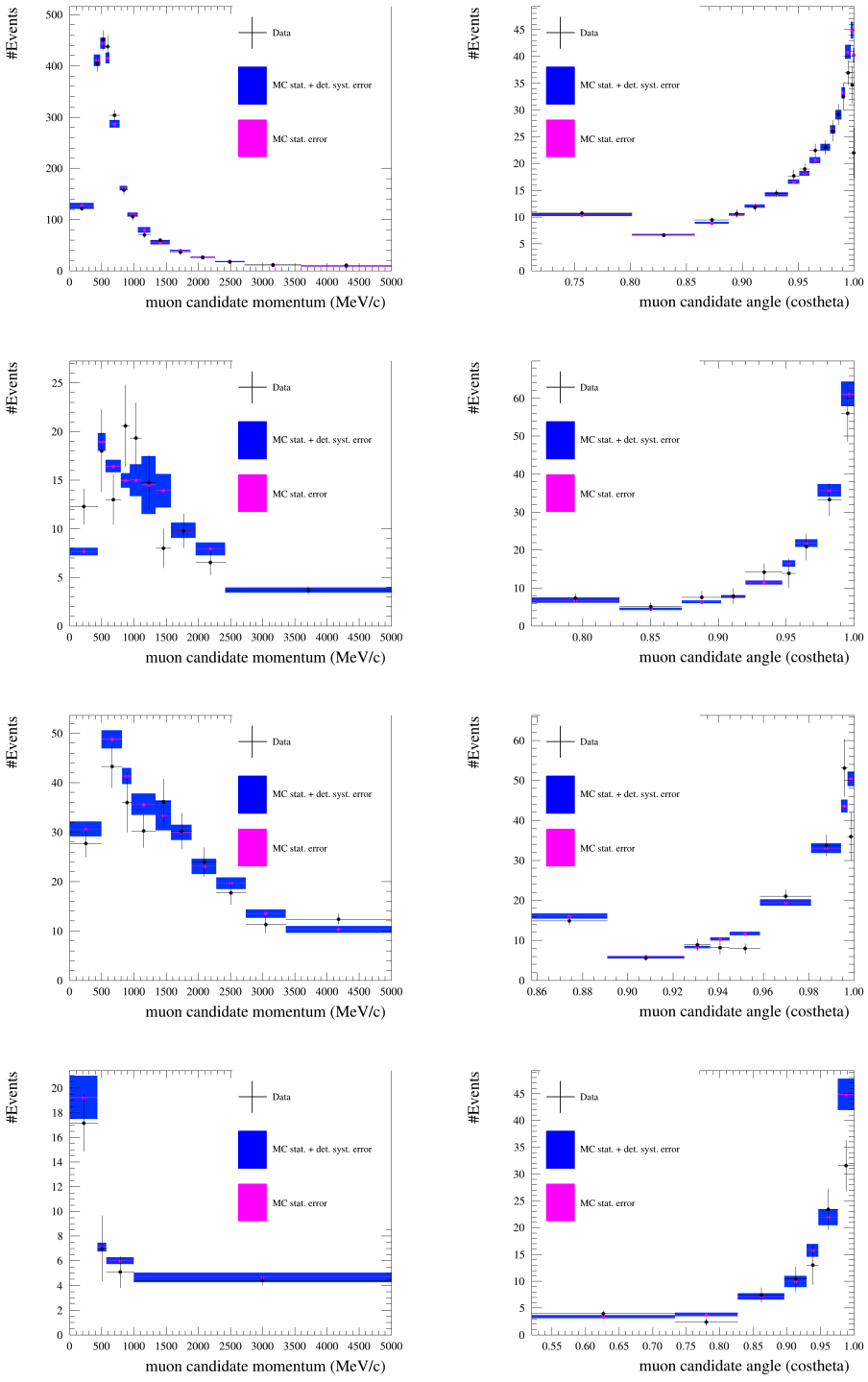

Figure 5.14: The statistical and detector systematic uncertainties on the number of events selected for each FGD2 sample, CC0π, CC1π^-, CC-Photon and CC-Other, from top to bottom, as a function of the antimuon momentum and angle.

Chapter 6

The Near Detector Fit

To better constrain the oscillation parameters detailed in section 2.13, comparisons between the number of neutrino events detected at the FD in data, and the prediction of the MC simulation are made. The modelled neutrino oscillation parameters are varied until the best agreement is found with data. Ideally, the model would depend only on the oscillation parameters such that variation in the event rate is a result of neutrino oscillations alone. However, in reality there are many non-oscillation parameters which effect the event rate, known as nuisance parameters. The event rate, N_{ν_β}, at the FD, Super-K is:

$$N_{\nu_\beta}(E_\nu) = \Phi_{\nu_\beta}(E_\nu) \times \sigma_{\nu_\beta}(E_\nu) \times \epsilon(E_\nu) \times P_{\nu_\alpha \to \nu_\beta}(E_\nu, L) \tag{6.1}$$

where $\Phi_{\nu_\beta}(E_\nu)$ is the neutrino flux, $\sigma_{\nu_\beta}(E_\nu)$ is the neutrino cross section, $\epsilon(E_\nu)$ is the event reconstruction efficiency at Super-K and $P_{\nu_\alpha \to \nu}(E_\nu, L)$ is the probability that a neutrino of flavour α oscillates to the neutrino flavour of interest, β. Uncertainties on any of these first three parameters will effect the ability of the experiment to truly

probe the PMNS matrix parameters. If the goal of an analysis is to only measure and constrain the flux and cross section parameters, the oscillation probability term from equation 6.1 itself becomes a nuisance parameter. Using data from ND280, which samples the unoscillated neutrino beam, it is possible to eliminate the additional oscillation probability nuisance term, assuming sterile neutrino oscillation is not present. The ND280 has been designed to reconstruct events to better understand these cross section and flux parameters. By using both the near and far detectors, it is possible to constrain the flux and cross section parameters and measure the PMNS matrix parameters.

T2K adopts two different oscillation analysis frameworks, invoking different statistical methods to measure the nuisance and oscillation parameters. The first method uses the analysis frameworks pTheta [106] and the Generic fitter for Upgraded ND Analysis Methods [107]. They are semi-frequentist, and use gradient descent techniques to find the combination of parameters which best describe the data. The Generic fitter for Upgraded ND Analysis Methods tool first fits to only the ND MC and data before relaying the best fit values and their uncertainties to the pTheta framework, via a covariance matrix. Using this input from the ND, alongside data from the FD, pTheta performs its own independent fit. By marginalising over the nuisance parameters (integrating away all parameters other than the parameter of interest), the oscillation parameters may be extracted as frequentist confidence limits.

An alternative technique to the two step approach of pTheta and Generic fitter for Upgraded ND Analysis Methods, is to perform a simultaneous fit. This method is used by Markov Chain for 3 flavour oscillation fitting (MaCh3) [108] by using Markov chain MC methods to find the Posterior Distribution Function (PDF) of the oscillation

parameters. Performing a simultaneous fit eliminates the need to make assumptions about the PDFs of the parameters, thus correlating the ND and FD models, and providing the fit more freedom to vary parameters from both models.

An independent MaCh3 ND only fit can also be performed. This chapter will detail the ND280 MC and data only MaCh3 fit with the inclusion of the new $\bar{\nu}$ CC multipi photon selection. A description of the ND model parameters: beamline flux parameters, neutrino cross section parameters, and ND280 detector systematic uncertainties will be made. The Bayesian methodology used by MaCh3 and an overview of the results of the ND fit will also be discussed.

6.1 Event Selection

The ND280 events are split into categories to better characterise the various neutrino interaction types. This section describes the FHC (ν-mode), RHC ($\bar{\nu}$-mode) and RHC-wrong sign (ν-mode) selections.

The FHC selection begins by selecting CC interactions in which the highest momentum negatively charged track is reconstructed as a muon. The selection categorised events according to their charged pion, photon and proton multiplicity. There is an additional splitting of events according to the angle of the reconstructed muon relative to the beam, to improve the 4π solid angle coverage at the ND, better reflecting the events selected at the FD [109]. If the muon track leaves at least 19 hits in the TPC it is described as low-angle. If it leaves fewer than 19 TPC hits, it is high-angle. The following samples were selected:

CC0π-0p Low-angle Forward: Events where the muon is low-angle and travels

forward, with no reconstructed protons, photons or pions.

CC0π-0p Low-angle Backward: Events where the muon is low-angle and travels backwards, with no reconstructed protons, photons or pions.

CC0π-0p High-angle: Events where the muon is high-angle and travels forward, with no reconstructed protons, photons or pions.

CC0π-Np Low-angle Forward: Events where the muon is low-angle and travels forward, at least one reconstructed proton, with no reconstructed photons or pions.

CC0π-Np Low-angle Backward: Events where the muon is low-angle and travels backwards, at least one reconstructed proton, with no reconstructed photons or pions.

CC0π-Np High-angle: Events where the muon is high-angle and travels forward, at least one reconstructed proton, with no reconstructed photons or pions.

CC1π^+ Low-angle Forward: Events where the muon is low-angle and travels forward, exactly one reconstructed positively charged pion with no reconstructed photons.

CC1π^+ High-angle Forward: Events where the muon is high-angle and travels forward, exactly one reconstructed positively charged pion with no reconstructed photons.

CC-Other Low-angle Forward: Events where the muon is low-angle and travels forward, more than one reconstructed positively charged pion and/or any number of pions with no reconstructed photons.

CC-Photon Low-angle Forward: Events with a reconstructed muon, which leave at least 19 TPC hits and travels forward, and at least one reconstructed photon.

The RHC $\bar{\nu}_\mu$ event selection described in section 4, has the following samples, all with a positively charged muon selected:

CC0π: Events with a reconstructed muon, with no reconstructed photons or pions.

CC1π^-: Events with a reconstructed muon, exactly one reconstructed pion with no reconstructed photons.

CC-Other: Events with a reconstructed muon, more than one reconstructed pion and/or any number of pions with no reconstructed photons.

CC-Photon: Events with a reconstructed muon, and at least one reconstructed photon.

The RHC ν_μ selection, selects the wrong-sign component of the $\bar{\nu}$-mode beam [90] as was discussed in section 3.1. These samples are useful in constraining the flux parameters for RHC events where the wrong-sign background is larger. The selection searches for the highest momentum negatively charged track which is reconstructed as a muon, similarly to the FHC selection, and resulted in the following samples:

CC0π: Events with a reconstructed muon, with no reconstructed photons or pions.

CC1π^+: Events with a reconstructed muon, exactly one reconstructed positively charged pion with no reconstructed photons.

CC-Other: Events with a reconstructed muon, more than one reconstructed positively charged pion and/or any number of pions with no reconstructed photons.

The reconstruction efficiency and purity for the ND samples are summarised in table 6.1.

The samples were binned according to the reconstructed muon kinematics: momentum and angle relative to the neutrino beam axis. The binning was defined such that each bin contained at least 20 MC events, and 1 data event. The bin width must also be greater than the resolution of the kinematic variable. The final sample kinematic

Selection	Sample	Efficiency (%)		Purity (%)	
		FGD1	FGD2	FGD1	FGD2
FHC ν_μ	CC0π-0p Fwd	32	36	76	79
	CC0π-0p Bwd	1	1	68	63
	CC0π-0p HA	4	4	71	71
	CC0π-Np Fwd	14	10	64	73
	CC0π-Np Bwd	1	1	84	82
	CC0π-Np HA	4	3	81	85
	CC1π^+ Fwd	27	23	61	63
	CC1π^+ HA	2	1	53	53
	CC-Other Fwd	21	20	42	43
	CC-Photon Fwd	44	45	50	51
RHC $\bar{\nu}_\mu$	CC0π	69.4	68.6	81.7	79.9
	CC1π^-	15.4	15.5	56.1	53.4
	CC-Other	24.1	21.6	19.7	19.2
	CC-Photon	39.6	42.4	41.3	38.5
RHC ν_μ	CC0π	60.3	60.3	55.9	52.8
	CC1π^+	30.3	26.0	44.4	44.8
	CC-Other	27.4	27.1	68.3	69.5

Table 6.1: The efficiency and purity of each of the ND samples used for the ND oscillation analysis. The FHC samples are described in [105] and the RHC ν_μ numbers are from this work [90].

Data Type	T2K Run	Data POT ($\times 10^{20}$)	MC POT ($\times 10^{20}$)
ν_μ-mode	2 Air	0.36	16.80
	2 Water	0.43	12.04
	3 Air	1.59	30.78
	4 Air	1.79	36.12
	4 Water	2.44	33.30
$\bar{\nu}_\mu$-mode	5 Water	0.43	22.11
	6 Air	3.41	33.03
	7 Water	2.44	33.30
ν_μ-mode	8 Air	4.15	44.53
	8 Water	1.58	27.17
$\bar{\nu}_\mu$-mode	9 Water	2.06	45.52
Total	-	20.68	301.40

Table 6.2: T2K data-taking runs used for this analysis for data and MC. The air/water labelling refers to whether the PØD modules were filled with water or not (air).

distributions shown in figures 4.16-4.21 are all binned using this method.

The fit included all available MC and data runs: 2-9. A summary of the total POT from the runs is shown in table 6.2. Sand MC, explained in chapter 4, was not included in this analysis, as the files were not prepared for the frameworks at the time of the completion of this work. Including sand MC is expected to have a minimal effect on the results [110].

6.2 Neutrino Flux Parameters

The neutrino flux was predicted using a simulation of the interactions occurring within the target including propagation of the outgoing particles through the horns [111]. Hadron production data collected by the NA61/SHINE experiment [112] using the T2K replica target, was used to tune the predictions of the mesons which exit the target. The nominal neutrino flux model was tuned to account for uncertainties in the interaction

length of the hadron in the material and the interaction multiplicity. The interaction length re-weighting impacts the probability a particle will interact while traversing the target. The re-weighting is dependent on the distance travelled by the hadron before interaction. The multiplicity re-weighting tunes how many particles exit an interaction and alters their kinematics, depending on the momentum and direction of the outgoing hadron [113]. The replica target data from NA61/SHINE was key to reducing the magnitude of the uncertainty in these corrections. Additional flux uncertainties arise from non-hadronic components such as the proton beam profile; uncertainty in the measurement of the POT; modelling of the horn current and associated field asymmetry; alignment of the target and horns; and the description of the materials with which interactions may occur.

The flux uncertainties were binned according to the flavour content of the neutrinos (ν_μ, ν_e, $\bar{\nu}_\mu$ and $\bar{\nu}_e$) and the detector of interest, ND280 and Super-K, as a function of the true neutrino energy. There are large correlations between all bins. Figure 6.1 shows the total flux uncertainty at the ND280 for all neutrino beam modes and flavours.

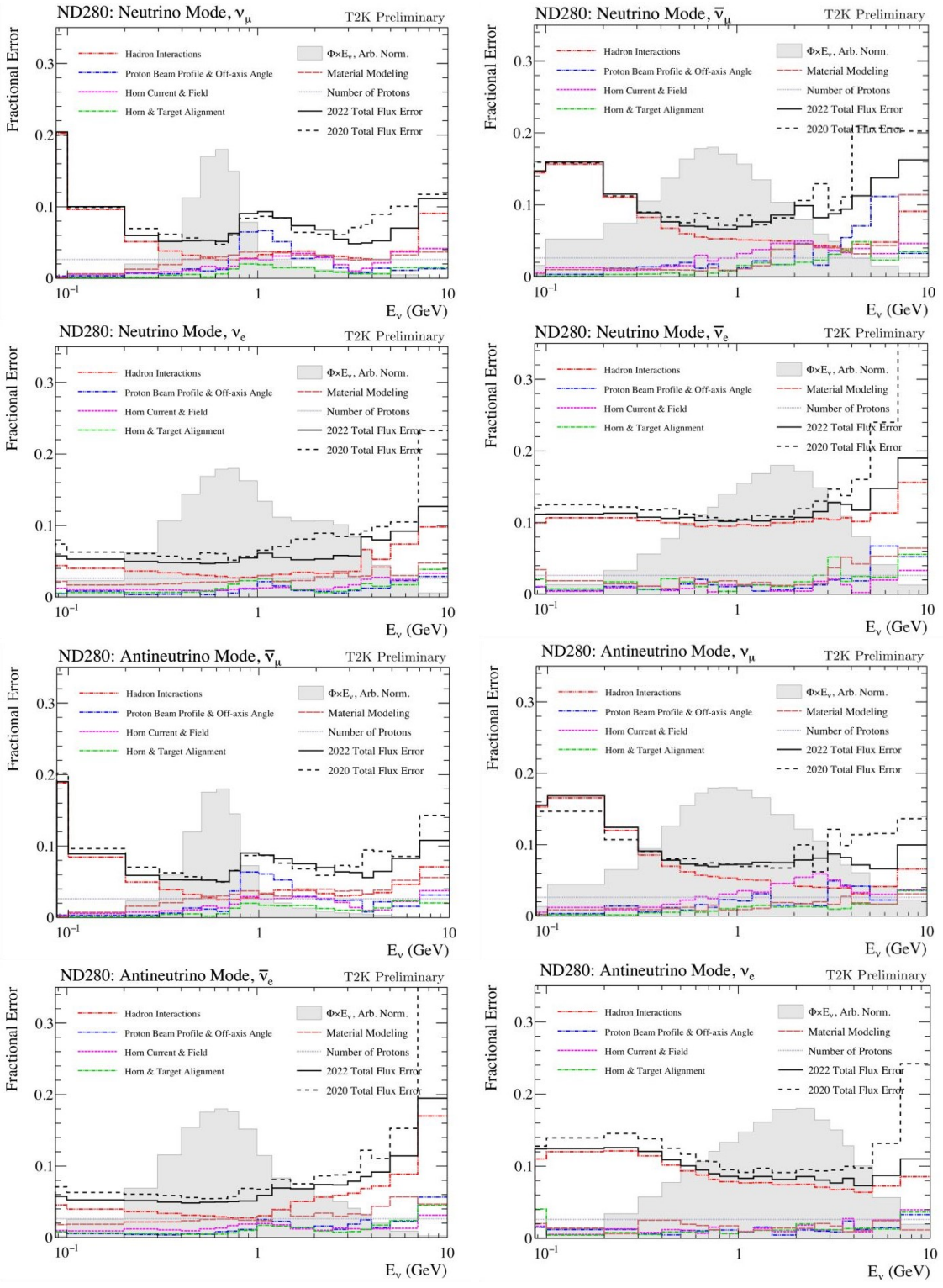

Figure 6.1: Total flux uncertainty at the ND280 as a function of true neutrino energy. Changes between the flux model used for the 2020 and 2022 analyses are both shown. Relative contributions of various sources of uncertainties are indicated via the colourful lines, with the total in black. The hadron interaction error is seen to be the dominant source of uncertainty across most of the momentum range [113].

At the T2K flux peak, $\sim$ 600 MeV, the total flux uncertainty at the ND280 detector is between $\sim$5 - 7% for the right sign ν and $\bar{\nu}$ mode contributions. The dominant source of flux uncertainty is listed in the figures, and show that hadronic interaction errors remain the dominant source of uncertainty in the flux model. At higher energies the proton beam profile error is dominant. The flux uncertainties are included in the oscillation analysis of T2K via a covariance matrix. A total of 100 bins are included in the matrix for both ND280 and Super-K samples. The central value of each parameter was set to nominal, and the covariance matrix used as the parameters prior constraints.

6.3 Neutrino Cross Section Parameters

The neutrino cross section model describes the probability of various interactions occurring with the ND280 target materials. The probability varies as a function of the neutrino energy, with certain interaction types becoming dominant at different neutrino energies as shown in figure 6.2.

The nominal cross section model is weighted to account for improved understanding of each of the different neutrino interaction types. The re-weighting is either applied as an event normalisation, scaling the probability that the interaction would or would not occur; or as a shape response which is dependent on the outgoing particles and their kinematics. The shape responses are referred to as splines and are discussed in section 6.4.1. A description of the cross section parameters implemented in the neutrino model now follows.

Charged Current Quasi Elastic (CCQE)

The CCQE interactions on carbon and oxygen (the target materials for T2K oscillation analyses at the ND) are modelled by the Spectral Function (SF) [115]. The majority

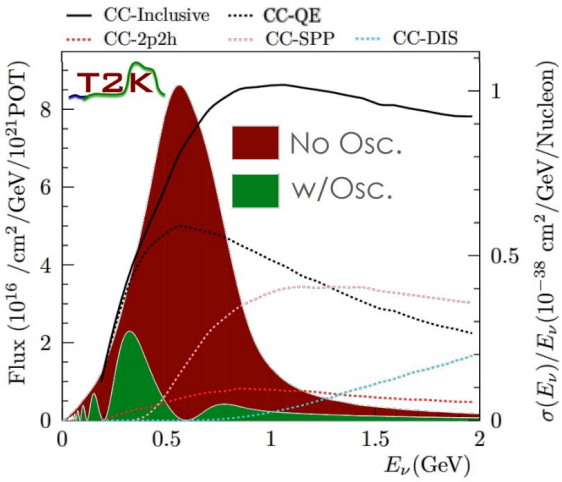

Figure 6.2: Neutrino flux and cross section as a function of the true neutrino energy. The flux assuming neutrinos do and do not oscillate is shown. The cross section contributions from each of the CC interaction modes is shown via the dashed colourful lines. The modes shown are CC-QE (black), CC-2p2h (red), CC single pion production - CC-SPP (pink), and CC-DIS (blue) [114].

of interactions at ND280 occur on carbon as most of the target material is scintillator. The oxygen target is only present in the water layers of FGD2. This model describes the probability that a nucleon of a certain momentum and 'removal energy' is found. The removal energy is the energy required to extract the nucleon from the nuclear potential. This shell-model description is driven by data from CCQE interactions in electron scattering, alongside inputs from theoretical models. For CCQE interactions, several parameters are used to account for uncertainties within the model.

- M_{QE}^{A}

  The axial mass, M_{QE}^{A}, is included in the form factors for CCQE interactions. The prior value is set to 1.03 GeV with an error of 60 MeV, which is determined using bubble chamber data [116]. This is the primary parameter used to modify the CCQE interaction model.

- Q^2 Normalisation

  The event rates at various true values of the neutrino-nucleus momentum transfer squared, Q^2, are scaled. The re-weighting is required to match the event rates of MINERνA data [117]. Three bins are defined: 0.25 - 0.5 GeV, 0.5 - 1.0 GeV and >1.0 GeV.

- Spectral Function (SF) shell model

  Several additional parameters are included to allow more freedom within the SF model. The nucleus behaviour within the nuclear shell is described by the Mean Field (MF) parameters. The nuclear shells are each assigned a weight to modify the probability that a neutrino CCQE interaction occurs. Normalisation and shape parameters are used for interactions on carbon in the S and P shells, and for interactions on oxygen in the S, $P_{1/2}$ and $P_{3/2}$ shells. Alongside these parameters are four additional splined parameters, two for oxygen and two for carbon, which consider the effect of Short Range Correlations (SRC) which may occur between nucleon pairs after they are produced [115]. The first two parameters change the ratio of pn and nn pairs considered in SRC. The other two parameters modify the missing momentum due to SRC.

- Pauli blocking

  Within the nucleus, nucleons may not occupy the same quantum state. When a neutrino interaction occurs, it must contain enough energy to excite the target nucleon to an energy level higher than the Fermi energy, as the states below this threshold are full. The energy levels below the Fermi energy are said to be 'blocked' by the Pauli exclusion principle [118]. As a result of this the neutrino cross section is suppressed at lower energies. Within the model, when the neutrino

momentum is below a threshold of 209 MeV, the event is weighted to zero. To represent this behaviour, four splined parameters for neutrino and $\bar{\nu}$ interactions on oxygen and carbon are included.

- Final State Interactions (FSI) and random phase approximations (RPA)

  To characterise the large model variation at low energy transfer, a series of parameters are implemented to allow freedom in the space. A total of 24 parameters are included. The parameters describe interactions on oxygen and carbon separately; ν and $\bar{\nu}$ interactions; three bins in low energy transfer, and are split into two types to cover the response due to FSI and RPA effects independently. FSI was defined in chapter 4, and these parameters account for corrections to the SF model, which do not include FSI. The RPA effect characterises the W boson's self interaction in the nuclear medium which alters the cross section of some processes [119].

- Binding energy

  The binding energy is the amount of energy required to remove a nucleon from the nucleus. The implementation method is unique for this parameter as the effect of the altered binding energy is applied to each event: as the momentum of the lepton increases the binding energy decreases, and vice versa. The application of this parameter may lead to events migrating between kinematic bins. An additional correction is also applied to the binding energy, as determined by electron scattering data [114].

2-particle 2-hole (2p2h)

In 2p2h neutrino interactions, the neutrino interacts with a bound nucleon pair. The

MC events are generated using the Valencia model [96], and are described using the following parameters:

- Normalisation parameters

  These tune the overall event rate for 2p2h interactions. Three parameters modify the ν and $\bar{\nu}$ interaction rates, and one parameter modifies the carbon to oxygen interaction rate. The carbon to oxygen ratio parameter is needed to better extrapolate to the FD, where only the oxygen cross section is considered.

- Splined parameters

  These parameters account for modifications to the neutrino energy and momentum transfer. The two models considered are for Δ-decay processes where a pion is produced, as described by the Nieves model, or pionless Δ-decay, which is predicted by the Martini model [120]. The parameters permit either extreme of the predicted Δ-decay process, alongside a combination of both production mechanisms. Four parameters are defined for carbon and oxygen separately, and also for np and nn pairs. Four additional parameters account for the energy dependence of the interaction when both extremes of the pion and pionless interaction types are considered. They are separated into high and low energy ν and $\bar{\nu}$ parameters. There is an additional parameter which modifies the ratio of pn to nn pairs which are produced during 2p2h ν interactions, or np to pp pairs for $\bar{\nu}$ interactions.

Single pion production (SPP)

The Rein-Sehgal model [97] is used by NEUT to model resonant (RES) SPP interactions. The relevant cross section parameters are:

- Axial mass, M_{RES}^{A} and form factor, C_5^A

  The form factor of SPP interactions is also dependent on the axial mass, M_{RES}^{A}, which is nominally 0.95 GeV in NEUT. Relative to outside data, this was found to be set too low [114], and therefore is re-weighted to a value of 1.06 GeV. The nominal value of the form factor C_5^A in NEUT is 1.01. External data [114] found this value is too high, and should be re-weighted to 0.95.

- Isospin-1/2 background

  The only SPP decay channel which is simulated by the Rein-Sehgal model is the excitation of a nucleon to a resonance which subsequently decays to a pion and a nucleon. Two parameters are introduced to account for decay modes where the pion does not reach a resonant-state. One parameter scales the rate of production for spin-1/2 events relative to spin-1 events. The second parameter introduces an additional scaling to the spin-1/2 backgrounds where the pion has low momentum, which are often a source of background to CC0π interactions at the FD.

- RES binding energy

  The binding energy of RES interactions is treated differently compared with CCQE interactions. In this case, a splined event-by-event re-weighting is applied as is standard. Four parameters are defined for ν and $\bar{\nu}$ which interact with carbon and oxygen.

- RES decay

  Using the Rein-Sehgal model, two different pion ejection methods may be implemented. The first method determines the isotropic ejection of the nucleon and pion as back-to-back, by considering the decay of the resonant state in

its centre-of-mass frame. The second method considers the case where the nucleon and pion final state are produced after the excitation of the initial-state nucleon which then produces an intermediate resonance and decays. This splined parameter allows the fit to determine the ratio of the two methods used.

- π^0 normalisation

  The rate of π^0 production due to RES interactions is tuned via two normalisation parameters for ν and $\bar{\nu}$ interactions separately.

- CC coherent

  A CC coherent neutrino interaction occurs when the nucleus remains in the same state as it was prior to the interaction, but a charged lepton and oppositely charged pion are emitted. Such interactions are included in the Rein-Sehgal model, but there is a 30% discrepancy between the modelled cross section value and that measured by MINERνA [121]. Therefore two normalisation parameters for events on oxygen and carbon are included to account for this difference.

- Pauli Blocking Single Pion

  Two splines are included to account for Pauli blocking occurring in interactions with one emitted pion, in a similar way to the parameters implemented for CCQE interactions. The two splines are split to tune carbon and oxygen interactions separately.

Deep Inelasic Scattering (DIS)

These interaction types refer to instances where the neutrino resolves the individual quarks within the nucleon. These interactions only occur if the neutrino has enough energy to break the quark bound state. To account for the variety of hadronic final

states, a customised hadronisation model was used for DIS interactions. The NEUT multi-pion production mode with Bodek-Yang corrections [98] is used for cases where the invariant hadronic mass, W, is $1.3 < W < 2.0$ GeV. For cases when $W > 2.0$ GeV, PYTHIA 5.7 [99] is used. Additional cross section parameters were included in the fit to allow more freedom.

- CC Bodek-Yang corrections

  To control the effect of the Bodek-Yang corrections applied to DIS interactions, a splined parameter is implemented. Two additional normalisation parameters, for ν and $\bar{\nu}$, are included to allow the rate of DIS interactions to vary.

- Multi-pion multiplicity

  Two splined parameters are used to control the production of multi-pion events. Differences between the multiplicity between the AGKY [122] and NEUT models are controlled by the first parameter. The second modifies the shape of the cross section as a function of the total invariant mass and number of pions, while keeping the total cross section fixed.

- Multi-pion Bodek-Yang vector and axial parameters

  To account for updates to the Bodek-Yang model of low Q^2 neutrinos [123] which were not migrated to the version of NEUT used in this analysis, two parameters are constructed to account for the changes.

- CC multi-pion normalisation

  Two normalisation parameters, one for ν and the other $\bar{\nu}$, control the number of CC multi-pion interactions which occur.

- CC Miscellaneous

  This single splined parameter is used to modify the distribution of other DIS topologies usually not containing pions, such as the production of η and K particles.

- NC DIS parameters

  Differing from the other DIS parameters, these two parameters vary the production of NC DIS and NC multi-pion interactions modelled by the Bodek-Yang model.

Other parameters

There are a series of additional parameters which do not fit into the previous categories:

- NC

  A normalisation parameter is included to model the rate of NC coherent interactions. Similarly, one normalisation parameter is included to account for NC interactions with one photon in the final state during non-RES NC scattering. Finally two additional normalisation parameters, for the near and FD separately, account for all other NC interactions such as multi-pion and DIS.

- Coulomb Correction

  Following a neutrino interaction, the outgoing lepton momentum will be altered due to the Coulomb potential of the charged nucleus. Two normalisation parameters are included for ν and $\bar{\nu}$ events separately to account for this effect.

- ν_e/ν_μ

  The cross section ratio for ν_e/ν_μ interactions, and also $\bar{\nu}_e/\bar{\nu}_\mu$ interactions differs from that in the interaction model. The differing mass of the outgoing lepton

results in changes to the phase space. This is because more momentum is required in an interaction which produces a muon than the lighter electron. There are also additional radiative corrections which are not implemented in the computation of the cross section which are dependent on the mass of the outgoing lepton. Two parameters are implemented for the ν and $\bar{\nu}$ cases separately to characterise these differences.

- Pion and Nucleon FSI

  A series of FSI parameters affecting pions are utilised to determine the probability of such an interaction occurring for a variety of FSI channels: QE scattering, charge exchange, absorption and hadron production. The splined parameters are introduced for each channel with an additional separation for charge exchange interactions for low and high energy pions. A further two FSI parameters were included to account for the nucleon FSI probability and the nucleon FSI pion production probability.

- Radiative Corrections

  To account for cases where an additional collinear photon is emitted alongside the lepton in a CCQE interaction, the radiative correction splined parameter is applied. The addition of these interactions may lead to differences in the measurements of ν_μ and ν_e interactions.

The prefit correlation matrix displaying all cross section parameters is shown in figure 6.3. A summary of the cross section parameters, their implementation method and prior values with uncertainties are summarised in appendix C.

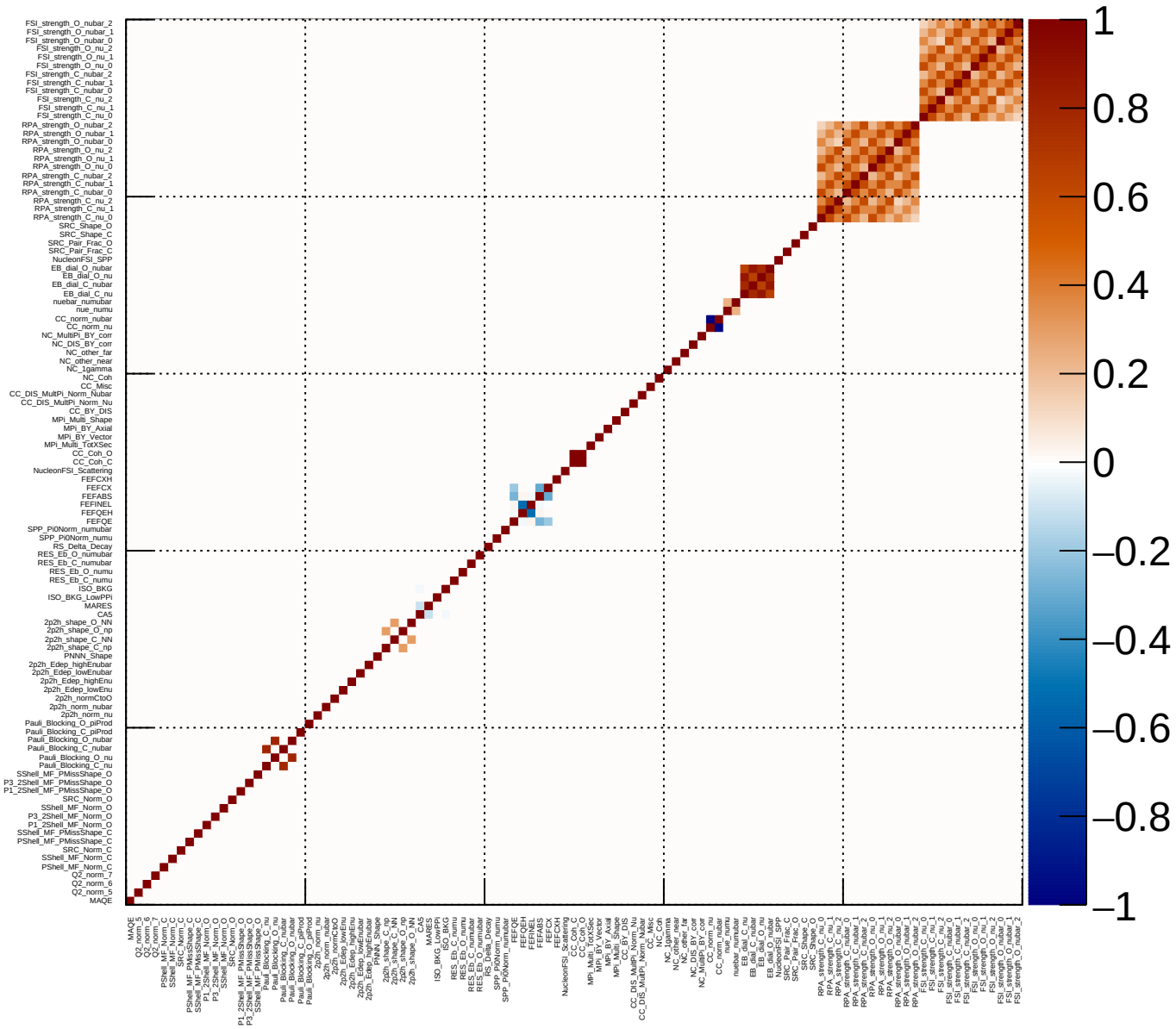

Figure 6.3: The prefit correlation matrix for all cross section parameters. The labels show the different cross section parameters which are typically very uncorrelated prefit. The regions where high correlations exist in the top right of the matrix are between the RPA and FSI strength variables. Some additional correlation is observed between the binding energy variables and some of the ν, $\bar{\nu}$ equivalent parameters.

6.4 ND280 Detector Parameters

A detailed description of the various sources of ND uncertainty was made in chapter 5. Ideally, to include these sources of uncertainty in the ND fit, each event should be allowed freedom for the detector systematic uncertainties to vary freely during the fit. However, generating a new MC model for each of these variations is a computationally intense task. To avoid this, two alternative methods were used. The first was used when considering variation systematic uncertainties, which typically describe reconstruction parameters that may migrate events between bins and samples. These systematic uncertainties are all treated as normalisation parameters. In the Psyche framework, 2000 toy experiments were generated, to ensure sufficient statistics to approximate a Gaussian distribution. In each toy experiment the detector systematic uncertainties were varied, and the variation on the number of events in each bin between the toy experiment and the MC was used to determine the systematic uncertainty on the bin. The uncertainty was described using a covariance matrix to include the correlation between samples and kinematic bins. The final covariance matrix contained a total of 3665 bins, and the correlation matrix of these parameters is shown in figure 6.4.

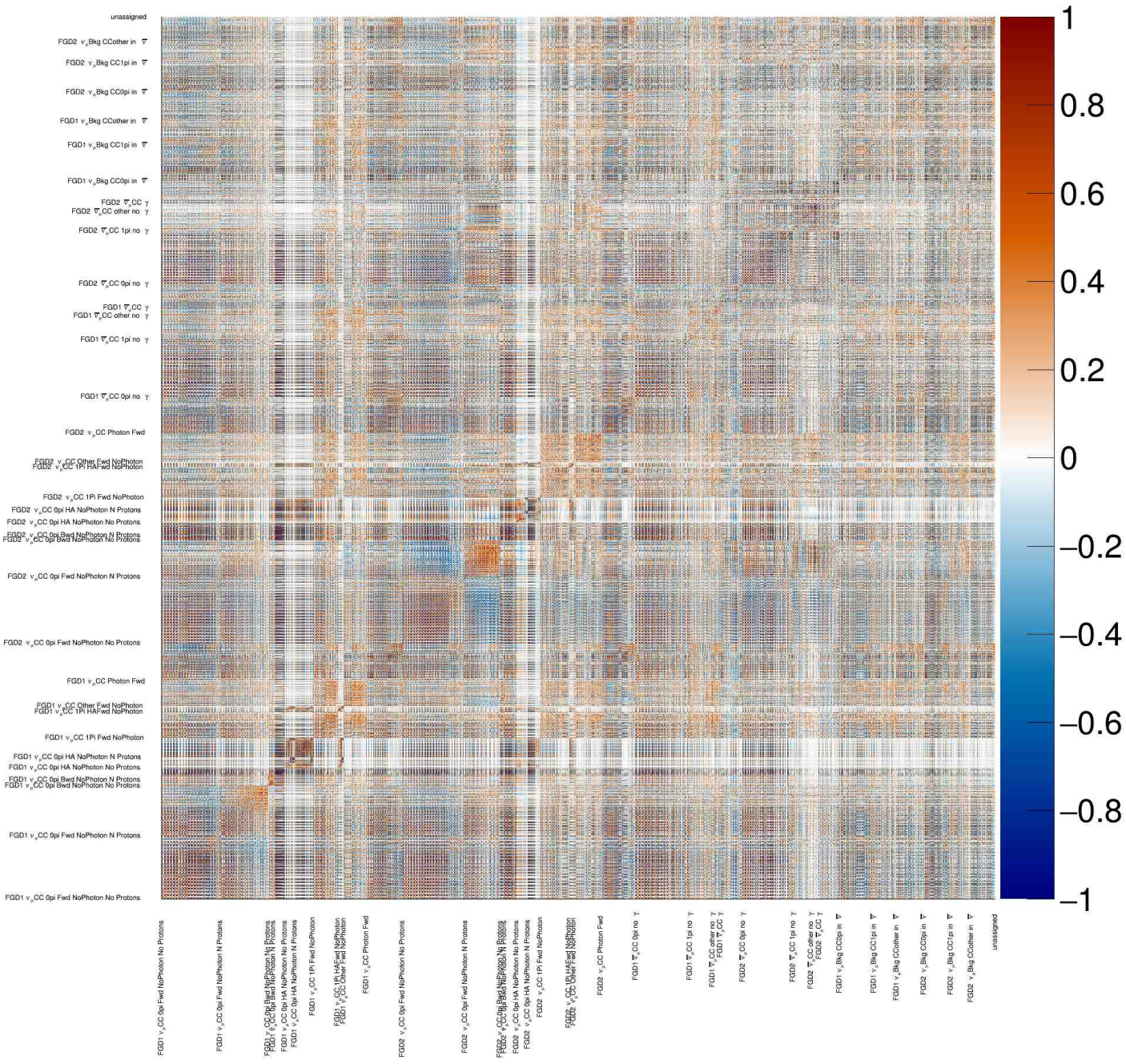

Figure 6.4: The ND280 detector correlation matrix used in the fit. The ND280 samples are indicated on either axis and are binned in reconstructed muon momentum and angle. Correlations between sample and kinematic bins are present due to event migration as the detector systematic uncertainties vary.

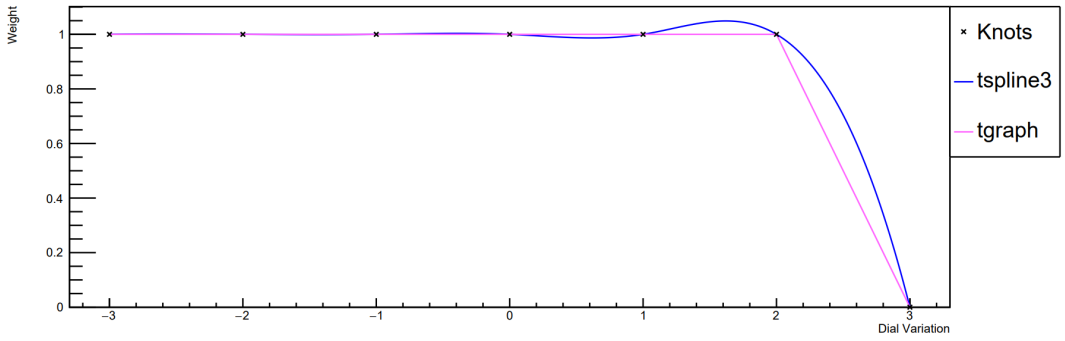

Figure 6.5: Example of a spline, showing the Pauli blocking oxygen $\bar{\nu}$ cross section parameter calculated for a single event. The TSpline3 and linear interpolation, labelled TGraph, are shown.

The other detector systematic uncertainties, referred to as weight-like systematic uncertainties, follow a splined approach, similar to that used for the cross section parameters [124]. An overview of the implementation of splines is given in section 6.4.1

6.4.1 Splines

To avoid producing multiple MC simulations to account for the cross section or detector responses, a weight is calculated for each parameter on an event-by-event basis. As the weight was calculated independently for each event, the sample kinematic distributions may change. The weights were calculated prior to the fit to reduce computation time during the fit. The cross section parameters used TSpline3 objects and the detector uncertainty parameters used monotonic spline objects as defined by ROOT [125], where weights are stored at specific parameter values, known as 'knots'. To extrapolate between these knots a 3rd-order polynomial was constructed, an example can be seen in figure 6.5.

The knots were defined such that the parameter was varied by 0, $\pm 1\sigma$, $\pm 2\sigma$ and $\pm 3\sigma$. The fit then sampled from the spline to determine the weight for any variation of

the parameter for each event. Many weights were calculated for each event according to the variation in all the flux, cross section and detector parameters, and multiplied together to get a final event re-weighting which was used during the fit.

6.5 Parameter Sensitivity

Before performing a ND fit, it is possible to estimate the expected sensitivity on the parameters using different methods. The methods considered were log likelihood (LLH) scans and sigma variations, which will be described in this section.

6.5.1 Log Likelihood Scans

To measure the sensitivity of a fit to each parameter, it is possible to scan the LLH distribution. This involves using two MC simulations. If the simulations are identical, $-2\text{LLH} = 0$. If in one simulation, a single parameter is varied between $\pm\sigma$, it is possible to observe the diverging agreement between the two MC simulations due to the single parameter variation. If the parameter does not affect the samples under consideration, for example a FD parameter with only ND MC simulations, then there should be no difference between the two MC simulations after varying the parameter. These LLH scans can be used to determine the sensitivity of the fit to certain parameters, and to demonstrate whether the addition of new samples has improved the constraints. The constraint on a parameter is determined to be greater relative to previous iterations of the analysis, before a change was implemented, if the 'U-shape' of the LLH distribution is narrower. It was possible to determine whether parameter sensitives were increased due to the updated $\bar{\nu}$ selection and addition of the new CC-Photon sample, by

comparing the LLH scan for the analysis described in this thesis, with the previous iteration of the analysis without the updates to the $\bar{\nu}$ selection [109]. Figure 6.6 shows a few of the cross section parameters both with and without the updated $\bar{\nu}$ photon selection.

The ν-mode selections for both sets of analyses were identical, therefore improvements in constraining the neutrino-type cross section parameters were not anticipated. This is observed as the two LLH curves are overlayed, and indistinguishable, as shown in figure 6.7.

Similarly, the CCQE and 2p2h parameters did not observe much improvement in their constraint, as the primary change between the two selections was the inclusion of the photon sample, which targets higher energy interaction types such as pion production and DIS. The small improvements observed, shown in the 2p2h $\bar{\nu}$ normalisation and $\bar{\nu}$ Pauli-blocking on carbon parameters of figure 6.6, may be due to the increased purity of the $\bar{\nu}$ CC0π sample due to the removal of photon events from that sample. The exact origin of this improvement should be studied further in the future. Such studies could involve repeating the analysis but altering the $\bar{\nu}$ selection by including the photon removal cuts, but not adding the CC-Photon sample itself.

The cross section parameter, $\bar{\nu}$ π^0 normalisation, observed a greater constraint due to the updated $\bar{\nu}$ photon selection as shown in figure 6.6. The relative contribution of each sample to the $\bar{\nu}$ π^0 normalisation parameter is shown in figure 6.8. The $\bar{\nu}$ FGD1 (FGD2) CC-Photon samples were both shown to contribute to the improved sensitivity by 44% (40%). This improvement was expected as the $\bar{\nu}$ CC-Photon sample primarily tags events with photons from π^0 decay. Therefore a change to the number of $\bar{\nu}$ π^0 interactions produced altered the event rate of the $\bar{\nu}$ CC-Photon sample.

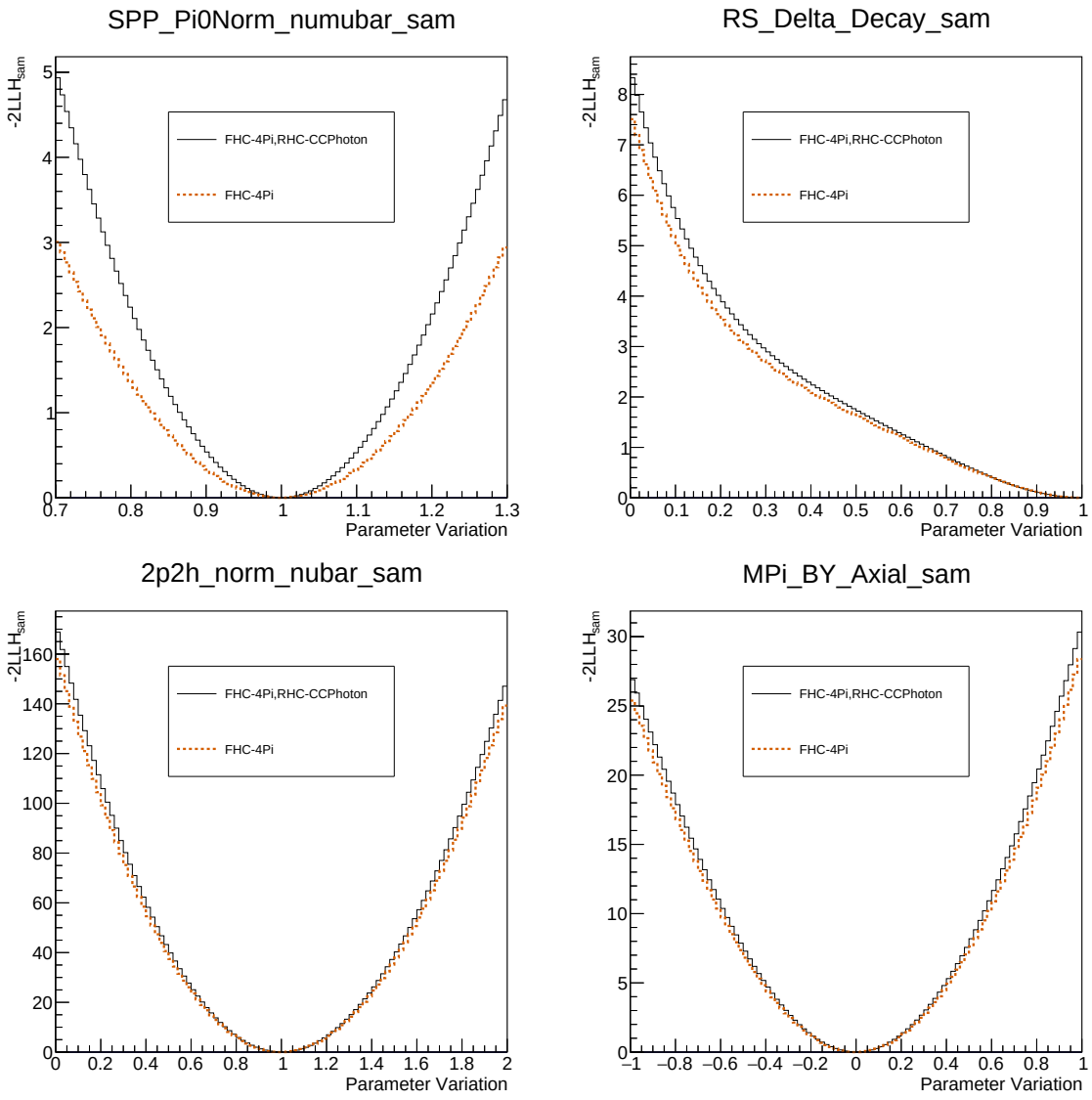

Figure 6.6: The LLH scans of the $\bar{\nu}$ π^0 normalisation, RES Δ decay, 2p2h $\bar{\nu}$ normalisation, Multi-pion Bodek-Yang Axial parameters (top left, top right, bottom left, bottom right, respectively). In black the $\bar{\nu}$ CC-Photon selection is shown, and in dashed red the previous iteration of the analysis, without $\bar{\nu}$ photon tagging.

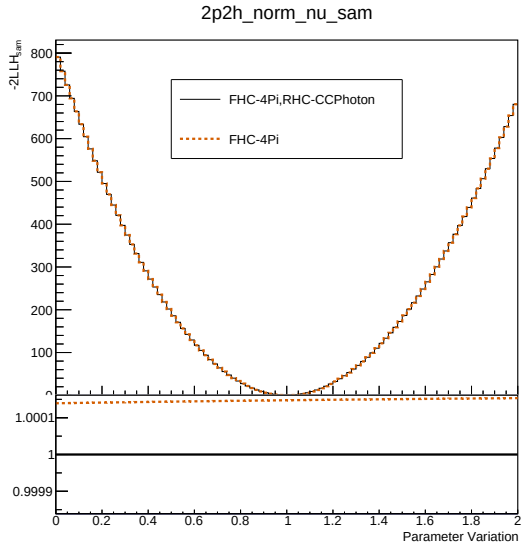

Figure 6.7: The LLH scan of the 2p2h ν normalisation parameter. In black the $\bar{\nu}$ CC-Photon selection is shown, and in dashed red the previous iteration of the analysis, without $\bar{\nu}$ photon tagging. There is very little difference between the two cases. The small fluctuation observed is due to the seeds changing between the fits.

In addition to the cross section parameter constraint, the $\bar{\nu}$ CC-Photon sample was shown to aid in constraining some of the ND systematic uncertainties. These were primarily the variables related to the ECal, which was expected as most events in the $\bar{\nu}$ CC-Photon sample are tagged using the ECal. The improvements due to the updated $\bar{\nu}$ selection are shown in figure 6.9.

6.5.2 Sigma Variations

It is important to assess which parameters will be most influential when determining the event rate of each sample. For example, it is expected the M_{QE}^{A} cross-section parameter will uniformly change the samples targeting CCQE type interactions, such as the CC0π samples. However, variation of this parameter is not expected to change the event rate of the $\bar{\nu}$ CC-Photon sample as significantly. This is because $\sim$12% of $\bar{\nu}$ CC-Photon

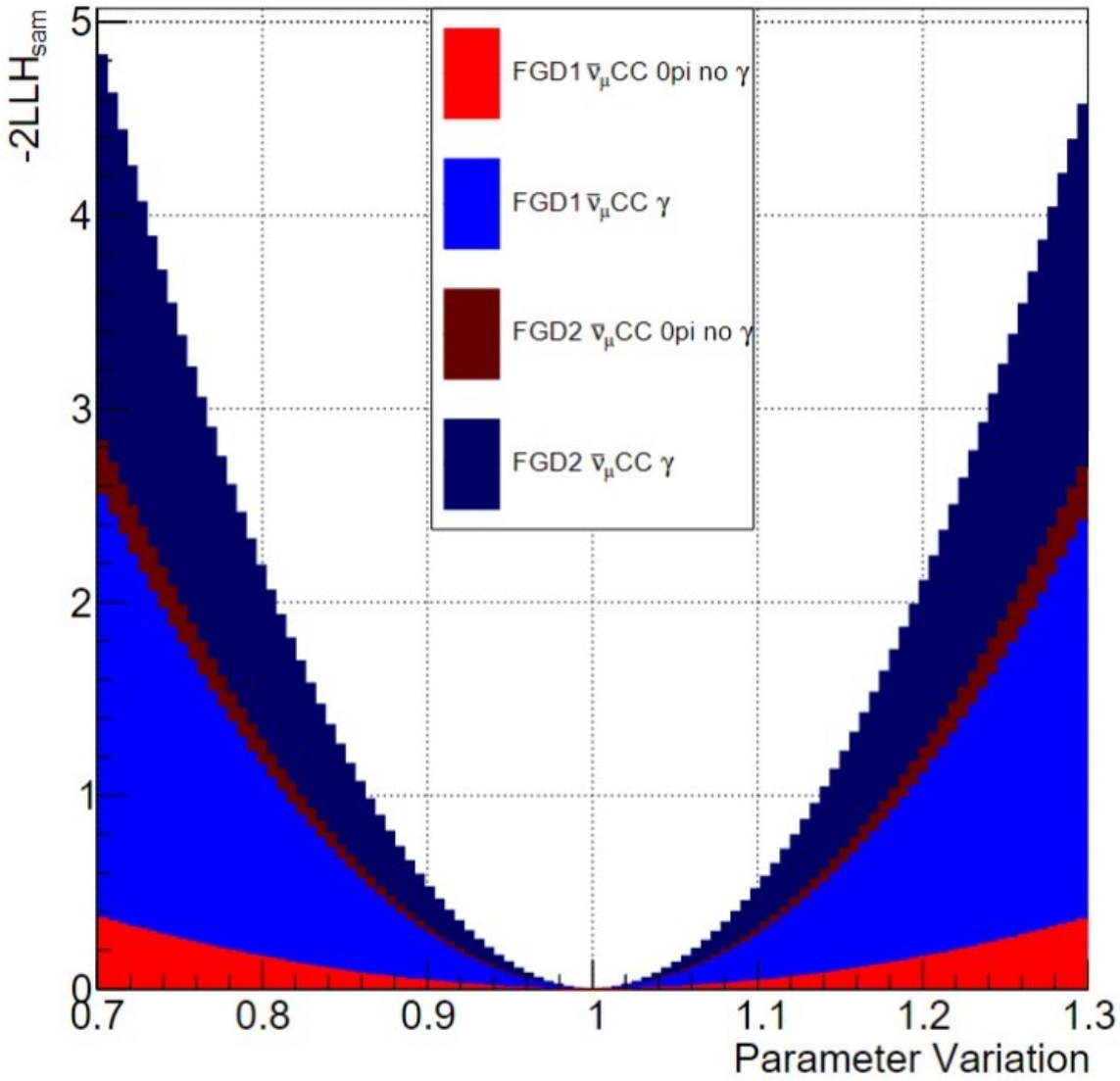

Figure 6.8: The LLH scan, using the updated $\bar{\nu}$ photon selection, split according to the relative sample contribution to the sensitivity of the $\bar{\nu}\pi^0$ normalisation parameter.

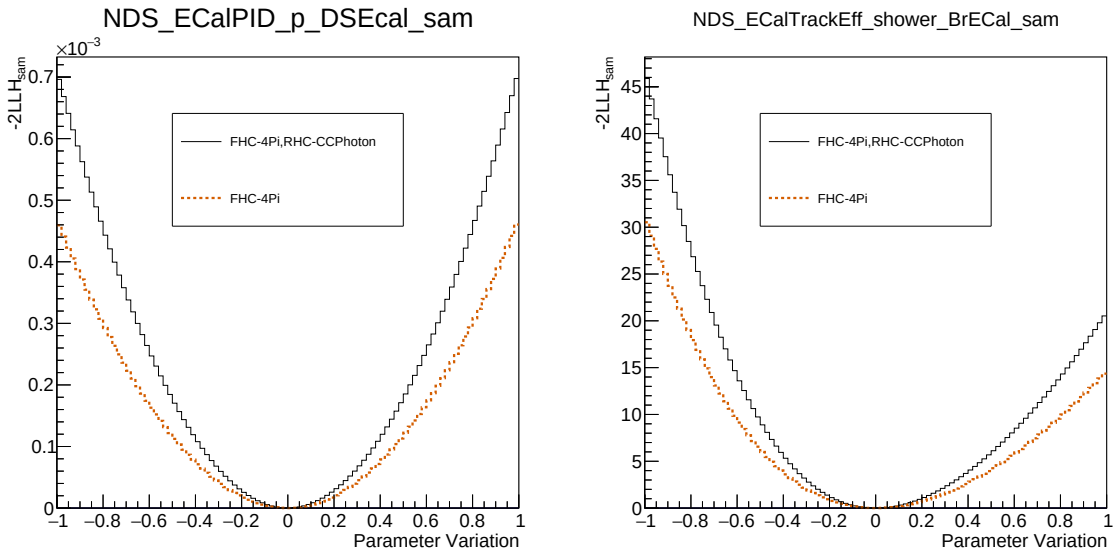

Figure 6.9: The LLH scans of the ECal PID of protons in the Ds ECal and ECal tracking efficiency of showers in the Br ECal. In black the $\bar{\nu}$ CC-Photon selection is shown, and in dashed, red the previous iteration of the analysis, without $\bar{\nu}$ photon tagging

events are CCQE interactions, relative to 67% of events in the $\bar{\nu}$ CC0π sample. This effect is shown in figure 6.10.

The sigma variation of the $\bar{\nu}$ π^0 normalisation parameter which the CC-Photon sample has been shown to provide additional constraint is shown in figure 6.11. The event rate was seen to vary more significantly for this sample due to this parameter than the M_{QE}^{A} parameter, as expected.

6.6 Markov Chain MC Methods

In order to determine whether the model accurately represents the data, a Bayesian statistical interpretation is considered in this thesis. A representation of the likelihood that the model, $\vec{\theta}$, accurately describes the data, D, is given by the PDF, P($\vec{\theta}$,D) [126]. This distribution is constructed using Bayes' theorem:

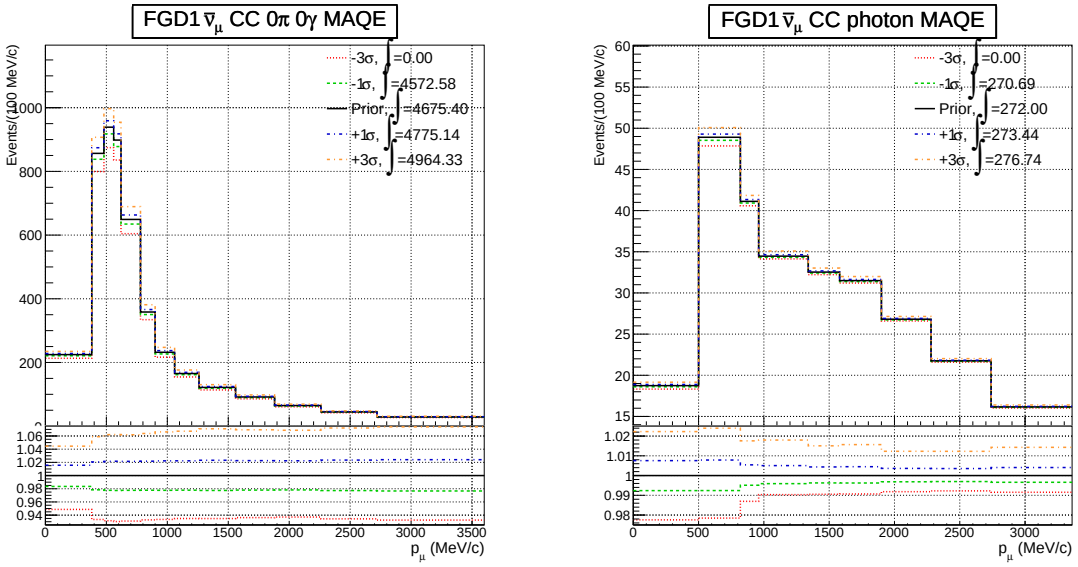

Figure 6.10: The $\bar{\nu}$ CC0π sample and $\bar{\nu}$ CC-Photon sample (left/right) event rates are shown as a function of the antimuon reconstructed momentum, with the M_{QE}^{A} parameter varied between ± 3, ± 1, 0σ. The ratio of the number of events in each bin for each sigma variation relative to the prior is shown below the plots.

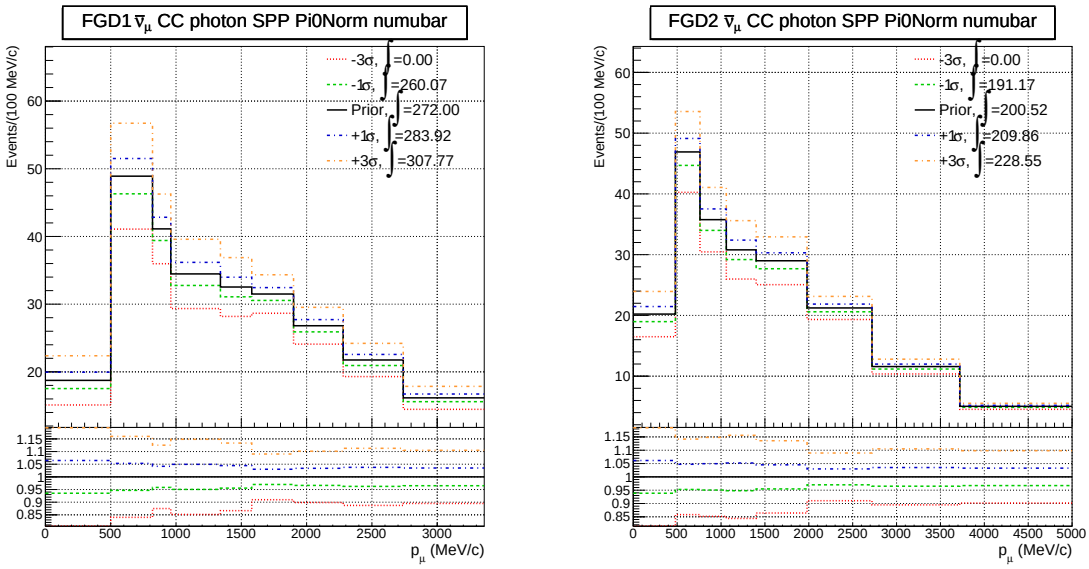

Figure 6.11: The $\bar{\nu}$ CC-Photon FGD1 (FGD2) sample event rates are shown left (right) as a function of the antimuon reconstructed momentum, with the $\bar{\nu}$ π^0 normalisation parameter varied between ± 3, ± 1, 0σ. The ratio of the number of events in each bin for each sigma variation relative to the prior is shown below the plots.

$$P(\vec{\theta}|D) = \frac{P(D|\vec{\theta})P(\vec{\theta})}{\int P(D|\vec{\theta})P(\vec{\theta})d\vec{\theta}} \tag{6.2}$$

where $P(D|\vec{\theta})$ is the likelihood that the data, D, is described correctly by the model assuming the set of parameters $\vec{\theta}$. The parameter $P(\vec{\theta})$ represents the prior information regarding the model $\vec{\theta}$, corresponding to the flux, cross section and detector parameters previously described. The goal of the Bayesian ND fit is to construct the PDF. Given the large number of parameters involved in the ND fit, the dimensionality of the PDF becomes difficult to analyse and interpret. To solve this issue it is possible to sample from the posterior probability distribution using MC methods.

These methods are known as Markov Chain Monte Carlo (MCMC) techniques. The full parameter space is sampled by conducting a semi-random walk where the PDF is sampled until enough values are considered such that their density is proportional to that of the PDF. The Markov chain determines the path of the random walk by assigning each possible next step according to some transition probability. This probability is only dependent on the current step, and forgets what occurred in previous steps. It is possible that the Markov chain converges at a stationary state, where the transition probability becomes constant. This can be thought of as sampling from the global minimum. Once this stationary state is found, the chain continues but now samples only from this region, which corresponds to the PDF.

Throughout the lifetime of the Markov chain, it must satisfy three 'regularity' conditions to reach a stationary state:

- **Irreducibility**

  The transition probability from a given point to any other state must be non-zero.

- **Aperiodicity**

  The step sequence may not repeat in a periodic manner.

- **Recurrence**

  Once the stationary distribution has been reached, future steps may only sample from the stationary distribution.

6.6.1 Metropolis-Hastings Algorithm

The Metropolis-Hastings algorithm provides a method of constructing a Markov chain which satisfies the regularity conditions [127]. The algorithm proposes a state, $\vec{\theta'}_n$, which is determined by a proposal function, $q(\vec{\theta'}_n|\vec{\theta}_n)$, which is dependent only on the current state. An acceptance probability for the proposed state is calculated to determine whether it is accepted. If the step is accepted, it becomes the next step in the chain, and the procedure is repeated. If it is rejected, the current state is kept, $\vec{\theta}_{n+1} = \vec{\theta}_n$. The acceptance probability, α, is:

$$\alpha = \min\left(1, \frac{\ln \mathcal{L}(\vec{\theta})}{\ln \mathcal{L}(\vec{\theta'})}\right) \tag{6.3}$$

where likelihoods, $\mathcal{L}(\vec{\theta})$ represents the PDF of a given set of parameters. A detailed description of the calculation of the likelihood is detailed in [128]. A random number is selected between 0 and 1, assuming a uniform distribution. If the value of α is smaller than the random number, the step is accepted. If it is larger, the step is rejected, and the chain remains at its current step. The acceptance probability is designed such that it is equal to 1 if the likelihood of the proposed step, $\mathcal{L}(\vec{\theta'})$, is greater than that of the current step, $\mathcal{L}(\vec{\theta})$.

The construction of this acceptance mechanism allows the MCMC to explore the entire PDF by accepting steps which result in a lower likelihood. This method also avoids getting stuck in any local minima of the likelihood.

It is important to determine at what point the MCMC has converged and reached the stationary state. The initial states with fluctuating transition probabilities will not be representative of the final PDF, and should be removed. These early steps are referred to as 'burn-in', and are removed from the analysis. Another important factor in ensuring the final PDF is reliable, is that the number of steps completed by the MCMC is sufficiently large. A series of diagnostic checks are carried out to ensure the performance of the MCMC satisfies these conditions and that a stationary distribution representing the final PDF is stable. More details on these methods can be found in [129].

6.6.2 Analysing the posterior probability distribution

After the MCMC chain has converged and the final PDF has been produced it should be analysed in an accessible and understandable format. The final distribution will be highly dimensional, and therefore difficult to interpret. To reduce the dimensionality to one parameter, marginalisation methods are used. This involves integrating away all parameters in the PDF except the parameter of interest. Using the one-dimensional PDF it is possible to estimate the postfit parameter value, alongside its uncertainty. Three methods were considered in determining the postfit value: calculating the mean and RMS of the distribution, fitting a Gaussian to the distribution, or taking the Highest Posterior Density (HPD) - the maximum of the distribution, where the error is the symmetric region covering 68% of the distribution starting from the HPD. If the

distribution was approximately Gaussian, all three methods should converge. However, if the posterior distribution was non-Gaussian, the HPD method was used.

6.6.3 Event Rate Comparisons

A measure of the goodness of fit can be performed by considering the number of events estimated for each ND sample. It is possible to then compare the number of events found in data, to the number of events predicted by the MC before and after the fit. The prior predictive distribution of the number of events was determined by constructing toy experiments. The nominal MC was re-weighted, referred to as a toy MC, according to some random throw of the prior distributions. This process was repeated to generate 3000 toy MC experiments, to reduce statistical fluctuations such that the estimated number of events per sample approximated a Gaussian distribution. From these toys, the mean value of the number of events was calculated. The RMS of the distribution was taken to be the error on the number of events. Following a ND fit, it is possible to also predict the number of events, known as the posterior predictive. In this case, random steps from the PDF were taken, and the MC was re-weighted to the parameter values at that step. Again, the process was repeated 3000 times, to obtain an estimate of the number of events. It was important to also compare the number of events in a sample as a function of the kinematics used in the fit. In section 6.8 the prior and posterior predictive event rate distributions following the data fit are shown.

6.7 Asimov Fits

It is important to ensure the oscillation analysis framework is robust and that the parameter constraints are understood. It is possible to test the framework by performing a fit to the MC simulation itself. In this case the 'data' is set to the nominal MC with the parameters assigned to their central value, with no parameter variation. Therefore, the fit should extract parameters very close to their prefit values. If this is not the case, investigations must be undertaken to check the parameter implementation and any issues with the fit convergence. The Asimov fits performed for this study involved 16 million steps with 1.6 million burn-in steps.

It is hoped in an Asimov fit, that the posterior probability values for each parameter will be centred at the prior value, as was the case for most parameters shown in figure 6.12. However, in some cases the 1D posterior probability postfit value may be pulled away from the prior value. An example of such a case is shown in figure 6.12, where the postfit Pauli blocking variables were higher than the prior. This was due to correlations with other cross section parameters, in this case, some of the FSI and RPA strength variables, as shown in figure 6.13. The FSI and RPA strength prior was close to the boundary, which leads to marginalisation issues. These issues were only with the visualisation of the distributions rather than the overall results of the N-dimensional fit, and were not an issue with the data fit, as the parameters were unlikely to be near the boundary, in data. When running an Asimov fit where the FSI and RPA strength variables were fixed, the postfit posterior distribution of the Pauli blocking cross section parameters were centred at the prior as expected.

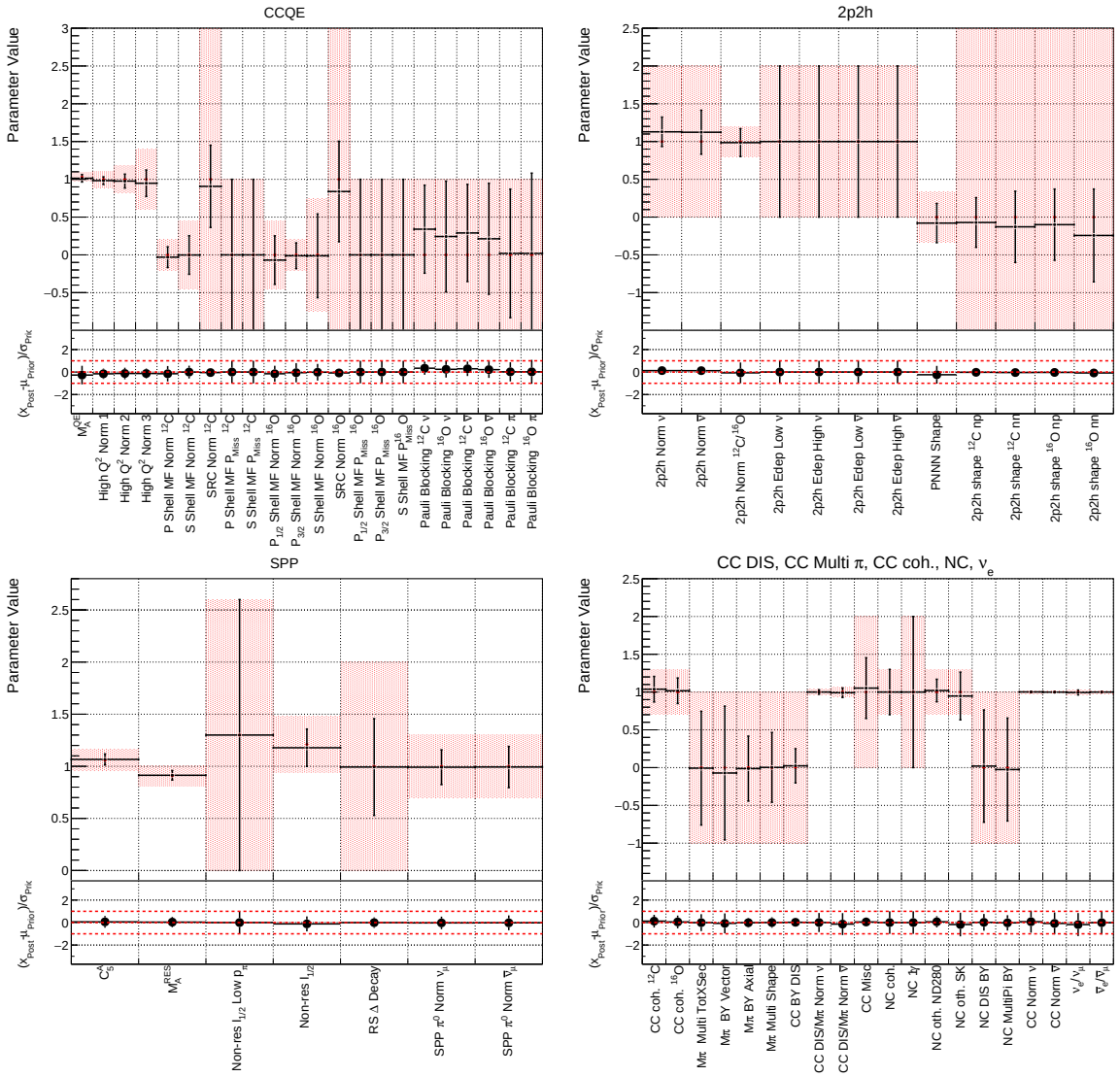

Figure 6.12: The posterior postfit parameters following an Asimov fit for the CCQE, 2p2h, SPP, and DIS cross section parameters, respectively. The red band shows the prior parameter value and the black cross indicates the postfit parameter value.

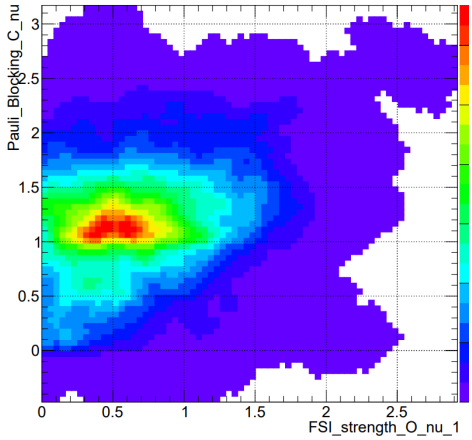

Figure 6.13: The postfit posterior probability distributions of one of the FSI strength parameters vs one of the Pauli blocking parameters.

6.8 Data Fit

The following data fit was performed with 20 million steps, with 2 million steps as burn-in. The prior and posterior predictive distributions for the $\bar{\nu}$ samples are shown in figures 6.14 to 6.17. The posterior predictive distributions showed better agreement than the prior predictive for each sample, with a large reduction in the systematic uncertainties. The $\bar{\nu}$ CC-Photon sample observed some over prediction of the number of events at higher momentum, and in the lowest momentum bin. The posterior predictive also overestimated the event rate in more forward going tracks.

A summary of the event rates for each $\bar{\nu}$ ND sample, and the total event rate of all ND samples, including ν samples, is shown in table 6.3. The -2log$\mathcal{L}_{\text{stat}}$ was evaluated for both the prior and posterior predictive rates to determine the agreement between MC and data in both cases. It was found to be smaller following the fit in the posterior event rate for every sample. The -2log$\mathcal{L}_{\text{stat}}$ of the $\bar{\nu}$ CC-Photon FGD1 (FGD2) sample decreased from 141.7 (100.8) to 119.4 (89.5) following the data fit.

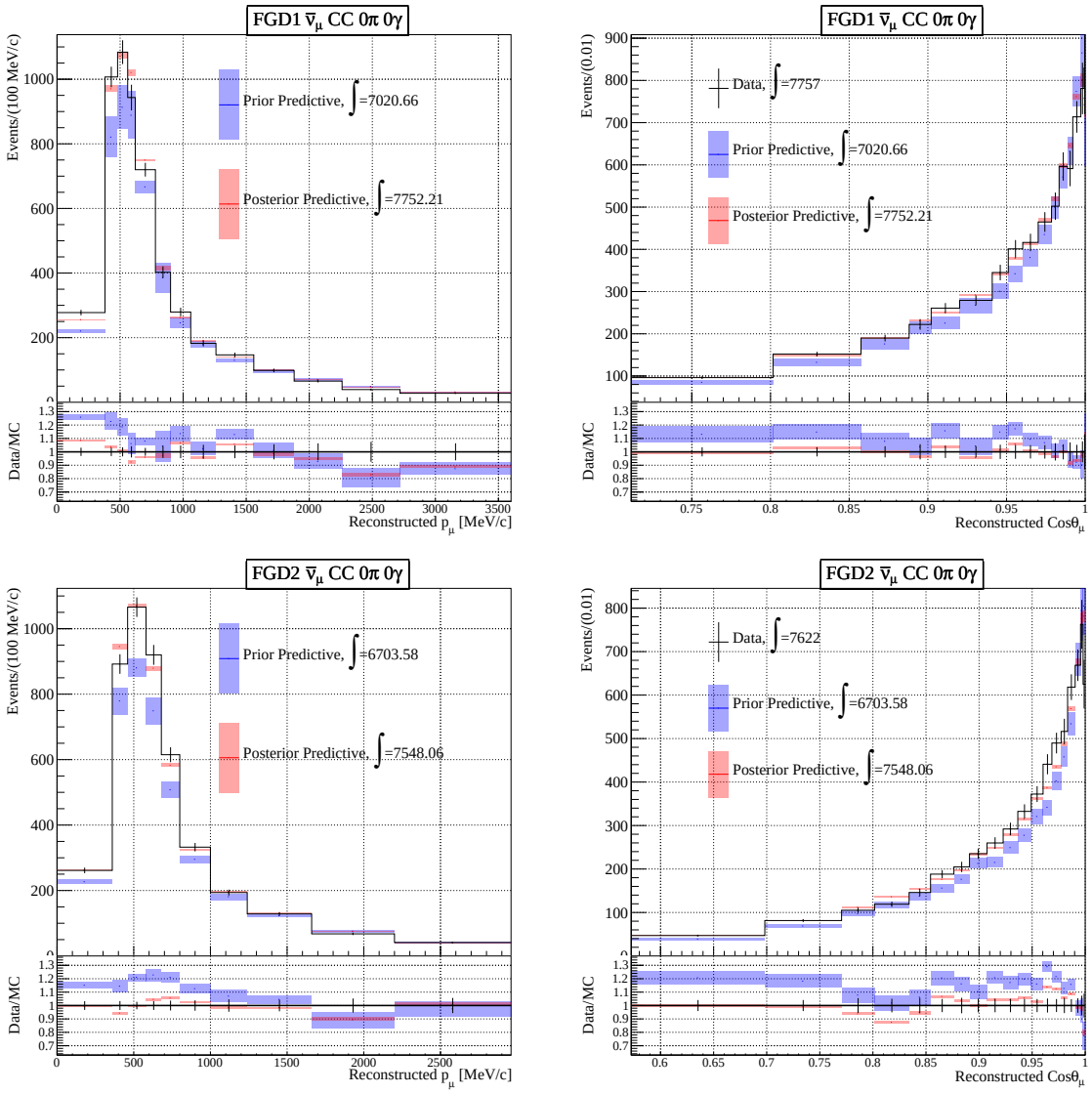

Figure 6.14: Prior and posterior predictive distributions of the $\bar{\nu}$ CC0π sample FGD1(FGD2), above (below), as a function of the antimuon kinematics. The systematic uncertainties for both prior and predictive cases are shown.

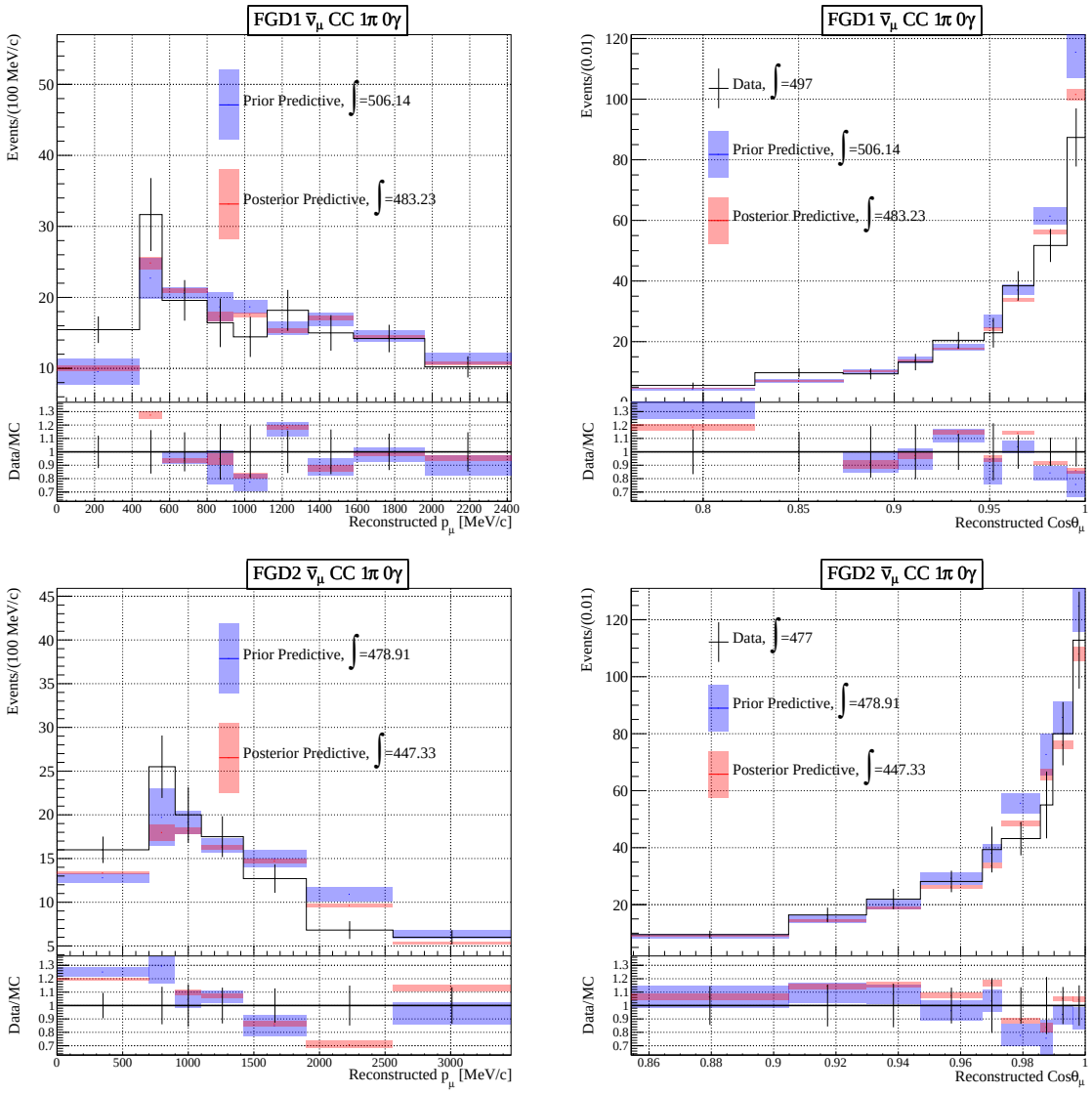

Figure 6.15: Prior and posterior predictive distributions of the $\bar{\nu}$ CC1π^- sample FGD1(FGD2), above (below), as a function of the antimuon kinematics. The systematic uncertainties for both prior and predictive cases are shown.

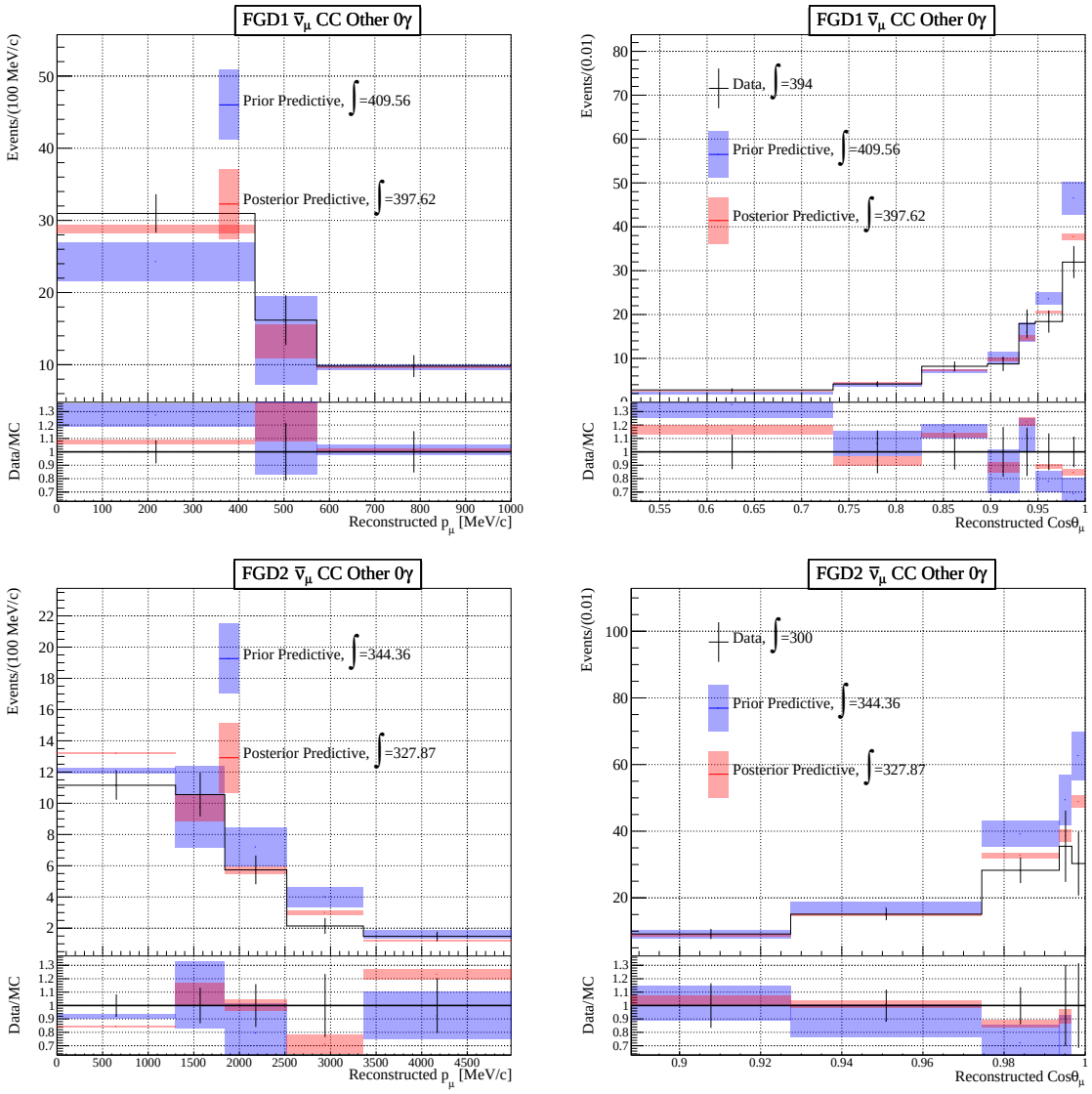

Figure 6.16: Prior and posterior predictive distributions of the $\bar{\nu}$ CC-Other sample FGD1(FGD2), above (below), as a function of the antimuon kinematics. The systematic uncertainties for both prior and predictive cases are shown.

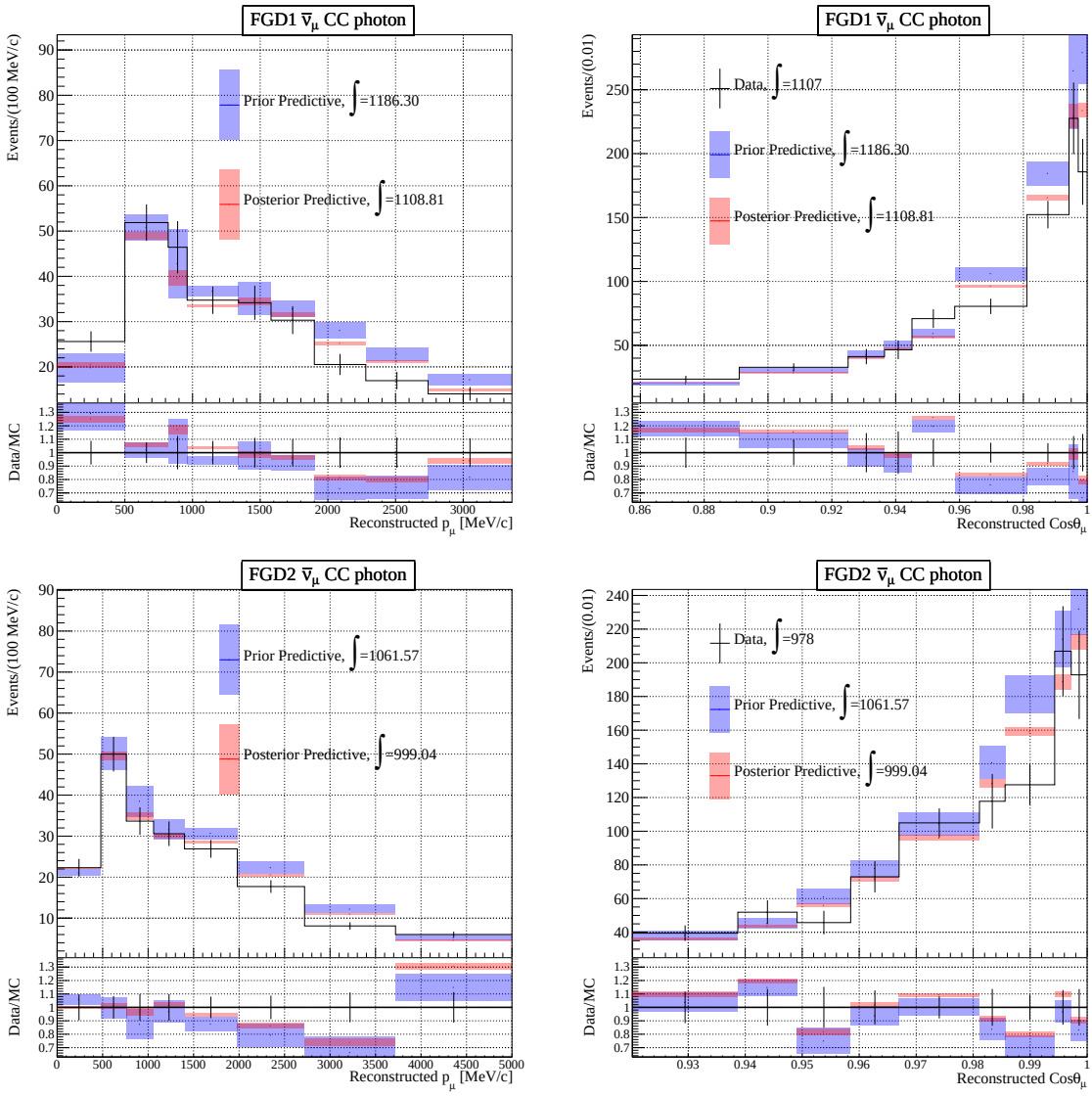

Figure 6.17: Prior and posterior predictive distributions of the $\bar{\nu}$ CC-Photon sample FGD1(FGD2), above (below), as a function of the antimuon kinematics. The systematic uncertainties for both prior and predictive cases are shown.

Sample	Data	Event Rate		-2log$\mathcal{L}_{stat}$	
		Prior	Posterior	Prior	Posterior
FGD1 $\bar{\nu}_\mu$CC 0π	7757	7001.4 ± 943.7	7752.5 ± 74.2	489.8	243.8
FGD1 $\bar{\nu}_\mu$CC $1\pi^-$	497	506.0 ± 63.3	483.1 ± 11.3	115.7	103.2
FGD1 $\bar{\nu}_\mu$CC-Other	394	407.7 ± 53.0	397.4 ± 9.6	39.3	23.0
FGD1 $\bar{\nu}_\mu$CC-Photon	1107	1182.9 ± 155.6	1108.5 ± 22.8	141.7	119.4
FGD2 $\bar{\nu}_\mu$CC 0π	7622	6686.6 ± 828.5	7549.0 ± 75.2	507.2	296.4
FGD2 $\bar{\nu}_\mu$CC $1\pi^-$	477	478.2 ± 59.7	447.5 ± 10.3	75.0	66.1
FGD2 $\bar{\nu}_\mu$CC-Other	300	342.6 ± 46.6	327.9 ± 8.2	29.4	22.0
FGD2 $\bar{\nu}_\mu$CC-Photon	978.0	1057.0 ± 135.0	999.2 ± 21.0	100.8	89.5
Total All Samples	150015.0	132826 ± 11954	145908 ± 390.4	6013.3	1747.7

Table 6.3: The event rates of each $\bar{\nu}$ sample for the prior and posterior data fit. The total all samples refers to the event rate uncertainty for all events including the ν and wrong-sign background ν samples.

Table 6.4 shows the fractional systematic uncertainty for each sample for both the prior and posterior predictive event rates. The total ND280 event rate uncertainty, with all samples for both ν-mode and $\bar{\nu}$-mode, reduced from 10.04% to 0.26% after the fit. Of the $\bar{\nu}$ samples, it was the CC0π samples which observed the greatest reduction in the fractional systematic uncertainty. The CC-Photon FGD1 (FGD2) sample saw the next highest reduction, at 2.05 (2.10)%, followed by CC$1\pi^-$, and lastly CC-Other. It is reassuring that the CC0π sample had the lowest fractional uncertainty as it is the sample with the most CCQE events, which are important to Super-K. The CC-Other sample is less important and has issues with mis-modelling, and a low purity, therefore there is not much concern about the larger uncertainty observed in these samples. The event rate uncertainties were reduced in all cases, demonstrating the improved agreement between data and MC following the fit.

The posterior postfit flux parameters for RHC-mode are shown in figure 6.18. A pull to higher values was observed in the low energy regions of the RHC $\bar{\nu}_\mu$ parameter.

Sample	Prior $\delta N/N(\%)$	Posterior $\delta N/N(\%)$
FGD1 $\bar{\nu}_\mu$CC 0π	13.48	0.96
FGD1 $\bar{\nu}_\mu$CC $1\pi^-$	12.50	2.34
FGD1 $\bar{\nu}_\mu$CC-Other	13.01	2.42
FGD1 $\bar{\nu}_\mu$CC-Photon	13.16	2.05
FGD2 $\bar{\nu}_\mu$CC 0π	12.39	1.00
FGD2 $\bar{\nu}_\mu$CC $1\pi^-$	12.49	2.29
FGD2 $\bar{\nu}_\mu$CC-Other	13.60	2.51
FGD2 $\bar{\nu}_\mu$CC-Photon	12.77	2.10
Total All Samples	10.04	0.26

Table 6.4: The fractional uncertainty on the event rates of each $\bar{\nu}$ sample for the prior and posterior data fit. The total all samples refers to the event rate uncertainty for all events including the ν and wrong-sign background ν samples.

At higher energies they were closer to nominal. A similar effect was seen in the RHC $\bar{\nu}_e$ parameter. The constraint on the $\bar{\nu}_e$ parameters saw little improvement, which is unsurprising as no $\bar{\nu}_e$ selections are present in this analysis. The flux parameters are highly correlated, therefore any shift in one parameter moves the others in the same direction. The penalty term of the stationary distribution for the flux parameters was -log$\mathcal{L}_{flux}$ = 50 - 60, which for each of the 100 flux parameters corresponded to a penalty term of $\mathcal{O}(1)$ each. The penalty term was determined for each step in the MCMC chain, and the average penalty for all steps once it had reached a stationary distribution is quoted.

The posterior postfit cross section parameters are shown in figures 6.19 and 6.20. Many CCQE, and CCQE binding energy parameters were shifted relative to their priors to account for the under-predicted event rate in the ν CC0π samples. The value of M_A^{QE} was shifted by 2σ away from the prior, closer to the generated value of 1.21 GeV/c^2. The 2p2h parameter constraints and shifts effect the samples which contain splitting relative to the proton multiplicity, only available in the ν-mode selection. The same was

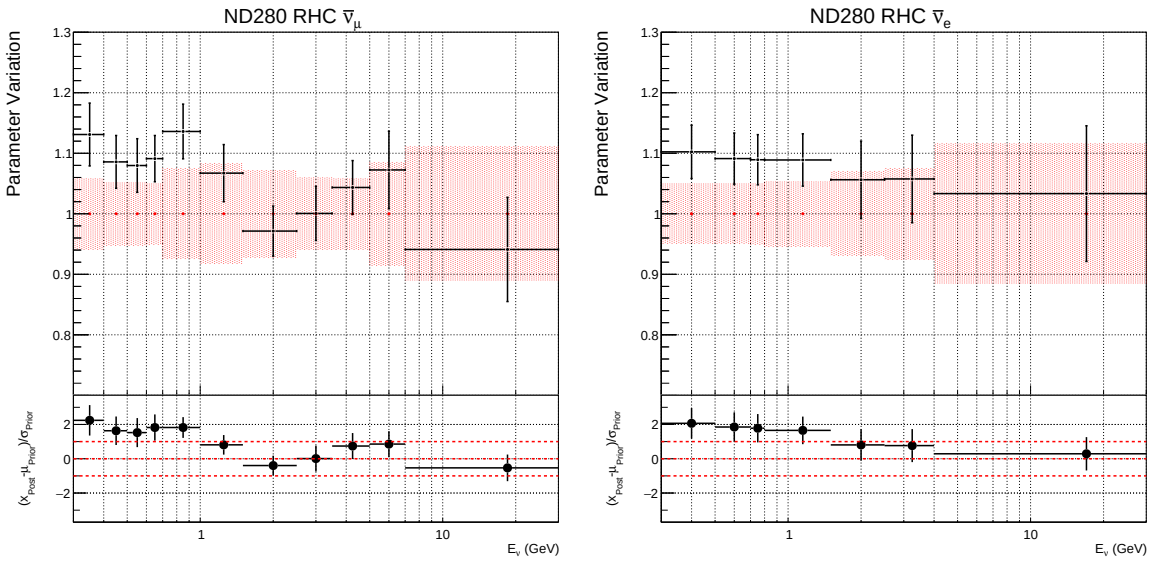

Figure 6.18: The posterior postfit parameters following a data fit for the RHC, $\bar{\nu}_\mu$, and $\bar{\nu}_e$ flux parameters respectively. The red band shows the prior parameter value and the black cross indicates the postfit parameter value.

typically true of the FSI parameters and SRC parameters, which were also constrained but are generally not shifted away from their prior values. The $\bar{\nu}$ π^0 normalisation parameter was shifted to a more negative value and some additional constraint on the errors was observed. The constraint on the equivalent parameter in ν interactions was of a similar magnitude to the $\bar{\nu}$ parameter, although they shifted in opposite directions. The binding energy parameters observed a large constraint relative to the prior as the error was set conservatively to 25 MeV. Some of the DIS parameters, such as the multi-pion parameters, were better constrained by the fit and shifted to negative values, such as multi-pion total cross section by 1σ, corresponding generally to a model closer to the nominal than the alternative models considered.

The penalty term for the cross section parameters during the MCMC data fit as a function of the step number is shown in figure 6.21. The postfit flux and cross

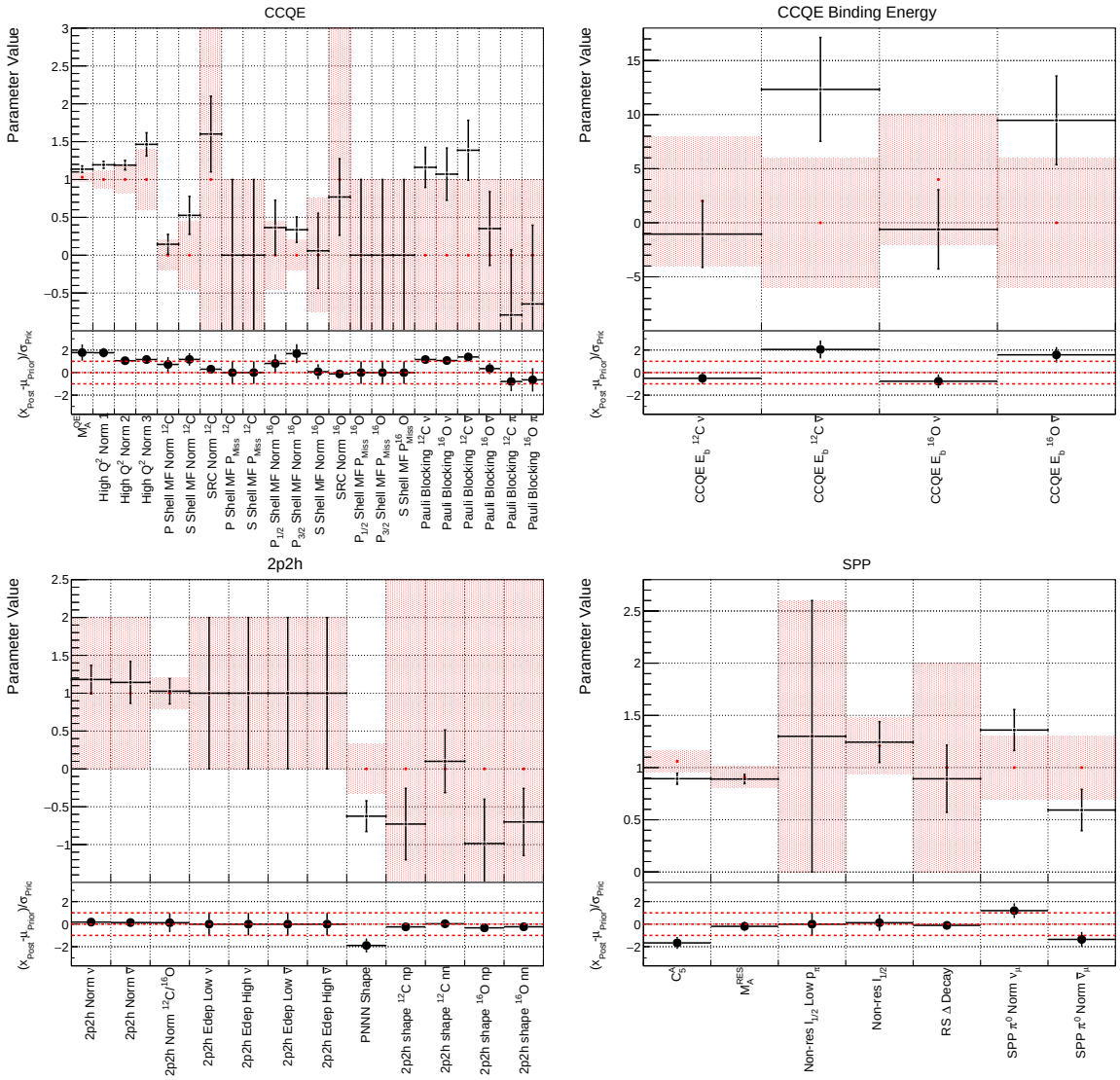

Figure 6.19: The posterior postfit parameters following a data fit for the CCQE, 2p2h, SPP, and CCQE binding energy cross section parameters, respectively. The red band shows the prior parameter value and the black cross indicates the postfit parameter value.

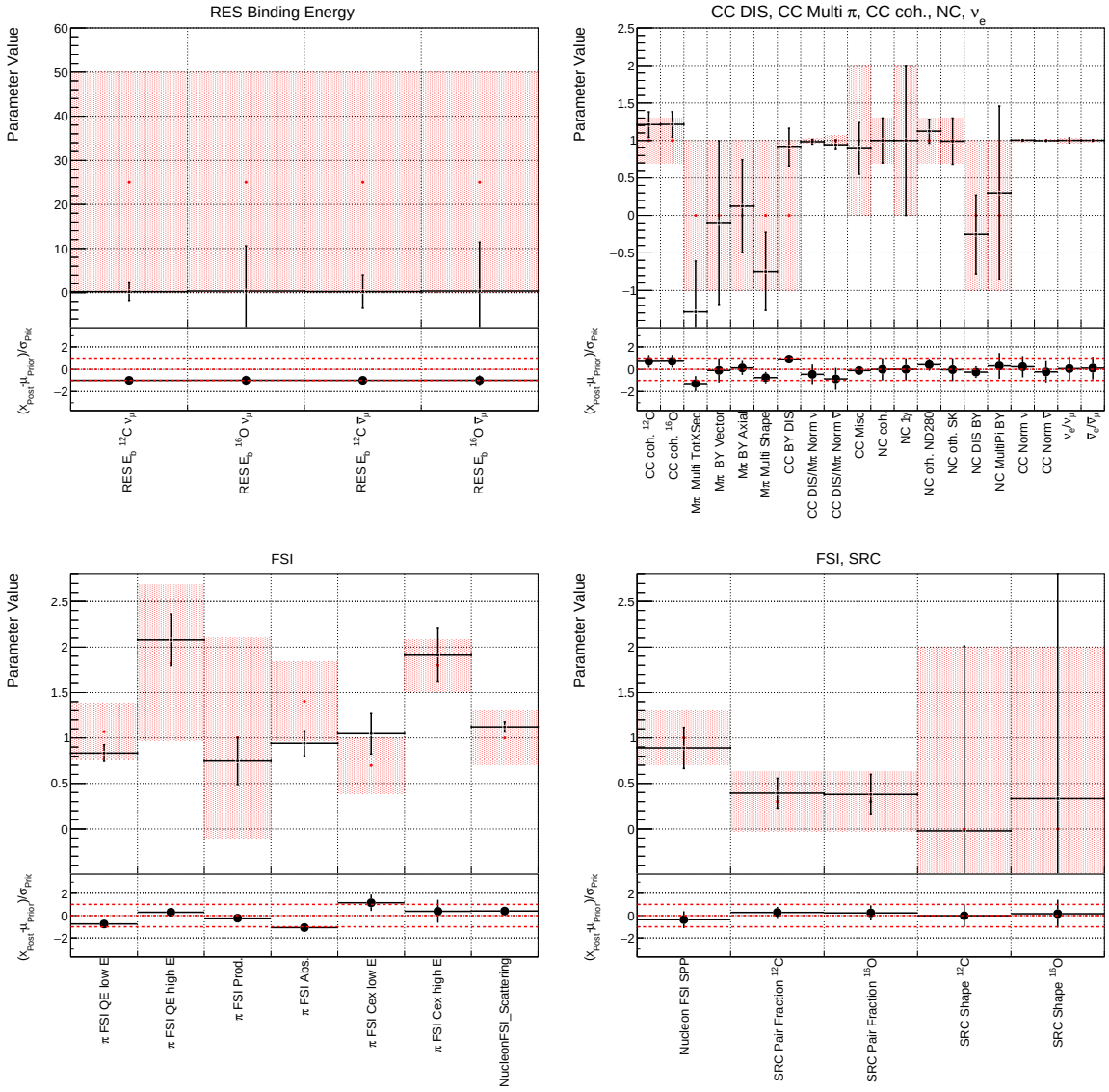

Figure 6.20: The posterior postfit parameters following a data fit for the RES, DIS and FSI cross section parameters. The red band shows the prior parameter value and the black cross indicates the postfit parameter value.

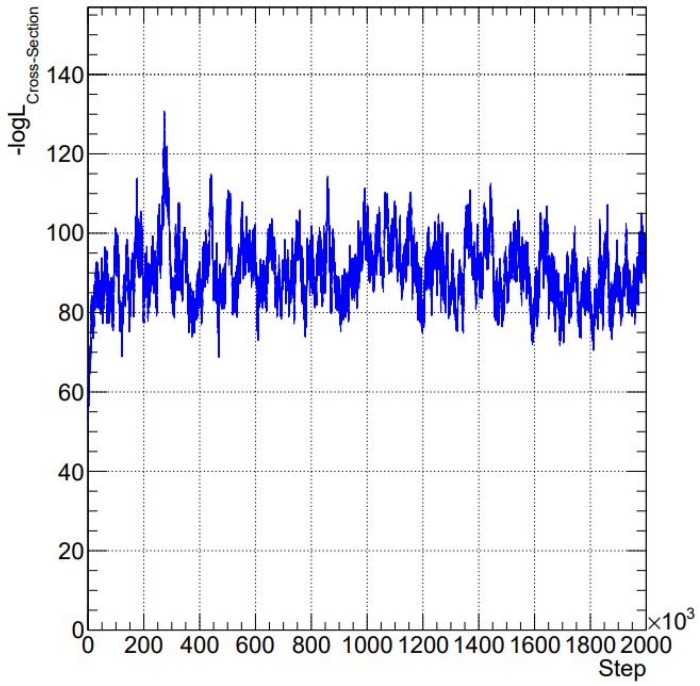

Figure 6.21: The cross section parameters penalty term as a function of the step number during the MCMC fit.

section correlation matrix is shown in figure 6.22. Correlations between cross section parameters were minimal prefit as seen in figure 6.3, but after the fit, some correlations were observed. This was expected as the parameters all affect different neutrino interaction types, and a preference to alter one aspect of the neutrino model changes the behaviour of other parameters effecting the same interaction type.

It is clear that the ND fit significantly reduced the uncertainties on the flux and cross section parameters. The CC-Photon sample has been shown to aid in constraining the $\bar{\nu}\ \pi^0$ parameter, and the event rate of the sample is more precisely understood after the fit. It is expected that when a joint ND and FD fit is performed, that a similar reduction in the errors will be observed.

6.9 Conclusions

In chapter 4 photon selection methods were described, with an emphasis on the ECal photon selection development. A new PID tool using BDTs was created to aid in increasing the purity of the muon candidate selected in $\bar{\nu}$ CC-Photon events. It will be beneficial to continue development of this tool to determine if it is useful in improving the purity of the other ND samples. The $\bar{\nu}$ CC-Photon sample has an efficiency of $\sim$40% and a purity of $\sim$42%. After applying the PID BDT tool, the purity of this sample became high enough that it is a useful sample in the ND fits.

Future work involving this PID BDT could involve applying it to the other ND samples, such as CC1π^- and CC-Other. It is not likely to be effective when applied to the CC0π sample, as backgrounds from pions and protons are not as prevalent. The tool is versatile in that it targets particle type rather than a topology, although the BDT has been optimised around the momentum regions which were specifically an issue to the

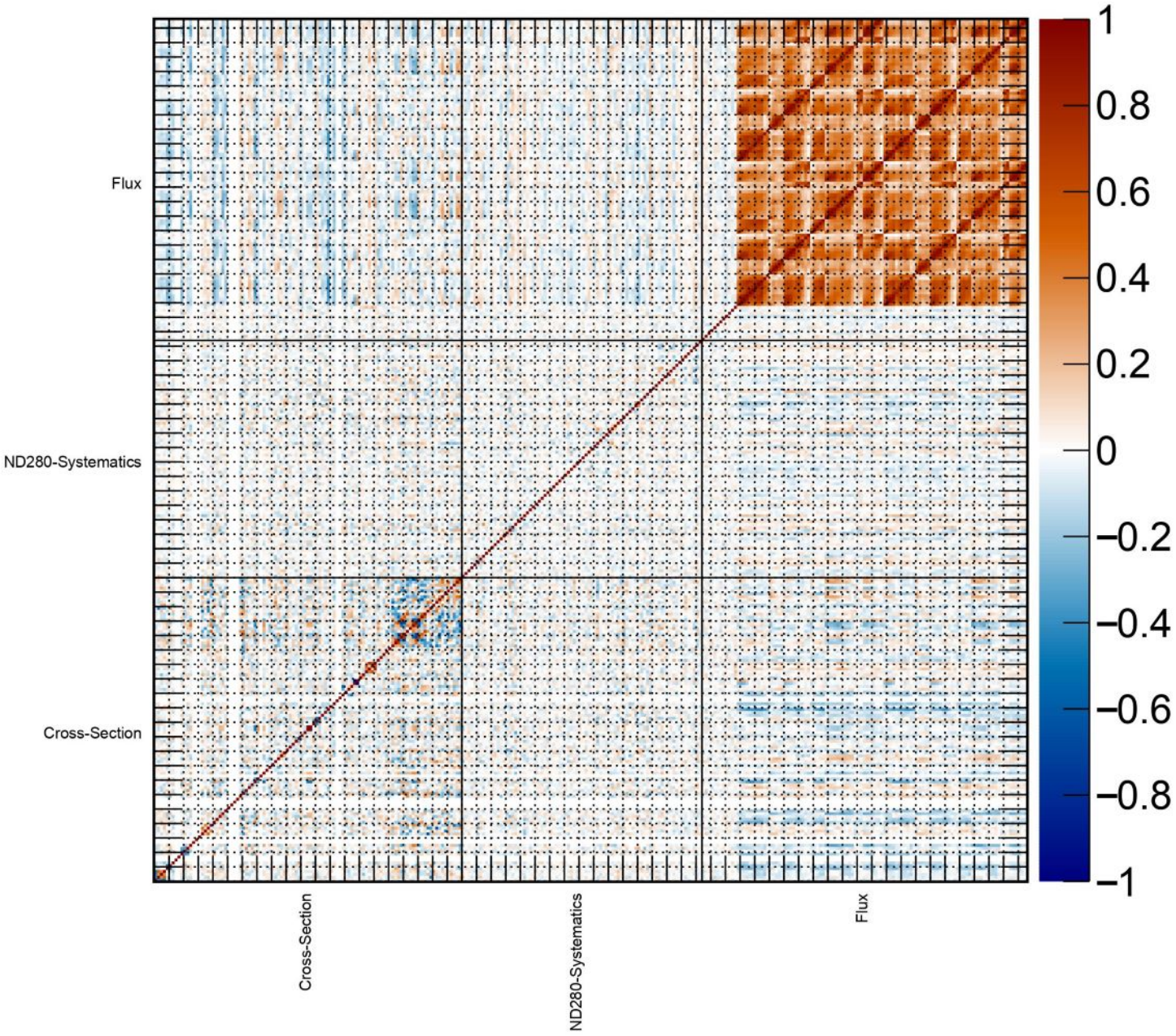

Figure 6.22: The postfit correlation matrix for the flux and cross section parameters following a data fit.

	Efficiency		Purity	
	Before BDT (%)	After BDT (%)	Before BDT (%)	After BDT (%)
CC0π	70	64	82	85
CC1π^-	15	13	56	68
CC-Other	24	20	20	30

Table 6.5: Preliminary future work applying the BDT cut to the other three antineutrino multipi samples. The sample efficiency and purity before and after the cut is applied is shown.

CC-Photon sample. When applying the BDT as is currently designed with no change to the cut values to the other multipi samples, the CC1π^- and CC-Other samples observe an increase in purity, with small decreases in efficiency. These improvements to purity are summarised in table 6.5. These samples may benefit from further investigation in implementing the BDT into their respective selections. Considerations for the new detector systematic uncertainties required for the PID BDT, and updates to the ECal related systematic uncertainties were detailed in chapter 5. It was found that the new systematic uncertainties were minimal.

The implementation of the new photon sample to the ND fitting framework was detailed in chapter 6 where it was shown that sensitivities to flux and cross section parameters were improved. The fractional uncertainty on the event rate of the ND samples was reduced from 10.04% to 0.26% as a result of the fit. The $\bar{\nu}$ CC-Photon FGD1 (FGD2) sample saw a reduction in the fractional uncertainty from 13.16 (12.77)% to 2.05 (2.10)% as a result of the ND fit. The reduction in uncertainties on these parameters will be propagated to the FD to improve measurements of the oscillation parameters.

Chapter 7

The Hyper-Kamiokande Experiment

Following from the successes of its predecessor, Super-K, a new large-scale water Cherenkov detector named Hyper-Kamiokande (Hyper-K), is under construction in Japan. The basic detector design is similar to Super-K, the main change being its fiducial mass, ∼180 kton, is eight times larger than its predecessor. A diagram of the detector is shown in figure 7.1.

Once construction is complete, the Hyper-K detector will act as the FD of the Tokai to Hyper-Kamiokande (T2HK) long-baseline experiment. The T2HK experiment will use a suite of near detectors and an upgraded T2K beamline. In addition, another water Cherenkov detector, the Intermediate Water Cherenkov Detector (IWCD), will be built approximately 750 m from the neutrino production target. The water level in the pit will be modifiable such that the buoyant detector may be raised and lowered thus altering the off-axis angle of the detector relative to the neutrino beam. A broader phase space may be accessed by sampling neutrinos from a variety of energy spectra

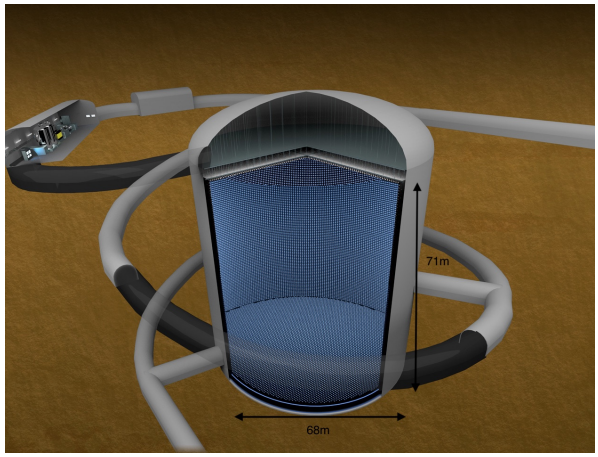

Figure 7.1: A schematic diagram of the Hyper-K detector [56].

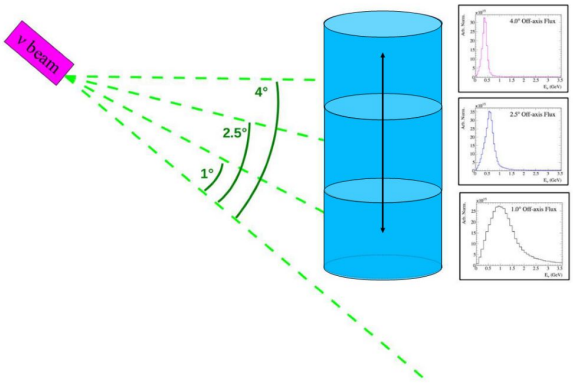

Figure 7.2: The IWCD at different off-axis angles, sampling various neutrino spectra [130].

at each off-axis angle, between 1-4°. Minimising the flux and cross section parameters, which behave as nuisance parameters in the oscillation analyses, will be possible due to the fundamentally equivalent technology systems of the IWCD and FD. The IWCD also will cover a full 4π solid angle - the same as the FD. A diagram of the system is shown in figure 7.2.

The Hyper-K physics programme will extend beyond the long baseline analyses of the T2HK experiment, studying a variety of fields such as nucleon decay and

astronomical neutrino sources. The physics goals of the experiment are detailed in section 7.4.

7.1 Far Detector Design

The detector will measure 68 m in height and 71 m in diameter, with a total volume of 258 m^3. It will be situated 8 km south of Super-K, in a newly excavated cavern in the Tochibora mine. The detector will be at the same off-axis angle and distance relative to the J-PARC beam as Super-K. The cavern will be situated under a 650 m rock overburden, which provides passive shielding for external backgrounds. The detector will comprise of two concentric cylindrical detectors an inner detector (ID) and an outer detector (OD). The ID will be instrumented with 20,000 50 cm PMTs and ∼800 higher resolution multi PMTs (mPMTs) [131]. Each mPMT will be formed of a cluster of 19 PMTs (8 cm in diameter), which will improve the event reconstruction efficiency of the system [56]. The OD will be instrumented with $\mathcal{O}$(1,000) OD photosensing units, comprising of an 8 cm PMT mounted in a wavelength shifting (WLS) plate [132]. The number of OD PMTs was being optimised through the time that this thesis was undertaken. The number of OD PMTs was assumed to be 10,000 while the work in section 9 was undertaken, and 7200 OD PMTs while the work in section 8 was carried out. The OD design is described in section 7.2, as one of the analysis topics detailed in this thesis relates to the OD. The FV for neutrino interactions will be located in the ID.

The front-end electronics (FEE) will be housed in a watertight container situated in the water to reduce the amount of cabling required, which would introduce additional radioactive backgrounds. Each FEE board will read out 24 PMT channels. The

channels may either instrument only ID PMTs or a combination of ID and OD PMTs [133]. The PMT information will be read out using a digitiser to determine the charge and time information of a single PMT hit. The FEE will be connected to the Data Acquisition (DAQ) systems via a series of optical fibres. The DAQ system design is detailed in section 7.3, as the other analysis topic covered in this thesis relates to the DAQ system. A high voltage cable will lead to the in-water electronic unit to power the PMT.

7.2 The Outer Detector

By introducing an additional detector enveloping the ID, where signal neutrino interactions occur, it can be deduced that any particles seen in the OD before the ID, must be background events. There will be 2 m of water at either top and end cap, the spherical regions at either end of the tank, of the OD and 1 m of water around the barrel width. Any particles observed in the OD should be tagged such that physics analyses may exclude these backgrounds. The OD will be optically separated from the ID to ensure Cherenkov light point of origin is known. As the OD will function to simply tag rather than understand the exact physics details of these particles, its design differs to that of the ID. It is more important that the OD detect as many background particles as is possible than that the reconstruction of the event is precise. Thus fewer and smaller PMTs will be used when compared with the ID.

There is also an emphasis on encouraging reflections such that all photons are detected even if there is a short time delay between direct detection and detection of reflective signal, to maximise the light detected, and thus increase the efficiency of the OD. The walls of the OD will be covered with highly reflective Tyvek to encourage these

reflections around the OD volume. More details on Tyvek are given in section 7.2.4. To ensure the reduced photocoverage area will not impact the detection efficiency of the OD, the PMTs will be surrounded by a 30×30 cm^2 WLS plate forming a single photosensing unit, as described in section 7.2.3. This increased surface area will redirect light via total internal reflection towards the PMT at the centre of the plate. The plate will also shift light from the ultra-violet range to the visible where the PMT quantum efficiency is highest.

A light injection system will be comprised of both diffuse and collimated inputs which will be used to calibrate the OD system. It will also aid in tracking the optical properties of the Tyvek and water. Diffuse sources will be mounted on the inner wall support structure of the OD, and they aim to produce light such that all OD PMTs are illuminated at the single photoelectron level. These diffuse sources must have voltage high enough such that the PMTs can be saturated. There will be 12 collimators positioned around the OD, six in the barrel and three at either end cap. These collimators will be used to determine the water absorption and scattering properties, by measuring the charge collected by the PMTs as the collimated light travels parallel to the PMT surface.

The OD electronics will readout the PMT signal continuously, and a trigger system will cycle through this data to determine whether or not the OD has observed a signal. If a trigger has been issued, the OD and ID data will be saved to disk with a flag that the OD has observed a signal. It will then be available for offline analysis to determine with higher precision whether or not background is present in the event; or if the OD background flag is sufficient that there can be confidence that the data is not useful and may be discarded from analyses. Details on the OD trigger system can be found

in section 7.2.6.

7.2.1 Physics Requirements

Due to the more shallow overburden at the Hyper-K cavern, and the increased detector size, it is expected that the cosmic ray muon flux will be approximately 15 times higher than at Super-K. This corresponds to a flux of 45 Hz or 4 million muons per day [134]. This represents a substantial background to all analyses, therefore the OD is required to have a very high cosmic muon tagging efficiency. Figure 7.3 shows the expected muon flux at Hyper-K as predicted using MC simulations. All simulations of the Hyper-K FD, as detailed in this thesis, are made using Water Cherenkov Simulation (WCSim), a software tool used to model water Cherenkov detectors using Geant4 [101]. WCSim simulates the geometry, detector response and physics events of interest. It is also possible to include the properties of the specific PMT and materials used in the 'real' detector, creating a more robust simulation. The hit and timing information of the physics events generated are saved, alongside the true data, such as vertex and energy. The hit information of simulated physics events are used to inform detector design decisions.

Cosmic-ray muons may also produce backgrounds indirectly by interacting with the cavern rock and surrounding support structure. These are so-called 'spallation backgrounds' and will result in a flux of neutrons incident on the detector. The emitted neutrons will produce a non-negligible background to low energy analyses. The neutrons may pass through the OD and interact within the ID, where they may be difficult to distinguish from low-energy neutrino interactions and neutron capture signals from high energy neutrino interactions. The spallation particles cannot be distinguished

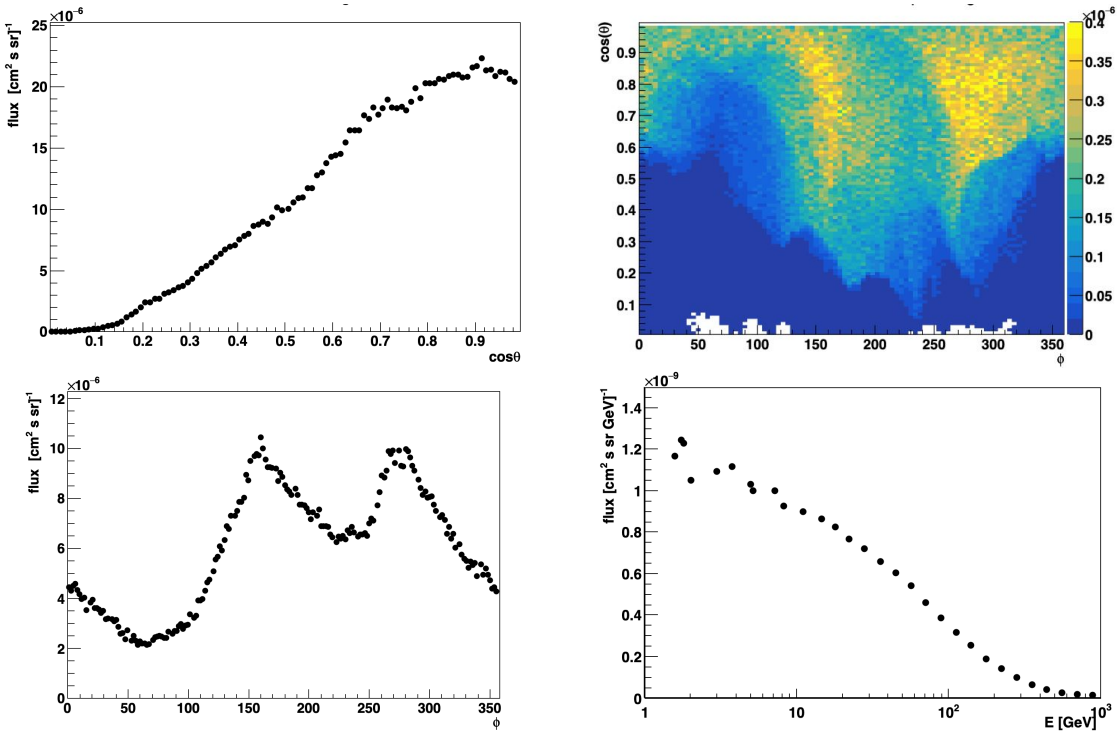

Figure 7.3: The MC simulation of the expected muon flux in the Tochibora mine. On the left, angular distribution ($\cos\theta$ and ϕ); the top right plot shows the angular correlation between $\cos\theta$ and ϕ variables; the bottom right plot is the energy distribution. These plots were produced using the MUSIC software [134].

from signal in the ID. However low energy offline analyses will rely on the detection of the initial cosmic muon to veto any activity which occurs in the 4 m around the muon track for several seconds following the detection of the initial muon [62]. This is especially important in cases where the muon only enters the OD, and the spallation particles enter the ID. The OD must therefore ensure a spatial accuracy of greater than 4 m when determining the entry and exit position of the muon.

The OD will act as both an active veto, and also a passive veto in shielding against low energy backgrounds from the naturally occurring radioactivity in the surrounding rocks. These backgrounds include gammas and neutrons.

While designing the OD it is also important to reduce background contamination from radioactivity in the materials. This is also important as water will circulate between the OD and ID. As the water temperature will be maintained at $\sim$14°C, the power consumption of the underwater electronics must be limited to not more than 1 W per channel [134].

It is important that the OD remains stable and performs reliably for the duration of the detector lifetime, which is expected to be around 20 years. This is especially important when it comes to failures of the PMTs and the underwater electronic units, as they cannot be replaced unless the water is drained, which would be a long and costly process. Details regarding the OD electronics can be found in section 7.2.5. A detailed study regarding how failures in the OD can be mitigated by optimising the layout in which the PMTs are connected to the electronic units, can be found in section 9.

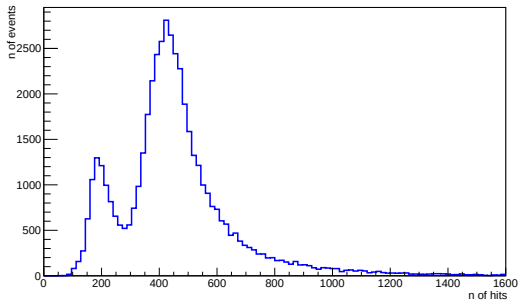

Figure 7.4: Number of hits produced by a cosmic muon in the OD. Total of 100,000 cosmic muons are simulated. Some OD PMTs register more than one photon per event.

7.2.2 Cosmic Muon Veto Analysis

To characterise the performance and ability of the OD to veto cosmic muons, the same method developed by the Super-K experiment is used. The impact point of the simulated muon on the OD wall is determined using information recorded by the ID. The hits surrounding the impact point in a sphere of radius 8 m, are counted. If the number of hits counted is above some threshold, N, the muon is vetoed. The distribution for the number of hits produced by a cosmic muon in the Hyper-K OD, as simulated by WCSim, is shown in figure 7.4. The distribution shows two peaks: the lower number of hits (NHits) peak, around 200 MeV, shows stopping cosmic muons, which do not exit the detector volume, and the higher peak, around 450 MeV, is for cases that the muon is through-going, entering and exiting the detector.

As the NHits threshold, N, decreases, the percentage of cosmic muons which are correctly tagged using this method increases. A distribution of the muon detection efficiency using this method can be seen in figure 7.5, where 10,000 cosmic muons are simulated. It can be assumed that for all cosmic muon simulations described in the remainder of this section that 10,000 cosmic muons were simulated with the properties

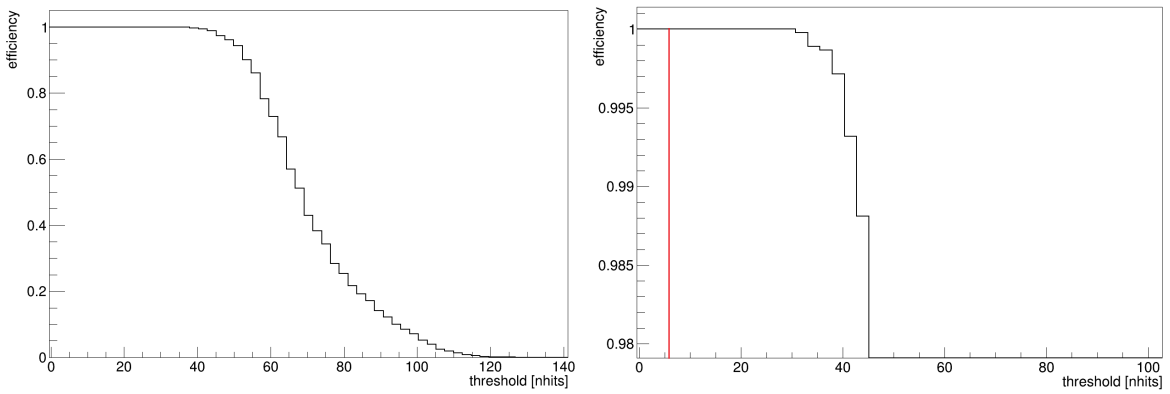

Figure 7.5: The cosmic muon detection efficiency across a range of NHits thresholds. The left plot shows the full distribution, and the right plot zooms in on the region closer to 100% muon detection efficiency. The red line indicates the estimated number of hits produced by dark noise, assuming a rate of 200 Hz/PMT.

as shown in figure 7.3.

As a tagged cosmic muon will result in an event being omitted from physics analyses, it is important to be confident in the tagging capabilities of the OD. The OD tagging should not be so conservative that it misidentifies dark noise as a cosmic muon, meaning valid physics events are rejected.

The threshold, N, should be well above dark noise to protect against fluctuations in dark noise rate and mitigate any increase in the dark noise as the PMTs age, which may induce an increase in rate. It should be noted that for the distribution shown in figure 7.5, that this estimate for the number of dark noise hits is for the full detector, not the 8 m spherical region. So in reality it is expected that there will be fewer dark noise hits, $\sim$1 hit, in the cluster.

The value of N has not yet been fixed as the detector design evolves; it may also be updated throughout the lifetime of the detector if conditions in the detector change.

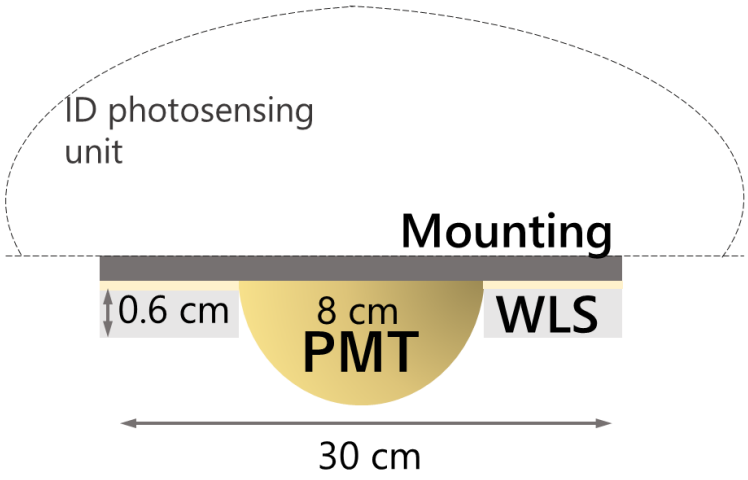

Figure 7.6: A diagram of the OD photosensing unit, showing a PMT, WLS plate and mounting [135].

7.2.3 Photosensing Units

A single photosensing unit will consist of an 8 cm diameter PMT surrounded by a 30 × 30 × 0.6 cm^3 WLS plate. The PMT and plate will then be mounted into an injection moulded frame which is attached to the OD support structure. A sheet of Tyvek will lie between the photosensing unit and the mounting frame to encourage reflections to return to the plate or PMT. A diagram of the photosensing unit is shown in figure 7.6.

Each photosensing unit must be compatible with the underwater environment of Hyper-K. The PMT must pass a series of requirements to successfully function in the OD volume. They must be waterproof and endure pressure >10 bars [134]. They must also perform consistently, without failure, for the lifetime of the detector, at least 20 years. There are additional physics requirements for the system to ensure accurate physics may be performed on the outputted signal of the PMTs.

By introducing a WLS plate to surround each PMT, the amount of light collected doubles. This increase in light is possible due to the total internal reflection within the

plate. The UV-spectrum photons which would normally be outside of the detection range of the PMT are absorbed by dopant molecules in the plate. These photons are then re-emitted isotropically a few nanoseconds later, at a larger wavelength, in the blue-green part of the electromagnetic spectrum, which is detectable by the PMT. The re-emitted photons are usually trapped by total internal reflection as the plate index of refraction of the WLS plate is larger than that of water, and reflective tape will coat the outer edges of the plate. In the event photons leak from the plate, it is still possible that they will be observed by a PMT after they have been reflected from the Tyvek which coats the walls of the OD. Various studies have been conducted both with simulation and lab measurements to determine the optimum WLS plate material and dopants. The base material of the plate will be polymethyl methacrylate (PMMA) with flurors of 1,4-bis(5-phenyloxazol-2-yl) benzene (POPOP) and Poly(p-phenylene oxide) (PPO) included. The geometry of the plate has also been considered to optimise the light collection efficiency. The hole for the PMT will be cylindrical with a diameter of 78 mm. The cladding reflector around the edges of the plate will be made of polymeric film.

7.2.4 Tyvek

To increase the light collection of the OD PMTs, the highly reflective material, Tyvek, will be fixed to all walls of the OD region, and wrapped around the support structure of the tank. The material is made of randomly layered polyethylene fibres: it is cost effective, and durable, ideal for conditions in the water of the tank, and a cost effective alternative to increasing the number of photosensing units.

As the tagging of cosmic muons does not rely on the timing information of the hit

detection as much as the physics analysis of the ID, the photons produced from the passing of a cosmic muon are allowed to reflect around the OD region repeatedly, thus increasing the light detection efficiency. Offline analyses cannot recover data lost at the triggering level. The number of photons detected by the photosensing unit will increase by 800% with the addition of Tyvek. Tyvek is an essential factor in the design of the OD, and it is important that as the detector ages, the reflectivity of the Tyvek does not drop below 80%.

7.2.5 Electronics

A combined ID and OD electronic system, referred to as a hybrid vessel, will supply the PMTs with high and low voltage (HV and LV, respectively) as well as read out the signal from the PMTs [133]. An independent ID only electronic system will also be used, as there will be many more ID PMTs than OD PMTs. This electronic system will be housed in a watertight vessel, which will then be installed underwater. By installing the electronics underwater, rather than on the surface of the detector, the cable lengths will be minimised, and the FEE will be only a short distance from the PMTs. Both factors will reduce signal loss. However if the electronics are underwater, they cannot be retrieved to be fixed or replaced until the water is drained. This is not expected to occur for at least 10 years of running. It is therefore important the watertight vessel is robust, and that the failures of HV, LV and electronic readout system is less than 10% after 10 years of operation for all channels. Each hybrid vessel will include 12 OD channels and 20 ID channels.

The electronic system is designed such that the HV supplied will be steady to ensure stability of the PMT gain: an important factor in measuring energy accurately. A long

cable will provide between 40 and 55 V to the LV power supply in the vessel. This cable will pick up voltage and current noise from various disturbances such as electrostatic discharge, to avoid damaging the FEE. The LV board will then provide energy to the digitisers and data processing boards. The HV board will provide power to two splitter boards via two inputs each. A single splitter board will instrument 12 channels. The vessel will contain two digitiser boards each. The 12 OD PMTs will be connected to the electronic system via underwater cables.

Requirements are made to preserve the longevity of each vessel and internal electronics. The HV and LV boards are both required to have failure rates less than 1% per 10 years of operation. The vessel and underwater conditions will also lead to potential failures, therefore there is an additional requirement that the yearly average failure rate per channel is less than 0.1%.

7.2.6 Triggering

Two different triggers will be used by the OD system to tag cosmic muons. The first is a simple trigger on the number of OD hits detected in a specified time window, where a trigger is issued if a certain threshold of hits is exceeded. The second trigger is more sophisticated and searches for clusters of hits in space and time. The trigger logic for the OD will be the same as the equivalent in the ID as described in section 7.3.1.1. The trigger may be issued if only OD hits or a combination of OD and ID hits are both present. A cosmic muon may sometimes enter the OD leaving hits, but not enter the ID. It may seem that triggering on these muons is not necessary as it will not impact on physics results if no coincidental ID hits are also present. However to tag muons isolated to the OD only, which may cause spallation neutrons, and therefore delayed

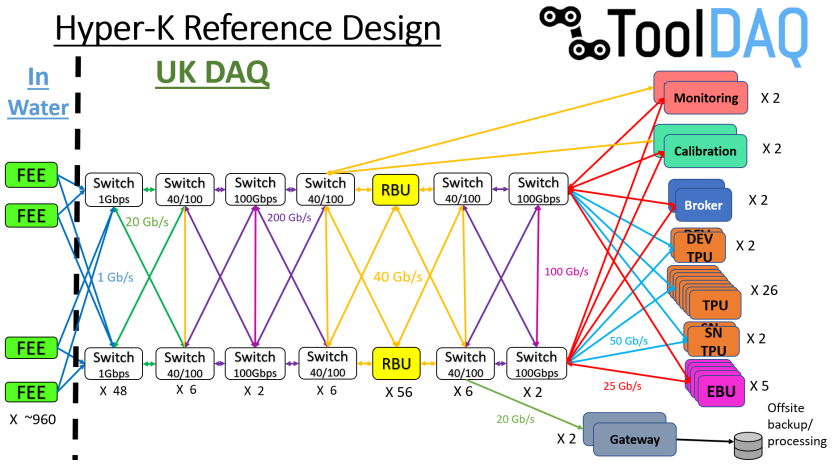

Figure 7.7: Reference design of the Hyper-K DAQ systems [136].

hits in the ID, the trigger may be issued when only OD hits are present.

As the dark rate of the OD photosensing units will be lower than the ID, the trigger threshold will be set to only a few hits. A balance must be met between tagging as many cosmic muons as possible and not accidentally flagging too many true physics signal events in the ID as cosmic muon events.

7.3 Data Acquisition System

The DAQ system will process the raw data as transferred from the FEE boards. The data will be processed via a series of processing nodes. The nodes consist of Readout Buffer Units (RBUs), Trigger Processing Units (TBUs), Event Builder Units (EBUs) and brokers, alongside other systems such as archiving, as shown in figure 7.7.

The raw data from the FEEs will be transferred via network switches to the RBUs. Once received by a RBU, data will be buffered and catalogued for at least 10 hours during normal data taking. Special measures will be taken to buffer raw data for longer

when a supernova trigger is initiated as detailed in section 7.3.2. After buffering, data will continue to the TPUs and EBUs, with brokers directing the task management. The brokers must tell the TPUs and EBUs whether they should analyse or save data respectively, and store records of the job allocation. A TPU will process the data through a series of trigger algorithms. When a task is allocated to a TPU, data will be split into short time slices of the order of ms. If at least one of the triggers is passed, the broker will alert the EBU that it must process the data from the TPU to be saved to disk. Once data has accumulated to a pre-defined limit, it will be archived off site for later analysis.

Optical fibres will connect the in-water electronic systems to the surface level DAQ system. The fibres will deliver power, clock and data connections to the electronics. Timing information will also be passed to the DAQ monitoring database in the back-end. Pairs of optical links and switches, one being active and the other a backup, will link the FEE boards to the RBUs via several layers. The initial optical fibres from the FEE to the DAQ system will transfer data and slow control commands. A series of switches will connect the FEE to the DAQ network such that a single computer may process data inputs from several FEE boards simultaneously.

In the event of a near supernova burst, the links may become saturated. To mitigate losses, the FEE units will also buffer information so that it may be held and transmitted again. As calculation of the supernova features are required within minutes of the neutrino burst, all FEE data should be recovered within 10 s.

7.3.0.1 Readout Buffer Unit

After passing between the layers of links, the binary data will first be processed by the RBUs. Here data will be sorted, validated, and hit information decoded. Data will be buffered and catalogued accordingly before being transferred to the back end network. The FEEs and RBUs work dynamically, meaning a specific RBU will not be hardwired to only communicate with a specified list of FEE boards. Once the FEE has successfully sent data packets to the RBU an acknowledgement statement will be sent to permit the FEE to delete the data from its send queue buffer. Once the RBU has performed its tasks, the hit information will be saved.

While the data is processed, it will also be stored on a secondary buffer for between 24 - 48 hours, in case a supernova alert is issued and the data needs to be recovered. During a near supernova burst a third buffer will be included, to ensure sufficient storage. This third buffer will only be used in the event of a supernova, therefore any information stored here will be permanent, with more than enough storage available to account for the supernova candidate producing the highest neutrino flux and therefore highest data output.

Once the RBU begins to buffer the data, it will also search for available downstream nodes to begin the data processing. When the RBU successfully connects to a downstream machine, it will package and transmit the data in short time slices, of the order of 10 ms. The RBU is also responsible for relaying monitoring information regarding node health and rates, such as deciding whether the rate is indicative of a supernova and thus the additional supernova buffer should be used. Once the data has been successfully buffered by the RBUs, it will be transferred to all the relevant back-end network servers.

7.3.0.2 Broker

The brokers will distribute trigger assignments among the TPUs regarding which time slice to consider in each data slice. The TPU trigger decision will then be fed-back to the broker such that the triggered data is added to a new job queue for the EBUs to process. Any flags such as supernova alerts or reports of issues from nodes will be processed by the broker to ensure appropriate action be taken and that messages are broadcast to the global DAQ system.

7.3.0.3 Trigger Processing Units

The TPUs will be responsible for determining whether a trigger should be issued on the time slice of data under consideration, and to then relay the outcome of the trigger back to the broker for further processing by the EBUs. Each time slice will contain an overlap with the time boundaries of the data slices preceding and following the slice of interest. After passing through the triggering algorithms which are described in section 7.3.1, the positive trigger data slices will be identified and communicated to the broker to be returned to the EBU. All data chunks processed by the TPUs will undergo a fast reconstruction of the event to be passed to the supernova TPUs (SNTPUs) for supernova detection. Both RBUs and the TPUs may be able to indicate the likelihood of a supernova from a large increase in the event rate.

The supernova TPU will be identical in terms of hardware to a standard TPU but it will instead look at longer time slices of data, on the order of 10 s. The reconstructed information from the TPU will be collected to search for more subtle increases in event rate that the standard TPU may have missed. The SNTPU will then determine whether a supernova event has occurred and relay the information back to the broker

and monitoring servers. The SNTPU will then attempt to determine the direction of the supernova.

7.3.0.4 Event Builder Units

The EBUs primary responsibility will be to write out all hits from the positively triggered events to disk. Using information communicated by the broker regarding the time slice which contained the positive trigger, the EBU will request the corresponding data slice from the RBUs. If time adjacent triggers are issued, the EBU will ensure no duplication of hits are being saved, before writing out the data for distribution to a local disk, with regular transfer of data to offsite archiving systems.

7.3.1 Triggering

The Hyper-K physics programme involves a broad range of neutrino energies in the MeV to GeV range. It is therefore necessary that the triggering scheme involves triggers targeting event types across the full phase space. The various trigger algorithms will run in parallel on the same time slice of data. The trigger decision will determine whether the data should be written to disk for offline analysis, or discarded. Before processing the data in the trigger, a pre-processing stage will be implemented to sort the hits in the readout window according to the time-stamp; to apply the calibration; and mask all inactive PMTs.

7.3.1.1 Triggers

The trigger algorithms which will be used vary greatly in complexity and two of them will be described. The simplest trigger algorithm is the NHits trigger: a cut on the

number of hits in a given time slice, where a positive trigger outcome results from the threshold being exceeded. This trigger primarily targets higher energy, $>$ 20 MeV, events [137].

Another trigger algorithm is test vertices, which was designed to target low energy events, $<$10 MeV, from solar neutrinos. In this algorithm, a grid of test vertices across the ID are considered. The time-of-flight is subtracted from the hit time, assuming the light emission occurs from the vertex candidate. If the majority of hits are consistent with that vertex candidate a trigger will be issued [138].

The DAQ group is continuing its development of a series of other triggers, with more sophisticated algorithms, such as the use of machine learning algorithms, to use alongside the NHits and test vertices triggers.

7.3.2 Supernova Trigger

The supernova detection programme of Hyper-K will be very important not only to neutrino physicists, but also to astronomers who rely on the neutrino signal as an alert for the observation of the delayed light signal. To ensure no supernova are missed, a dedicated supernova trigger is being developed. If the supernova burst occurred nearby, the hit rate is expected to elevate for a few seconds. This means if the hit rate were elevated in multiple EBUs, a trigger on the event would be issued. For supernova burst neutrinos further away, but within $\sim$ 80 kpcs, a different algorithm based on that used by Super-K will be used [139].

Using the reconstructed parameters outputted by the TPU, two checks will be performed. The number of triggers with energy above 7 MeV occurring within the FV which are not associated with a muon track will be counted. The dimensionality of

the clusters vertex distribution is expected to be 3D, populating the entire tank, unlike background which will be 1D and point-like. Once a supernova burst neutrino event has occurred, an alert will be issued to the external physics community and Hyper-K will begin its reconstruction of the direction and distance of the supernova candidate. An updated warning would then be communicated with this information.

7.4 Physics Programme

The Hyper-K experiment will be capable of achieving world-leading measurements in a wide variety of areas. This section will describe the broad physics analysis programme that the experiment will investigate.

7.4.1 Accelerator Neutrinos

A variety of neutrino oscillation experiments have measured the neutrino oscillation parameters, however there remains a few variables which are not fully understood. These are primarily the octant of θ_{23}, measurements of θ_{13}, mass ordering, determining whether δ_{CP} is conserved, neither 0 or π, and also precision measurements of the value of δ_{CP}. The Hyper-K FD will be able to detect neutrinos from a broad range of sources, with varying energies and baselines making it the perfect future experiment to resolve these unknowns.

Continuing the work of T2K, Hyper-K will use the upgraded accelerator neutrino beam from J-PARC, and a suite of NDs to establish the future T2HK long baseline programme. The neutrino beam will use the same facility and technology as was described in section 3.1, although upgrades are planned to increase the flux of neutrinos

produced. The main ring beam power is expected to increase from 750 kW to 1.3 MW, corresponding to an increase in protons per pulse (ppp) of 2.45×10^{14} ppp to 3.2×10^{14} ppp, by 2026. The repetition cycle will also decrease from 2.48 s to 1.16 s. By increasing the current of the electromagnetic horns from 250 kA to 320 kA, the neutrino flux will increase by 10% with an additional reduction in wrong sign backgrounds. Both the improvements to the main ring and the neutrino beamline will result in an exposure of accelerator neutrino corresponding to 2×10^{22} POT over the period of a decade [140].

The NDs must reduce the cross-section and flux systematic uncertainties to less than 3%. The addition of new upgraded detectors at the ND site should aid in reducing these uncertainties, however limitations still exist in achieving such a large reduction of error from 6% to less than 3%. The addition of the IWCD, with an identical target as the FD, will aid in reducing these uncertainties.

The two primary goals of the long baseline analyses will be to measure the value of δ_{CP}, and to determine the mass ordering. To measure CP violation in the neutrino sector, the ratio of electron neutrino appearance to electron antineutrino appearance is made. The ratio of accelerator neutrino data, $\nu : \bar{\nu}$ will be taken at 1:3, due to the reduced antineutrino cross section. After 10 years of operation, Hyper-K will be able to exclude 62% of true δ_{CP} values to 5σ, as can be shown in figure 7.8. After 10 years of operation $\sin^2\theta_{23} = 0.5$ should be excluded to 3σ. The octant degeneracy should also be determined, dependent on the true $\sin^2\theta_{23}$ value, as shown in figure 7.9.

When studying both the $\nu_\mu \rightarrow \nu_e$ appearance channel, and the $\nu_\mu \rightarrow \nu_\mu$ disappearance channel, it is found that at the first oscillation peak, the neutrino maximum will be more significant (less significant) when the mass ordering is normal (inverted). The opposite is true for the antineutrino equivalent appearance channel.

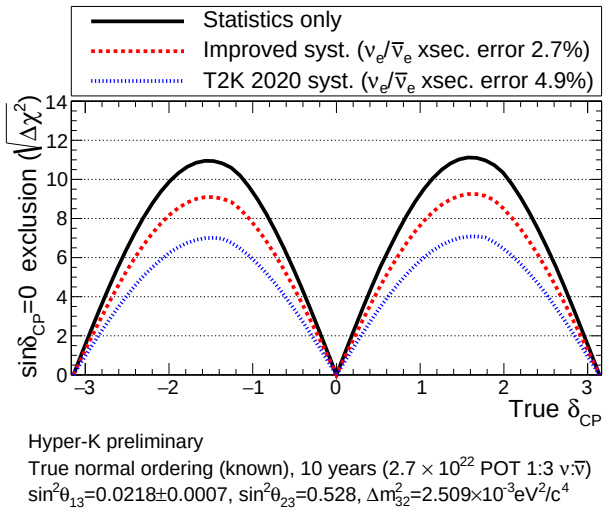

Figure 7.8: The $\sin\delta_{CP}$=0 exclusion as a function of true δ_{CP} after 10 years of operation under different systematic uncertainty models [141]

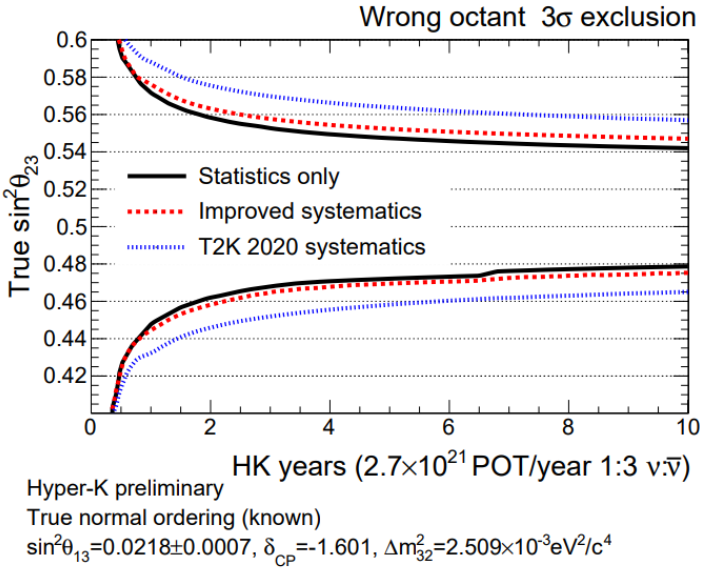

Figure 7.9: Wrong octant exclusion as a function of true $\sin^2\theta_{23}$ under different systematic uncertainty models and years of operation [141].

As matter effects enhance this result, experiments with a long baseline will be more sensitive to determining the mass ordering. The baseline of the T2HK experiment will be comparatively small, 295 km, and the use of other non-accelerator sources, such as atmospheric neutrinos, will enhance Hyper-K's ability to determine the mass ordering. As degeneracies between the measurement of δ_{CP} and the mass ordering exist, it is important that the mass ordering is determined to make a robust measurement of δ_{CP}. By combining data from accelerator and atmospheric neutrinos, the Hyper-K experiment will be capable of making precise measurements of many of the oscillation parameters.

7.4.2 Astrophysical Source Detection

By separating atmospheric neutrino data samples into both neutrino-like and antineutrino-like samples, it will be possible to exploit the enhancement in oscillation, due to matter effects, to determine the mass ordering. If samples of up-going electron neutrinos are selected, additional resonances which occur due to the normal ordering will be evident in the flux spectrum as is shown in figure 7.10.

Atmospheric neutrino samples will be separated according to their flavour, using the shape of the Cherenkov ring, and for higher energy events it will be possible to separate ν_e samples into neutrino and antineutrino-mode separately using statistical methods [142]. The neutrino mass ordering sensitivity after 10 years of operation is shown in figure 7.11.

Alongside oscillation analyses involving atmospheric neutrinos, the Hyper-K FD will be sensitive to measuring the properties of solar neutrinos. Although the solar oscillation parameters are known to a high precision, there remains a 2σ tension on

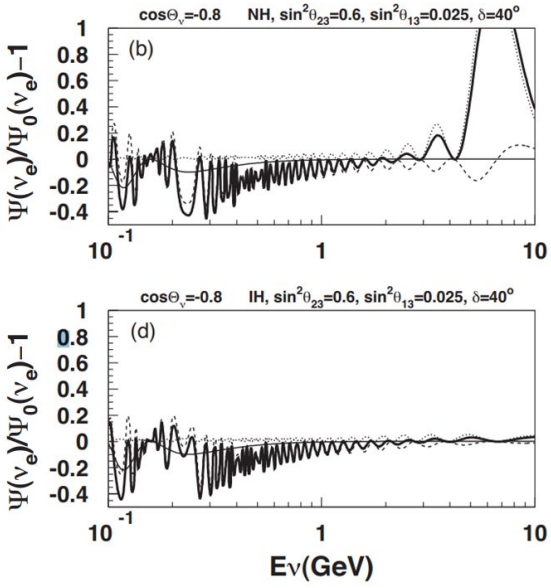

Figure 7.10: The ratio of the oscillated ν_e flux spectrum to the non-oscillated spectrum, as a function of the neutrino energy. Upward going neutrinos are selected with cosθ_ν = -0.8. The total flux is shown by the thick black line with various oscillation terms shown in dashed lines. The top plot shows the normal ordering and the bottom plot the inverted ordering, with all other oscillation parameters remaining constant [56].

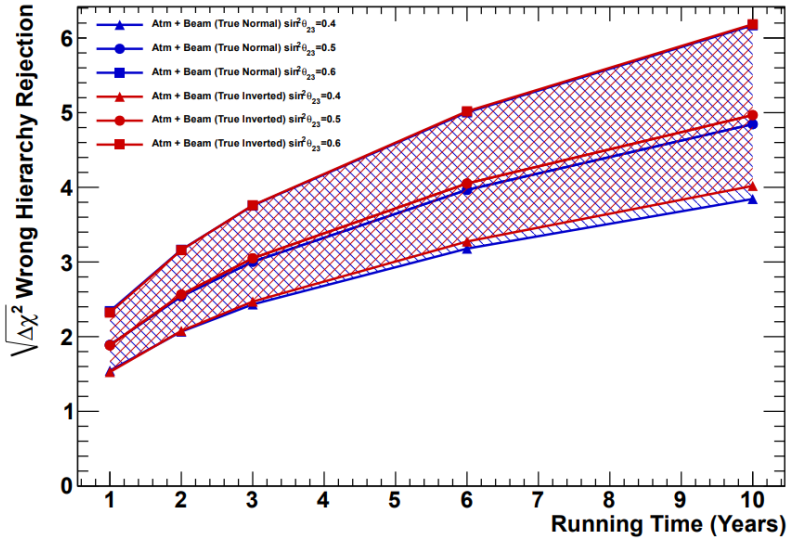

Figure 7.11: The neutrino mass ordering sensitivity using atmospheric and accelerator neutrino data, as a function of the time assuming $\sin^2\theta_{23} = 0.4$ (triangle), 0.5 (circle), and 0.6 (square). The blue (red) band denotes the normal (inverted) ordering [56].

the measurement of Δm^2_{21} between solar neutrino experiments and reactor experiment KamLAND [39]. This discrepancy arises from results by Super-K on measuring the day-night asymmetry that arises due to matter effects. Hyper-K is expected to measure the day-night asymmetry with precision between 4-5σ. Solar neutrinos also exhibit a phenomena known as the upturn in the survival probability. This upturn is due to a shift in the survival probability between the matter dominant energy region and the vacuum dominant region, due to the MSW effect. Understanding the shape of this upturn is important when excluding exotic models to explain neutrino oscillations. Hyper-K should be able to measure this upturn in the energy spectrum to the 3σ level.

The Hyper-K FD will be equipped to detect a variety of other astrophysical sources, such as supernova neutrinos. Supernovae are formed during the final stages of a star's lifetime. A supernova may be created when a white dwarf star reignites its nuclear fusion

process, where the star's temperature has increased allowing accretion, gravitational attraction of matter into a massive object, or stellar collision, where a binary companion merges. Alternatively a supernova may also occur if a massive star suddenly undergoes a gravitational core collapse. This process occurs once the fusion of iron begins: when the fusion energy produced is not enough to counteract the effects of the star's own gravity [143]. The energy released by a supernova is one of the most energetic phenomena in the Universe. Approximately 99% of the energy released during a supernova burst will be carried away by neutrinos. These will largely escape through the outer layers of the star without disturbance due to the small weak interaction cross section with matter, making neutrinos the perfect probe into the inner workings of a supernova collapse. To date, only one supernova neutrino burst has been detected. The supernova, SN1987a, was detected in 1987 by the Kamiokande, IMB, and Baksan experiments [144] [145] [146]. The neutrinos were detected primarily via inverse beta decay interactions and ν_e scattering. These experiments only detected 25 supernova neutrino events combined, whereas due to Hyper-K's increased FV, and updated technologies, far many more neutrinos are expected to be detected from an equivalent supernova, as is shown in figure 7.12.

The remaining 1% of energy released during the core-collapse is emitted as optical light, which is of great interest to astronomers. There may be a time delay between when neutrino experiments detect the supernova neutrinos and when astronomical telescopes observe the light from the event, due to the explosion mechanism of the supernova, as the neutrinos exit the core of the collapsing star. If a premature signal from neutrinos were present, a warning system from neutrino experiments may alert astronomers that a supernova event was about to occur and provide directional information within 1°, to aid

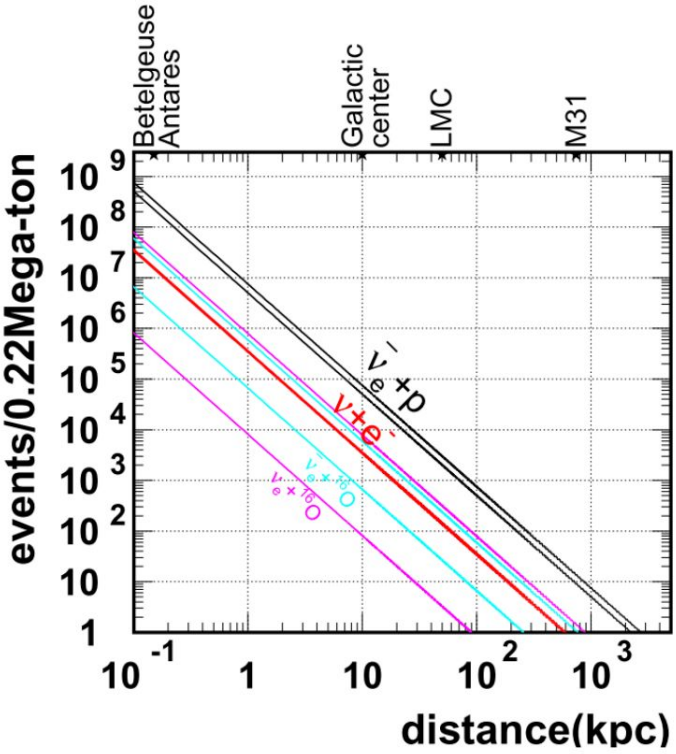

Figure 7.12: The expected supernova event rate for each neutrino interaction type as a function of the supernova distance. The bands show the variation due to neutrino oscillation parameter choices [56].

in pointing telescopes to the correct location [147]. Astrophysicists will also be able to analyse the characteristics of the supernova using reconstructed neutrino information. Comparing various theoretical supernova models and measuring the distance of the supernova will all be possible depending on the number of neutrinos observed. For example a 10 kpc galactic supernova will produce between 54,000 - 90,000 neutrino events in the Hyper-K FD in the span of a few tens of seconds [148].

In addition to the supernova neutrinos from core collapse that are yet to be observed on Earth, the relic neutrinos from past supernovae are still present and observable. These neutrinos are referred to as supernova relic neutrinos SNR or the diffuse supernova neutrino background. Supernova neutrino data is used to better understand the creation of heavy elements during stellar formation. This background is yet to be observed at experiments such as Super-K due to their low flux and energy.

7.4.3 Nucleon Decay Searches

The Hyper-K experiment will continue the search of its predecessor: Kamiokande and Super-K, to observe the decay of a nucleon, the original purpose of Kamiokande [19]. Nucleon decay is an important aspect of the Sakharov conditions which describe the formation of the Universe. One of the conditions states that baryon number must be violated. Nucleon decay observation is only possible if the baryon number is violated, and it is therefore an important probe to proving this condition is satisfied. The Standard Model does not predict baryon number violation, but other theories such as the Grand Unification Theories do. These theories also often include mechanisms in which neutrinos have mass. The lifetime of a proton in such a theory would be in excess of 10^{30} years [149]. The large FV of Hyper-K will be of great benefit in such a

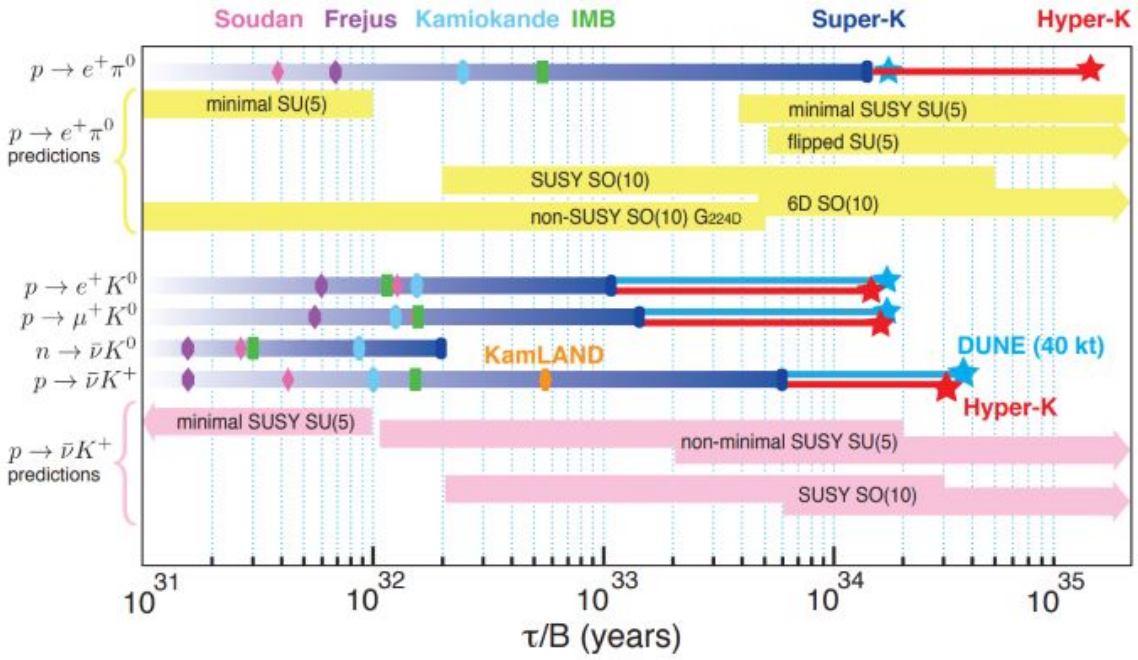

Figure 7.13: The experimental limits on the rate of nucleon decay as set by historic experiments, and predicted limits for the Hyper-K experiments [150].

search due to the low number of signal events anticipated, although the importance in reducing backgrounds will be evident in such a study. Hyper-K expects to be sensitive to a variety of decay channels, such as $p \to e^+\pi^0$ and $p \to \bar{\nu}K^+$. The sensitivities for various channels is shown in figure 7.13.

Chapter 8

Data Rate Calculations

Once the Hyper-K FD becomes operational, it will be expected to read out data continuously for its lifetime. The DAQ system must be capable of processing a continuous flow of data, and also peaks of higher rates of data. The system will read out the detector output, known as the instantaneous data rate, and will process this output via a sophisticated triggering sequence to decide whether or not the data should be saved to disk, the triggered data rate. It should be robust in both capabilities for all event types. A diagram showing the flow of data through the DAQ system is shown in figure 8.

In this study to determine the data rate of each source, for each PMT type: ID 20" PMT, OD PMT and mPMT; the hit rate was first estimated. The hit rate refers to the

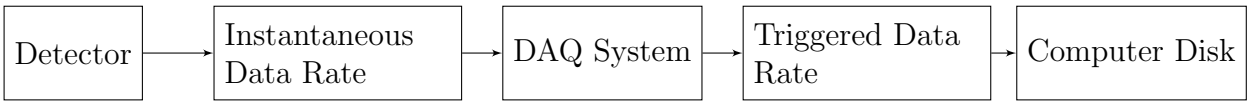

Figure 8.1: Diagram of the data progression from detector to being saved to disk.

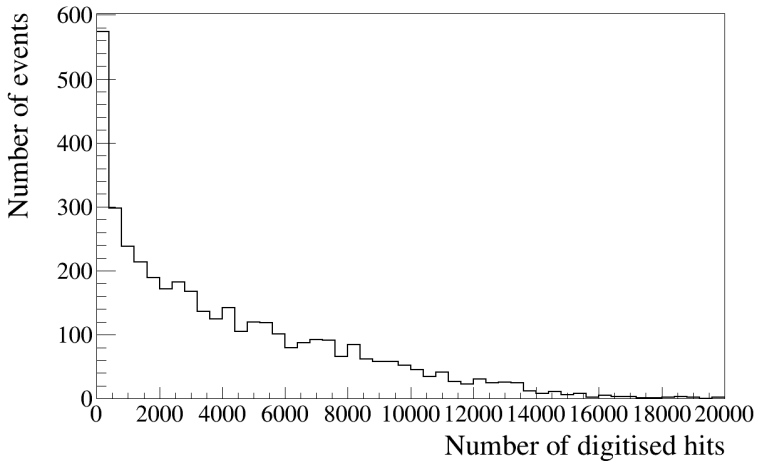

Figure 8.2: The number of digitised hits detected by the 20" PMT for simulated beam neutrinos which have undergone oscillation.

rate of the total number of digitised hits detected by the PMTs during operation. For some categories of events this was based on simulation, for example beam events, and experimental results were used in other cases such as dark noise. Two separate estimates were made for the hit rate: the average and maximum rates. In the case of simulation, the average was taken as the mean of the digitised hit distribution, discounting events with no hits, and the maximum was the right-most bin containing events of the plot. An example of a NHits distribution used for beam neutrinos is shown in figure 8.2.

This calculation produced a conservative estimate of the data rate as the DAQ system must be over-designed rather than under-designed, so that raw data will not be lost, even in a 'worst-case scenario'. When using simulations to calculate the hit rate, a series of DAQ parameters were set. As all electronic parameters are not yet final, a conservative value was set for unknown parameters. The integration window, the duration of time saved by the electronics after a pulse is recorded, was known and set to 200 ns. The dead time, the time taken to digitise the data before becoming ready for

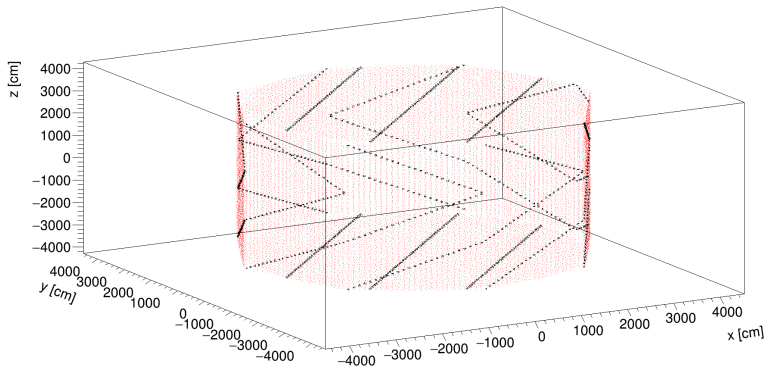

Figure 8.3: Simulation of the Hyper-K FD. The red points indicate 20" PMTs, and the black the clusters of 3" PMTs forming a singular mPMT. The placement of the mPMTs is inaccurate and should be evenly distributed in a similar way to the 20" PMTs.

data taking at the next trigger, was set to 0 ns. Setting the dead time to 0 ns, meaning the data is constantly being read out without intermission, was unrealistic, but does provide the most conservative estimate given the value was not known. To convert the hit rate to a data rate, a conversion of 12 bytes per hit was assumed for all PMT types.

A caveat of this work relates to the simulation of the mPMT position in the detector. The mPMTs should be evenly distributed across the ID, however due to limitations in the capabilities of the computing software this was not possible. A number of mPMTs was set in WCSim, and they were then arranged by cells and constrained to produce stripes of mPMTs as can be seen in figure 8.3. A cell is defined as a flat modular detection section [151]. These cells are used to configure the curvature of the detector, but may contain more than one PMT per cell.

The impact of this incorrect simulation on the mPMT data rate calculation was a decrease in the true hit rate. It is therefore important that when the software is updated with a more realistic mPMT placement, the mPMT simulations be repeated to ensure the data rate does not increase significantly.

Another limitation was that the number of mPMTs set in the simulation has a lower bound of 866 mPMTs which is likely greater than the final number installed. This results in a slight inflation of the data rate, due to the additional mPMTs.

8.1 Event Types of Interest

This section describes the sources of data which the FD must process. It considers the sources which produce the most data on average. Sources such as atmospheric neutrinos are expected to occur at a rate of a few per day, and therefore were not included in this analysis.

8.1.1 Beam Neutrinos

As detailed in chapter 7, the J-PARC neutrino beam will increase its spill frequency to 0.86 Hz [152]. It was assumed that each spill will produce a neutrino interaction at the FD. Simulations of these beam neutrinos were used to estimate the number of hits detected per event. The neutrinos were generated assuming the Hyper-K flux, where the hadron-focusing horn current is 320 kA, which were then passed to NEUT [93] using a simple detector geometry (cylinder of water) to simulate the neutrino interactions. Figures 8.2 and 8.4 show the NHits distribution and the simulated track energy.

Neutrinos are produced by the beam with a fixed energy distribution. However, after travelling to the FD and oscillating the neutrinos at the peak of the distribution will have oscillated into other flavours, resulting in a depleted energy peak. As the experiment was designed such that oscillation is maximal at the energy peak, the tails of the energy distribution will not be impacted by this effect as greatly, driving the average

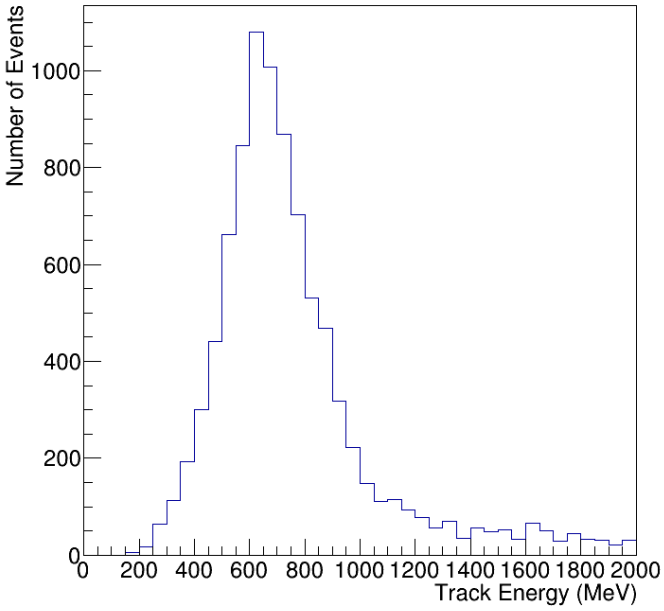

Figure 8.4: The energy of the charged lepton track as reconstructed by WCSim following a beam neutrino interaction.

energies to higher values. To account for this effect, the neutrino energy distribution was weighted to account for maximal oscillation from $\nu_\mu \rightarrow \nu_e$. In theory, neutrino oscillations will also decrease the rate of beam neutrinos producing events, however, this was not factored into the calculations, to ensure a conservative rate.

8.1.2 Cosmic Muons

A simulation of 10,000 cosmic muons, as described in section 7.2.1, was used to estimate the hit rate. A cosmic muon rate of 45 Hz is expected at the FD [134]. This simulation only contained single-muons, and no multi-muon events. Multi-muon events, where more than one muon enters the detector at the same time, and the muon tracks are all parallel and in coincidence, will generate more hits than a single event. Their omission from this work will shift the mean to lower values, however the maximum number of hits was set to 30,000 hits, which is more than one hit per PMT in the 200 ns time window. It was hoped that this maximum hit value will provide an estimate of a multi-muon event, as the average number of hits from one cosmic muon was approximately 7500 hits, so this maximum value is four times greater than the single muon average. This was also without considering correlations in the energy of the muons during multi-muon cosmic showers, and overlaps of hits in the same time window. However multi-muon cosmic muon simulations should be added to this work when available.

8.1.3 Radioactivity

Trace amounts of naturally occurring radioactivity are expected to be present in the water and detector materials. These arise from long-lived naturally occurring isotopes ^{238}U, ^{232}Th which decay to stable isotopes via long decay chains. Backgrounds are

Source	Activity (Bq)	
	ID 20 ” PMT	OD PMT and 3” PMT in mPMT
Bi-214 in PMT	25.5	2.0
Tl-208 in PMT	8.36	2.0
K-40 in PMT	17.6	3.2

Table 8.1: Radioactivity sources considered and expected activity calculated based on studies conducted by the subgroups at Hyper-K [153] [154]

dominated by ^{214}Bi and ^{208}Tl from those chains (respectively) and these will contribute to the observed event rates as they have relatively high end points (3.27 MeV and 4.99 MeV respectively). The PMT units and the water will likely contribute the largest amounts of these sources of radioactivity. Four dominant sources of radioactivity were considered for this work. Sources with lower rates or which produce a negligible number of hits were omitted from the sources of interest. The ^{214}Bi in the entire water volume had an activity of $\sim$300 Bq. Only ID hits from radioactivity in water were considered as the number of hits from the OD PMTs and mPMTs from this source was negligible. The three sources from the PMT glass and their activities are listed in table 8.1.

The activities were calculated using experimental measurements. At the time of this work, the OD photosensing unit radioactivity calculation was not complete. As the OD photosensing unit will contain 3” PMTs, results from measurements of 3” PMTs from the mPMT group were used to provide an estimate. To determine the hit rate, these activities were added to the simulation software. For the PMTs it was only radioactivity from the PMT glass which was considered. The event vertices were not simulated from the WLS plate or PMT covers as the majority of detectable radioactivity will be from the PMT due to the proximity of the glass to the photosensor relative to the WLS plate or cover.

PMT Type	Number of PMTs in Detector	Average Rate per PMT (kHz)	Maximum Rate per PMT (kHz)
20" ID	20,000	10	10
3" OD	7200	1	1
mPMT	820	5.7	9.5

Table 8.2: Average and maximum measured dark noise rates for each PMT type.

8.1.4 Dark Noise

Experimental results were used to estimate the contribution from dark noise. A separate dark noise measurement was made for each of the three separate PMT types as is seen in table 8.2. The dark noise hit rate was determined to be the dark noise rate per PMT multiplied by the number of each PMT type in the detector.

8.1.5 Supernova

Thus far, the sources discussed were expected to produce a constant rate of hits. A supernova event would likely only occur once, if at all, during the lifetime of the detector, given the only other case of supernova burst neutrino detection was in 1987 [144]. The FD should be prepared for such an event at any point in its lifetime. During a supernova burst event, a large flux of neutrinos will arrive at the detector in a short time window of approximately 20 s. The closer the supernova is to the Earth, the higher the expected flux of neutrinos. Figure 8.5 shows the digitised hit time for a 10 kpc supernova.

Therefore it is the nearest supernova candidate which the DAQ system must be designed to accommodate. The nearest supernova candidate is Betelgeuse which is at a distance of 200 pc. There is no simulation of Betelgeuse due to the large computation resources required to process such an event, meaning extrapolations must be made from other simulations already available, for supernovae further away. Using a simulation of

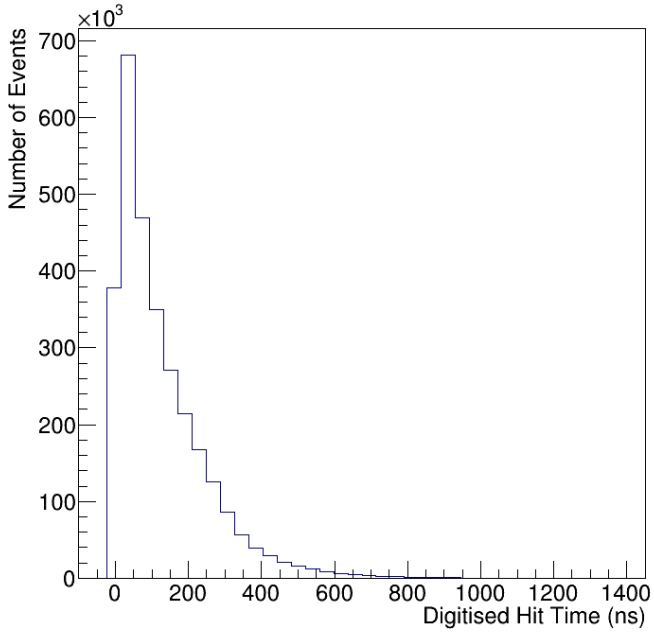

Figure 8.5: Digitised hit time of neutrinos produced by a 10 kpc supernova.

Supernova Distance	Average Hits per neutrino interaction	Average Hits Total
10 kpc	127	3.2×10^6
200 pc	127	8.0×10^9

Table 8.3: Supernova neutrino hits per PMT type as determined by simulation and extrapolation to nearer distances. Simulation at 200 pc is not possible.

a 10 kpc supernova, assuming the Nakazato model, it was possible to extrapolate to the number of hits from a 200 pc supernova using a $\frac{1}{r^2}$ dependence on the total supernova neutrino hits to distance, r [155]. The 10 kpc supernova simulation contained 25,000 neutrinos which were all detected within 20 s. The supernova trigger will read out longer than the 20 s of expected neutrino events to ensure all data is recorded as detailed in 7.3.2, however for this analysis it was assumed all physics events related to the supernova occurred in 20 s. The hit rate for both the 10 kpc supernova and extrapolation calculation for a 200 pc supernova is seen in tables 8.3 and 8.4].

Supernova Distance	Average Hits Total (20" PMTs)	Average Hits Total (OD PMTs)	Average Hits Total (mPMTs)
10 kpc	3.2×10^6	4.8×10^5	6.9×10^4
200 pc	8.0×10^9	1.2×10^9	1.7×10^8

Table 8.4: Supernova neutrino hit extrapolation using $\frac{1}{r^2}$ dependence on the total supernova hits to distance, r. The 200 pc supernova represents the nearest supernova candidate: Betelgeuse.

8.2 Peak Data Rate

The DAQ system must be capable of reading out data from every PMT when fired at the same time. This does not represent a likely physics case, although a supernova event could lead to a lot of activity in a short space of time. The DAQ system should be designed to accommodate such an occasion. This scenario represents the peak amount of data possible, totalling 0.52 MB. Within the integration window of the digitisers of the electronic boards, 200 ns, this would correspond to a peak rate of 2.6 TB/s. The constraint on the DAQ system which will be most strained in this peak is the DAQ links: the 60 RBUs, which are detailed in section 7.3. They are the first step in the DAQ, and receive the raw data. If each link, providing 20 Gb/s of data read out, were saturated, 150 GB/s could be read out. To buffer the maximum hypothesised data rate of 2.6 TB/s, the RBUs must buffer information for 17 s.

8.3 Instantaneous Data Rate

The majority of Hyper-K's FD operation will expect a stable rate of input data. The instantaneous data rate represents the average data read out by the DAQ system at any given point in time. Once this data has been received, it will be sent to the triggering system to decide whether or not the data should be saved to disk or discarded. The

	20" PMT Data Rate		OD PMT Data Rate		mPMT Data Rate		Total Data Rate	
	(GB/s)	(TB /day)	(GB/s)	(TB /day)	(GB/s)	(TB /day)	(GB/s)	(TB /day)
Average	2.5	212	0.06	5.0	0.04	3.5	2.5	220
Maximum	2.7	232	0.12	10.5	0.09	8.0	2.6	250

Table 8.5: Percentage of each PMT type and source when determining the detector instantaneous data rate.

DAQ system aims to reduce the size of the data rate through the use of triggers, so that only interesting physics events are saved, while simultaneously rejecting backgrounds. The instantaneous data rate is calculated using:

$$\text{Instantaneous Data Rate (B/s)} = \text{Hit Rate}_{\text{all sources}}(\text{hit/s}) \times \text{bytes/hit (B/hit)} \quad (8.1)$$

where

$$\text{Hit Rate}_{\text{all sources}} = \text{Hit Rate}_{\text{beam}} + \text{Hit Rate}_{\text{cosmic}} + \text{Hit Rate}_{\text{dark noise}} + \text{Hit Rate}_{\text{radioactivity}}$$

and bytes/hit = 12.

The average and maximum instantaneous data rates for all three PMT types can be seen in table 8.5.

The dominant PMT type producing the instantaneous data is expected to be the 20" ID PMTs, with the dominant source of data coming from dark noise, as can been seen in figure 8.6. The average data rate of the FD is expected to be between 2.5 and 2.6 GB/s.

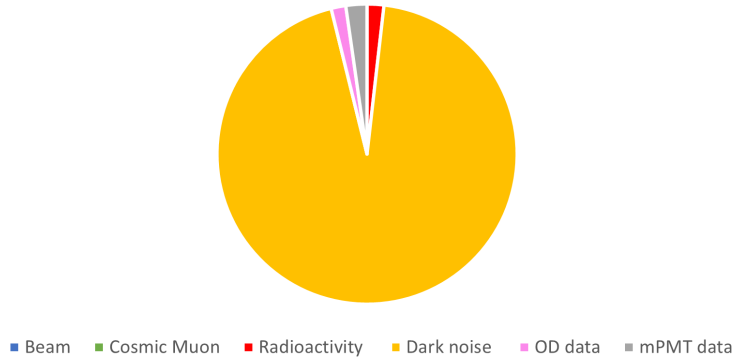

Figure 8.6: Instantaneous data rate contributions from various data types for all three PMT types.

8.4 Triggered Data Rate

The triggering system can be summarised into three different trigger types: low energy, cosmic muon and beam. Each trigger has a different DAQ window of data saved. The low energy trigger aims at reading out solar and atmospheric neutrino type events, but the majority of the unavoidable background coincidentally detected will be from dark noise and radioactivity events with a DAQ window of 1.5 μs. The cosmic muon trigger will include data from cosmic muons, and background from dark noise and radioactivity with a length of 50 μs. The final beam trigger will include data from beam events, and background from cosmic muons, dark noise and radioactivity: it will read out 1 ms of data. The rate of low energy triggers will be dictated by the rate of false triggers which is set to 10 kHz according to the trigger architecture described in section 7.3.1. It was also assumed that every cosmic and beam trigger produced will be issued and saved. Therefore for every 1 s of data which the detector reads out, only 18 ms of the data will be saved to disk, as is demonstrated in figure 8.7.

To determine the rate of each trigger the following equation was used, with the

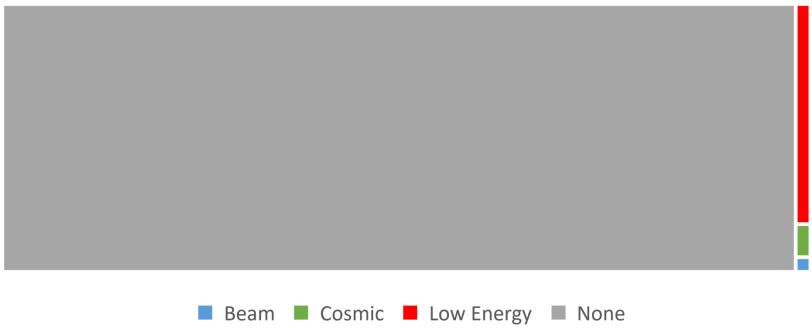

Figure 8.7: Fraction of each trigger type read out in a second. Less than 2% of the data is expected to result in a trigger.

beam case, Data Rate$_{(b)}$, used as an example:

$$\begin{aligned} \text{Data Rate}_{(b)} &= \text{Events Rate}_{(b)} \times \text{Hits}_{(b)} \times \text{B/hit} \\ \text{Hits}_{(b)} &= \text{Hits/Event}_{(b)} + t_{(b)} \times \begin{bmatrix} \text{Hits Rate}_{(r)} + \\ +\text{Hits Rate}_{(dn)} + \\ +\text{Events Rate}_{(c)} \times \text{Hits/Event}_{(c)} \end{bmatrix} \end{aligned}$$

where B/hit is Bytes/hit = 12, Events Rate$_{(b,\ c)}$ = Rate of beam or cosmic muon events respectively, Hits/Event$_{(r,\ dn)}$ = Hit rate for radioactivity, dark noise respectively, $t_{(b)}$ = DAQ window for beam trigger = 1 ms. A summary of the calculated triggered data rates for each trigger is shown in table 8.6.

A summary of the percentage of each trigger type saved to disk can be seen in figure 8.8 assuming that data was read out continuously at the specified rates, with beam every day of the year.

The dominant trigger type saved to disk is expected to be the low energy trigger due to its acceptance rate of 10 kHz. The 20" ID PMTs read out the most data, with

	Low Energy		**Cosmic Muon**		**Beam**	
	Average	Maximum	Average	Maximum	Average	Maximum
20" PMT Data Rate						
(MB/s)	36.7	40.0	9.6	2.2	2.2	2.5
(TB/day)	3.17	3.45	0.8	1.9	0.19	0.2
OD PMT Data Rate						
(MB/s)	0.6	1.4	0.3	1.1	0.04	0.2
(TB/day)	0.05	0.12	0.02	0.1	0.003	0.013
mPMT Data Rate						
(MB/s)	0.9	1.8	0.5	2.4	0.05	0.3
(TB/day)	0.08	0.15	0.05	0.2	0.004	0.02
Total Data Rate						
(MB/s)	38.2	43.1	10.4	25.7	2.2	2.9
(TB/day)	3.3	3.7	0.9	2.2	0.2	0.3

Table 8.6: Triggered data rate per PMT type for each of the three trigger types.

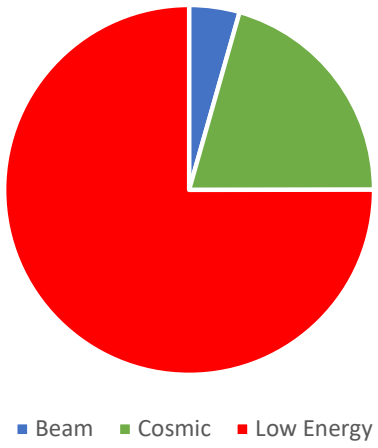

Figure 8.8: Percentage of data saved to disk which arises from each of the three primary trigger types.

a smaller comparative amount of data read out by the OD PMTs and mPMTs. The cosmic muon trigger had the largest variation in data rate, from 10. to 25.7 MB/s as the average and maximum data rates, respectively. This variation was due to the large difference in the amount of hits cosmic muons produce due to their broad direction and energy spectrum.

8.5 Supernova Trigger

The final trigger type considered was the supernova trigger, which is independent of the other DAQ triggers. The DAQ window was assumed to be 20 s as described in section 8.1.5. The trigger will read out the supernova signal events, alongside any other sources: beam, cosmic muon, dark noise and radioactivity. Although it is expected that the dominant source will be from supernova events. In the case that Betelgeuse, a 200 pc supernova candidate, goes supernova, the data read out by the trigger would be between 0.2 and 0.7 TB of data. Any other supernovae further away than Betelgeuse, would produce less data. Were the DAQ window to increase, the amount of data read out by the trigger would increase. The trigger will read out on the order of hours of data, although the exact length will be specified at a later date. Therefore, an additional check was made to see how much data would be recorded were a supernova trigger issued with an additional hour of raw data, with no supernova, also saved to disk, as seen in figure 8.9.

Were an hour of data read out alongside the supernova events, the other sources of data become more dominant. For an hour of data, and a 200 pc supernova burst, between 9.3 and 10.6 TB of data would be read out. After the initial supernova burst, the activity will return to normal levels where dark noise becomes the dominant source.

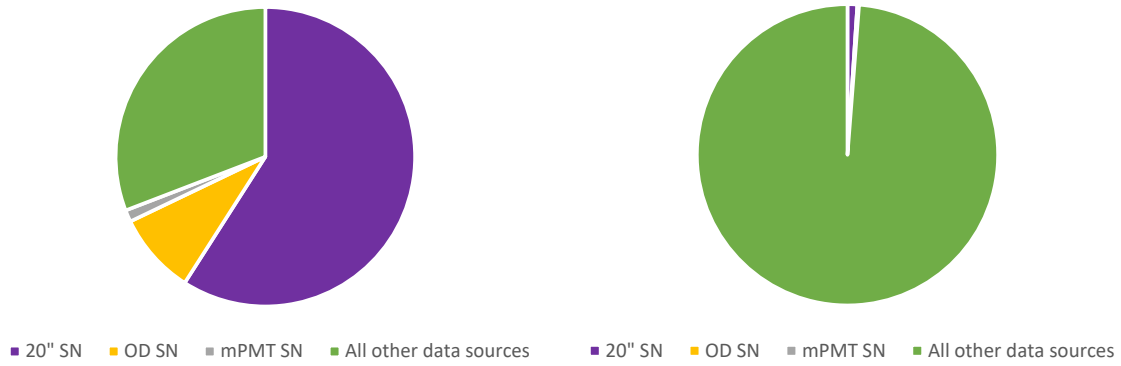

Figure 8.9: Percent contribution of different data types in a supernova trigger. Left plot shows data taking for 20 s, and right plot for an hour of data saved.

8.6 Conclusion

It is important that the DAQ system has been designed to handle all sources of signal and background which the detector will detect. In this chapter both the detector output and the triggered output data rates were evaluated to ensure redundancy was considered in the design of the system for all signal sources. It is important that data rate calculations are repeated during the design phase of the detector as various aspects of the detector design evolve. During this period, the data rate read out by the detector may change, and it is important that the DAQ system is modified appropriately according to the developments.

Chapter 9

Outer Detector Failure Scenarios

The OD of the Hyper-K FD must perform reliably for the lifetime of the experiment. It is therefore important to ensure the longevity of the OD in its design. There are two ways that an OD PMT may fail: the first from random PMT failure occurring for a variety of mechanical or electronic issues. The second reason is if its corresponding electronic canister stops working. In this case, multiple PMTs would fail and a region of the OD would have lower PMT coverage. The work in this section describes the way the OD has been designed to mitigate these losses.

9.1 Random PMT Failures

The Hyper-K OD PMTs will be recent models, and tests of their longevity and stability are ongoing. To evaluate the Hyper-K PMT failure rate, conservative estimates were made based on information from the Super-K experiment. Following the refurbishment of the Super-K detector in 2006, the detector has observed an OD PMT failure rate of less than 0.5% per year [85]. The primary causes of OD PMTs failing in Super-K were

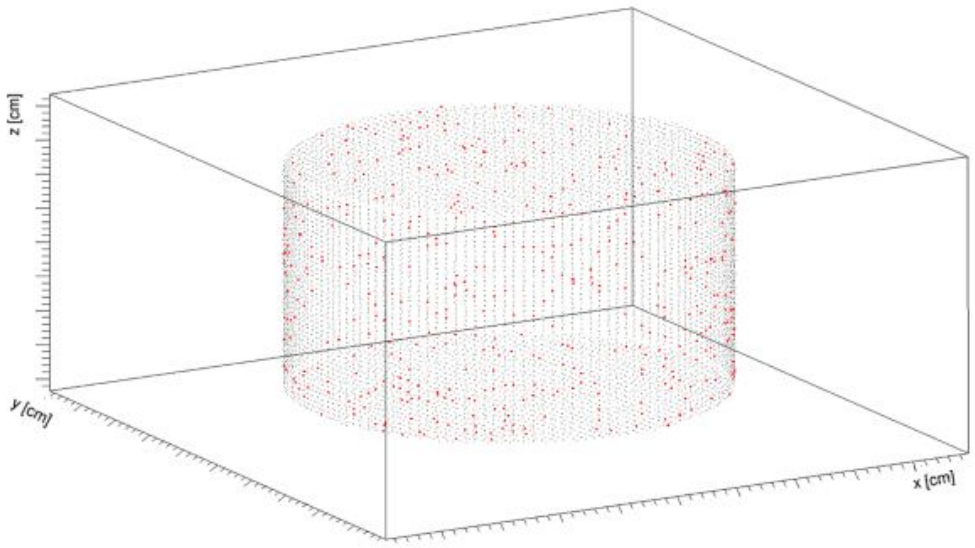

Figure 9.1: Simulation of the Hyper-K OD with randomly selected failed OD PMTs, corresponding to 5% of the OD PMTs, shown by red dots; the black dots mark the position of the remaining active OD PMTs.

from flooding of the base housing (70% of cases), and the PMT becoming a 'flasher' - where internal electric discharges generate optical radiation and electrical noise. If the PMT becomes a 'flasher' it is masked out (27% of cases), meaning data from the PMT is no longer included in physics analyses. The PMT is also masked out by the DAQ system if no signal is observed, due to failures. It can be assumed that using a 0.5% failure rate per year is a conservative estimate for the Hyper-K OD, as newer technologies should mitigate these issues, thus reducing the PMT failure rate. Under the assumption that the FD will be operational without intervention for at least ten years, it can be estimated that approximately 5% of the OD PMTs will have failed after ten years. As each failure in this instance would be independent, a random distribution of failed PMTs was anticipated as was simulated in figure 9.1.

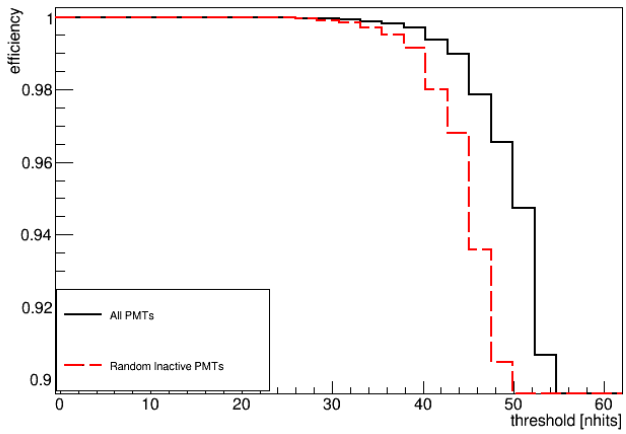

Figure 9.2: The muon detection efficiency with a fully active detector shown in black, and a partially instrumented detector, with 5% of PMTs randomly selected and made inactive, shown in red.

In section 7.2.2, the OD cosmic muon tagging method was described. The muon detection efficiency was determined based on the muons tagged using this method. The detection efficiency was then compared between different failure scenarios, as a measure of the impact of various scenarios on the ODs cosmic muon detection. In figure 9.2, a plot of the muon detection efficiency with a fully instrumented detector, and also an aged detector where 5% of PMTs have randomly failed is shown.

When the fully instrumented, no failure scenario, NHits threshold was calculated, the maximum value which retains a 100% detection efficiency is NHits = 35. The efficiency was defined as the percent of cosmic muons which are simulated that are also tagged by the OD. If an equivalent NHits threshold was used for the aged detector, where random PMT failures are considered, 0.1% of cosmic muons would be missed using this clustering technique. To regain these missed muons in the aged detector, and achieve 100% detection efficiency, the NHits threshold would have to decrease by 10 hits, to 25 hits. This reduced NHits threshold is still well above the dark noise

expected, therefore the detector will be capable of performing consistently even when aged, when only considering this source of failure.

9.2 Electronic Canister Failures

In addition to PMTs failing as the detector ages, the electronic canisters which read out the OD PMTs will be subject to failures. In the original baseline design each electronic canister would readout 72 OD PMTs (or 64 OD PMTs) each. These PMTs would all be clustered to a region due to constraints from the cabling. When this study was conducted, the OD electronic canister was designed to be independent of the ID electronics; however conclusions from this study motivated combining the OD and ID electronics into a single electronic canister. Therefore, the 72 OD PMT (and 64 OD PMT) per canister design used in this work, reflect older designs no longer considered by the experiment.

Several design features of the OD will make it resilient to failures of these electronic canisters. The Tyvek surrounding the OD walls will allow the light produced by a muon to be detected across a broader region, approximately 10 m, of the detector. To mitigate instances where a canister, and therefore multiple PMTs, fail, interleaving of PMTs to adjacent electronic canisters will increase the partially instrumented area during failures, rather than having holes of entirely un-instrumented detector. A caveat of introducing interleaving will be the increased cable length required: which inflates both cost and radioactivity. An example of a proposed, two-fold, interleaving pattern is shown in figure 9.3. By introducing interleaving, the loss of one electronic canister will not result in a block of PMTs all failing. In the example shown above, it would result in half of the PMTs being lost, which will improve detection efficiency for cosmic

Figure 9.3: An example of an interleaved pattern referred to as two-fold interleaving. A cell uses a 4x4 chequer board pattern, where blue diamonds (showing a single PMT) are connected to one canister, and grey diamonds are connected to a second, independent, electronic canister.

muons which leave hits in this half-instrumented region.

It is possible to introduce more interleaving referred to as n-fold interleaving, where n is the number of canisters instrumenting a small region of PMTs. One-fold interleaving corresponds to no interleaving and two-fold interleaving to the pattern shown in figure 9.3. The area which a single canister instruments increases by n, and the density of PMTs readout by a single canister reduces by $1/n$. Due to the proposed installation procedures, the cable length will also increase as a factor of n.

To demonstrate the effect of introducing interleaving, an 8 x 8 PMT region on the topcap of the OD was selected. The same muons were simulated twice, with an altered detector instrumentation, as shown in figure 9.4. One had all PMTs in the 8 x 8 region inactive, and the other was half active according to the interleaving pattern shown in figure 9.3.

The muon detection efficiency for both of these scenarios is shown in figure 9.5. For the maximum threshold in the no failure scenario, i.e. at 35 hits, 1% of cosmic muons were missed without interleaving, but only ∼0.0015% were missed when interleaving

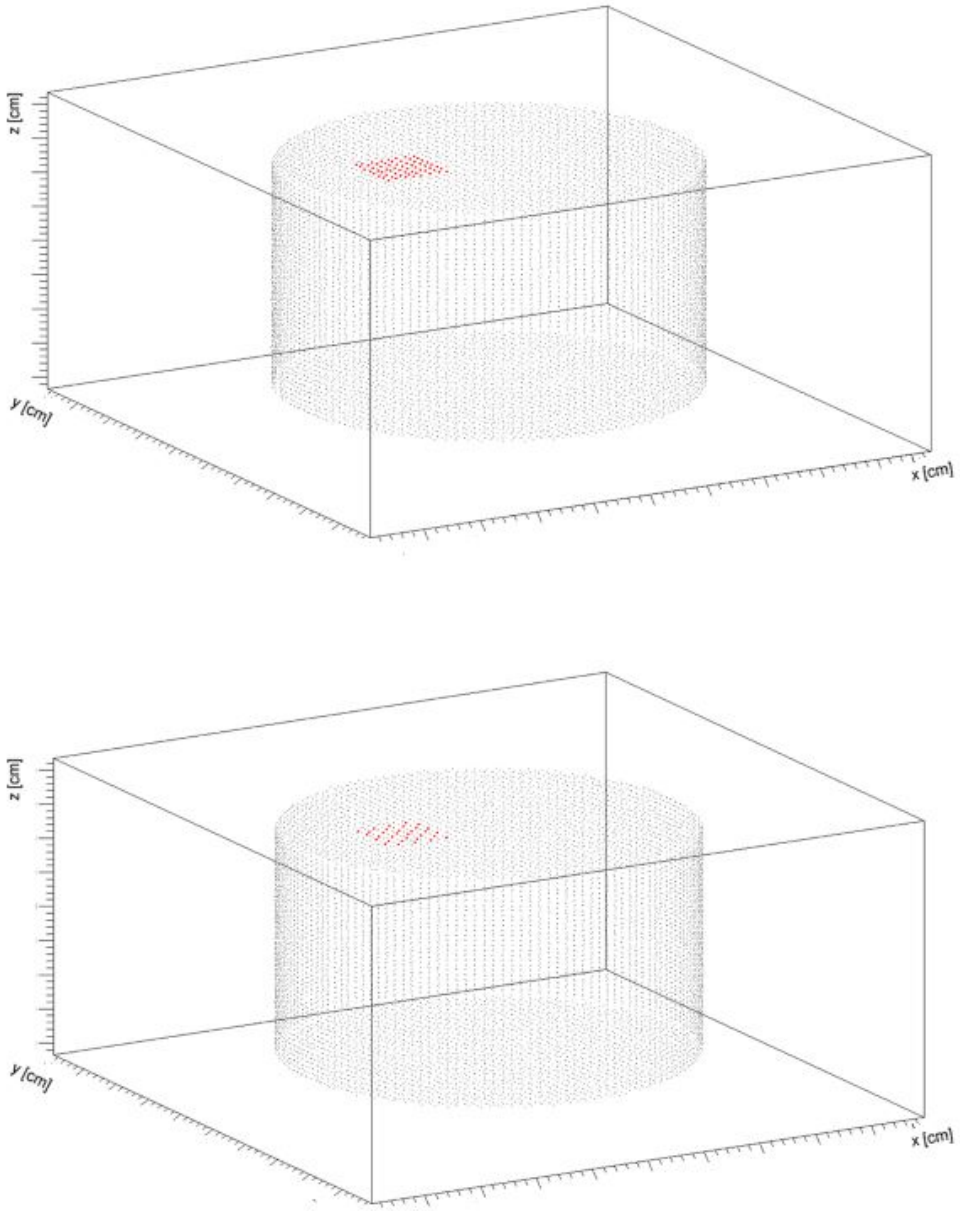

Figure 9.4: The top diagram shows an 8 x 8 region of PMTs on the OD topcap which are inactive. On the bottom, half of the same 8 x 8 region of PMTs on the OD topcap with the interleaved pattern implemented is made inactive. Inactive PMTs are shown with red dots; the black dots mark the position of the remaining active OD PMTs.

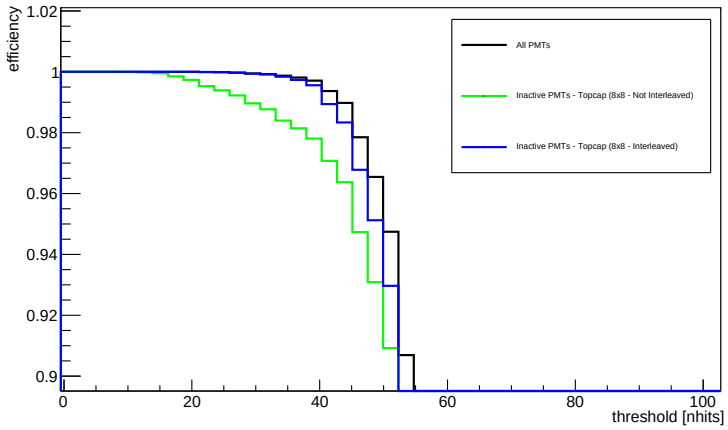

Figure 9.5: Cosmic muon detection efficiency when the 8x8 region is lost, with interleaving (blue), and without interleaving (green). Black line indicates case where all PMTs are active, and no failure has occurred.

was introduced.

A caveat of these results was that in reality, in the interleaved scenario the same number of PMTs would be lost as with the non-interleaved case. The additional PMTs lost would expand beyond the 8 x 8 region, which could lead to degradation in the detection efficiency. This study did not account for this and the effects of simply losing more PMTs between scenarios. However, as the seed of the cosmic muons simulation remained constant in both cases, the effect that interleaving has in general within a specified region could be analysed.

Due to the angular distribution of the incoming cosmic muons (typically downward-going), the topcap of the detector is most important to instrument. The rest of the work described in this chapter instead focuses on the barrel of the OD. This is due to the complexity in instrumenting the edge of the barrel region given it is a circle. It is important the edge of the topcap will be more densely instrumented so that corner clipping muons, which will not leave a signal in the ID, are observed. A more

complicated design for the topcap will likely be needed to mitigate failure scenarios, and they will be dependent on the final installation design of these PMTs.

The failure of a single electronic canister with interleaving will leave the detector without an entirely inactive region. However if multiple canisters instrumenting the same region were to fail, an inactive region would emerge. In the case of two canisters in the same region failing, the shape of the overlap between the canisters will vary, making the inactive region either square or rectangular, as shown in figure 9.6. In both cases, an equal number of PMTs would be inactive, and the number of PMTs in the overlapped region would also be equal.

The only difference between the two scenarios was the shape of the canister readout region and the shape of the overlapped inactive region. In figure 9.7 the effect of the shape difference is shown via the muon detection efficiency.

At almost all NHits thresholds, the more rectangular overlapped inactive region had a higher detection efficiency than the square case. This is because the Cherenkov ring for a muon is circular, and therefore more likely to be contained in the square inactive overlapped region, meaning it passes through the OD undetected or leaves fewer hits than a rectangular inactive region.

In addition to the shape of the overlap region, it is also possible to reduce the number of PMTs in the inactive section. There are construction limitations to this, and a smaller overlap region would result in longer thinner canister columns, meaning the cable length would also increase. However three column widths were considered in the detector design resulting in 16, 24 or 32 columns surrounding the barrel. Dependent on how many columns will be used, a series of different tiling options are present. Three different tiling options which result in two canisters overlapping are shown in figure 9.8.

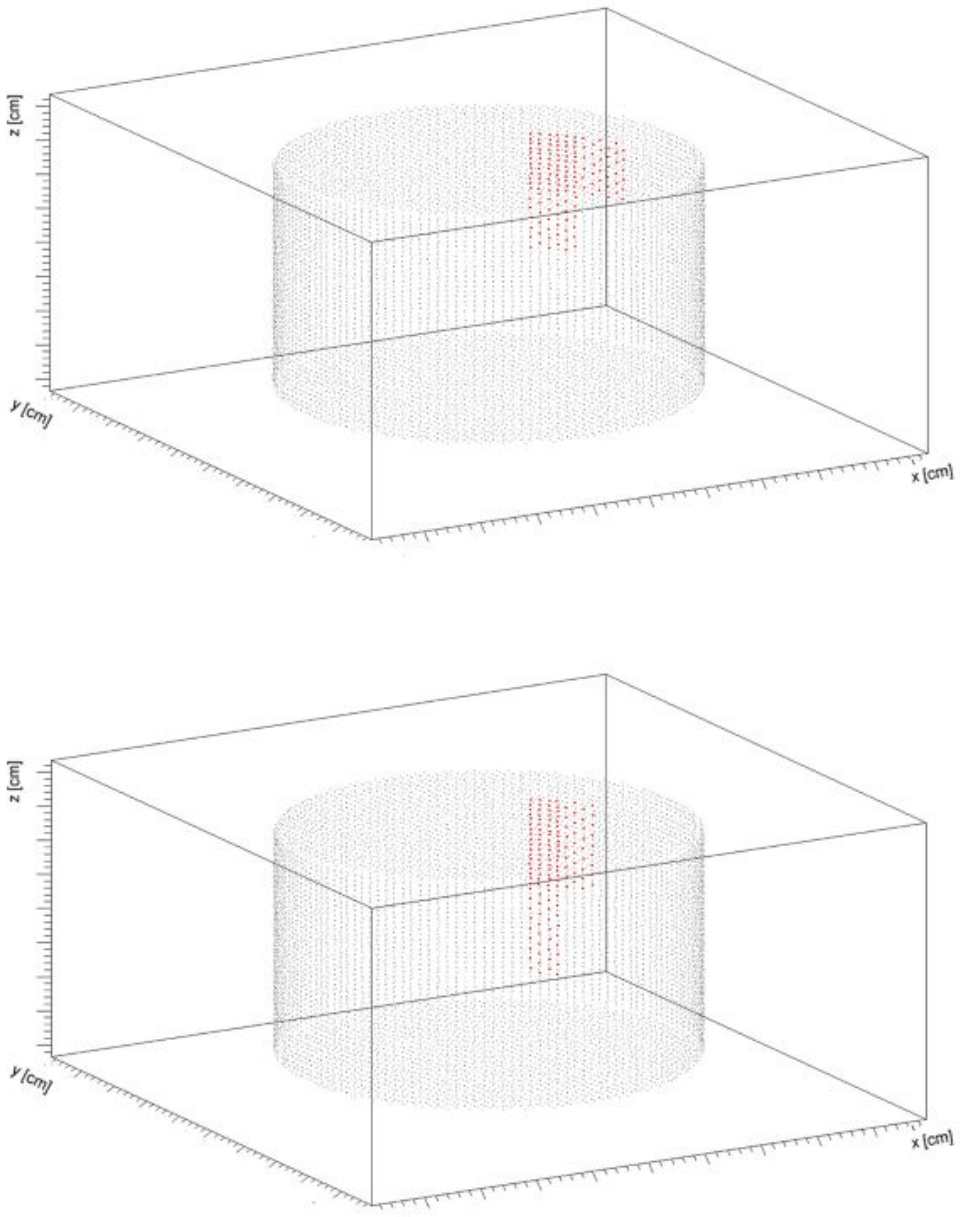

Figure 9.6: The left plot shows two failed interleaved canisters with the overlap forming a more square shape. The right overlap region forms a more rectangular shape. The red points indicate the inactive PMTs, and the black points the active PMTs.

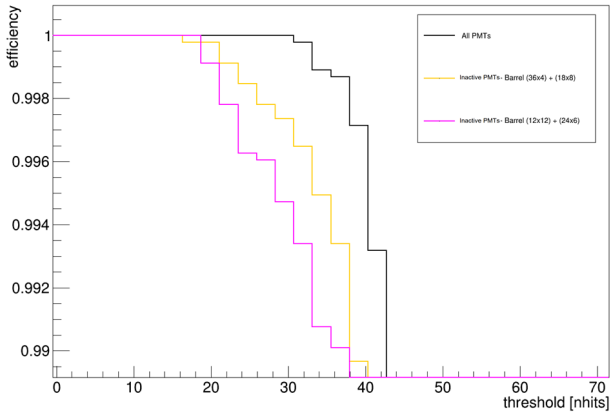

Figure 9.7: The cosmic muon detection efficiency is shown for the more rectangular region in yellow, the square case in pink, and in black the no failure scenario is shown.

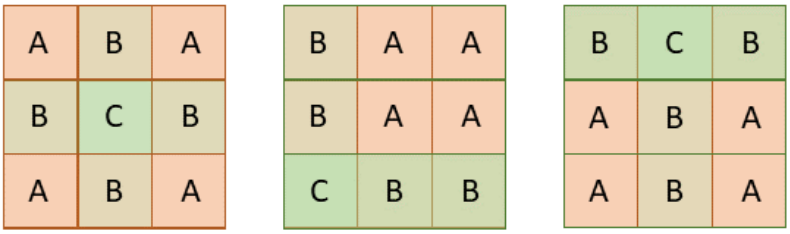

Figure 9.8: The three tiling options available in the 24 column scheme. The orange squares, labelled A, represent an unaffected, active PMT segment, the darker green, labelled B, shows a failed canister, and the lighter green, labelled C shows the overlap of two failed canisters. The left configuration is referred to as the cross-shape, the centre as the L-shape and the right as the T-shape.

An example of all three tiling schemes is shown in figure 9.9, with the top left diagram displaying the 'L' shape for the 16 column configuration with a 36 x 4 PMT and 18 x 8 PMT canister overlapping. The top right also shows the L-shape but in the 24 column scenario with a 36 x 4 PMT and 12 x 12 PMT canister overlapping. The bottom diagram in figure 9.9 shows another option in the 24 column case where the overlap is instead a cross shape. The cosmic muon detection efficiency for these scenarios is shown in figure 9.10. Following discussions with the OD group, it was decided that the T-shape could be approximated to be half the efficiency of the cross-shape and L-shape combined, due to the geometry symmetry. The overlapped region in two canister failures may occur in any of the 9 spaces in the 3 x 3 region as shown in figure 9.8. An average scenario was also calculated in the efficiency curves for any double failure in the 3 x 3 grid.

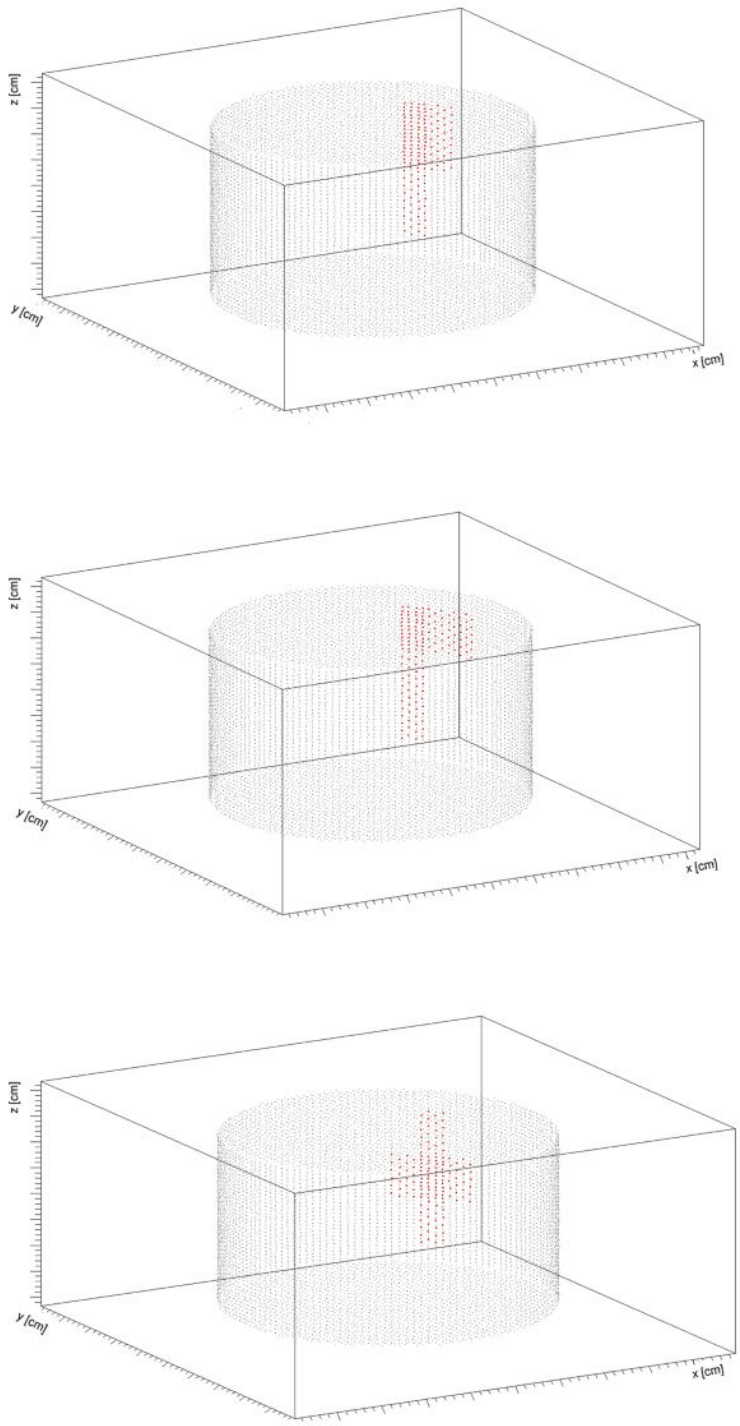

Figure 9.9: The simulated failed electronic canisters in the case where two overlapping canisters fail. The top configurations show the L-shape tiling, with the left displaying the 16 column case, and the right showing the 24 column instance. The bottom diagram also demonstrates a tiling option in the 24 column scheme: in this diagram the cross shape is shown.

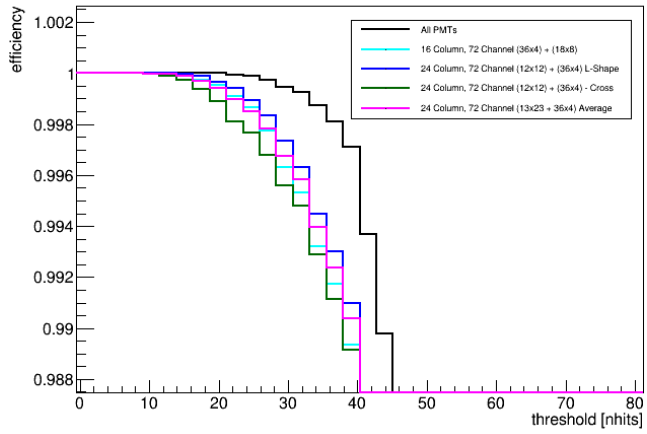

Figure 9.10: The cosmic muon detection efficiency where two adjacent canisters fail. The 16 column L-shape (cyan), 24 column L-shape (blue), 24 column cross-shape (green), 24 column averaged performance (pink) and no failure cases (black) are shown.

The cross-shape is shown in figure 9.10 to perform worse than the L-shape as the detection efficiency curve of the cross-shape was below the L-shape. This decreased performance was for a similar reason to the worse performance of the square region. In the cross shape scenario, there were four half active regions (due to two-fold interleaving) surrounding the fully inactive space. Therefore the number of hits occurring around this central inactive point was decreased as the number of active PMTs surrounding this point is lower. The efficiency curve shown in figure 9.10 shows a slight preference for the 24 column scheme. This was likely because it had 24 fewer PMTs in the inactive region than the 16 column case. This was true despite the fact that the 16 column scenario benefits from having only an L-shape overlap region regardless of which canisters fail due to its 2 x 2 canister configuration.

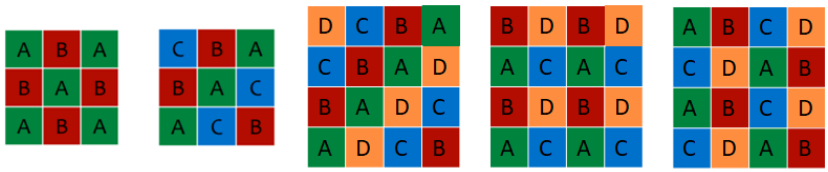

Figure 9.11: The interleaving patterns for two, three and four-fold interleaving are shown. From left to right, the two-fold, three-fold, and three four-fold interleaving patterns are shown. The four-fold patterns are referred to as the diagonal, square and rhombus shapes from left to right. Each box represents a single PMT, with the colours/letters indicating which electronic canister reads out the PMT.

9.2.1 Interleaving

The previous section focused on two-fold interleaving which has been shown to be a useful tool in mitigating the loss in cosmic muon detection efficiency during two canister failure scenarios. By increasing the n-fold of the interleaving the efficiency improved further when considering canister failures. Two, three and four-fold interleaving options were considered. Four-fold was the maximum considered, as the installation procedures become more complex as a function of n, and the cable length also increases, thus increasing the radioactive background in the detector. The interleaving patterns considered for two, three and four-fold interleaving are shown in figure 9.11.

When considering these scenarios with increased n-fold interleaving, failures of up to four canisters were considered. Throughout the detector's lifetime, it is possible that a single electronic canister will fail. The probability that two adjacent overlapping canisters fail is reduced. This probability of more canisters in the same region failing decreases further, and this factor should be considered when deciding how important additional interleaving will be. Table 9.1 demonstrates the probability of N canisters failing in the same area assuming four-fold interleaving. Table 9.2 shows the number of canisters in the same region expected to fail across the entire OD. These tables

N failures	Probability
0	65.61%
1	29.16%
2	4.86%
3	0.36%
4	0.01%

Table 9.1: Probability of N canisters failing in one segment of the detector, assumes four-fold interleaving and 1% of electronic canisters fail per year over 10 years.

N failures	Coverage in same region	Expected number of occurrences
1	75%	10
2	50%	1.7
3	25%	0.13
4	0%	<0.01

Table 9.2: Probability of multiple canister failures in the same region across the entire OD, assuming four-fold interleaving and 1% of electronic canisters fail per year over 10 years.

are produced assuming 1% of electronic canisters fail per year over 10 years. For this work the 32-column case with an electronic canister instrumenting 72 OD PMTs was assumed, meaning ∼140 canisters instrument the full OD.

In the case of two failures, there are six possible combinations of double canister failure, e.g. canisters A and B, or A and C, and so on. Therefore the probability of two canister failure is $6 \times (0.1)^2 \times (1 - 0.1)^2$. In the one and three failure scenarios, four canister combinations exist, and only one combination when either no canisters or all four fail. Multiplying the probability of failure from table 9.2 with the 35 instrumentation regions, each containing four canisters, provides the expected number of occurrences.

These calculations were purely mathematical and do not account for correlations in the detector region where multiple canisters would fail. These correlations could

occur due to human error during installation. Accounting for these factors would likely increase the probability of multiple failures in the same region.

In figure 9.12 the muon detection efficiency and inefficiency for a single canister failure is shown. The bottom plot in figure 9.12 contains a line to demonstrate the inefficiency at 10^{-6}. This line represents the inefficiency goal of the OD at the time of this work. The statistics used for this analysis was limited relative to the rate of cosmic muons expected in data, 10,000 simulated muons relative to the 4 million muons per day in data, meaning reaching this inefficiency threshold was not possible. The plots shown demonstrated a preference for four-fold interleaving with a slight preference for the diamond configuration. Each of the three four-fold patterns were further tested as shown in figure 9.13.

A slight preference for the square shape was demonstrated. However this preference was marginal and consideration of the complexity of each installation procedure would likely take precedence when deciding which of these interleaving patterns was most suitable in a four-fold interleaving scheme. In figure 9.14 the muon detection efficiency when different interleaving patterns were considered during two canister failure is shown. The L-shaped pattern with 16 column was assumed.

When two canisters fail, a crossing effect was observed between the two-fold and three-fold interleaving curves. Two-fold interleaving was more efficient than the three-fold case at high NHits threshold, as the inactive PMTs are located in a smaller region of space. Whereas at lower NHits thresholds, the three-fold case performed better than two-fold, as the effect of losing all PMTs in a small region becomes greater than the benefits of a smaller affected region. The four-fold case remained quite robust against these effects and maintained a higher detection efficiency than both the two and three-

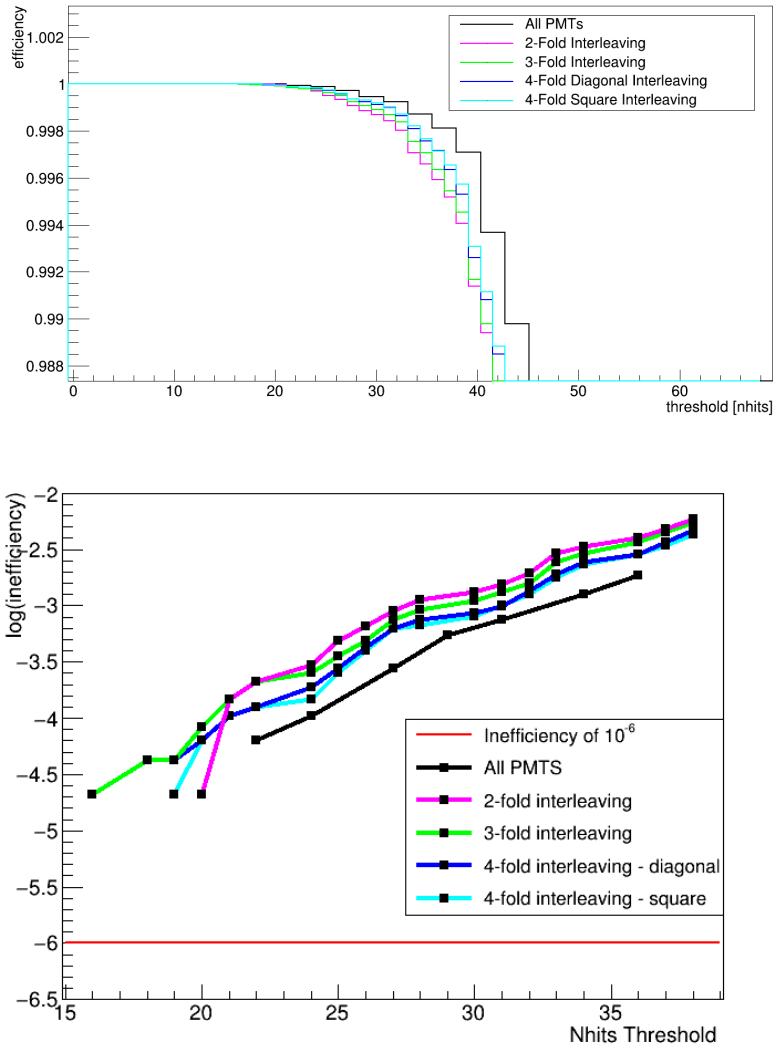

Figure 9.12: Cosmic muon detection efficiency (top) and inefficiency (bottom) when a single electronic canister fails for the n-fold patterns. The pink line corresponds to two-fold interleaving, green with three-fold, dark blue with four-fold, diagonal, and light blue four fold, square interleaving. The black line shows the baseline without any failures.

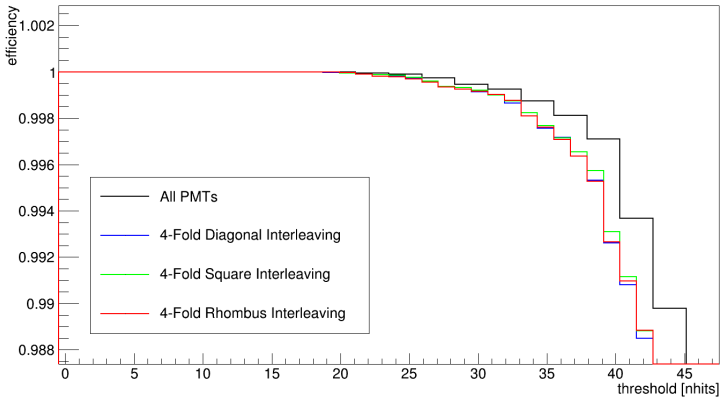

Figure 9.13: Four-fold interleaving patterns for single canister failure. Blue shows the diagonal pattern, green the square and red the rhombus pattern.

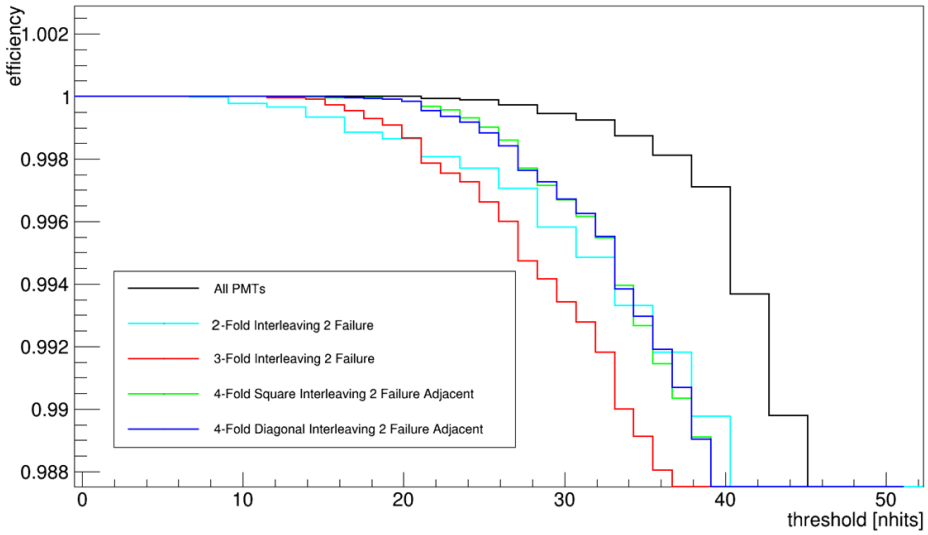

Figure 9.14: Muon detection efficiency when two canisters fail for various n-fold interleaving patterns. The light blue shows the two-fold case, red, the three fold, green the four-fold square, dark blue the four-fold diagonal interleaving patterns, and black the no failure case. In the four-fold case the PMTs which fail are adjacent, rather than separated by an active PMT.

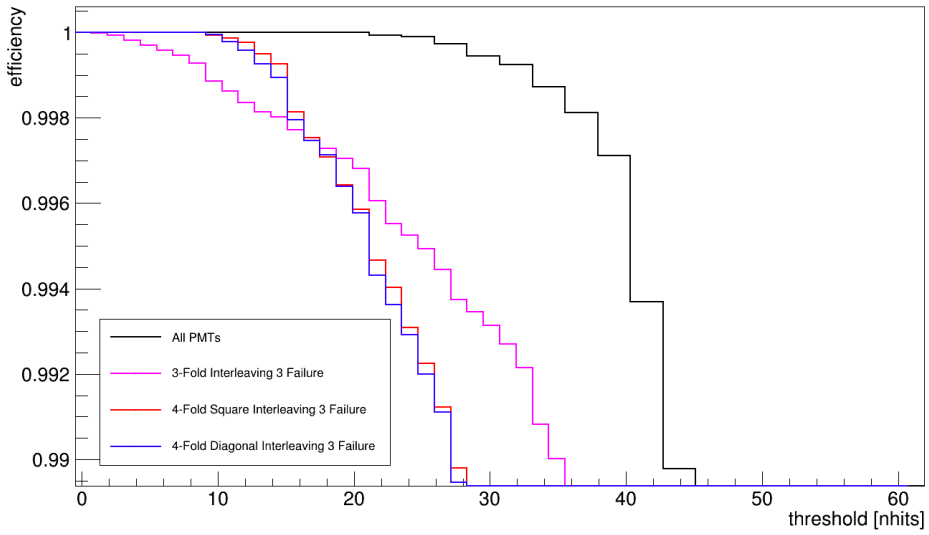

Figure 9.15: Muon detection efficiency when three electronic canisters fail in the same region for each n-fold interleaving pattern. The pink line shows three-fold interleaving, red line shows four-fold square interleaving, blue shows four-fold diagonal interleaving and black shows no failures.

fold interleaving cases. In the case of four-fold interleaving, checks were also made to ensure the efficiency did not vary significantly based on which of the four canisters failed. This is better illustrated using the rightmost pattern of figure 9.11. Considerations related to the difference between canister A and B being inactive, relative to A and D being inactive, were made. Little effect was observed on the muon detection efficiency when two adjacent PMTs failed relative to two diagonal PMTs failing. The case where three and four electronic canisters fail are shown in figures 9.15 and 9.16 respectively.

The same crossing effect was observed in the three canister failure case. The four canister failure demonstrates the importance in a functional OD, and that the failure rates estimated were accurate. Based on the calculations made in table 9.2, the probability of four canisters failing in the same region were near zero, however

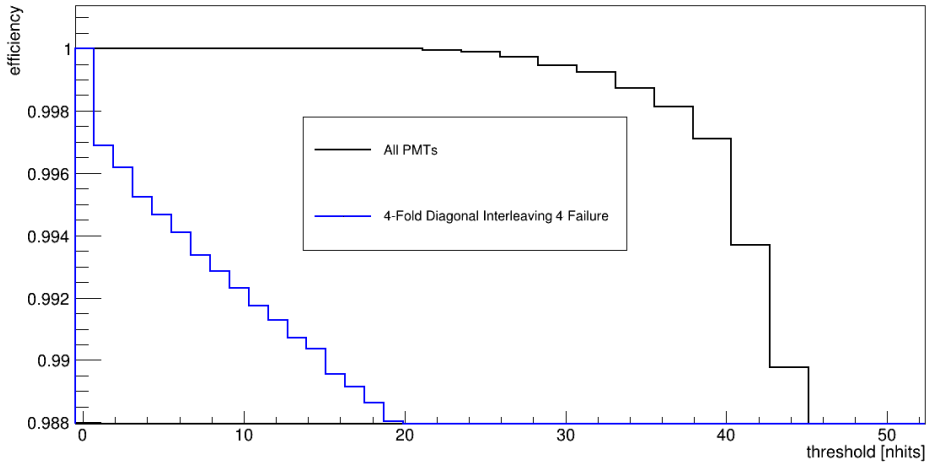

Figure 9.16: Muon detection efficiency when four electronic canisters fail in the same region for four-fold interleaving pattern. The blue line shows the four-fold interleaved four canister failure scenario and black shows no failures.

this may not be true if care is not taken during installation, or the failure rates were underestimated.

A summary of the muon detection efficiency for 24 column, four-fold interleaving for a 72-PMT electronic canister across one, two, three and four canister failures is shown in figure 9.17. The results shown in these plots, in conjunction with tables 9.1 and 9.2, emphasise the importance of introducing interleaving to the design of the detector. It will influence the NHits threshold chosen and guide the maximum acceptable dark noise rate of the OD photosensing units. These results prove the importance of mitigating the issues electronic canister failure will cause the OD system. A new OD electronic design was implemented after this work was completed as described in section 7.2.5. This design will effectively implement a three-fold interleaving pattern. In addition, fewer PMTs will be connected to each canister, meaning a 72 PMT region without interleaving will now be instrumented by around five or six canisters.

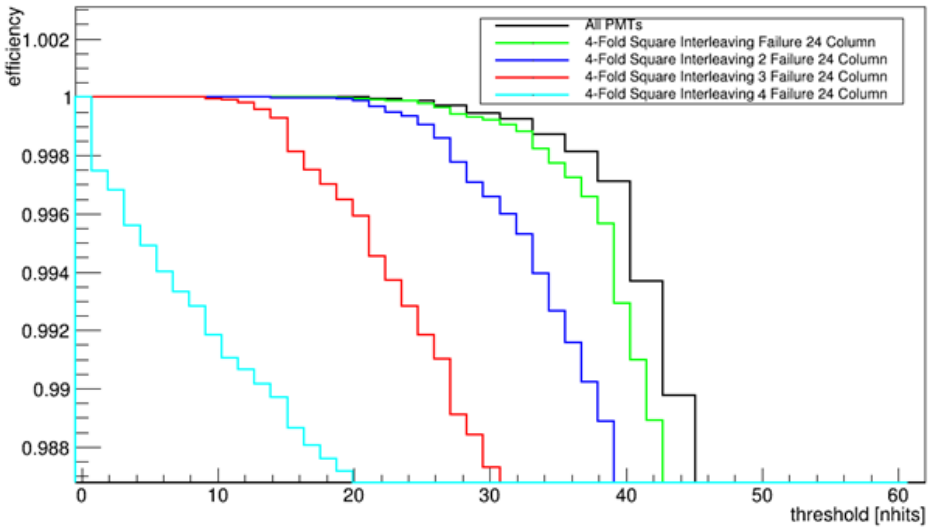

Figure 9.17: Muon detection efficiency for a 24 column, four-fold 72-PMT electronic canister scenario, where one (green line), two (dark blue line), three (red line) and four (light blue line) electronic canisters have failed in the same region. The black line shows the case where no PMTs have failed.

9.3 Conclusions

After simulating various scenarios in which PMTs and electronic units fail, it was determined that various interleaving schemes could be implemented to mitigate the cosmic muon detection efficiency loss. These studies aided in decision making when determining that a change in the electronic unit design of the experiment should be implemented - switching to a combined ID and OD electronic unit. This change will result in fewer OD PMTs being connected to each electronic unit. It is unlikely that complex interleaving schemes will be required following this change, although some degree of interleaving will likely be utilised. It is important that these studies will be repeated with all updates to the detector design to ensure all failure modes are mitigated in the design before construction begins.

Chapter 10

Conclusions

The field of neutrino physics has evolved in recent years, entering an era of precision measurements of the oscillation parameters. Existing experiments such as T2K, continue to produce world-leading measurements and constraints of the oscillation parameters, and these analyses are well understood due to a robust understanding of the ND and FDs used. In chapters 4 - 6, an update to the ND oscillation analysis, including a new physics sample tagging photons in $\bar{\nu}$ interactions was detailed.

As neutrino physics enter a new era of precision measurements, with large-scale detectors such as Hyper-K being constructed, both old and new challenges emerge. With improvements in technology, and a greater understanding of the successes and failures of its predecessors, the detector design has been developed to ensure a broad scope of physics may be explored. Studies to ensure that the detector will be capable of reading out all data incident upon it, and that the longevity of the OD has been carefully considered, were both described in chapters 8 and 9.

The ND280 is able to constrain the systematic uncertainties on the flux and cross section parameters, which behave as nuisance parameters in oscillation analyses, to less

than 5% in most samples [63]. In this thesis, a new ND sample, selecting $\bar{\nu}$ events with a photon in the final state, was developed and implemented alongside the existing samples to aid in reducing these systematic uncertainties further. The sample has an efficiency of $\sim$ 40%, and a purity of $\sim$ 42%. To ensure the purity of the sample was sufficiently high to be used in the ND fit, a new PID tool using BDT techniques was designed. The BDT aided in correctly identifying the antimuon candidate, increasing the instances that the antimuon was correctly identified in photon events from $\sim$55% to 78%. The implementation of the new photon sample was detailed in chapter 6 where it was shown that sensitivities to flux and cross section parameters were improved. The fractional uncertainty on the event rate of the $\bar{\nu}$ FGD1 (FGD2) CC-Photon sample was reduced from 13.09 (14.02)% to 2.1 (2.08)% as a result of the ND fit.

In future iterations of the ND fit, new data from the upgraded ND will be included. The installation of the Super-FGD, High Angle TPCs and time-of-flight detectors will be completed in 2024. The improved reconstruction capabilities of these detectors will lead to new ND samples. One useful addition to the antineutrino samples will be neutron tagging in CC0π events. These events can be detected using the Super-FGD, and tagging may also be possible using the existing ECal.

The Hyper-Kamiokande experiment is a future large-scale water Cherenkov detector, currently under construction in Japan. The experimental physics programme will cover a broad range of topics, such as long baseline neutrino oscillation parameter measurements, searches for nucleon decay and observation of potential supernova neutrino bursts. The detector has been designed to ensure accurate reconstruction of physics events for the duration of the experiment.

The DAQ system must be designed appropriately to ensure that all of these physics

analyses may be conducted, by reading out all physics event types continuously, for the duration of the experiment. The study conducted in this thesis considered the event rates, and the average and maximum hits produced by each event type. It was determined that the average data rate incident upon the detector was between 2.5 - 2.6 GB/s. Following the processing of these events through a sophisticated trigger system, targeting events across a broad energy range, the event rate saved for offline analysis will be reduced to the $\mathcal{O}(10)$ MB/s. In extreme cases, such as during a near supernova neutrino burst, the event rate will increase dramatically to between 9.1 - 9.7 TB in an hour. The DAQ system should be designed with the capability to read out data in all scenarios, from average to extreme.

The OD design must be robust in its task of tagging cosmic ray muon backgrounds for the lifetime of the detector. As the detector ages, the PMTs and electronics will begin to fail. It is possible to mitigate some of this drop in muon detection efficiency which occur as the detector ages, by carefully considering the electronic canister layout and the cabling from the PMTs to the electronics. Interleaving the cabling of the PMTs which instrument a region of the detector will aid in cases of failure. As the n-fold of the interleaving increases, the number of PMTs which fail in the confined region will reduce by a factor of n. Since these studies were conducted, it was decided that the electronic canister design would change to a combined ID and OD electronic canister. The change means fewer PMTs will be connected to each electronic canister. The decision was made in part as a result of these studies as it displayed a clear need to ensure that the impact of the loss of electronic canisters would be minimal, and therefore ensure a consistently high cosmic ray muon detection efficiency throughout the lifetime of the experiment.

Appendix A

Muon PID BDT Parameters

FGD1 muon-proton BDT training sample variable distribution for signal and background events. These are the distributions the BDT is training on, in the specified range shown in the plots. Figures A.1 to A.5 show the distributions of the input variables for the FGD1 proton-muon BDT.

The distributions for the FGD1 pion-muon BDT input variables are shown in figures A.6 to A.10

A.1 BDT Input Variable Data MC Comparison

This section shows the comparison between data and MC for each input sample when applied to the PØD control sample.

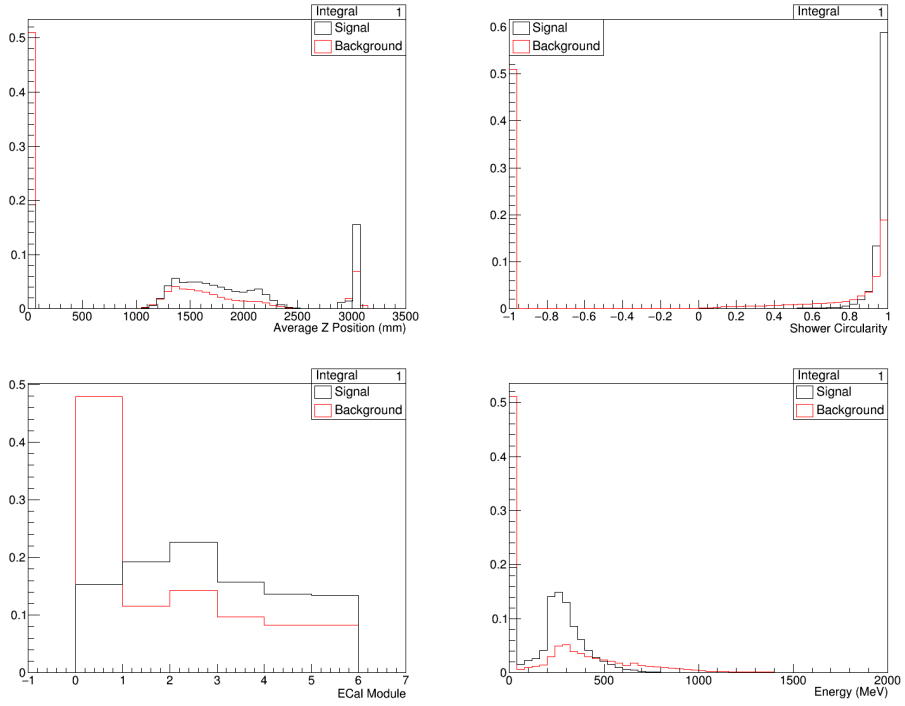

Figure A.1: Particle gun training event input variable distributions: Average Z position of ECal object (top left), ECal object shower circularity (top right), the ECal module of the object (bottom left), ECal energy (bottom right).

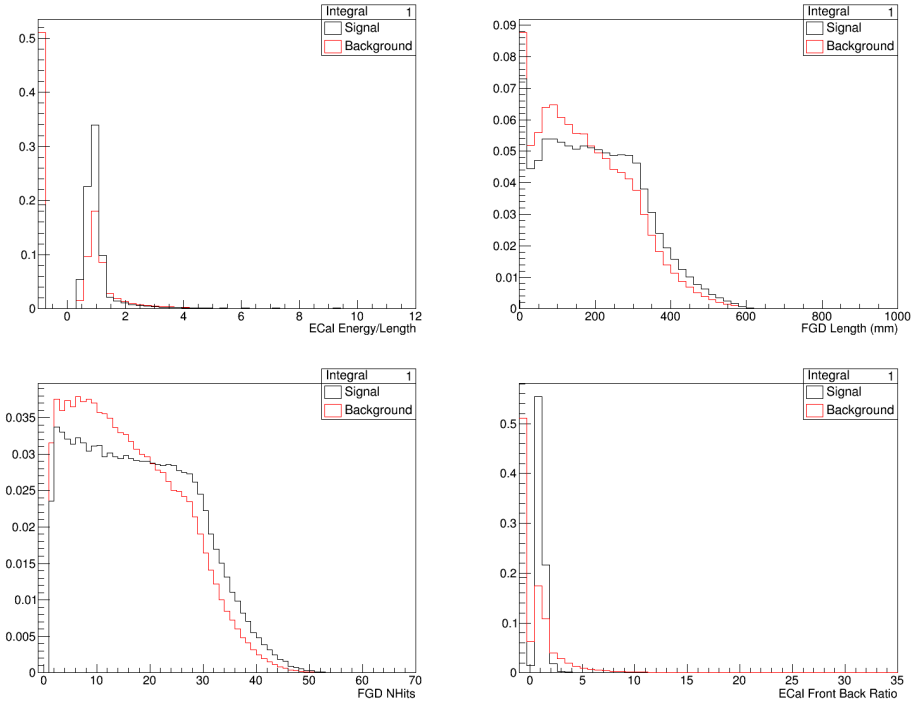

Figure A.2: Particle gun training event input variable distributions: ECal energy/length (top left), FGD object length (top right), number of FGD hits (bottom left), ECal object front back ratio (bottom right).

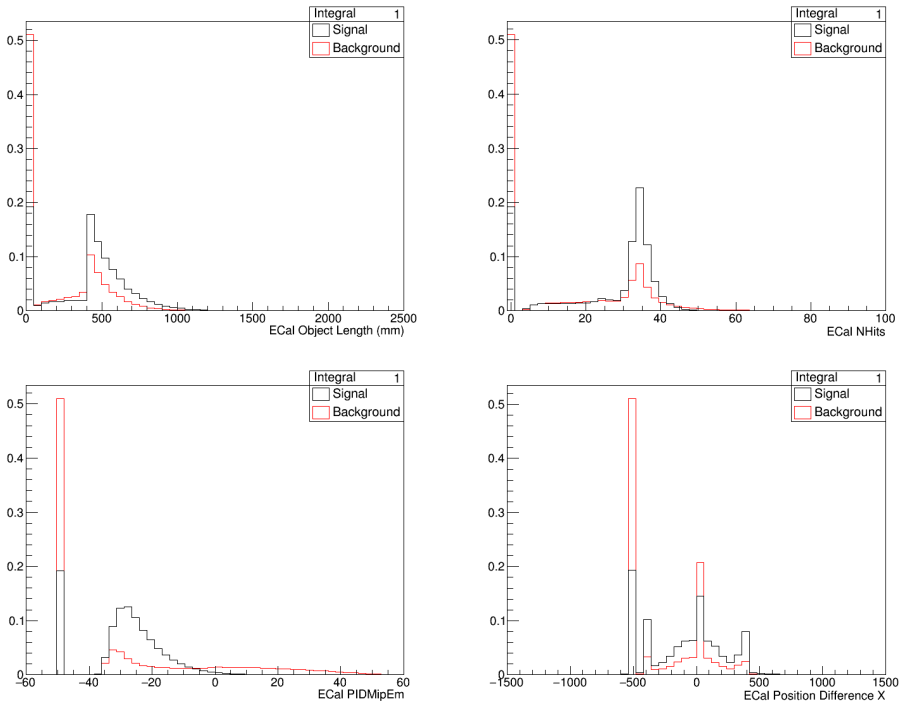

Figure A.3: Particle gun training event input variable distributions: ECal object length (top left), number of hits in ECal from object (top right), ECal object PIDMipEm (bottom left), X position difference between end and start position of ECal object (bottom right).

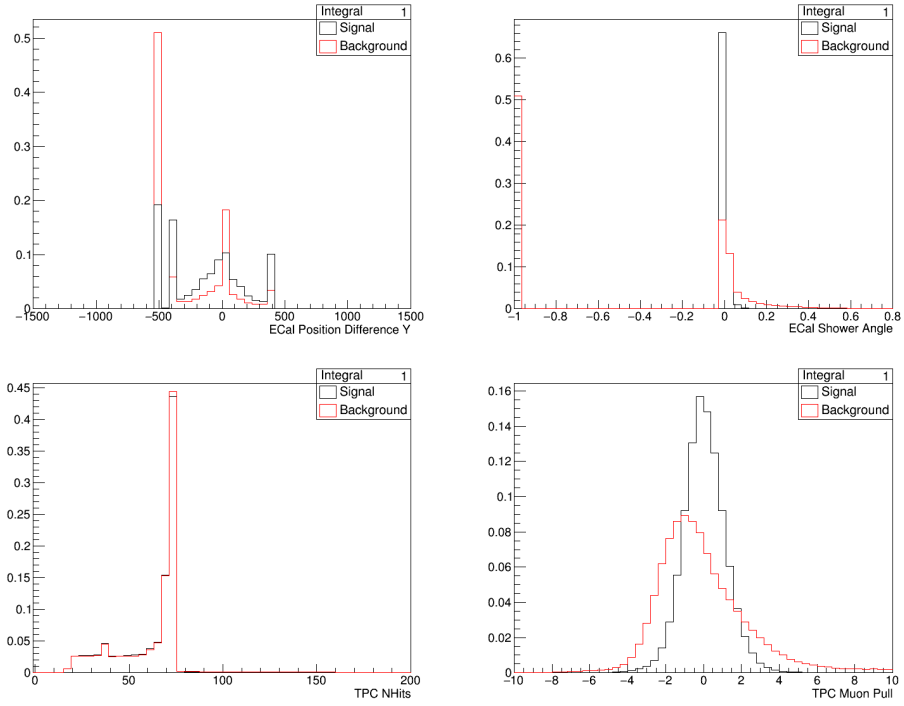

Figure A.4: Particle gun training event input variable distributions: Y position difference between end and start position of ECal object (top right), ECal shower angle (top right), number of hits in TPC (bottom left), TPC muon pull (bottom right).

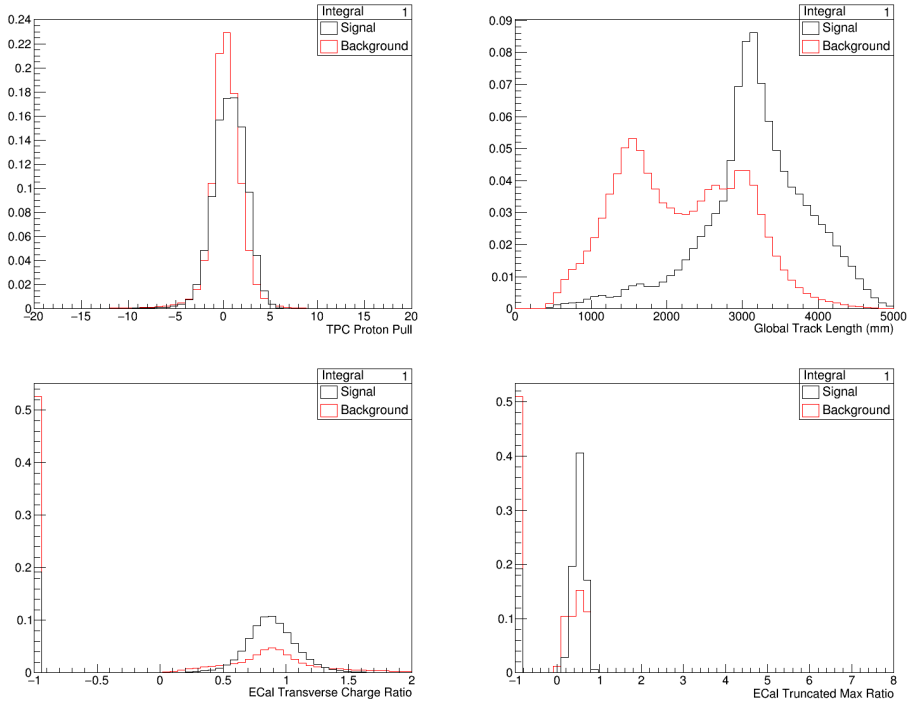

Figure A.5: Particle gun training event input variable distributions: TPC proton pull (top left), global track length (top right), ECal object transverse charge ratio (bottom left), ECal object truncated max ratio (bottom right).

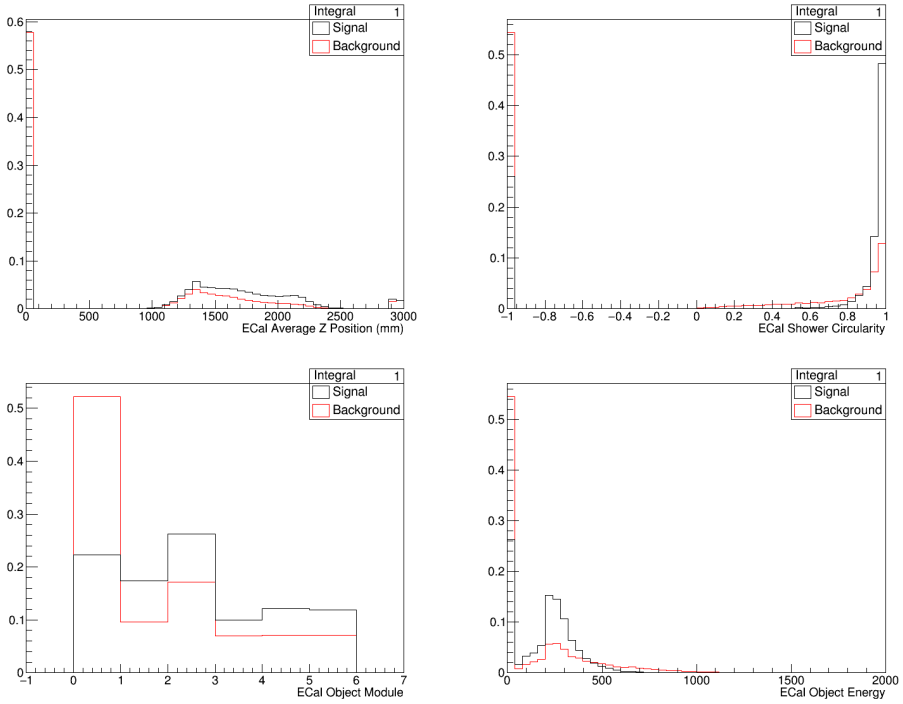

Figure A.6: Particle gun training event input variable distributions: Average Z position of ECal object (top left), ECal object shower circularity (top right), the ECal module of the object (bottom left), ECal energy (bottom right).

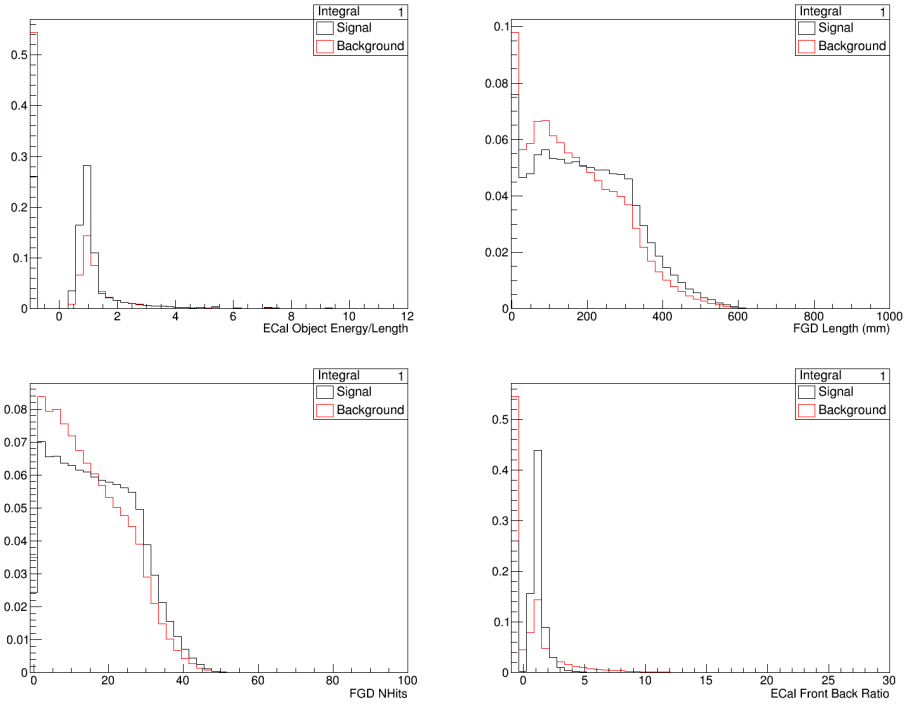

Figure A.7: Particle gun training event input variable distributions: ECal energy/length (top left), FGD object length (top right), number of FGD hits (bottom left), ECal object front back ratio (bottom right).

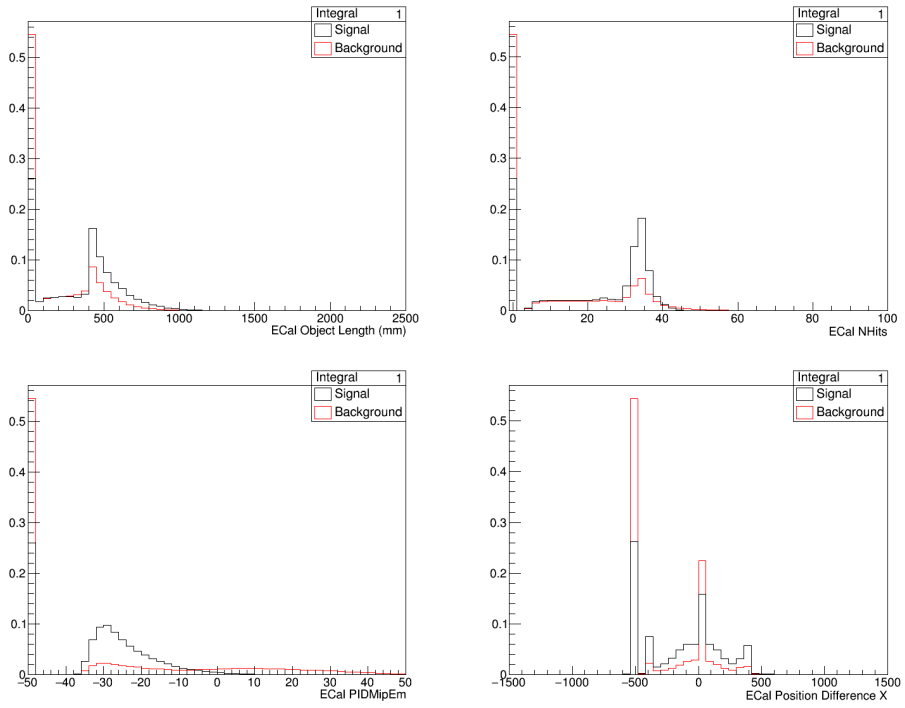

Figure A.8: Particle gun training event input variable distributions: ECal object length (top left), number of hits in ECal from object (top right), ECal object PIDMipEm (bottom left), X position difference between end and start position of ECal object (bottom right).

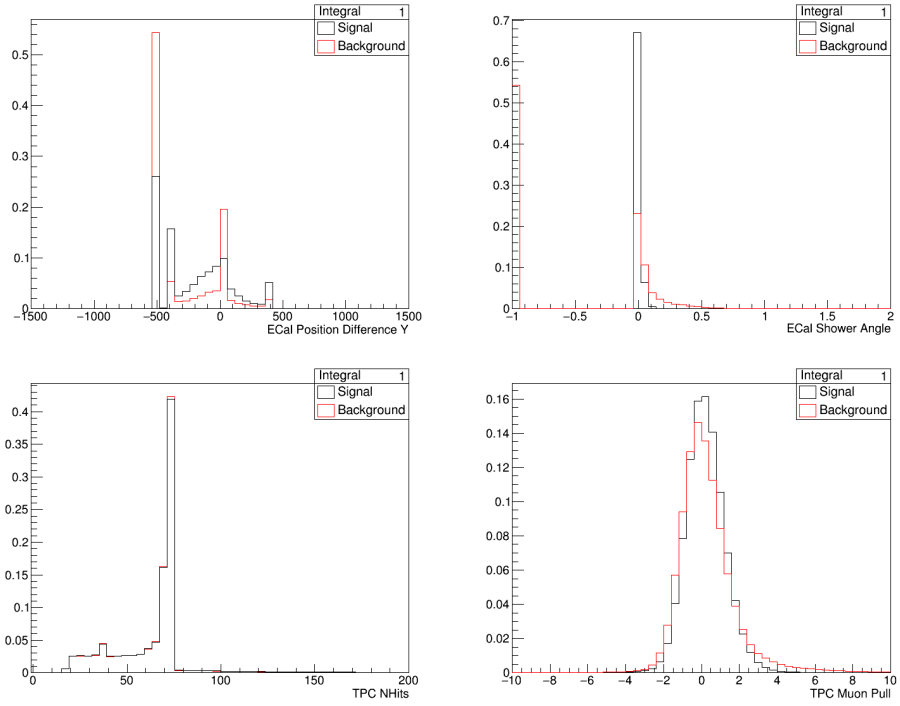

Figure A.9: Particle gun training event input variable distributions: Y position difference between end and start position of ECal object (top right), ECal shower angle (top right), number of hits in TPC (bottom left), TPC muon pull (bottom right).

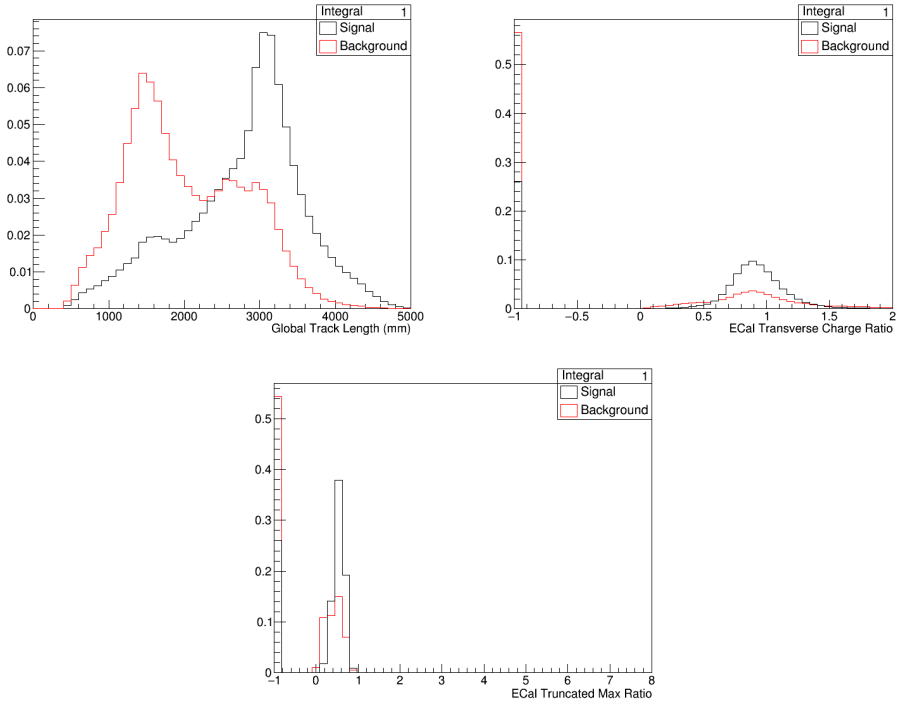

Figure A.10: Particle gun training event input variable distributions: global track length (top left), ECal object transverse charge ratio (top right), ECal object truncated max ratio (bottom).

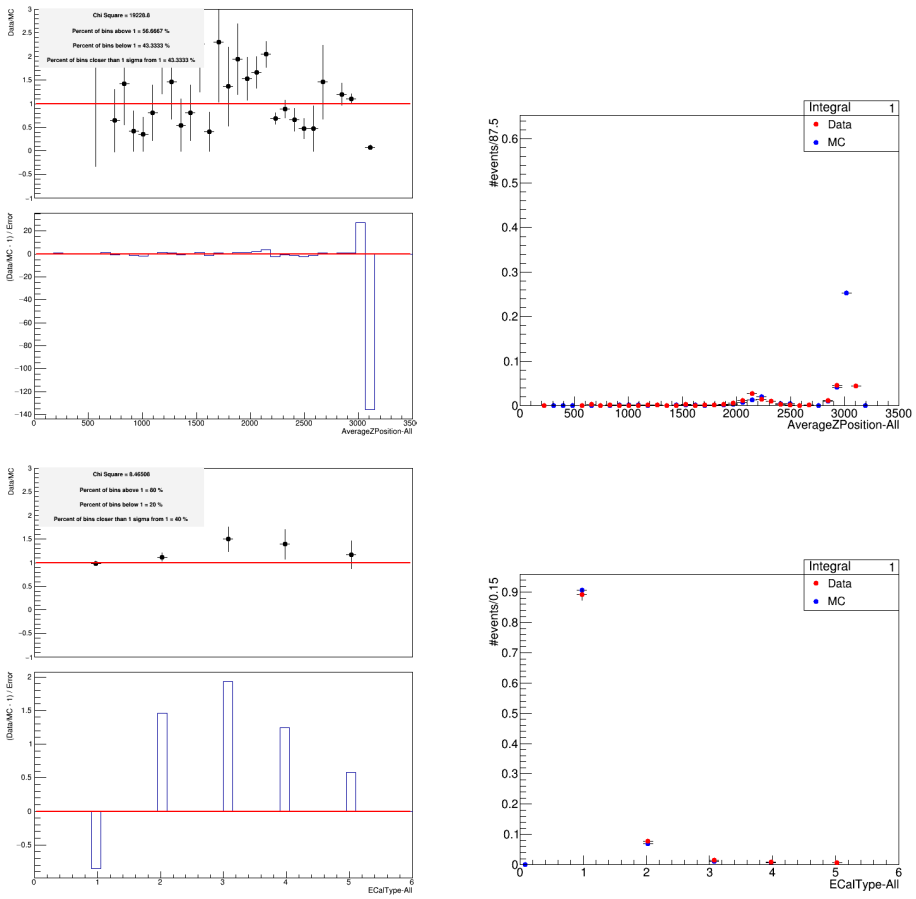

Figure A.11: Comparison of data and MC for each input variable. Left shows Data-MC and (Data-MC -1)/Error. Right shows variable distribution for data and MC. Here top plot is for ECal object average Z position, bottom is for ECal object ECal module entered.

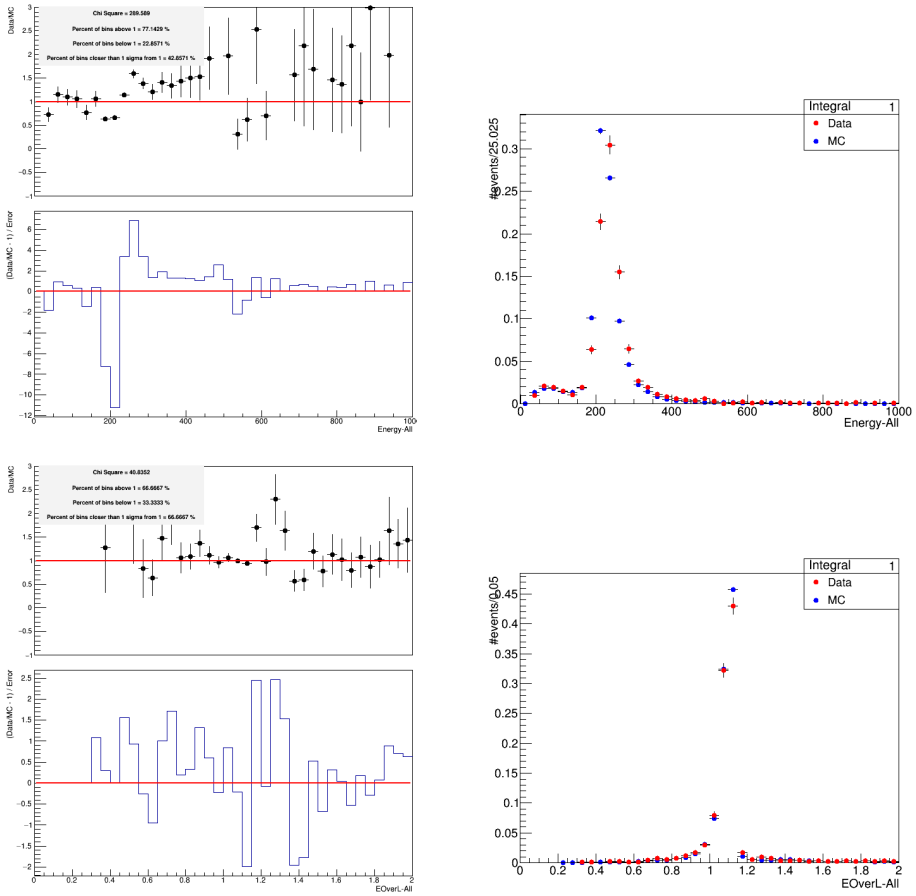

Figure A.12: Comparison of data and MC for each input variable. Left shows Data-MC and (Data-MC -1)/Error. Right shows variable distribution for data and MC. Here top plot is for ECal object energy, bottom is for ECal object energy/length.

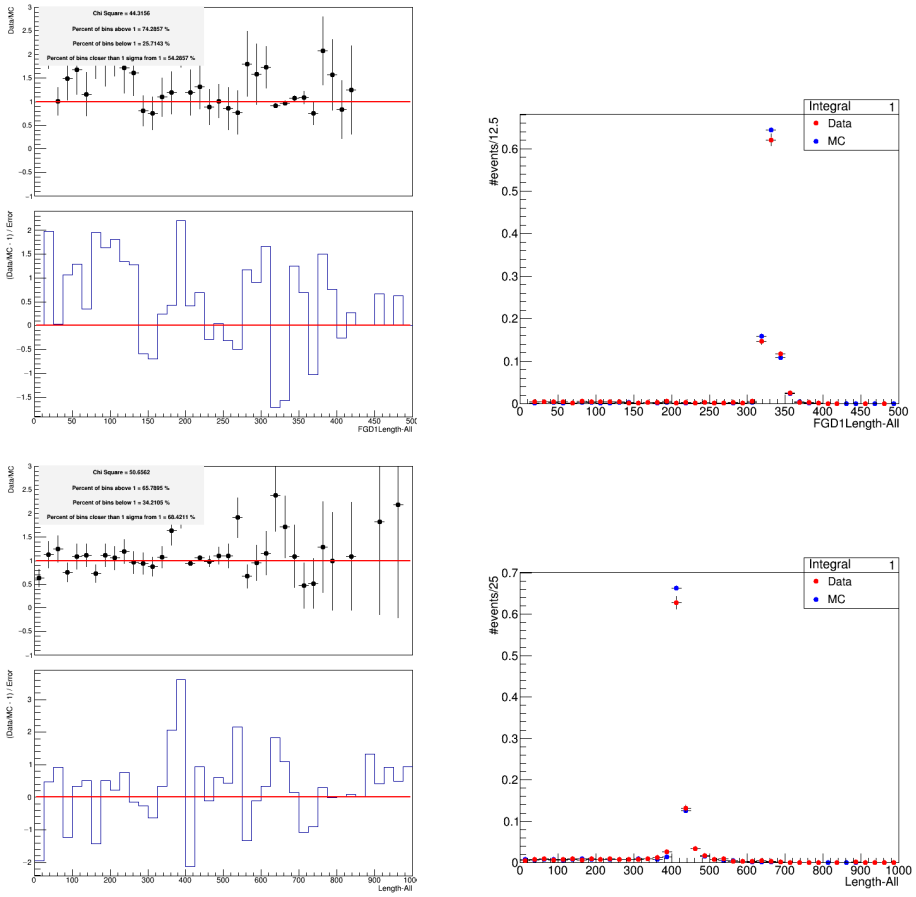

Figure A.13: Comparison of data and MC for each input variable. Left shows Data-MC and (Data-MC -1)/Error. Right shows variable distribution for data and MC. Here top plot is for FGD length, bottom is for ECal object length.

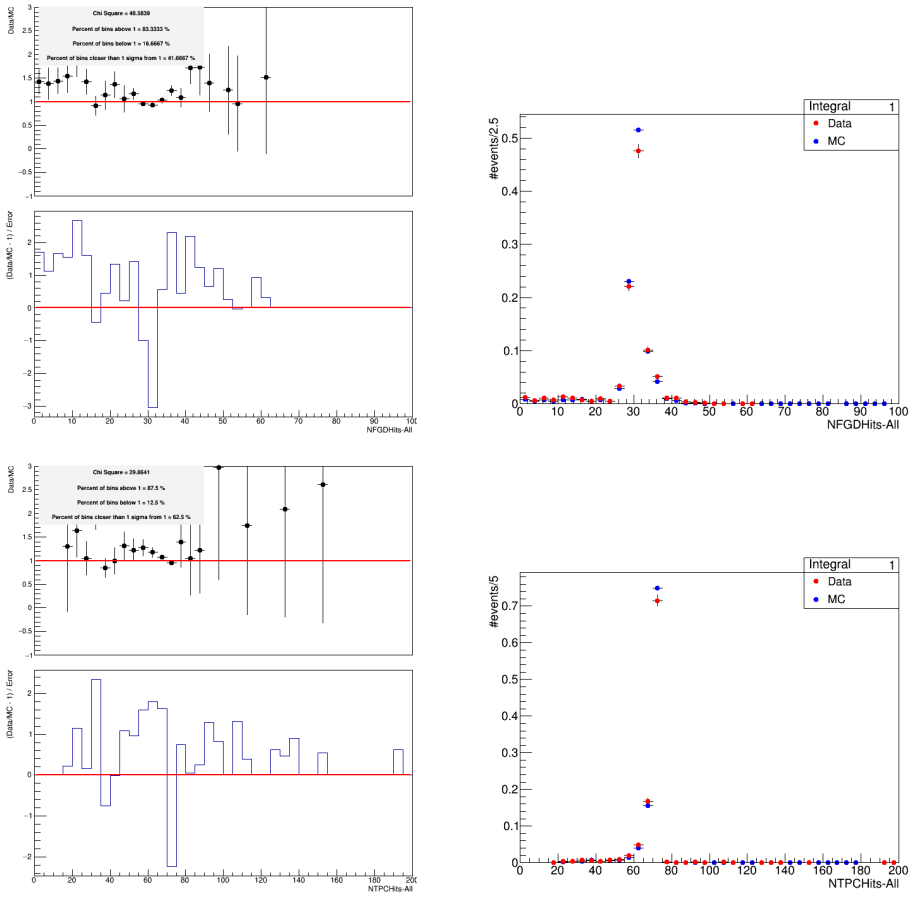

Figure A.14: Comparison of data and MC for each input variable. Left shows Data-MC and (Data-MC -1)/Error. Right shows variable distribution for data and MC. Here top plot is for number of FGD hits, bottom is for number of TPC hits.

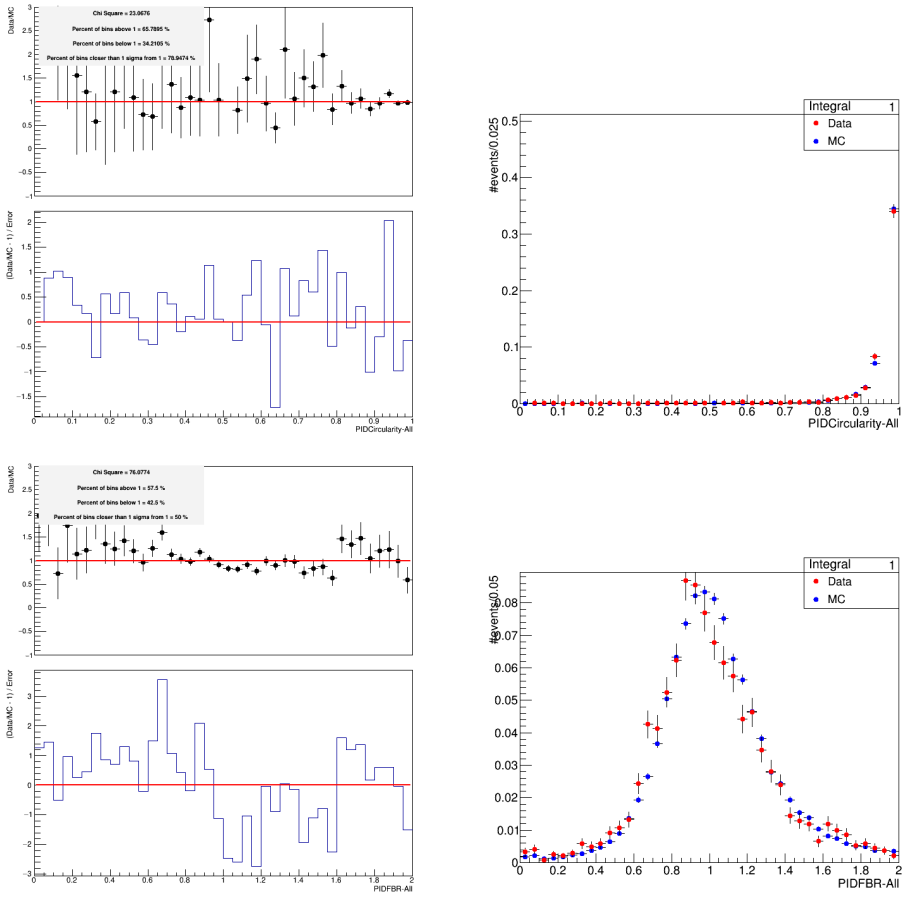

Figure A.15: Comparison of data and MC for each input variable. Left shows Data-MC and (Data-MC -1)/Error. Right shows variable distribution for data and MC. Here top plot is for ECal object circularity, bottom is for ECal object front back ratio.

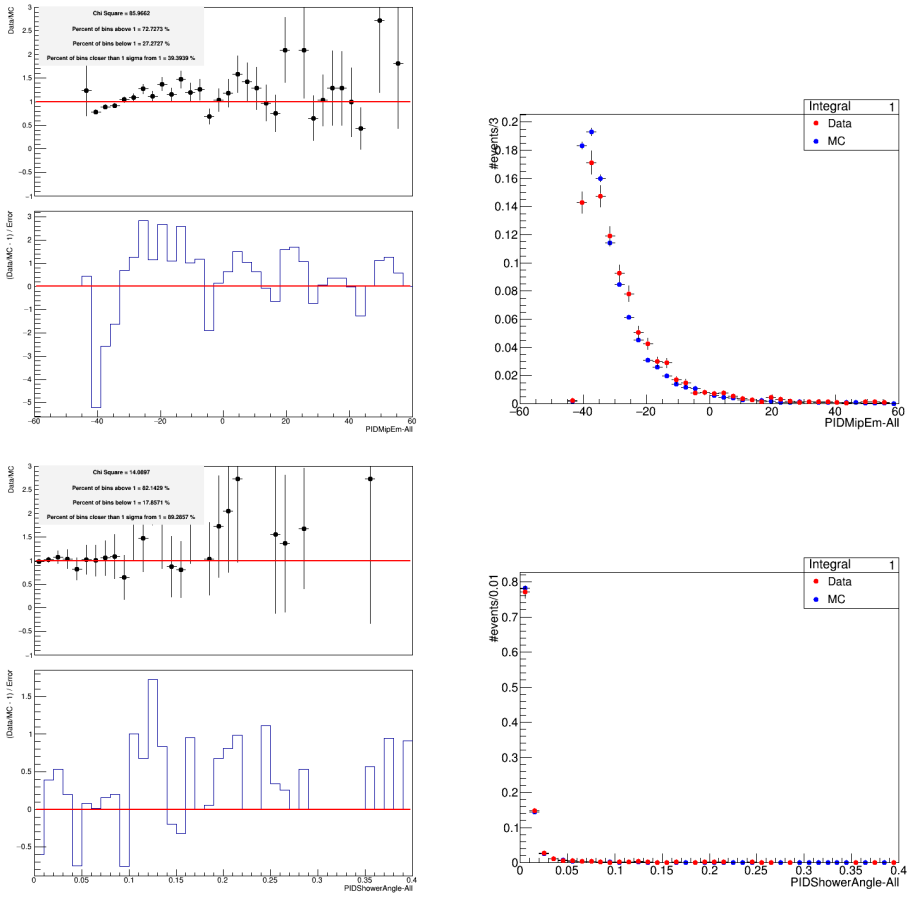

Figure A.16: Comparison of data and MC for each input variable. Left shows Data-MC and (Data-MC -1)/Error. Right shows variable distribution for data and MC. Here top plot is for ECal object PIDMipEm, bottom is for ECal object shower angle.

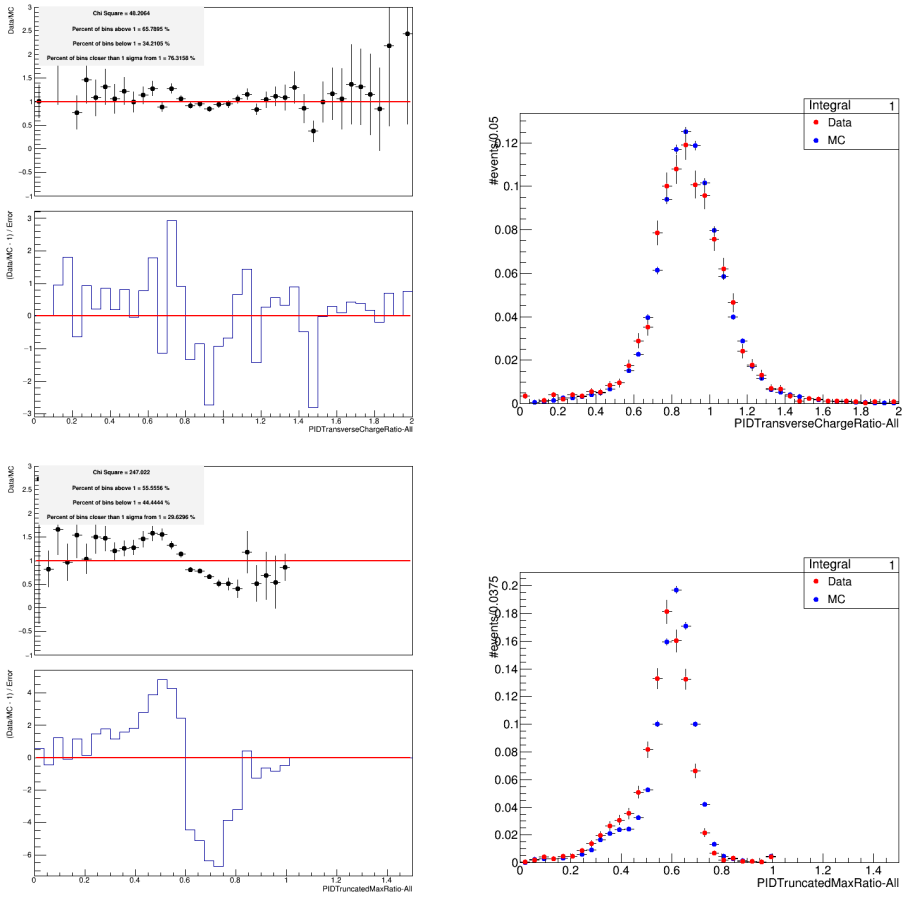

Figure A.17: Comparison of data and MC for each input variable. Left shows Data-MC and (Data-MC -1)/Error. Right shows variable distribution for data and MC. Here top plot is for ECal object transverse charge ratio, bottom is for ECal object truncated max ratio.

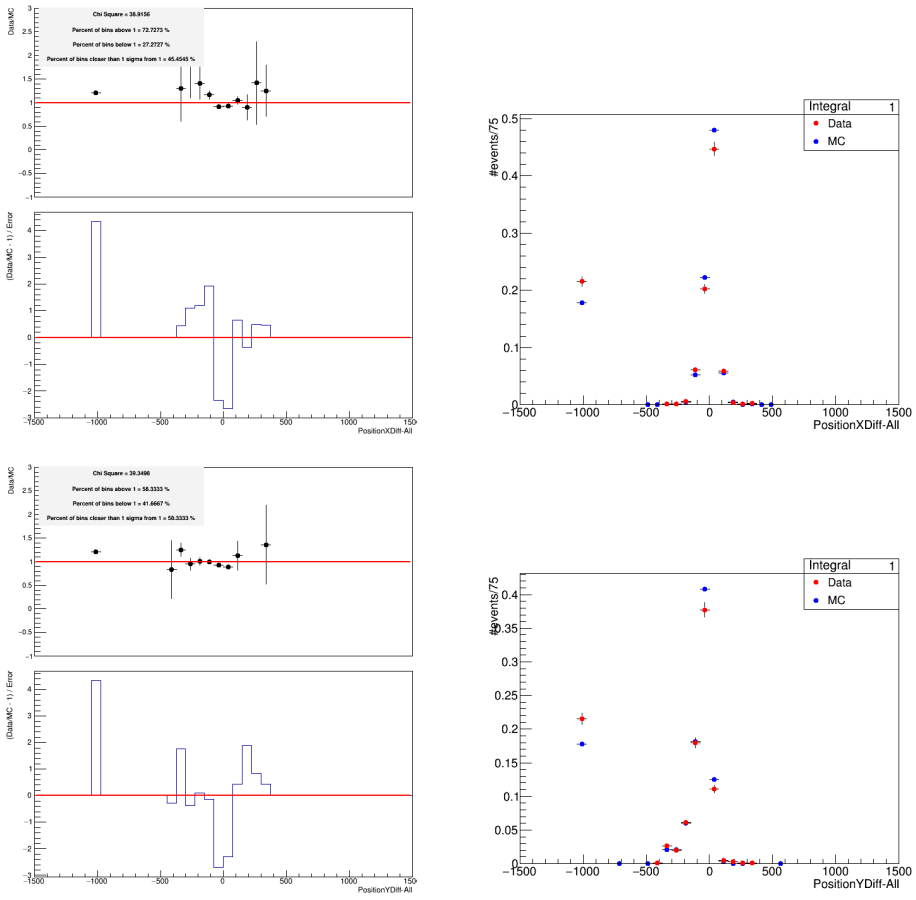

Figure A.18: Comparison of data and MC for each input variable. Left shows Data-MC and (Data-MC -1)/Error. Right shows variable distribution for data and MC. Here top plot is for X position difference between end and start position of ECal object and bottom is for Y position difference between end and start position of ECal object.

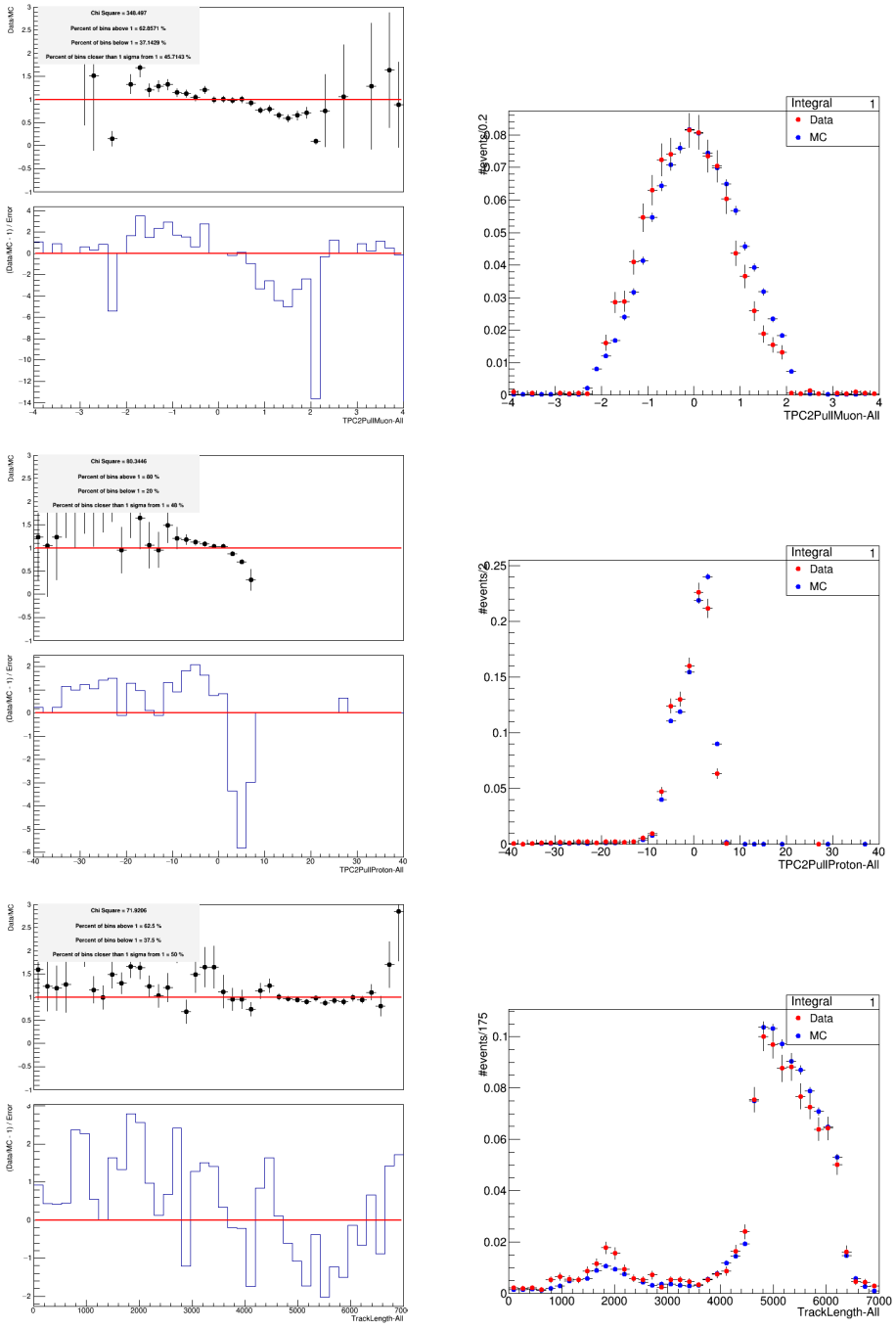

Figure A.19: Comparison of data and MC for each input variable. Left shows Data-MC and (Data-MC -1)/Error. Right shows variable distribution for data and MC. Here top plot is for TPC muon pull, middle is TPC proton pull and bottom is global track length.

Appendix B

ND280 Detector Systematic Uncertainties

This part of the appendix shows the single detector systematics of the $\bar{\nu}$ CC-Photon sample. A detailed description of each systematic was provided in chapter 5.

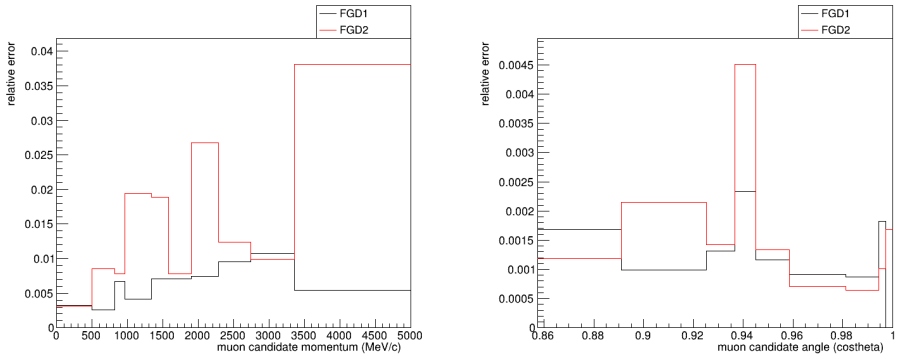

Figure B.1: Average differential detector uncertainty for b-field systematic error for all four samples in terms of the reconstructed lepton momentum (left distributions) and angle (red distributions). The black line shows the error for FGD1 samples, and red for FGD2 samples.

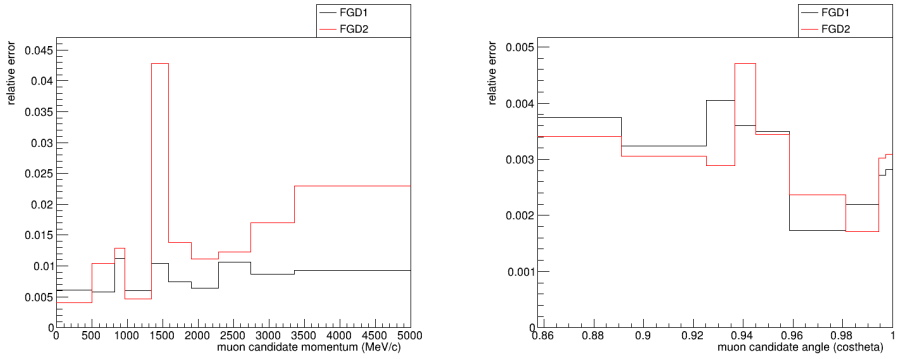

Figure B.2: Average differential detector uncertainty for momentum resolution systematic error for all four samples in terms of the reconstructed lepton momentum (left distributions) and angle (red distributions). The black line shows the error for FGD1 samples, and red for FGD2 samples.

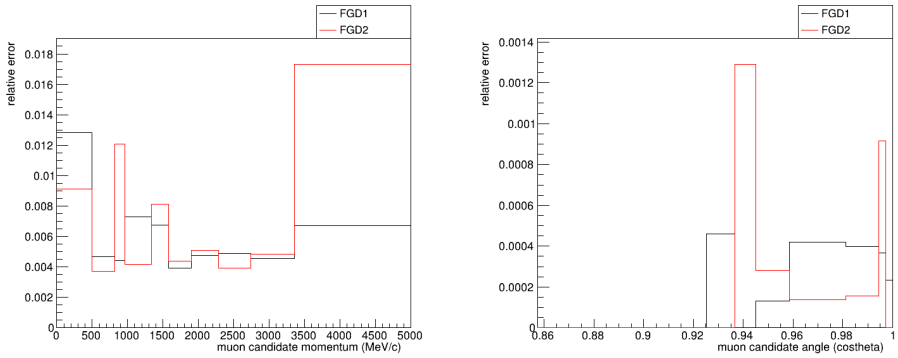

Figure B.3: Average differential detector uncertainty for momentum scale systematic error for all four samples in terms of the reconstructed lepton momentum (left distributions) and angle (red distributions). The black line shows the error for FGD1 samples, and red for FGD2 samples.

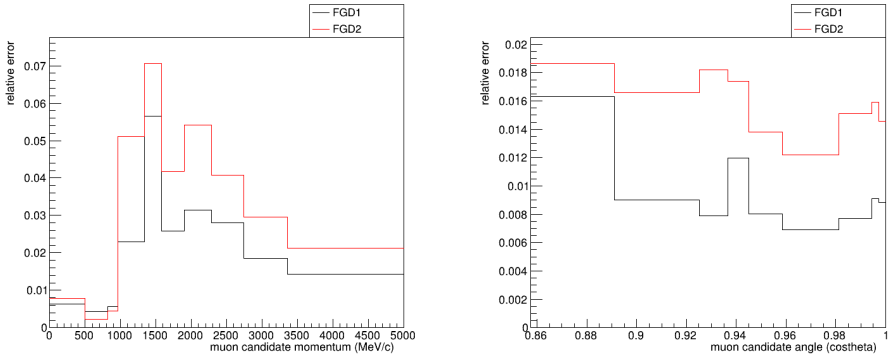

Figure B.4: Average differential detector uncertainty for TPC PID systematic error for all four samples in terms of the reconstructed lepton momentum (left distributions) and angle (red distributions). The black line shows the error for FGD1 samples, and red for FGD2 samples.

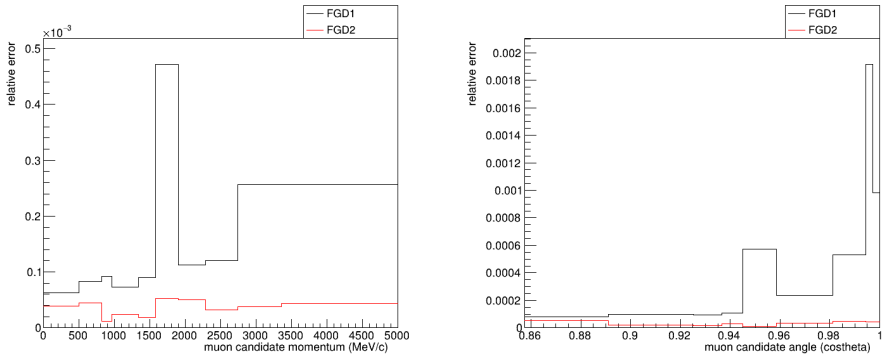

Figure B.5: Average differential detector uncertainty for charge ID efficiency systematic error for all four samples in terms of the reconstructed lepton momentum (left distributions) and angle (red distributions). The black line shows the error for FGD1 samples, and red for FGD2 samples.

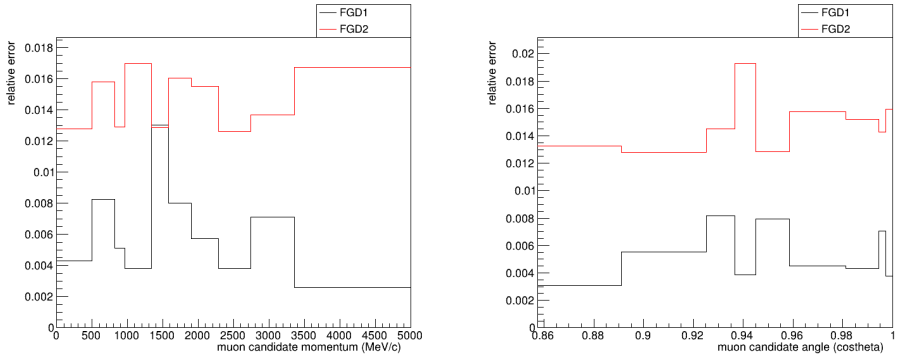

Figure B.6: Average differential detector uncertainty for TPC tracking efficiency systematic error for all four samples in terms of the reconstructed lepton momentum (left distributions) and angle (red distributions). The black line shows the error for FGD1 samples, and red for FGD2 samples.

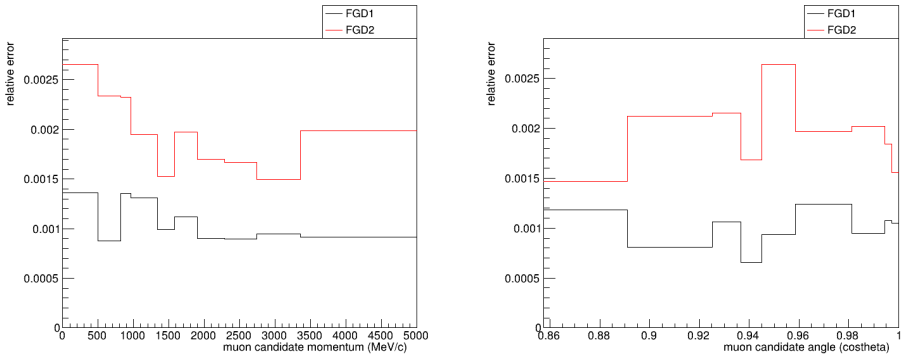

Figure B.7: Average differential detector uncertainty for TPC-FGD matching efficiency systematic error for all four samples in terms of the reconstructed lepton momentum (left distributions) and angle (red distributions). The black line shows the error for FGD1 samples, and red for FGD2 samples.

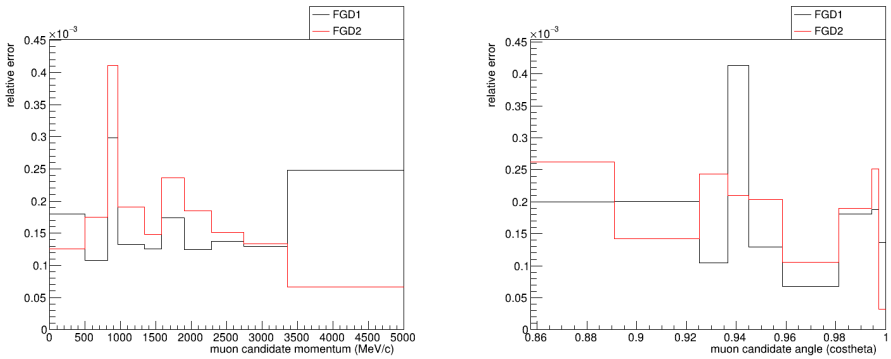

Figure B.8: Average differential detector uncertainty for TPC clustering efficiency systematic error for all four samples in terms of the reconstructed lepton momentum (left distributions) and angle (red distributions). The black line shows the error for FGD1 samples, and red for FGD2 samples.

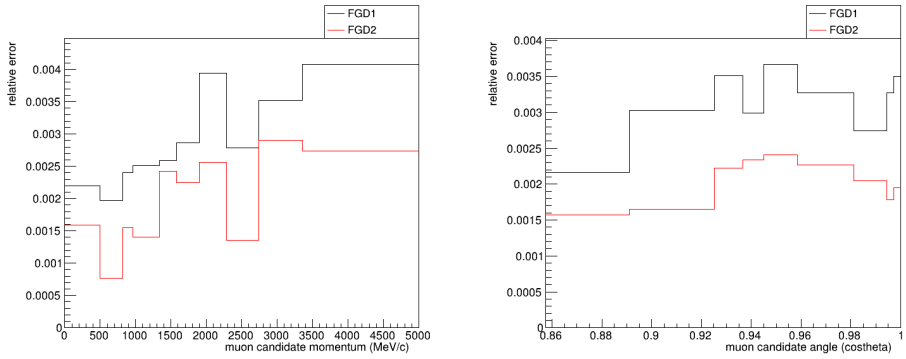

Figure B.9: Average differential detector uncertainty for Michel electron systematic error for all four samples in terms of the reconstructed lepton momentum (left distributions) and angle (red distributions). The black line shows the error for FGD1 samples, and red for FGD2 samples.

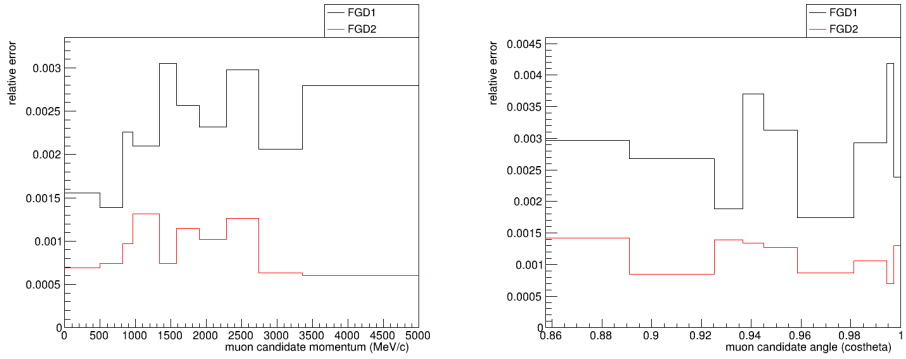

Figure B.10: Average differential detector uncertainty for FGD hybrid tracking efficiency systematic error for all four samples in terms of the reconstructed lepton momentum (left distributions) and angle (red distributions). The black line shows the error for FGD1 samples, and red for FGD2 samples.

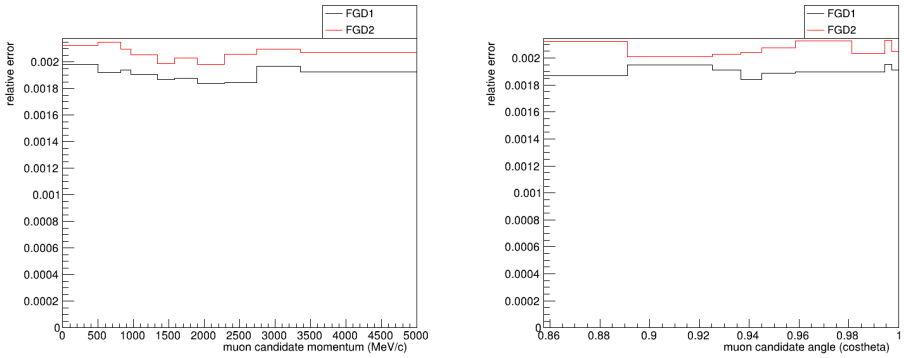

Figure B.11: Average differential detector uncertainty for pileup systematic error for all four samples in terms of the reconstructed lepton momentum (left distributions) and angle (red distributions). The black line shows the error for FGD1 samples, and red for FGD2 samples.

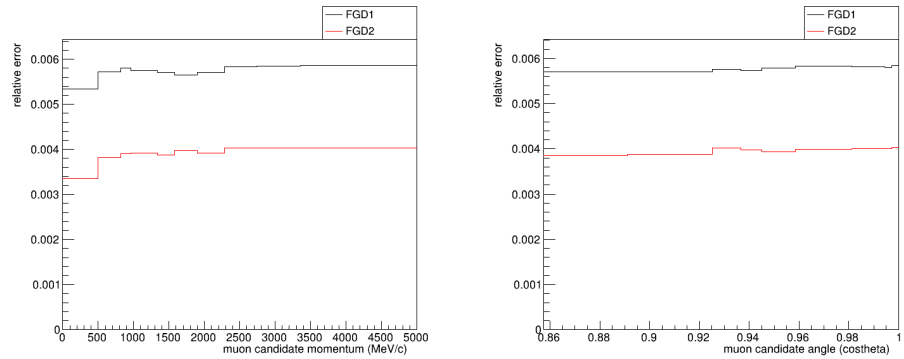

Figure B.12: Average differential detector uncertainty for FGD mass systematic error for all four samples in terms of the reconstructed lepton momentum (left distributions) and angle (red distributions). The black line shows the error for FGD1 samples, and red for FGD2 samples.

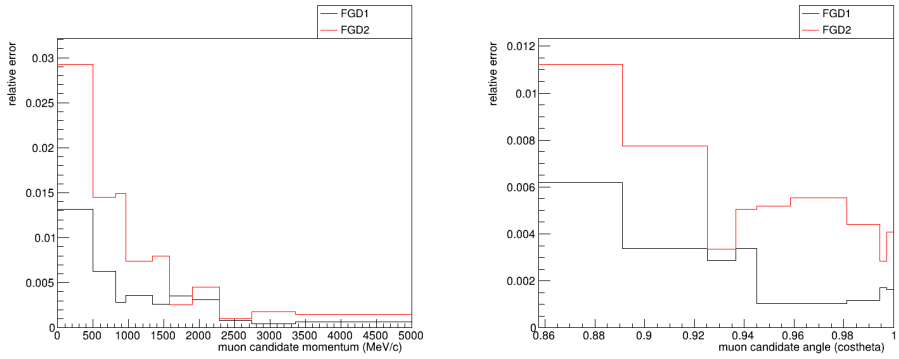

Figure B.13: Average differential detector uncertainty for OOFV systematic error for all four samples in terms of the reconstructed lepton momentum (left distributions) and angle (red distributions). The black line shows the error for FGD1 samples, and red for FGD2 samples.

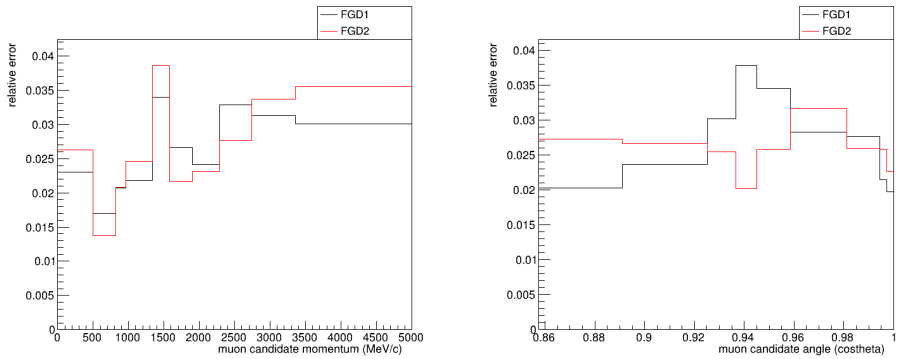

Figure B.14: Average differential detector uncertainty for SI pion systematic error for all four samples in terms of the reconstructed lepton momentum (left distributions) and angle (red distributions). The black line shows the error for FGD1 samples, and red for FGD2 samples.

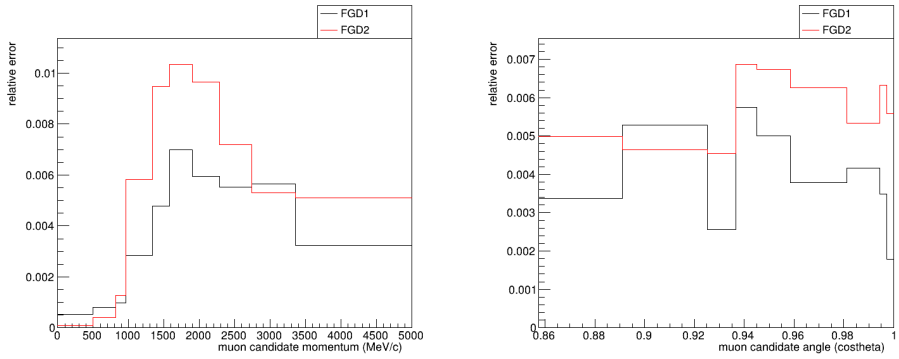

Figure B.15: Average differential detector uncertainty for SI proton systematic error for all four samples in terms of the reconstructed lepton momentum (left distributions) and angle (red distributions). The black line shows the error for FGD1 samples, and red for FGD2 samples.

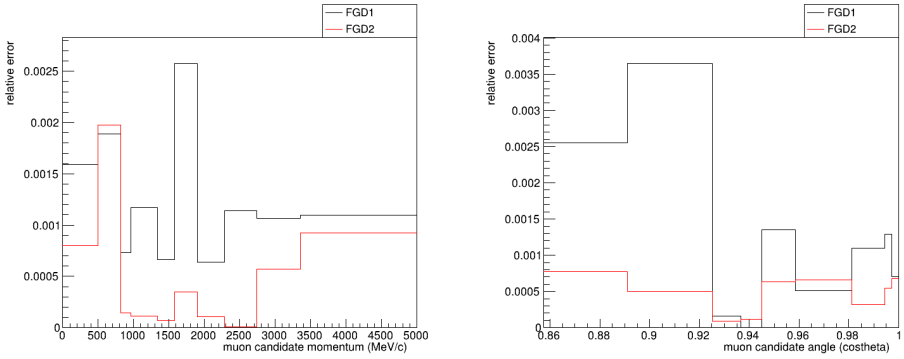

Figure B.16: Average differential detector uncertainty for ECal PID systematic error for all four samples in terms of the reconstructed lepton momentum (left distributions) and angle (red distributions). The black line shows the error for FGD1 samples, and red for FGD2 samples.

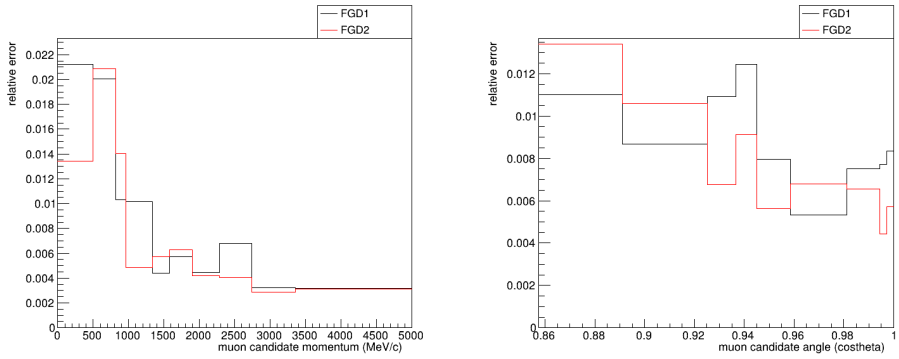

Figure B.17: Average differential detector uncertainty for ECal photon pileup systematic error for all four samples in terms of the reconstructed lepton momentum (left distributions) and angle (red distributions). The black line shows the error for FGD1 samples, and red for FGD2 samples.

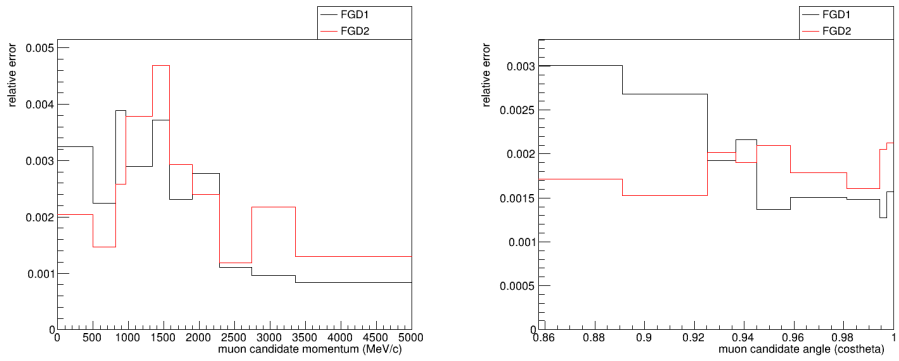

Figure B.18: Average differential detector uncertainty for TPC-ECal matching efficiency systematic error for all four samples in terms of the reconstructed lepton momentum (left distributions) and angle (red distributions). The black line shows the error for FGD1 samples, and red for FGD2 samples.

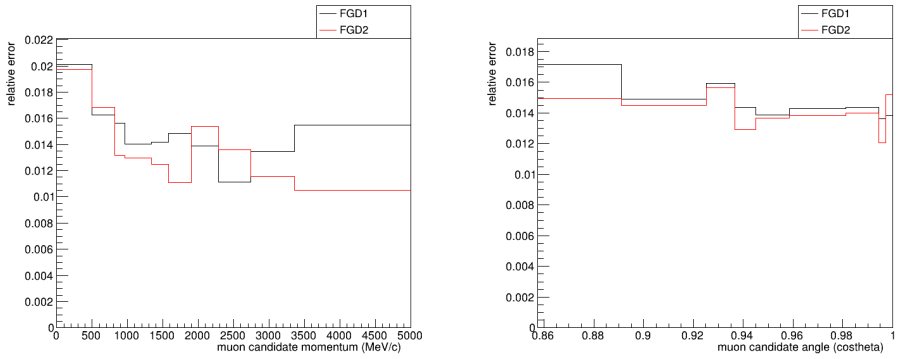

Figure B.19: Average differential detector uncertainty for ECal tracking efficiency systematic error for all four samples in terms of the reconstructed lepton momentum (left distributions) and angle (red distributions). The black line shows the error for FGD1 samples, and red for FGD2 samples.

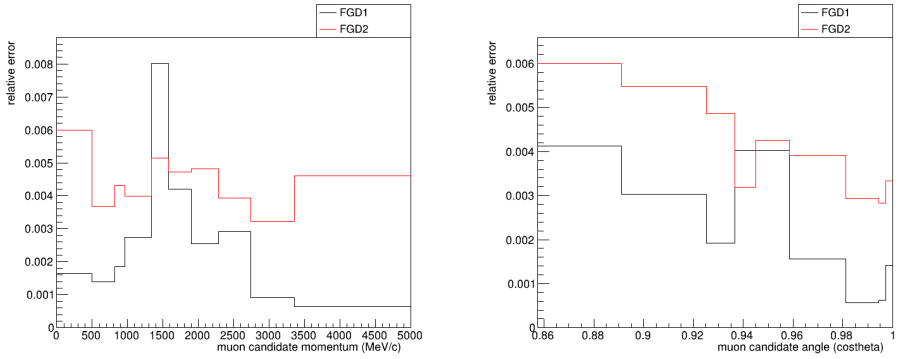

Figure B.20: Average differential detector uncertainty for muon PID BDT systematic error for the CCPhoton sample in terms of the reconstructed lepton momentum (left distributions) and angle (red distributions). The black line shows the error for FGD1 samples, and red for FGD2 samples.

Appendix C

ND Fit Cross Section Parameters

The cross section parameters used in the ND fit is shown with the implementation method and prior values and uncertainties are shown.

Parameter	Type	Prefit
CCQE		
M_{QE}^{A}	Spline	1.03 ± 0.06
Q^2 norm 1	Norm	1 ± 0.11
Q^2 norm 2	Norm	1 ± 0.18
Q^2 norm 3	Norm	1 ± 0.40
S-Shell MF norm ^{12}C	Norm	0 ± 0.2
P-Shell MF norm ^{12}C	Norm	0 ± 0.45
S-Shell MF norm ^{16}O	Norm	0 ± 0.75
$P_{1/2}$-Shell MF norm ^{16}O	Norm	0 ± 0.45
$P_{3/2}$-Shell MF norm ^{16}O	Norm	0 ± 0.25
SRC norm ^{12}C	Norm	1 ± 2
SRC norm ^{16}O	Norm	1 ± 2
S-Shell MF p_{miss} shape ^{12}C	Shape	0 ± 1
P-Shell MF p_{miss} shape ^{12}C	Shape	0 ± 1
S-Shell MF p_{miss} shape ^{16}O	Shape	0 ± 1
$P_{1/2}$-Shell MF p_{miss} shape ^{16}O	Shape	0 ± 1
$P_{3/2}$-Shell MF p_{miss} shape ^{16}O	Shape	0 ± 1
Pauli blocking ^{12}C ν	Shape	0 ± 1
Pauli blocking ^{16}O ν	Shape	0 ± 1
Pauli blocking ^{12}C $\bar{\nu}$	Shape	0 ± 1
Pauli blocking ^{16}O $\bar{\nu}$	Shape	0 ± 1
RPA ^{12}C $\bar{\nu}$ 0 - 2	Shape	0 ± 1
RPA ^{12}C ν 0 - 2	Shape	0 ± 1
RPA ^{16}O $\bar{\nu}$ 0 - 2	Shape	0 ± 1
RPA ^{16}O ν 0 - 2	Shape	0 ± 1
FSI ^{12}C $\bar{\nu}$ 0 - 2	Shape	0 ± 1
FSI ^{12}C ν 0 - 2	Shape	0 ± 1
FSI ^{16}O $\bar{\nu}$ 0 - 2	Shape	0 ± 1
FSI ^{16}O ν 0 - 2	Shape	0 ± 1
SRC Pair Frac ^{12}C	Norm	0.3 ± 0.33
SRC Pair Frac ^{16}O	Norm	0.3 ± 0.33
SRC Shape ^{12}C	Shape	0 ± 2
SRC Shape ^{16}O	Shape	0 ± 2
Binding Energy		
Eb C ν	Shape	2 ± 6
Eb C $\bar{\nu}$	Shape	0 ± 6
Eb O ν	Shape	4 ± 6
Eb O $\bar{\nu}$	Shape	0 ± 6
Eb α	Shape	0 ± 1

Table C.1: The CCQE parameters included in the ND fit, with the parameter type described and their prior values and uncertainties.

2p2h		
2p2h norm ν	Norm	1 ± 1
2p2h norm $\bar{\nu}$	Norm	1 ± 1
2p2h norm C to O	Norm	1 ± 0.2
2p2h E_{dep} low E_ν	Shape	0 ± 3
2p2h E_{dep} high E_ν	Shape	0 ± 3
2p2h E_{dep} low $E_{\bar{\nu}}$	Shape	0 ± 3
2p2h E_{dep} high $E_{\bar{\nu}}$	Shape	0 ± 3
PNNN Shape	Shape	0 ± 0.33
2p2h shape C np	Shape	1 ± 1
2p2h shape C NN	Shape	1 ± 1
2p2h shape O np	Shape	1 ± 1
2p2h shape O NN	Shape	1 ± 1
SPP		
C^5_{RES}	Shape	1.06 ± 0.1
M^A_{RES}	Shape	0.91 ± 0.1
Non-Res $I_{1/2}$	Shape	1.21 ± 0.27
Non-Res $I_{1/2}$ Low p_π	Shape	1.3 ± 1.3
RS Δ decay	Shape	1 ± 1
SPP π^0 norm ν_μ	Norm	1 ± 0.3
SPP π^0 norm $\nu_{\bar{\mu}}$	Norm	1 ± 0.3
RES E_b ^{12}C ν	Shape	25 ± 25
RES E_b ^{16}O ν	Shape	25 ± 25
RES E_b ^{12}C $\bar{\nu}$	Shape	25 ± 25
RES E_b ^{16}O $\bar{\nu}$	Shape	25 ± 25
Multi-pion and DIS		
Mπ Multi TotXSec	Shape	0 ± 1
Mπ BY Vector	Shape	0 ± 1
Mπ BY Axial	Shape	0 ± 1
Mπ Multi shape	Shape	0 ± 1
CC BY DIS	Shape	0 ± 1
CC DIS Multiπ Norm ν	Norm	1 ± 0.035
CC DIS Multiπ Norm $\bar{\nu}$	Norm	1 ± 0.065
CC Misc	Norm	1 ± 1

Table C.2: The 2p2h, RES, DIS parameters included in the ND fit, with the parameter type described and their prior values and uncertainties.

FSI		
FEFQE	Shape	1.069 ± 0.313
FEFQEH	Shape	1.824 ± 0.859
FEFINEL	Shape	1.002 ± 1.101
FEFABS	Shape	1.404 ± 0.432
FEFCX	Shape	0.697 ± 0.305
FEFCXH	Shape	1.800 ± 0.288
Nucleon FSI Scattering	Shape	1 ± 0.3
Nucleon FSI SPP	Shape	1 ± 0.3
Other		
CC COH ^{12}C	Norm	1 ± 0.3
CC COH ^{16}O	Norm	1 ± 0.3
NC COH	Norm	1 ± 0.3
NC 1γ	Norm	1 ± 1
NC other near	Norm	1 ± 0.3
NC other far	Norm	1 ± 0.3
CC norm ν	Norm	1 ± 0.2
CC norm $\bar{\nu}$	Norm	1 ± 0.1
ν_e/ν_μ	Norm	1 ± 0.0282843
$\bar{\nu}_e/\bar{\nu}_\mu$	Norm	1 ± 0.0282843

Table C.3: The other parameters included in the ND fit, with the parameter type described and their prior values and uncertainties.

Bibliography

[1] F. Wilson. Fermi's theory of beta decay. *American Journal of Physics*, 36:1150, Dec 1968.

[2] J. Chadwick. Intensitätsverteilung im magnetischen Spectrum der β-Strahlen von radium B + C. *Verhandl. Dtsc. Phys. Ges.*, 16:383, 1914.

[3] W. Pauli. Dear radioactive ladies and gentlemen. *Phys. Today*, 31N9:27, 1978.

[4] L. M. Brown. The idea of the neutrino. *Phys. Today*, 31N9:23–28, 1978.

[5] E. Fermi. Tentativo di una teoria dei raggi β. *Il Nuovo Cimento (1924-1942)*, 11(1):1–19, Jan 1934.

[6] C. L. Cowan, F. Reines, F. B. Harrison, H. W. Kruse, and A. D. McGuire. Detection of the free neutrino: A Confirmation. *Science*, 124:103–104, 1956.

[7] G. Danby, J-M. Gaillard, K. Goulianos, L. M. Lederman, N. Mistry, M. Schwartz, and J. Steinberger. Observation of high-energy neutrino reactions and the existence of two kinds of neutrinos. *Phys. Rev. Lett.*, 9:36–44, Jul 1962.

[8] K. Kodama et al. Observation of tau neutrino interactions. *Phys. Lett. B*, 504:218–224, 2001.

[9] M. Goldhaber, L. Grodzins, and A. W. Sunyar. Helicity of neutrinos. *Phys. Rev. Lett.*, 109:1015–1017, Feb 1958.

[10] The KATRIN Collaboration. Direct neutrino-mass measurement with sub-electronvolt sensitivity. *Nature Physics*, 18:160–166, 2022.

[11] The ALEPH Collaboration, The DELPHI Collaboration, The L3 Collaboration, and The OPAL Collaboration. Precision electroweak measurements on the Z resonance. *Physics Reports*, 427(5-6):257–454, May 2006.

[12] K. N. Abazajian et al. Light sterile neutrinos: A white paper. *arXiv:1204.5379 [hep-ph]*, Apr 2012.

[13] J. A. Formaggio and G. P. Zeller. From eV to EeV: Neutrino cross sections across energy scales. *Rev. Mod. Phys.*, 84:1307–1341, Sep 2012.

[14] T. Katori. Meson exchange current (MEC) models in neutrino interaction generators. *arXiv:1304.6014 [nucl-th]*, 2013.

[15] M. Lawe. *Study of Charged Current Neutral Pion Production in the T2K Near Detector*. PhD thesis, University of Sheffield, 2014. Available at `https://etheses.whiterose.ac.uk/8562/`.

[16] D. D'Angelo et al. Recent Borexino results and prospects for the near future. *EPJ Web of Conferences*, 126, 02008, May 2014.

[17] J. N. Bahcall, W. A. Fowler, I. Jr. Iben, and R. L. Sears. Solar neutrino flux. *The Astrophysical Journal*, 137:344–346, Jan 1963.

[18] R. Davis, D. S. Harmer, and K. C. Hoffman. Search for neutrinos from the Sun. *Phys. Rev. Lett.*, 20:1205–1209, May 1968.

[19] K. S. Hirata et al. Observation of ^{8}B solar neutrinos in the Kamiokande-II detector. *Phys. Rev. Lett.*, 63:16–19, Jul 1989.

[20] W. Hampel et al. GALLEX solar neutrino observations: Results for GALLEX IV. *Phys. Lett. B*, 447:127–133, 1999.

[21] J. N. Abdurashitov et al. Measurement of the solar neutrino capture rate with gallium metal. *Phys. Rev. C*, 60:055801, Oct 1999.

[22] Q. R. Ahmad et al. Direct evidence for neutrino flavor transformation from neutral current interactions in the Sudbury Neutrino Observatory. *Phys. Rev. Lett.*, 89:011301, 2002.

[23] T. J. Haines et al. Calculation of atmospheric neutrino-induced backgrounds in a nucleon-decay search. *Phys. Rev. Lett.*, 57:1986–1989, Oct 1986.

[24] K. S. Hirata et al. Observation of a small atmospheric muon-neutrino / electron-neutrino ratio in Kamiokande. *Phys. Lett. B*, 280:146–152, 1992.

[25] Y. Fukuda et al. Evidence for oscillation of atmospheric neutrinos. *Phys. Rev. Lett.*, 81:1562–1567, Aug 1998.

[26] N. Cabibbo. Unitary symmetry and leptonic decays. *Phys. Rev. Lett.*, 10:531–533, Jun 1963.

[27] L. Wolfenstein. Parametrization of the Kobayashi-Maskawa matrix. *Phys. Rev. Lett.*, 51:1945–1947, Nov 1983.

[28] M. Agostini et al. Final results of GERDA on the search for neutrinoless double-β decay. *Phys. Rev. Lett.*, 125:252502, Dec 2020.

[29] D. Q Adams et al. New direct limit on neutrinoless double beta decay half-life of ^{128}Te with cuore. *Phys. Rev. Lett.*, 129:222501, Nov 2022.

[30] S. Abe et al. Search for the majorana nature of neutrinos in the inverted mass ordering region with KamLAND-Zen. *Phys. Rev. Lett.*, 130:051801, Jan 2023.

[31] N. Burlac and G. Salamanna. The LEGEND-200 LAr instrumentation in the search of neutrinoless double beta decay. *Nucl. Instrum. Meth. A*, 1048:167943, 2023.

[32] V. Albanese et al. The SNO+ experiment. *Journal of Instrumentation*, 16(08):P08059, Aug 2021.

[33] J. Baker, R. Arnold, and C. Augier et al. Probing new physics models of neutrinoless double beta decay with SuperNEMO. *Eur. Phys. J. C 70, 927–943*, 2010.

[34] R. N. Cahn, D. A. Dwyer, S. J. Freedman, W. C. Haxton, R. W. Kadel, Yu. G. Kolomensky, K. B. Luk, P. McDonald, G. D. Orebi Gann, and A. W. P. Poon. White paper: Measuring the neutrino mass hierarchy. *arXiv 1307.5487 [hep-ex]*, 2013.

[35] C. Giganti, S. Lavignac, and M. Zito. Neutrino oscillations: The rise of the PMNS paradigm. *Progress in Particle and Nuclear Physics*, 98:1–54, Jan 2018.

[36] A. Alavi-Harati et al. Observation of direct CP violation in $k_{S,L} \to \pi\pi$ decays. *Phys. Rev. Lett.*, 83:22–27, Jul 1999.

[37] S. P. Mikheev and A. Yu. Smirnov. Neutrino Oscillations in an Inhomogeneous Medium: Adiabatic Regime. *Sov. Phys. JETP*, 65:230–236, 1987.

[38] L. Wolfenstein. Neutrino oscillations in matter. *Phys. Rev. D*, 17:2369–2374, May 1978.

[39] S. Abe et al. Precision measurement of neutrino oscillation parameters with KamLAND. *Phys. Rev. Lett.*, 100(22), Jun 2008.

[40] C. D. Shin et al. Observation of reactor antineutrino disappearance using delayed neutron capture on hydrogen at RENO. *Journal of High Energy Physics*, 2020(4):29, Apr 2020.

[41] The Double Chooz Collaboration. Double Chooz θ_{13} measurement via total neutron capture detection. *Nature Physics*, 16(5):558–564, Apr 2020.

[42] The Double Chooz Collaboration. The Double Chooz antineutrino detectors. *The European Physical Journal C*, 82(9):804, Sep 2022.

[43] K. Eguchi et al. First results from KamLAND: Evidence for reactor antineutrino disappearance. *Phys. Rev. Lett.*, 90:021802, Jan 2003.

[44] S. Abe et al. Precision measurement of neutrino oscillation parameters with KamLAND. *Phys. Rev. Lett.*, 100:221803, Jun 2008.

[45] M. H. Ahn et al. Measurement of neutrino oscillation by the K2K experiment. *Physical Review D*, 74(7), Oct 2006.

[46] S. Yamamoto et al. Improved search for $\nu_\mu \rightarrow \nu_e$ oscillation in a long-baseline accelerator experiment. *Phys. Rev. Lett.*, 96(18), May 2006.

[47] P. Adamson et al. First observations of separated atmospheric ν_μ and $\bar{\nu}_\mu$ events in the MINOS detector. *Physical Review D*, 73(7), Apr 2006.

[48] N Agafonova et al. Study of neutrino interactions with the electronic detectors of the OPERA experiment. *New Journal of Physics*, 13(5):053051, May 2011.

[49] P. Adamson et al. Measurement of neutrino and antineutrino oscillations using beam and atmospheric data in MINOS. *Phys. Rev. Lett.*, 110(25), Jun 2013.

[50] D.G. Michael et al. The magnetized steel and scintillator calorimeters of the MINOS experiment. *Nuclear Instruments and Methods in Physics Research Section A: Accelerators, Spectrometers, Detectors and Associated Equipment*, 596(2):190–228, Nov 2008.

[51] P. Adamson et al. Combined analysis of ν_μ disappearance and $\nu_\mu \to \nu_e$ appearance in MINOS using accelerator and atmospheric neutrinos. *Phys. Rev. Lett.*, 112(19), May 2014.

[52] N. Agafonova et al. Discovery of tau neutrino appearance in the CNGS neutrino beam with the OPERA experiment. *Phys. Rev. Lett.*, 115(12), Sep 2015.

[53] K. Abe et al. The T2K experiment. *Nuclear Instruments and Methods in Physics Research Section A: Accelerators, Spectrometers, Detectors and Associated Equipment*, 659(1):106–135, Dec 2011.

[54] P. Adamson et al. First measurement of muon-neutrino disappearance in NOvA. *Physical Review D*, 93(5), Mar 2016.

[55] K. Abe et al. T2K neutrino flux prediction. *Physical Review D*, 87(1), Jan 2013.

[56] Hyper-Kamiokande Proto-Collaboration. Hyper-Kamiokande design report. *arXiv 1805.04163 [physics.ins-det]*, 2018.

[57] B. Abi et al. Deep Underground Neutrino Experiment (DUNE), far detector technical design report, volume I: Introduction to DUNE. *arXiv:2002.02967 [physics.ins-det]*, 2020.

[58] R. Abbasi et al. Strong constraints on neutrino nonstandard interactions from TeV-scale ν_μ disappearance at IceCube. *Phys. Rev. Lett.*, 129:011804, Jun 2022.

[59] S. Aiello et al. Determining the neutrino mass ordering and oscillation parameters with KM3NeT/ORCA. *The European Physical Journal C*, 82(1), Jan 2022.

[60] IceCube Collaboration. Observation of high-energy neutrinos from the galactic plane. *Science*, 380(6652):1338–1343, 2023.

[61] R. L. Workman et al. Review of Particle Physics. *PTEP*, 2022:083C01, 2022.

[62] K. Abe et. al. Solar neutrino measurements in Super-Kamiokande-IV. *Phys. Rev. D*, 94:052010, Sep 2016.

[63] The T2K Collaboration. Constraint on the matter–antimatter symmetry-violating phase in neutrino oscillations. *Nature 520*, pages 339–344, 2020.

[64] M. A. Acero et al. First measurement of neutrino oscillation parameters using neutrinos and antineutrinos by NOvA. *Phys. Rev. Lett.*, 123:151803, Oct 2019.

[65] C.D Shin and Z. Atif et al. Observation of reactor antineutrino disappearance using delayed neutron capture on hydrogen at RENO. *J. High Energ. Phys 29*, 2020.

[66] D. Adey et al. Measurement of the electron antineutrino oscillation with 1958 days of operation at Daya Bay. *Phys. Rev. Lett.*, 121:241805, Dec 2018.

[67] A. Gando et al. Constraints on θ_{13} from a three-flavor oscillation analysis of reactor antineutrinos at KamLAND. *Phys. Rev. D*, 83:052002, Mar 2011.

[68] A. Gando et al. Reactor on-off antineutrino measurement with KamLAND. *Phys. Rev. D*, 88:033001, Aug 2013.

[69] K. Abe et al. Improved constraints on neutrino mixing from the T2K experiment with 3.13×10^{21} protons on target. *Phys. Rev. D*, 103:112008, Jun 2021.

[70] K. Abe et al. J-PARC neutrino beamline upgrade technical design report. *arXiv 1908.05141 [physics.ins-det]*, Aug 2019.

[71] S. Bhadra et al. Optical transition radiation monitor for the T2K experiment. *Nuclear Instruments and Methods in Physics Research Section A: Accelerators, Spectrometers, Detectors and Associated Equipment*, 703:45–58, Mar 2013.

[72] A. Fiorentini et al. Flux prediction and uncertainty updates with NA61 2009 thin 2 target data and negative focussing mode predictions. *Technical Note TN-217*, 2018.

[73] K. Matsuoka et al. Design and performance of the muon monitor for the T2K neutrino oscillation experiment. *Nuclear Instruments and Methods in Physics Research Section A: Accelerators, Spectrometers, Detectors and Associated Equipment*, 624(3):591–600, Dec 2010.

[74] K. Abe et al. Measurements of the T2K neutrino beam properties using the INGRID on-axis near detector. *Nuclear Instruments and Methods in Physics*

Research Section A: Accelerators, Spectrometers, Detectors and Associated Equipment, 694:211–223, Dec 2012.

[75] S. Assylbekov et al. The T2K ND280 off-axis pi–zero detector. *Nuclear Instruments and Methods in Physics Research Section A: Accelerators, Spectrometers, Detectors and Associated Equipment*, 686:48–63, Sep 2012.

[76] P. A. Amaudruz et al. The T2K fine-grained detectors. *Nuclear Instruments and Methods in Physics Research Section A: Accelerators, Spectrometers, Detectors and Associated Equipment*, 696:1–31, Dec 2012.

[77] N. Abgrall et al. Time projection chambers for the T2K near detectors. *Nuclear Instruments and Methods in Physics Research Section A: Accelerators, Spectrometers, Detectors and Associated Equipment*, 637(1):25–46, 2011.

[78] D Allan et al. The electromagnetic calorimeter for the T2K near detector ND280. *Journal of Instrumentation*, 8(10):P10019–P10019, Oct 2013.

[79] K. Abe et al. T2K ND280 upgrade – technical design report. *arXiv 1901.03750 [physics.ins-det]*, Oct 2020.

[80] A. Blondel et al. A fully-active fine-grained detector with three readout views. *Journal of Instrumentation*, 13(02):P02006, Feb 2018.

[81] A. Korzenev et al. *Plastic Scintillator Detector with the Readout Based on an Array of Large-Area SiPMs for the ND280/T2K Upgrade and SHiP Experiments.* Physical Society of Japan, 2019.

[82] K. Abe et al. Measurements of $\bar{\nu}_\mu$ and $\bar{\nu_\mu} + \nu_\mu$ charged-current cross-sections without detected pions or protons on water and hydrocarbon at a mean anti-

neutrino energy of 0.86 GeV. *Progress of Theoretical and Experimental Physics*, 2021(4):043C01, Mar 2021.

[83] T. Odagawa et al. Design and performance of a scintillation tracker for track matching in nuclear-emulsion-based neutrino interaction measurement. *Nucl. Instrum. Meth. A*, 1034:166775, May 2022.

[84] M. Antonova et al. Baby MIND: a magnetized segmented neutrino detector for the WAGASCI experiment. *Journal of Instrumentation*, 12(07):C07028–C07028, Jul 2017.

[85] S. Fukuda et al. The Super-Kamiokande detector. *Nuclear Instruments and Methods in Physics Research Section A: Accelerators, Spectrometers, Detectors and Associated Equipment*, 501(2):418–462, Apr 2003.

[86] The T2K Experiment. Sketch of the SK detector located at: `https://www.t2k.org/docs/plotsx/general/t2ksk/`, 2014.

[87] K. Abe et al. Evidence for the appearance of atmospheric tau neutrinos in Super-Kamiokande. *Phys. Rev. Lett.*, 110(18), May 2013.

[88] C. Simpson et al. Sensitivity of Super-Kamiokande with gadolinium to low energy antineutrinos from pre-supernova emission. *The Astrophysical Journal*, 885(2):133, Nov 2019.

[89] K. Abe et al. First gadolinium loading to Super-Kamiokande. *Nuclear Instruments and Methods in Physics Research Section A: Accelerators, Spectrometers, Detectors and Associated Equipment*, 1027:166248, Mar 2022.

[90] K. Fusshoeller et al. Muon antineutrino and neutrino charged-current multiple pion selections in antineutrino mode. *Technical Note TN-273*, 2020.

[91] T. Doyle. *Development of New Off-Axis Near Detector Samples for the T2K Oscillation Analysis*. PhD thesis, Lancaster University, 2022. `https://doi.org/10.17635/lancaster/thesis/1655`.

[92] A. Finch, D. R. Hadley, and T. Wachala. ND280 reconstruction for production 7. *Technical Note TN-329*, 2022.

[93] Y. Hayato. A neutrino interaction simulation program library NEUT. *Acta Physica Polonica B, 40(9):2477-2489*, July 2009.

[94] O. Benhar, A. Fabrocini, and S. Fantoni. The Nucleon Spectral Function in Nuclear Matter. *Nucl. Phys. A*, 505:267–299, 1989.

[95] R. A. Smith and E. J. Moniz. Neutrino reactions on nuclear targets. *Nucl. Phys. B*, 43:605, 1972. [Erratum: Nucl.Phys.B 101, 547 (1975)].

[96] R. Gran, J. Nieves, F. Sanchez, and M. J. Vicente Vacas. Neutrino-nucleus quasi-elastic and 2p2h interactions up to 10 GeV. *Physical Review D*, 88(11), Dec 2013.

[97] D. Rein and L. M. Sehgal. Neutrino Excitation of Baryon Resonances and Single Pion Production. *Annals Phys.*, 133:79–153, 1981.

[98] A. Bodek and U. Yang. Update to the Bodek-Yang Unified Model for Electron- and Neutrino- Nucleon Scattering Cross Sections. In *Proceedings of the 35th International Conference of High Energy Physics (ICHEP 2010). July 22-28*, page 292, Jan 2010.

[99] T. Sjostrand. High-energy physics event generation with PYTHIA 5.7 and JETSET 7.4. *Comput. Phys. Commun.*, 82:74–90, 1994.

[100] A. Ershova et al. Study of final-state interactions of protons in neutrino-nucleus scattering with INCL and NuWro cascade models. *Phys. Rev. D*, 106:032009, Aug 2022.

[101] S. Agostinelli et al. Geant4—a simulation toolkit. *Nuclear Instruments and Methods in Physics Research Section A: Accelerators, Spectrometers, Detectors and Associated Equipment*, 506(3):250–303, 2003.

[102] C. Bojechko et al. CC multiple plion nu-mu event selctions in the ND280 tracker using run 1+2+3+4 data. *Technical Note TN-152*, 2013.

[103] G. Barker et al. Implementation of the second generation PID for the ND280 tracker ECals. *Technical Note TN-111*, 2012.

[104] P. Bartet et al. ν_μ CC event selections in the ND280 tracker using run 2+3+4 data. *Technical Note TN-212*, 2015.

[105] T. A. Doyle et al. ND280 FHC samples with photon and proton information for the 2021 oscillation analysis. *Technical Note TN-421*, 2022.

[106] K. Yasutome et al. Six sample joint oscillation analysis with T2K run1–10 data including a new multi-ring μ like sample. *Technical Note TN-430*, 2023.

[107] A. Blanchet et al. Generic fitter for upgraded near detector analysis methods. *Technical Note TN-458*, 2023.

[108] E. Atkin et al. Measuring oscillation parameters in a joint ND280+SK analysis using Markov chain Monte Carlo methods. *Technical Note TN-429*, 2024.

[109] Y-H.Xu. ν_μ CC selection with improved acceptance for the near detector fits. *Technical Note TN-453*, 2022.

[110] C. Wret. Updated production studies without sand. Technical Report TN-395, 2020. Presentation found at `https://t2k.org/asg/fluxmeasure/2020meetings/8-december-2020/nd-fit-with-new-psyche-new-production-no-sand`.

[111] K. Abe et al. Measurements of neutrino oscillation parameters from the T2K experiment using 3.6×10^{21} protons on target. *The European Physical Journal C*, 83(9), Sep 2023.

[112] N. Abgrall et al. Measurements of $\pi^{\pm}$, $k^{\pm}$, k^0_s, λ and proton production in proton–carbon interactions at 31 GeV/c with the NA61/SHINE spectrometer at the CERN SPS. *The European Physical Journal C*, 76(2), Feb 2016.

[113] L. Berns et al. Flux prediction and uncertainty with NA61/SHINE 2010 replica target measurements. *Technical Note TN-401*, 2022.

[114] J. Chakrani et al. NIWG model and uncertainties for 2021 oscillation analysis. *Technical Note TN-414*, 2021.

[115] O. Benhar, A. Fabrocini, S. Fantoni, and I. Sick. Spectral function of finite nuclei and scattering of GeV electrons. *Nucl. Phys. A*, 579:493–517, 1994.

[116] E. Atkin et al. NIWG model and uncertainties for 2019-2020 oscillation analysis. *Technical Note TN-344*, 2020.

[117] L. Aliaga et al. Design, calibration, and performance of the MINERvA detector. *Nuclear Instruments and Methods in Physics Research Section A: Accelerators, Spectrometers, Detectors and Associated Equipment*, 743:130–159, Apr 2014.

[118] A. Bodek. Pauli blocking for a relativistic fermi gas in quasielastic lepton nucleus scattering. *arXiv:2111.03631 [nucl-th]*, 2021.

[119] A. Redij and C. Wilkinson. Implementation of the random phase approximation model in NEUT and NIWGReweight. *Technical Note TN-207*, 2014.

[120] M. Martini, M. Ericson, G. Chanfray, and J. Marteau. Unified approach for nucleon knock-out and coherent and incoherent pion production in neutrino interactions with nuclei. *Physical Review C*, 80(6), Dec 2009.

[121] A. Higuera et al. Measurement of coherent production of $\pi^{\pm}$ in neutrino and antineutrino beams on carbon from e_{ν} of 1.5 to 20 GeV. *Phys. Rev. Lett.*, 113(26), Dec 2014.

[122] T. Yang, C. Andreopoulos, H. Gallagher, and P. Kehayias. A hadronization model for the MINOS experiment. *AIP Conf. Proc.*, 967(1):269–275, 2007.

[123] A. Bodek and U. Yang. Axial and vector structure functions for electron- and neutrino- nucleon scattering cross sections at all q^2 using effective leading order parton distribution functions. *arXiv 1011.6592 [hep-ph]*, 2013.

[124] E. Miller. Reparameterisation of ND280 detector systematics for the 2024 oscillation analysis. *Technical Note TN-464*, 2023.

[125] R. Brun and F. Rademakers. ROOT — an object oriented data analysis framework. *Nuclear Instruments and Methods in Physics Research Section A:*

Accelerators, Spectrometers, Detectors and Associated Equipment, 389(1):81–86, 1997.

[126] D. Barrow et al. SK atmospheric T2K beam joint fit technical note, MaCh3 details. *Technical Note TN-426*, 2022.

[127] W. K. Hastings. Monte Carlo sampling methods using Markov chains and their applications. *Biometrika*, 57(1):97–109, Apr 1970.

[128] K. Skwarczynski. *Constraining neutrino cross-section and flux models using T2K Near Detector with proton information in Markov chain Monte Carlo framework.* PhD thesis, National Centre for Nuclear Research, 2023. Available at `https://bip.ncbj.gov.pl/artykuly/89/postepowania-doktorskie`.

[129] S. Brooks, A. Gelman, G. Jones, and X. L. Meng. *Handbook of Markov Chain Monte Carlo (1st ed.).* Chapman and Hall/CRC, 2011.

[130] M. Scott. An intermediate water cherenkov detector at J-PARC. In *Proceedings of the 10th International Workshop on Neutrino-Nucleus Interactions in Few-GeV Region (NuInt15).* Journal of the Physical Society of Japan, Dec 2016.

[131] J. Kisiel. Photodetection and electronic system for the Hyper-Kamiokande water Cherenkov detectors. *Nuclear Instruments and Methods in Physics Research Section A: Accelerators, Spectrometers, Detectors and Associated Equipment*, 1055:168482, 2023.

[132] G. Burton et al. OD design summary report. *Technical Note TN-0055*, 2023.

[133] The Hyper-Kamiokande Collaboration. Supply of low and high voltage boards for the Hyper-Kamiokande detector. *Technical Note TN-0044*, 2023.

[134] The Hyper-Kamiokande Collaboration. Outer Detector Technical Report. *Technical Note TN-0064*, 2022.

[135] M. Lamers James. The Hyper-Kamiokande Outer Detector. Poster presented at Lepton Photon, Melbourne, 2023.

[136] T. Dealtry et al. Hyper-K DAQ: Initial design technical note. *Technical Note TN-0073*, 2023.

[137] H. O'Keeffe. Hyper-Kamiokande: Electronics, DAQ, simulation and construction. Presentation at NNN17, 2017.

[138] F. Nova. GPU in modern detectors. Presentation at NNN17, 2017.

[139] K. Abe et al. Real-time supernova neutrino burst monitoring at Super-Kamiokande. *Astrophys. J.*, 2016.

[140] K. Abe et al. J-PARC neutrino beamline upgrade technical design report. *arXiv 1908.05141 [physics.ins-det]*, 2019.

[141] T. Dealtry. Hyper-Kamiokande oscillation physics. Presentation at NuPhys, 2023.

[142] L. K. Pik. *Study of the neutrino mass hierarchy with the atmospheric neutrino data collected in Super-Kamiokande IV*. PhD thesis, Kyoto University, 2019. Available at `https://www-sk.icrr.u-tokyo.ac.jp/sk/_pdf/articles/mjiang_dt.pdf`.

[143] H. Janka. Explosion mechanisms of core-collapse supernovae. *Annual Review of Nuclear and Particle Science*, 62(1):407–451, 2012.

[144] K. Hirata et al. Observation of a neutrino burst from the supernova SN1987A. *Phys. Rev. Lett.*, 58:1490–1493, Apr 1987.

[145] T. Haines et al. Neutrinos from SN1987a in the IMB detector. *Nuclear Instruments and Methods in Physics Research Section A: Accelerators, Spectrometers, Detectors and Associated Equipment*, 264(1):28–31, 1988.

[146] E. N. Alekseev, L. N. Alekseeva, I. V. Krivosheina, and V. I. Volchenko. Detection of the Neutrino Signal from Supernova 1987A Using the INR Baksan Underground Scintillation Telescope. In *European Southern Observatory Conference and Workshop Proceedings*, volume 26 of *European Southern Observatory Conference and Workshop Proceedings*, page 237, Jan 1987.

[147] Al Kharusi et al. SNEWS 2.0: a next-generation supernova early warning system for multi-messenger astronomy. *New Journal of Physics*, 23(3):031201, Mar 2021.

[148] K. Abe et al. Supernova model discrimination with Hyper-Kamiokande. *The Astrophysical Journal*, 916(1):15, Jul 2021.

[149] J. Hisano. Proton decay in SUSY GUTs. *Progress of Theoretical and Experimental Physics*, 2022(12):12B104, Jan 2022.

[150] V. A Kudryavtsev and for the DUNE Collaboration. Underground physics with dune. *Journal of Physics: Conference Series*, 718(6):062032, May 2016.

[151] T. Dealtry, A. Himmel, J. Hoppenau, and J. Lozier. Simulating water cherenkov detectors using WCSim. Software found at: `https://github.com/WCSim/WCSim`.

[152] M Friend. J-PARC accelerator and neutrino beamline upgrade programme. *Conf. Ser. 888 012042*, 2017.

[153] Y. Nishimura. The box-and-line PMT (R12860). *Technical Note TN-0009*, 2020.

[154] FD2 Photosensor sub WG. Characterization of photomultiplier tubes for the FD mPMT in Hyper-Kamiokande. *Technical Note Hyper-Kamiokande TN-0049*, 2023.

[155] K. Abe et al. Supernova model discrimination with Hyper-Kamiokande. *The Astrophysical Journal*, 916(1):15, July 2021.